博士論文

# Molecular Studies of Solvation for Polymers in Ionic Liquids

**(イオン液体中における高分子の溶媒和に関する分子論的研究)**

廣澤　和

# Contents

# Chapter 1

# General Introduction

## 1.1 Ionic Liquids

Ionic liquids (ILs) are molten salts having melting temperatures lower than 100 °C.[1] In general, ionic substances have much higher melting temperature than room temperature because they are easily crystallized by strong Coulombic interactions between their components. For example, NaCl has melting temperature at 801 °C. As you know, salts have not been regarded as solvents because their melting tempratures are too high. However, there are salts which have lower melting temperature than 100 °C, and they are called ILs. ILs exist as liquid at moderate temperature and can be used as "solvents" in vairous processes, including extraction, chemical reactions, electrochemical processes, and dissolution of solutes having poor solubility into conventional solvents. ILs are regarded as solvents which are composed of only ions. Thus, their physical properties are very different from conventional neutral molecular solvents or water. For example, ILs exhibit high ion conductivity because their components are dessociated ions. In addition, ILs have negligible volatility due to strong and complicated interactions between IL-ions such as Coulombic interactions, hydrogen bonds, and van der Waals interactions. Furthermore, typical ILs are thermally stable and non-flammable and they can be used as solvents even under harsh environments.[2]

Here, I summarize the history of ILs briefly.[3] The firstly reported IL is $[EtNH_3][NO_3]$ which was found by Walden in 1914.[4] The melting point of $[EtNH_3][NO_3]$ is 12 °C and it can be regarded as a room temperature IL. Subsequently, about 50 years later, Yoke *et al.* reported that mixtures of copper chlorides and alkylammonium chlorides have melting temperature around room temperature.[5] In 1970-1980s, chloroaluminate-based molten salt mixtures were developed.[6–9] Through the pioneering works by Osteryoung and Hussey, it was found that mixtures

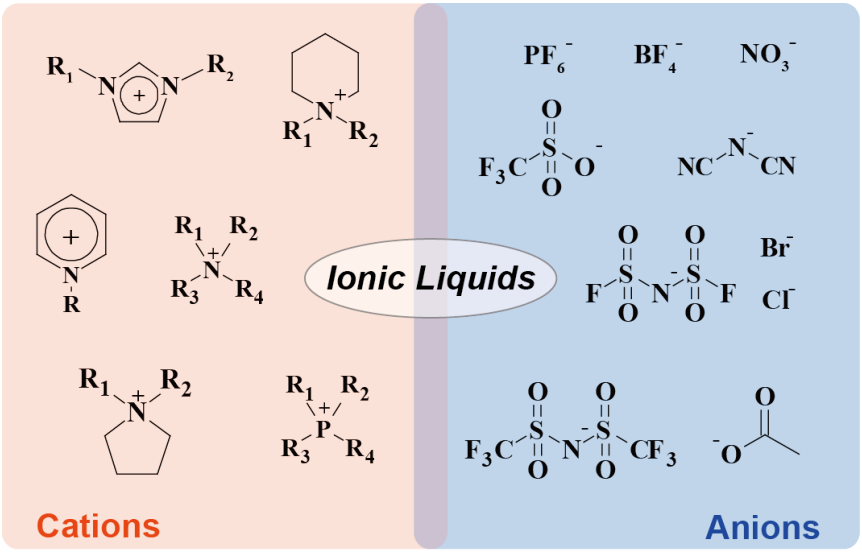


Figure 1.1: Chemical structures of typical cation and anion species of ionic liquids.

of *N*-butylpyridinium chloride ($[C_4Py][Cl]$)/$AlCl_3$ and 1-ethyl-3-methylimidazolium chloride ($[C_2mIm][Cl]$)/$AlCl_3$ have melting points lower than 40 °C.[7,8] Importantly, they also showed that the molten salt mixtures can be used as electrolytes for batteries and spectroscopic solvents. Despite their superior electrochemical properties to conventional solvents, the chloroaluminate-based salt mixtures have disadvantage of being reactive with water and air. The disadvantage seriously prevented application of the chloroaluminate-based salt mixtures. In 1992, Wilkes *et al.* reported an IL, 1-ethyl-3-methylimidazolium tetrafluoroborate ($[C_2mIm][BF_4]$, melting point: 15 °C) which can be easily handled under the coexistence of air and water.[10] The report remarkablly extended the range of application of ILs. Since then, ILs have attracted attention as novel solvents in various research fields and numerous ILs have been developed until now.

Typical cation and anion species of ILs are summarized in Figure 1.1. As shown in Figure 1.1, the IL ions have common structural features. At first, IL ions, especially cations, have bulky structure and charge of the ions are delocalized. Combination of smaller ions results in rather high melting temperature (for example, NaCl, KCl, and LiBr). Regarding this point, Ueno *et al.* discussed the degree of dissociation, *i.e.*, "ionicity" of ion species in ILs based on physicochemical properties of the ions.[11] In their report, the ionicity was defined as the proportion of ions that contribute to ionic conduction from all the diffusing species. They evaluated the ionicity for various ILs and pointed out that the ionicity of IL ions are strongly correlated with Lewis acidity of cation species and Lewis basicity of anion species

(Figure 1.2); the lower Lewis acidity of cations (or Lewis basicity of anions) is, the higher the ionicity of ILs becomes. Thus, the charge delocalization in ion species is an important factor for increasing the ionicity of ILs, and further lowering their melting temperatures. In addition, the structure of IL ions is often asymmetric and

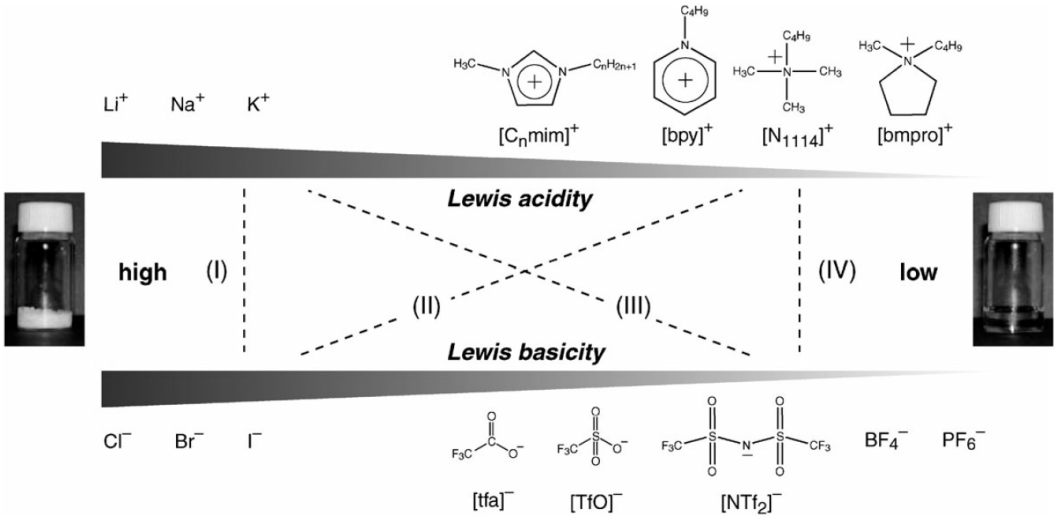


Figure 1.2: Typical ion species of ILs arranged in order of Lewis acidity for cations and Lewis basicity for anions. Combination of ions are classified into (I) strong Lewis acid and strong Lewis base, (II) weak Lewis acid and strong Lewis base, (III) strong Lewis acid and weak Lewis base, and (IV) weak Lewis acid and weak Lewis base.[11]

conformationally flexible. Hamaguchi and Holbrey found the crystal polymorphism for 1-butyl-3-methylimidazolium chloride ([$C_4$mIm][Cl]), indicating the coexistence of two distinct conformers of $[C_4mIm]^+$ in liquid state of $[C_4mIm]^+$-based ILs.[12–15] Berg *et al.* confirmed the conformational equilibrium of the conformers in liquid state of imidazolium-based ILs by means of Raman spectroscopy and *ab initio* calculations.[16] Furthermore, such strucrual isomerism was also observed for a flexible anion species, bis(trifluoromethanesulfonyl)amide ($[TFSA]^-$).[17] The coexistence of structural isomers of ions increases conformational entropy in liquid state of ILs, which results in lowering of melting temperature. Hence, flexibility and assymetry of the ions' structure are also important feature for ILs to exist as liquid at low temperature.

Figure 1.1 also shows that there are many variations of cation and anion species of ILs. Therefore, the solvation atmosphere of ILs can be controlled to construct specific affinities to target solute by designing structure of IL ions. By utilizing the designability of the solvation atomosphere, various ILs have been developed for many applications. In the following section, I introduce several important applications of ILs.

## 1.2 Dissolution of Various Solutes into Ionic Liquids

ILs have unique solvation environment due to their high ionic atmosphere. Therefore, extraction of molecules or ions from water by ILs has attracted attention. It was reported that ILs can extract organic compounds,[18] metal ions,[19,20] and proteins[21] from aqueous phase with large distribution coefficient. Importantly, thermoresponsive liquid-liquid phase separation is often observed for binary systems of ILs/water or ILs/organic solvents.[22–26] The response of miscibility to external stimuli enables more efficient extraction of solute by ILs. Ohno *et al.* developed an IL whose mixture with water shows liquid-liquid phase separation by heating, and utilized the IL for extraction of a protein from aqueous solution.[27] The IL/water mixture shows phase separation at higher temperature than 22 °C. One can extract protein from aqueous solution by simply changing temperature of the IL/water mixture as shown in Figure 1.3. As ILs are non-volatile and chemically stable, they do not emit volatile organic compound into environment. Thus, ILs are expected to be novel media for "clean" liquid-liquid extraction.[18]

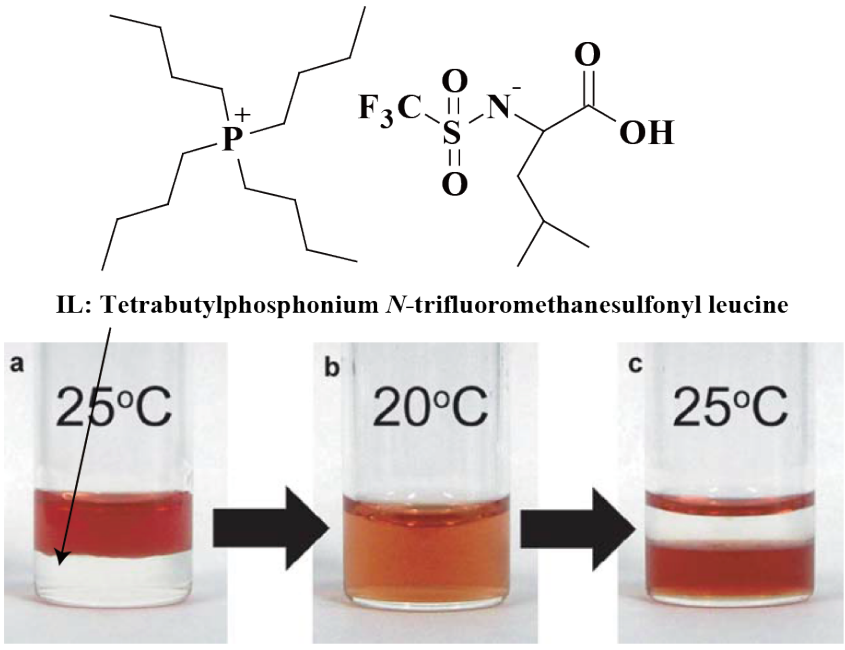


Figure 1.3: Extraction of a protein, cytochrome C from aqueous phase (upper phase) to IL phase (lower phase) by temperature change. (a) an aqueous solution of cytochrome C was added to the IL at 25 °C; (b) the homogeneous IL/water mixture was obtained at 20 °C; (c) biphasic mixture was regenerated at 25 °C and cytochrome C was extracted into the IL phase.[27]

Another popular application of ILs in chemical industry is for electrochemical devices such as fuel cells,[28,29] actuators[30,31] and lithium-ion batteries.[2] Several

kinds of IL-based electrolytes (for example, LiTFSA/1-ethyl-3-methylimidazolium bis(fluorosulfonyl)imide ([$C_2$mIm][FSA])) are able to contain large amount of $Li^+$ ion and exhibit comparable charge-discharge ability with conventional electrolytes.[32] Recently, Ueno *et al.* reported that an equimolar complex of tetraglyme (G4) and LiTFSA shows IL-like solvent properties: they have thermal stability, low flammability, and low volatility.[33,34] In the complex ([Li(G4)][TFSA]), $Li^+$ ions are solvated by G4 and stably exist as solvated ions (Figure 1.4(a)).[34] [G4(Li)][TFSA] shows desired properties for electrolytes of lithium ion batteries such as high ionicity, high lithium transference number, high $Li^+$ concentration, and electrochemical stability. The IL-based electrolytes are non-volatile and non-flammable media and thus they offer more advanced safety than conventional molecular-solvent-based electrolytes.

Application of ILs for $CO_2$ gas separation is also an important topic. It is reported that imidazolium-based ILs absorb $CO_2$ gas with high selectivity (Figure 1.4(b)).[35,36] Thus, ILs can be used for $CO_2$ separation from mixed gases, for example, containing $H_2$, $N_2$, and $CH_4$. The relation between solubility of $CO_2$ gas and structure of ion species has been studied by Aki *et al.*[37] They pointed out that ILs having flurine-based anions, such as $[TFSA]^-$, $CF_3SO_3^-$, and $PF_6^-$ have high $CO_2$ solubility. It indicates that $CO_2$ is selectively solvated by the fluorine-based anion species. Such a selective solvation is one of the characteristics of ILs.

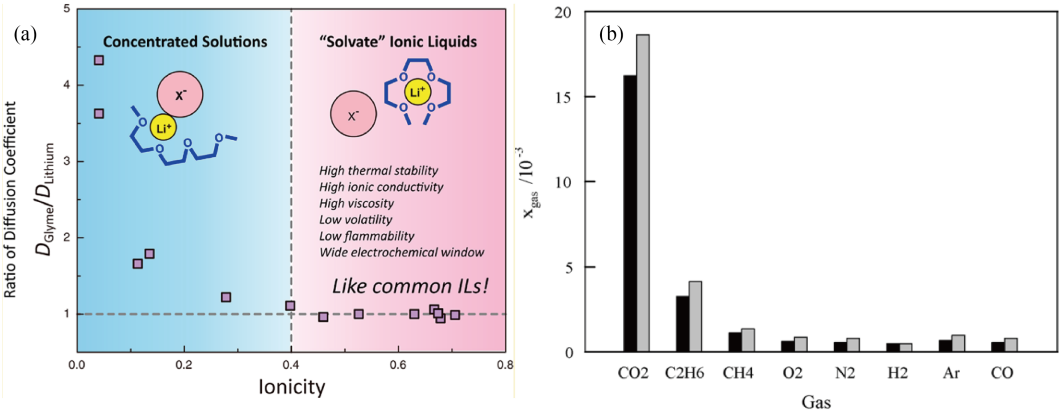


Figure 1.4: (a) Relation between the ionicity and diffusion coefficient of glyme and $Li^+$ in ILs, [Li(G4)][X] where X corresponds to various anion species. $Li^+$ ions are stably solvated by G4 and ionicity of the ions is higher in [Li(G4)][X] having weaker Lewis basic anion, such as $[TFSA]^-$.[34] (b) Mole fraction solubility of gases in [$C_4$mIm][$BF_4$] (dark bars) and in [$C_4$mIm][$PF_6$] (gray bars) at 0.1 MPa partial pressure of the gases at 300 K.[35]

Polymer materials are important in industry due to their flexibility, plasticity, and functionality. By using ILs as solvents for polymers, we can add properties

of ILs to conventional polymer materials. The combination with polymers enables immobilization of ILs by which one can prevent leakage of liquids in various industrial applications of ILs, including batteries and $CO_2$ separation processes mentioned above. Furthermore, there are unique dissolution phenomena of polymers in ILs; ILs often dissolve polymers having poor solubility into conventional solvents. The solvation for polymers in ILs is important from viewpoints of both application and fundamental polymer sciences. I introduce research topics of polymer dissolution phenomena by ILs in the following section.

## 1.3 Application of Ionic Liquids as Solvents for Polymers

### 1.3.1 Dissolution of Cellulose in Ionic Liquids

Native cellulose molecules are insoluble in water and conventional organic solvents due to their multiple intra- and intermolecular hydrogen-bonding networks. Hence, the dissolution process of cellulose into solvents has been a bottleneck in the processing of cellulose. Conventional cellulose processing systems use polar solvents such as *N*-methylmorpholine *N*-oxide (NMMO),[38] $NaOH/CS_2$,[39] $[Cu(NH_3)_4(H_2O)_2](OH)_2$,[40] and LiCl/dimethylacetamide.[41] Even with such solvents, heating at high temperature is often required for dissolution of cellulose. Thus, low energy efficiency, emittion of the toxic vapor into environment, and thermal degradation of the solvents and cellulose itself have been crucial problems in the cellulose processing.[42]

Some kinds of ILs possess dissolution ability for biopolymers such as silk,[43] wool,[44] chitin,[45] and even for cellulose which have poor solubility in conventional solvents. In 2002, Swatloski *et al.* found that an IL, $[C_4mIm][Cl]$ dissolves cellulose at 100 °C.[46] Until now, several cellulose-dissolving ILs have been reported.[42,47–49] The representive cellulose-dissolving ILs are summarized in Figure 1.5. For example, Ohno *et al.*

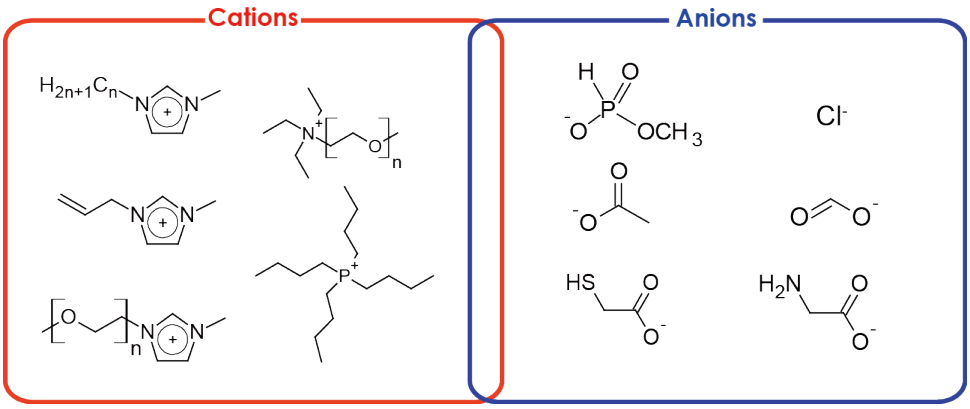


Figure 1.5: Typical cation and anion species which compose cellulose-dissolving ILs.

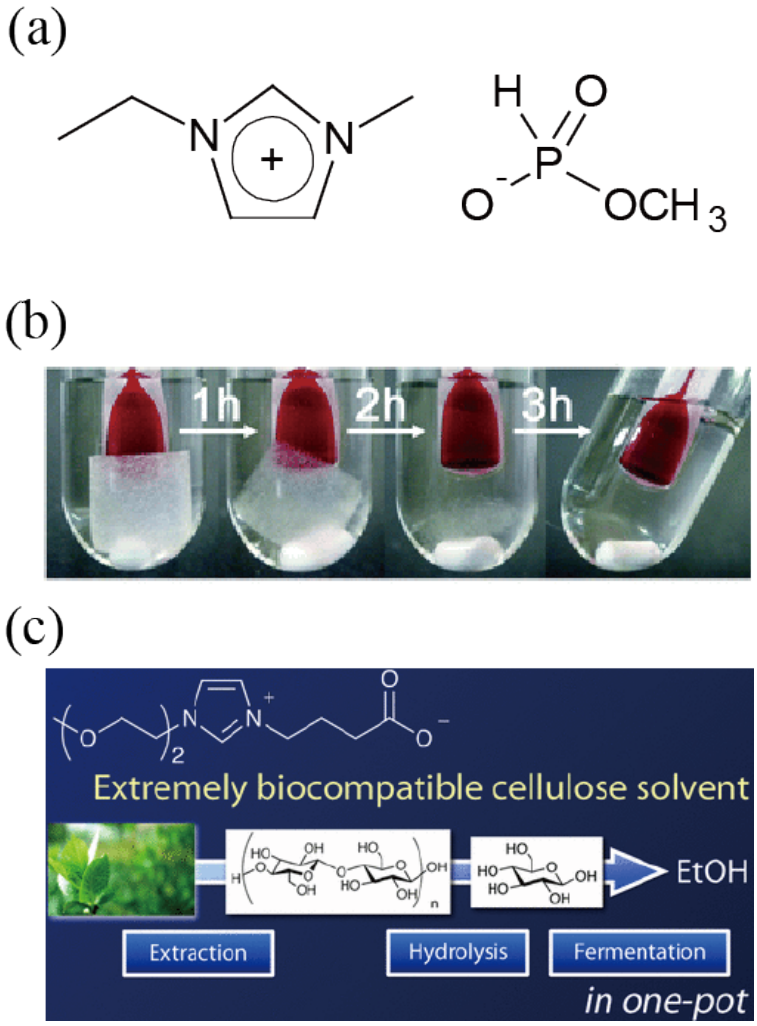


Figure 1.6: (a) Chemical structure of a cellulose-dissolving IL, $[C_2mIm][CH_3HPO_3]$. (b) Dissolution of a cellulose (filter paper: 1 wt%) into an IL, 1-ethyl-3-methylimidazolium methylphosphonate ($[C_2mIm][CH_3HPO_3]$).[48] (c) One-pot conversion of cellulose-containing biomass into ethanol using a liquid zwitterion. At first, cellulose is dissolved in the liquid zwitterion. Subsequently, hydrolysis reaction for cellulose was carried out through dilution of the solution by acetate buffer containing cellulase. Finally, glucose, a product of the hydrolysis reaction, was decomposed into ethanol by addition of a fermentation enzime, *Escherichia coli*.[50]

reported that a phosphonate-based IL, 1-ethyl-3-methylimidazolium methylphosphonate $[C_2mIm][CH_3HPO_3]$ is able to dissolve cellulose at room temperature (Figure 1.6(a), (b)).[48] The IL can extract cellulose from native bran under mild heating condition.[51] For application of the ILs to biomass processing, hydrolysis reaction of cellulose in ILs has been studied.[52,53] Recently, Kuroda *et al.* developed an liquid zwitterion having both cellulose-dissolution ability and biocompatibility.[50] They succeeded in one-pot conversion of a cellulose-containing biomass into ethanol; cellulose is dissolved, hydrolyzed by cellulase, and decomposed into ethanol by fermentation

reaction in the liquid zwitterion (Figure 1.6(c)). As cellulose is the most abundant biomass on the earth, such a simple biomass processing of cellulose using biocompatible ILs is expected to be a green energy production methodology in the future. In the field of biomaterials, fabrication of polysaccharide ion gels and films using ILs is also reported.[54] Because these ILs are capable of dissolving cellulose under mild conditions and they are non-volatile solvent, they allow for improvement in energy efficiency and environment affinity of cellulose processing.

To develop ILs that have higher cellulose-dissolving abilities, or for optimizing cellulose processing conditions, understanding the solvated structure of cellulose in ILs is essential. In general, resolving the microscopic solution structure is simpler for monomeric solutes than for polymeric ones. For this reason, the greater part of structural investigations on cellulolse in IL systems targeted the structure of monosaccharides. From a viewpoint of microscopic interactions between cellulose (or its monomeric unit, glucose or cellobiose) and ILs, solvatochromic analysis was performed and it is found out that hydrogen bond basicity of IL anion species is closely linked to solubility of cellulose in the ILs.[48,55] Furthermore, NMR relaxation measurement[56] and neutron diffraction experiments[57,58] elucidated that anion species of cellulose-dissolving ILs form hydrogen bonds with hydroxyl groups of glucose. It was also reported that the dissolution of cellulose in an IL 1-ethyl-3-methylimidazolium acetate ($[C_2mIm][CH_3COO]$) is exothermal,[59] meaning that the interactions between the IL and cellulose are enthalpically favored. On the chain conformation of cellulose, small-angle X-ray scattering (SAXS) and small-angle neutron scattering (SANS) studies were performed on cellulose in pure IL ($[C_2mIm][CH_3COO]$) and IL containing a co-solvent (DMF/$[C_2mIm][CH_3COO]$ mixture of the molar ratio of 9:1).[60,61] Despite these reports, microscopic solvation structure and mesoscopic chain characteristics of cellulose have not been adequately studied.

### 1.3.2 Phase Transition of Polymers in Ionic Liquids

Stimuli-responsive phase transition of polymers in ILs is also an important research field. As is well-known, poly(*N*-isopropylacrylamide) (PNIPAm) dissolves into water at room temperature but exhibits phase separation at higher temperature than 32 °C.[62] Such phase behavior is called a lower critical solution temperature (LCST)-type phase separation in increasing temperature. LCST-type phase behavior is a common feature of aqueous polymer solution or hydrogel systems; Poly(*N*-alkylacrylamide)s,[63] polyethers,[64–66] and cellulose derivatives[67] having hydrophobic

groups also show LCST-type phase separation in water. From a thermodynamic viewpoint, such LCST-type phase behavior is characterized by negative change in both enthalpy and entropy upon mixing; $\Delta H_{\mathrm{m}} < 0$ and $\Delta S_{\mathrm{m}} < 0$, respectively. In the case of aqueous solution, the origin of negative $\Delta S_{\mathrm{m}}$ is ascribed to formation of the hydration shell around hydrophobic side chains of polymers.[68–71] The thermo-sensitivity of aqueous polymer solutions and hydrogels has been applied for stimuli-sensive polymer materials such as the drug delivery system.[72,73]

On the other hand, an opposite phase behavior, upper critical solution temperature (UCST)-type phase separation has been observed for various polymers in non-aqueous solvents at moderate temperature range.[74–77] For example, polystyrene with high molecular weight in cyclohexane solution exhibits demixing around 30 - 40 °C in decreasing temperature.[77] Several neutral polymers exhibit LCST-type phase behavior in non-aqueous systems at high temperature, typically higher than 150 °C.[74,76–78] Nevertheless, common phase behavior of polymer in non-aqueous solvents around room temperature is UCST-type, not LCST.

Combination of polymer and ILs enables us to add unique properties of ILs to conventional polymer matrials. Especially, immobilization of ILs using polymer gels has been intensively studied for electrochemical applications. Watanabe *et al.* synthesized ion gel by carrying out *in situ* polymerization reaction of methyl methacrylate (MMA) in [$C_2$mIm][TFSA].[79,80] The ion gels can hold large amount of ILs by the effects of osmotic pressure, and they can be used as solid electrolytes in vairous electrochemical devices[81] and gas separation membranes.[82,83] Through the studies for the solubility of polymers and ILs, stimuli-resonsive phase transition of polymers in ILs was found.

It was reported that poly(benzyl methacrylate) (PBnMA) and its derivatives show an LCST-type phase separation in a hydrophobic IL, [$C_2$mIm][TFSA] (Figure 1.7).[85,86] Furthermore, a cross-linked PBnMA gel swollen with [$C_2$mIm][TFSA] shows discontinuous LCST-type volume phase transition by heating.[85] Unlike the case of typical non-aqueous solvents, LCST-type phase separation in ILs is commonly observed for various polymers such as PBnMA derivatives, polyethers, and poly(*n*-butylmethacylate) (PnBMA) at relatively moderate temperature.[84,87–89] It indicates that the ILs construct specific solvation structure around the polymer, as in the case of the hydration shell in aqueous polymer solutions.

The stimuli-responsive polymers can be utilized for fabrication of self-assembly polymer/IL composite materials. It was reported that some kinds of block copoly-

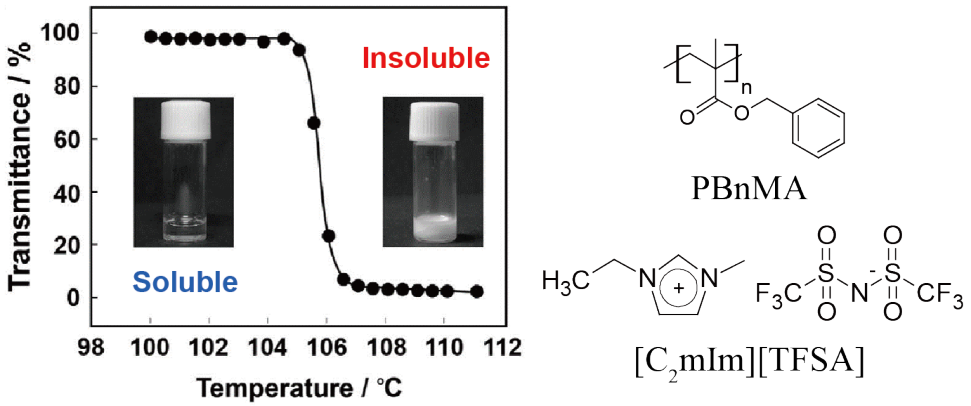


Figure 1.7: Lower critical solution temperature (LCST)-type phase separation of PBnMA in [$C_2$mIm][TFSA] solutions, together with chemical structure of PBnMA and [$C_2$mIm][TFSA].[84]

mers exhibit self-assembly and exhibit unimer-micelle transition[90,91] and sol-gel transition[92–95] in response to temperature change. The thermo-responsive self-assembly dramatically enhances moldability of the ion gels. One of the characteristics of the phase behavior of polymers in ILs is that their phase transition temperatures ($T_c$s) are strongly affected by slight chemical modification on polymer side chain or IL ions. For example, LCST of poly(2-phenylethyl methacrylate) (PPhEtMA), having slightly different chemical structure from PBnMA, is 63 K lower than that of PBnMA.[86] This drastic effect of chemical modifications on $T_c$ indicates that one can control the phase behavior and physical properties of polymer/IL composite systems by designing the chemical structure of polymers or ILs.[94,95]

Several investigations on structural aspects of the thermo-responsive polymer in IL systems have been performed. In 2003, Holbrey *et al.* reported that imidazolium-type ILs form liquid clathrate with alkylbenzenes (Figure 1.8).[96] The clathrate formation is driven by selective solvation of IL cations for the aromatic solutes via cation-$\pi$ interactions. This study indicates that ILs easily form ordered structure in the coexistence of solutes that have specific affinity to IL ion species. The characteristic of ILs as "structure-forming solvents" is similar to $H_2O$: both of ILs and $H_2O$ form partially ordered structure around specific solutes. Furthermore, Fujii *et al.* investigated the solvation structure of monomeric BnMA molecules in [$C_2$mIm][TFSA] by means of high-energy X-ray total scattering and all-atom molecular dynamics (MD) simulations.[97] They found that [$C_2$mIm] cations orderly locate above and below the phenyl group of BnMA whereas [TFSA] anions are rather randomly distributed around the equatorial position of the benzyl group (Figure 1.9). This partially ordered solvation

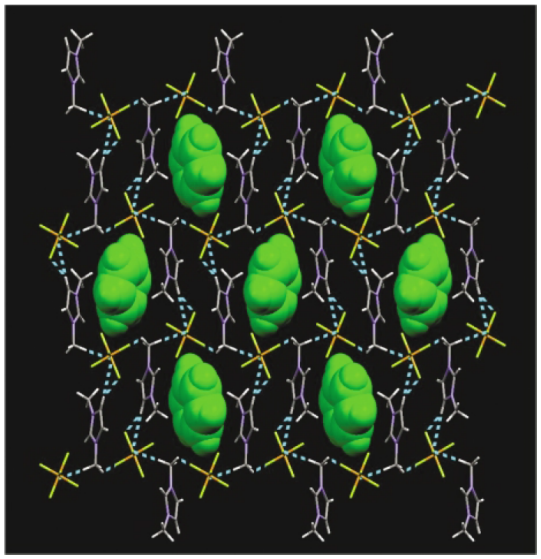

Figure 1.8: Packing in the crystal structure of $[C_1mIm][PF_6]\cdot 0.5C_6H_6$ where benzene molecules are shown in green.[96]

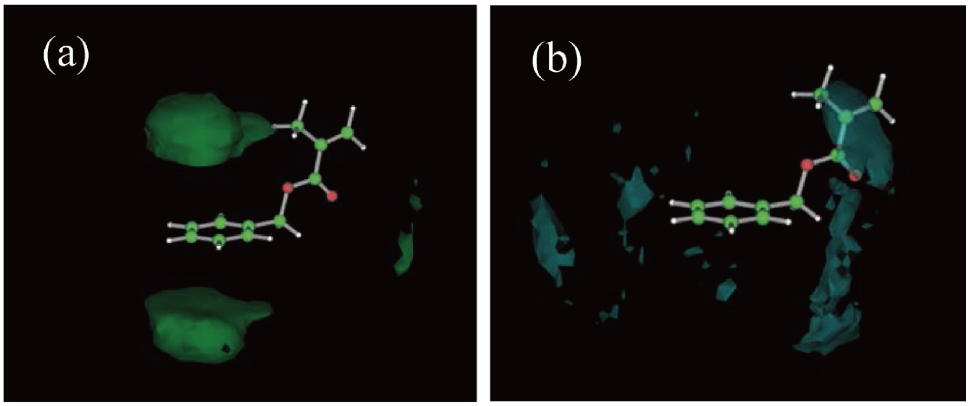


Figure 1.9: Space distribution function for center of mass of (a) $C_2mIm^+$ and (b) $TFSA^-$ around BnMA. The green and gray clouds represent the isoprobability surface of 1.8 times larger probability density than that of bulk.[97]

structure of BnMA (or PBnMA) in [$C_2$mIm][TFSA] solution decreases $\Delta S_m$, resulting in the observed LCST-type phase behavior of PBnMA in [$C_2$mIm][TFSA]. Fujii *et al.* also investigated chain conformation of PBnMA in dilute solution of [$C_2$mIm][TFSA] by SANS.[98] They elucidated that the PBnMA chains are molecularly dispersed and exist as independent Gaussian chains in [$C_2$mIm][TFSA] but suddenly form aggregates at $T_c$. Structure of other thermo-responsive polymers in IL solutions have been also studied by SANS.[89,99,100] According to the structural study, the polymers exist as Gaussian chains in ILs and show aggregates formation or the spinodal decomposition on the vicinity of the phase transition temperature. The phase separation of polymer in IL was also characterized from viewpoint of thermodynamics, utilizing high-resolution differencial scanning calorimetry (DSC) measurement.[101] $\Delta H_m$ and $\Delta S_m$ values of PBnMA in [$C_2$mIm][TFSA] are evaluated by the DSC measurement, and it was found that both $\Delta H_m$ and $\Delta S_m$ are significantly smaller than those of PNIPAm in water. It indicates that phase equilibrium of the system is controlled by a slight change in the free energy of mixing. However, the mechanism of thermo-responsive phase separation of polymer in IL has not yet been adequetely clarified. Especially, understanding of the above-mentioned strong dependence of $T_c$ on the chemical structure in IL system is still insufficient.

## 1.4 Outline of the Dissertation

As reviewed in the previous sections, a lot of composite systems of polymer and IL have been reported and expected to be novel materials. The unique properties of polymers in IL systems obviously originate from specific solvation for polymers by ILs. However, structural study on the polymer in IL systems is inadequate and thus the physical origin of the properties of the systems is still unclear at the present stage. As ILs have complicated structure, it is often difficult to extract information about chain characteristics of polymer or polymer-IL interactions from experimental data.

In this doctoral dissertation, I performed structural analysis by scattering measurements on the polymer in IL solutions. Figure 1.10 shows the conceptual illustration for various scattering techniques and observable structural information from them. I utilized high-energy total X-ray scattering (HEXTS) experiment with the aid of all-atom MD simulations to investigate the microscopic solvation structure with high spacial resolution. Small-angle X-ray scattering (SAXS), small-angle neutron scattering (SANS), and static light scattering (SLS) experiments are also used to characterize the chain conformation, aggregated structure, and inhomogeneity of

polymers in ILs. Furthermore, dynamics of polymer chains are studied by dynamic light scattering (DLS) experiments. By means of the various scattering techniques, I succeeded in obtaining rich structural information for polymer in IL solutions.

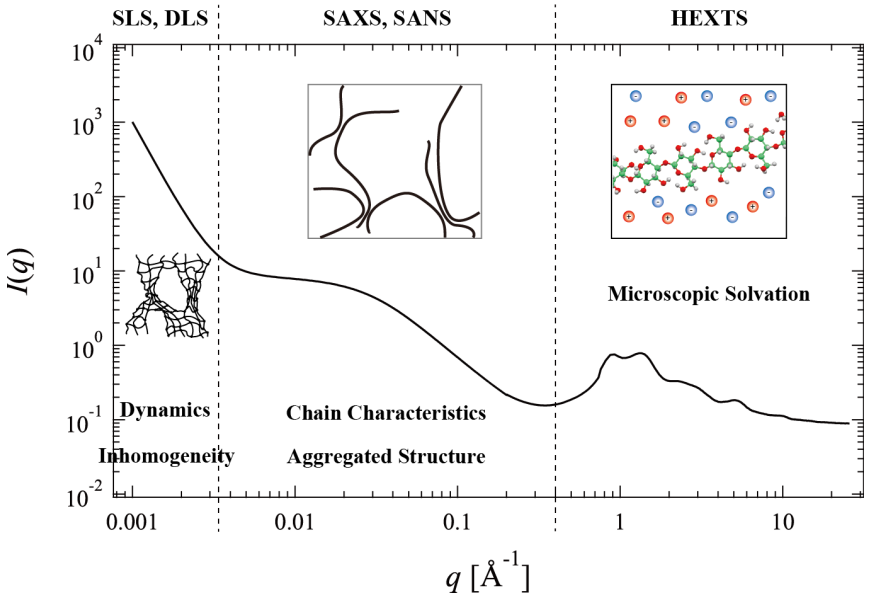


Figure 1.10: Illustration for typical scattering profiles from polymer solution and observable structural information from various scattering techniques. $q$ and $I(q)$ are the magnitude of scattering vector and scattering intensity, respectively.

Chapter 2 and 3 are focused on the cellulose dissolution phenomena in ILs. Here, glucose and cellobiose, monomeric units of cellulose molecule, are used as model molecules to approximate microscopic structure of cellulose. In Chapter 2, I investigated the microscopic solvation structure of glucose in a phosphonate-based IL ($[C_2mIm][CH_3HPO_3]$). As $[C_2mIm][CH_3HPO_3]$ has high cellulose-dissolving ability, characterization of liquid structure of $[C_2mIm][CH_3HPO_3]$ itself is benefical for future development of superior cellulose-dissolving ILs. Firstly, I focused on the packing of ions and interactions between cations and anions in neat $[C_2mIm][CH_3HPO_3]$. Secondly, I evaluated microscopic interactions between glucose and $[C_2mIm][CH_3HPO_3]$, including space distribution of the ions, orientation of interaction, and coordination number of the ions around glucose. In Chapter 3, I investigated the mesoscopic chain conformation and aggregated structure of cellulose in $[C_2mIm][CH_3HPO_3]$. Microscopic intramolecular interactions in cellulose molecules were studied by the HEXTS and MD simulation analysis on cellobiose. The mesoscopic structure of cellulose chains was investigated by SAXS, SLS, and DLS experiments. Eventually, the chain

conformation of cellulose was realized based on the insight about microscopic intramolecular interactions in cellulose molecules.

Furthermore, I extended the structural study to the stimuli-resonsive phase separation phenomena of polymers in ILs. In Chapter 4, I focused on the drastic effect of structural modification on the phase equilibrium of thermo-responsive polymers in ILs. I chose PPhEtMA in [$C_2$mIm][TFSA] solution as a model system. The solvated structure and thermodynamic parameters of PPhEtMA in [$C_2$mIm][TFSA] are evaluated by SANS and DLS experiments. Here, a deuterated $d_8$-[$C_2$mIm][TFSA] was used as a solvent to make a clear contrast between the polymer and the IL. In comparion with the previously reported structure of PBnMA in the IL, I discussed the origin of the large difference in LCST of PBnMA and PPhEtMA from the viewpoint of polymer-IL interactions.

Although the pressure effects on phase equilibrium of solution have been extensively studied in aqueous system, the pressure effects on IL solution is an unexplored research field. In Chapter 5, I used hydrostatic pressure as an external stimulus and studied pressure-response of a polymer in an IL. I investigated the pressure dependence of phase separation temperetaure and solvated structure of PPhEtMA in [$C_2$mIm][TFSA] solution by DLS measurement at elevated hydrostatic pressure. The observed pressure effects in the IL solution were compared with that in aqueous polymer solution. Eventually, I pointed out a fundamental difference in the mechanism of LCST-type phase transition in IL solution and in aqueous solution.

## Reference


[1] Welton, T. *Chem. Rev.* **1999**, *99*, 2071–2083.

[2] Galinski, M.; Lewandowski, A.; Stepniak, I. *Electrochim. Acta* **2006**, *51*, 5567–5580.

[3] Wilkes, J. S. *Green Chem.* **2002**, *4*, 73–80.

[4] Walden, P. *Bull. Acad. Imper. Sci. (St. Petersburg)* **1914**, *1800*, 405–422.

[5] Yoke, J. T.; Weiss, J. F.; G., T. *Inorg. Chem.* **1963**, *2*, 1210–1216.

[6] Koch, V. R.; Miller, L. L.; Osteryound, R. A. *J. Am. Chem. Soc.* **1976**, *98*, 5277–5284.

[7] Robinson, J.; Osteryound, R. A. *J. Am. Chem. Soc.* **1979**, *101*, 323–327.

[8] Wilkes, J. S.; Levisky, J. A.; Wilson, R. A.; Hussey, C. L. *Inorg. Chem.* **1982**, *21*, 1263–1264.

[9] Gale, R. J.; Gilbert, B.; Osteryoung, R. A. *Inorg. Chem.* **1978**, *17*, 2728–2729.

[10] Wilkes, J. S.; Zawarotko, M. J. *J. Chem. Soc. Chem. Commun.* **1992**, 965–967.

[11] Ueno, K.; Tokuda, H.; Watanabe, M. *Phys. Chem. Chem. Phys.* **2010**, *12*, 1649–1658.

[12] Hayashi, S.; Ozawa, R.; Hamaguchi, H. *Chem. Lett.* **2003**, *32*, 498–499.

[13] Saha, S.; Hayashi, S.; Kobayashi, A.; Hamaguchi, H. *Chem. Lett.* **2003**, *32*, 740–741.

[14] Ozawa, R.; Hayashi, S.; Saha, S.; Kobayashi, A.; Hamaguchi, H. *Chem. Lett.* **2003**, *32*, 948–949.

[15] Holbrey, J. D.; Reichert, W. M.; Nieuwenhuyzen, M.; Johnston, K. R., S. Seddon; Rogers, R. D. *Chem. Commun.* **2003**, 1636–1637.

[16] Berg, R. W.; Deetlefs, M.; Seddon, K. R.; Shim, I.; Thompson, J. M. *J. Phys. Chem. B* **2005**, *109*, 19018–19025.

[17] Fujii, K.; Fujimori, T.; Takamuku, T.; Kanzaki, R.; Umebayashi, Y.; Ishiguro, S. *J. Phys. Chem. B* **2006**, *110*, 8179–8183.

[18] Huddleston, J. G.; Willauer, R. P., H. D. Swatloski; Visser, A. E.; Rogers, R. D. *Chem. Commun.* **1998**, 1765–1766.

[19] Dai, S.; Ju, Y. H.; Barnes, C. E. *J. Chem. Soc., Dalton Trans.* **1999**, 1201–1202.

[20] Visser, A. E.; Swatloski, R. P.; Reichert, W. M.; Griffin, S. T.; Rogers, R. D. *Ind. Eng. Chem. Res.* **2000**, *39*, 3596–3604.

[21] Du, Z.; Yu, Y. L.; Wang, J. H. *Chem. Euro. J.* **2007**, *13*, 2130–2137.

[22] Lachwa, J.; Szydlowski, J.; Najdanovic-Visak, V.; Rebelo, L. P. N.; Seddon, K. R.; da Ponte, M. N.; Esperança, H. J. R., J. M. S. S. Guades *J. Am. Chem. Soc.* **2005**, *127*, 6542–6543.

[23] Fukumoto, K.; Ohno, H. *Angew. Chem. Int. Ed.* **2007**, *46*, 1852–1855.

[24] Lachwa, J.; Szydlowski, J.; Makowska, A.; Seddon, K. R.; Esperança, J. M. S. S.; Guedes, H. J. R.; Rebelo, L. P. N. *Green. Chem.* **2006**, *8*, 262–267.

[25] Crosthwaite, J. M.; Aki, S. N. V. K.; Maginn, E. J.; Brennecke, J. F. *J. Phys. Chem. B* **2004**, *108*, 5113–5119.

[26] Crosthwaite, J. M.; Muldoon, M. J.; Aki, S. N. V. K.; Maginn, E. J.; Brennecke, J. F. *J. Phys. Chem. B* **2006**, *110*, 9354–9361.

[27] Kohno, Y.; Saita, S.; Murata, K.; Nakamura, N.; Ohno, H. *Polym. Chem.* **2011**, *2*, 862–867.

[28] Matsuoka, H.; Nakamoto, H.; Susan, M. A. B. H.; Watanabe, M. *Electrochim. Acta* **2005**, *50*, 4015–4021.

[29] Lee, S. Y.; Ogawa, A.; Kanno, M.; Nakamoto, H.; Yasuda, T.; Watanabe, M. *J. Am. Chem. Soc.* **2010**, *132*, 9764–9773.

[30] Imaizumi, S.; Kato, Y.; Kokubo, H.; Watanabe, M. *J. Phys. Chem. B* **2012**, *116*, 5080–5089.

[31] Ding, J.; Zhou, D.; Spinks, G.; Wallace, G.; Forsyth, S.; Forsyth, M.; MacFarlane, D. *Chem. Mater.* **2003**, *15*, 2392–2398.

[32] Ishikawa, M.; Sugimoto, T.; Kikuta, M.; Ishiko, E.; Kono, M. *J. Power Sources* **2006**, *162*, 658–662.

[33] Orita, A.; Kamijima, K.; Yoshida, M.; Dokko, K.; Watanabe, M. *J. Power Sources* **2011**, *196*, 3874–3880.

[34] Ueno, K.; Yoshida, K.; Tsuchiya, M.; Tachikawa, N.; Dokko, K.; Watanabe, M. *J. Phys. Chem. B* **2012**, *116*, 11323–11331.

[35] Jacquemin, J.; Husson, P.; Majer, V.; C., G. M. F. *Fluid Phase Equilib.* **2006**, *240*, 87–95.

[36] Blanchard, L. A.; Hancu, D.; Beckman, E. J.; Brennecke, J. F. *Nature* **1999**, *6*, 399.

[37] Aki, S. N. V. K.; Mellein, B. R.; Saurer, E. M.; Brennecke, J. F. *J. Phys. Chem. B* **2004**, *108*, 20355–20365.

[38] Rosenau, T.; Potthast, A.; Sixta, H.; Kosma, P. *Prog. Polym. Sci.* **2001**, *26*, 1763–1837.

[39] Hermanutz, F.; Gähr, F.; Uerdingen, E.; Meister, F.; Kosan, B. *Macromol. Symp.* **2008**, *262*, 23–27.

[40] Burchard, W.; Habermann, N.; Klüfers, P.; Seger, B.; Wilhelm, U. *Angew. Chem. Int. Ed.* **1994**, *33*, 884–887.

[41] Terbojevich, M.; Cosani, A.; Conio, G.; Ciferri, A.; Bianchi, E. *Macromolecules* **1994**, *18*, 640–646.

[42] Wang, H.; Gurau, G.; Rogers, R. D. *Chem. Soc. Rev.* **2012**, *41*, 1519–1537.

[43] Phillips, D. M.; Drummy, L. F.; Conrady, D. G.; Fox, D. M.; Naik, R. R.; Stone, M. O.; Trulove, P. C.; Long, H. C. D.; Mantz, R. A. *J. Am. Chem. Soc.* **2004**, *126*, 14350–14351.

[44] Xie, H.; Li, S.; Zhang, S. *Green Chem.* **2005**, *7*, 606–608.

[45] Qin, Y.; Lu, X.; Sun, N.; Rogers, R. D. *Green Chem.* **2010**, *12*, 968–971.

[46] Swatloski, R. P.; Spear, S. K.; Holbrey, J. D.; Rogers, R. D. *J. Am. Chem. Soc.* **2002**, *124*, 4974–4975.

[47] Fukaya, Y.; Sugimoto, A.; Ohno, H. *Biomacromolecules* **2006**, *7*, 3295–3297.

[48] Fukaya, Y.; Hayashi, K.; Wada, M.; Ohno, H. *Green Chem.* **2008**, *10*, 44–46.

[49] Sun, N.; Rahman, M.; Qin, Y.; Maxim, M. L.; Rodriguez, H.; Rogers, R. D. *Green Chem.* **2009**, *11*, 646–655.

[50] Kuroda, K.; Satria, H.; Miyamura, K.; Tsuge, Y.; Ninomiya, K.; Takahashi, K. *J. Am. Chem. Soc.* **2017**, *139*, 16052–16055.

[51] Abe, M.; Fukaya, Y.; Ohno, H. *Green Chem.* **2010**, *12*, 1274–1280.

[52] Kuroda, K.; Miyamura, K.; Satria, H.; Takada, K.; Ninomiya, K.; Takahashi, K. *ACS Sustainable Chem. & Eng.* **2016**, *4*, 3352–3356.

[53] Kuroda, K.; Inoue, K.; Miyamura, K.; Satria, H.; Takada, K.; Ninomiya, K.; Takahashi, K. *Catalysts* **2017**, *7*, 108.

[54] Takada, A.; Kadokawa, J. *Biomolecules* **2015**, *5*, 244.

[55] Zu, A.; Wang, J.; Wang, H. *Green Chem.* **2010**, *12*, 268–275.

[56] Remsing, R. C.; Swatloski, R. P.; Rogers, R. D.; Moyna, G. *Chem. Commun.* **2006**, *12*, 1271–1273.

[57] Youngs, T. G. A.; Hardacre, C.; Holbrey, J. D. *J. Phys. Chem. B* **2007**, *111*, 13765–13774.

[58] Youngs, T. G. A.; Holbrey, J. D.; Mullan, C. L.; Norman, S. E.; Lagunas, M. C.; D'Agostino, C.; Mantle, M. D.; Gladden, L. F.; Bowron, D. T.; Hardacre, C. *Chem. Sci.* **2011**, *2*, 1594–1605.

[59] Andanson, J. M.; Pádua, A. A. H.; Costa Gomes, M. F. *Chem. Commun.* **2015**, *51*, 4485–4487.

[60] Rein, D. M.; Khalfin, R.; Szekely, N.; Cohen, Y. *Carbohydr. Polym.* **2014**, *112*, 125–133.

[61] Endo, T.; Hosomi, S.; Fujii, S.; Ninomiya, K.; Takahashi, K. *Molecules* **2017**, *22*, 178.

[62] Halperin, A.; Kröger, M.; Winnik, F. M. *Angew. Chem. Int. Ed.* **2015**, *54*, 15342–15367.

[63] Ito, S. *Koubunshi Ronbunshu* **1989**, *7*, 437–443.

[64] Aoki, S.; Koide, A.; Imabayshi, S.; Watanabe, M. *Chem. Lett.* **2002**, 1128–1129.

[65] Heymann, E. *Trans. Faraday Soc.* **1935**, *31*, 846–864.

[66] Saeki, S.; Kuwahara, N.; Nakata, M.; Kaneko, M. *Polymer* **1977**, *18*, 1027–1031.

[67] Chatterjee, T.; Nakatani, A. I.; Adden, R.; Brackhagen, M.; Redwine, D.; Shen, H.; Li, Y.; Wilson, T.; Sammler, R. L. *Biomacromolecules* **2012**, *13*, 3355–3369.

[68] Shibayama, M.; Mizutani, S.; Nomura, S. *Macromolecules* **1996**, *29*, 2019–2024.

[69] Ono, Y.; Shikata, T. *J. Am. Chem. Soc.* **2006**, *128*, 10030–10031.

[70] Frank, H. S.; Evans, M. W. *J. Chem. Phys.* **1945**, *13*, 507–532.

[71] Kauzmann, W. *Nature* **1987**, *325*, 763–764.

[72] Kataoka, K.; Miyazaki, H.; Bunya, M.; Okano, T.; Sakurai, Y. *J. Am. Chem. Soc.* **1998**, *120*, 12694–12695.

[73] Schmaljohann, D. *Adv. Drug Deliv. Rev.* **2006**, *58*, 1655–1670.

[74] Cowie, J. M. G.; Mcewen, I. J. *J. Chem. Soc. Faraday Trans.* **1976**, *72*, 526–533.

[75] Hayashi, S.; Hamada, F.; Nakajima, A. *J. Polym. Sci. Part C* **1966**, *15*, 285–294.

[76] Pfohl, O.; Hino, T.; Prausnitz, J. M. *Polymer* **1995**, *36*, 2065–2073.

[77] Yu, J.; Wang, Z.; Chu, B. *Macromolecules* **1992**, *25*, 1618–1620.

[78] Cowie, J. M. G.; Mcewen, I. J. *J. Polym. Sci.: Polym. Phys.* **1974**, *12*, 441–443.

[79] Susan, M. A. B. H.; Kaneko, T.; Noda, A.; Watanabe, M. *J. Am. Chem. Soc.* **2005**, *127*, 4976–4983.

[80] Noda, A.; Watanabe, M. *ElectroChim. Acta.* **2000**, *45*, 1265–1270.

[81] Ueki, T.; Watanabe, M. *Macromolecules* **2008**, *41*, 3739–3749.

[82] Fujii, K.; Makino, T.; Hashimoto, K.; Sakai, T.; Kanakubo, M.; Shibayama, M. *Chem. Lett.* **2015**, *44*, 17–19.

[83] Gu, Y.; Lodge, T. P. *Macromolecules* **2011**, *44*, 1732–1736.

[84] Ueki, T. *Polymer Journal* **2014**, *46*, 646–655.

[85] Ueki, T.; Watanabe, M. *Langmuir* **2007**, *23*, 988–990.

[86] Kodama, K.; Nanashima, H.; Ueki, T.; Kokubo, H.; Watanabe, M. *Langmuir* **2009**, *25*, 3820.

[87] Lee, H.-N.; Lodge, T. P. *J. Phys. Chem. Lett.* **2010**, *1*, 1962–1966.

[88] Kodama, K.; Tsuda, R.; Niitsuma, K.; Tamura, T.; Ueki, T.; Kokubo, H.; Watanabe, M. *Polymer Journal* **2011**, *43*, 242–248.

[89] Hoarfrost, M. L.; He, Y.; Lodge, T. P. *Macromolecules* **2013**, *46*, 9464–9472.

[90] Tamura, S.; Ueki, T.; Ueno, K.; Kodama, K.; Watanabe, M. *Macromolecules* **2009**, *42*, 1315.

[91] Ueki, T.; Watanabe, M.; Lodge, T. P. *Macromolecules* **2009**, *42*, 1315–1320.

[92] He, Y.; Lodge, T. P. *Macromolecules* **2008**, *41*, 167–174.

[93] Kitazawa, Y.; Ueki, T.; Niitsuma, K.; Imaizumi, S.; Lodge, T. P.; Watanabe, M. *Soft Matter* **2012**, *8*, 8067–8074.

[94] Kitazawa, Y.; Ueki, T.; Imaizumi, S.; Lodge, T. P.; Watanabe, M. *Chem. Lett.* **2014**, *43*, 204–206.

[95] Kitazawa, Y.; Ueki, T.; McIntosh, L. D.; Tamura, S.; Niitsuma, K.; Imaizumi, S.; Lodge, T. P.; Watanabe, M. *Macromolecules* **2016**, *49*, 1414–1423.

[96] Holbrey, J. D.; Reichert, W. M.; Nieuwenhuyzen, M.; Sheppard, O.; Hardacre, C.; Rogers, R. D. *Chem. Commun.* **2003**, 476–477.

[97] Matsugami, M.; Fujii, K.; Ueki, T.; Kitazawa, Y.; Umebayashi, Y.; Watanabe, M.; Shibayama, M. *Anal. Sci.* **2013**, *29*, 311–314.

[98] Fujii, K.; Ueki, T.; Niitsuma, K.; Matsunaga, T.; Watanabe, M.; Shibayama, M. *Polymer* **2011**, *52*, 1589–1595.

[99] Lee, H. N.; Newell, N.; Bai, Z.; Lodge, T. P. *Macromolecules* **2012**, *45*, 3627–3633.

[100] Asai, H.; Fujii, K.; Ueki, T.; Sawamura, S.; Nakamura, Y.; Kitazawa, Y.; Watanabe, M.; Han, Y.-S.; Kim, T.-H.; Shibayama, M. *Macromolecules* **2013**, *46*, 1101–1106.

[101] Ueki, T.; Arai, A. A.; Kodama, K.; Kaino, S.; Takada, N.; Morita, T.; Nishikawa, K.; Watanabe, M. *Pure & Appl. Chem.* **2009**, *81*, 1829–1841.

# Chapter 2

# Microscopic Solvation Structure of Glucose in a Phosphonate-type Ionic Liquid



## 2.1 Introduction

As mentioned in Chapter 1, several ILs dissolve cellulose under mild condition. The cellulose-dissolving ILs are expected to be novel solvents. For understanding of the cellulose dissolution mechanism, microscopic interactions between IL and celluose is the most important structural information. Several structural investigations have been performed on microscopic solvation structure of cellulose (or its monomeric units, glucose or cellobiose) in ILs. As for polarity of IL, solvatochromic analyses were performed and it was found that hydrogen bond basicity of IL anion species is closely linked to solubility of cellulose in the ILs.[1,2] NMR relaxation measurement[3] and neutron diffraction experiments[4,5] elucidated that anion species of cellulose-dissolving ILs form hydrogen bonds with hydroxyl groups of glucose. Despite these reports, microscopic solvation structure of cellulose in ILs is still unclear at the present stage.

Glucose is a monomeric component of cellulose, and thus it can be regarded as a model molecule to approximiate the microscopic solvation structure of cellulose. In this chapter, I investigated solvation structure of glucose in $[C_2mIm][CH_3HPO_3]$ by

high-energy X-ray total scattering (HEXTS) experiment and all-atom MD simulations. Firstly, I focused on the liquid structure of neat $[C_2mIm][CH_3HPO_3]$ to find out the structural characteristics of the IL. Based on this result, I further investigated the solvation structure of glucose in $[C_2mIm][CH_3HPO_3]$.

## 2.2 Experimental

### 2.2.1 Materials

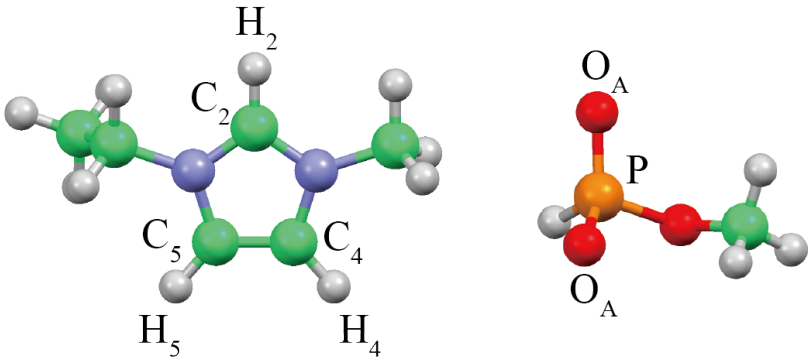


1-ethyl-3-methylimidazolium methylphosphonate

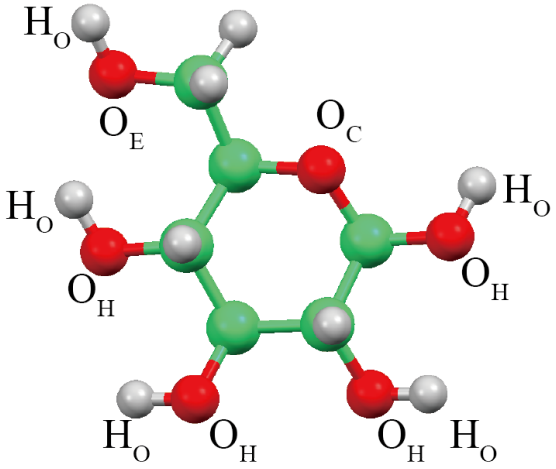


glucose

Figure 2.1: Schematic illustration for the chemical structure of $[C_2mIm][CH_3HPO_3]$ and glucose. Indices given for the atom species are also shown.

Schematic illustration for the chemical structures of $[C_2mIm][CH_3HPO_3]$ and D-glucose are shown in Figure 2.1. Dimethylphosphite and 1-ethylimidazole were purchased from Wako and TCI Co., respectively. They were used after purification by distillation. D-glucose was purchased from Aldrich Co. and used without further purification. The ionic liquid, $[C_2mIm][CH_3HPO_3]$ was synthesized accord-

ing to the previously reported procedure as mentioned below.[6] 1-ethylimidazole and dimethylphosphite were dissolved in tetrahydrofuran (THF). Ar gas was bubbled through the solution for 10 min. Then the solution was reacted for 24 h at 80 °C in a pressure vessel. After removing THF by evaporation, the resulting liquid was washed with diethylether at least three times. After removal of diethylether, the residual liquid was dried in vacuo at 80 °C for 24 h with liquid $N_2$ trap. Then, $[C_2mIm][CH_3HPO_3]$ was obtained as a clear and colorless liquid. Chemical characterization of the synthesized IL was performed using $^1H$ NMR spectroscopy. The $^1H$ NMR (300 MHz, $CDCl_3$) spectra for $[C_2mIm][CH_3HPO_3]$ are following: $\delta = 1.58$ (3H, $t$, $NCH_2CH_3$), 3.58 (3H, $d$, $OCH_3$), 4.10 (3H, $s$, $NCH_3$), 4.37 (2H, $q$, $NCH_2CH_3$), 6.91 (1H, $d$, $PH$), 7.33 (2H, $d$, $NCHCHN$), 10.81 (1H, $s$, $NCHN$). Water content in the IL was estimated by Karl Fischer titration method to be around 300 ppm.

### 2.2.2 High-Energy X-ray Total Scattering

HEXTS measurements were performed at BL04B2 beamline of SPring-8 (Japan Synchrotron Radiation Research Institute, Japan).[7,8] All the measurements were carried out under room temperature. The monochromatized X-ray of 61.6 keV (wavelength $\lambda = 0.2012$ Å) was obtained using a Si (220) monochromator. Glucose in $[C_2mIm][CH_3HPO_3]$ solutions of 10 – 30 wt% were injected into a planar type cell (Figure 2.2).

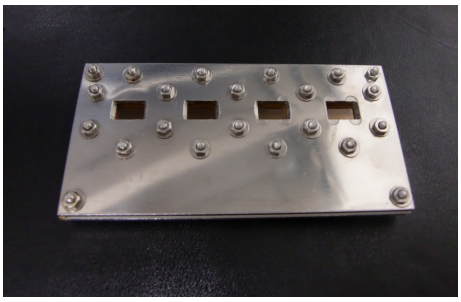

Figure 2.2: The sample cell used in HEXTS experiments which is composed of aluminium flat plate and polyimide film.

The scattering angle $2\theta$ was scanned in the range of $2\theta = 0.3 - 42$ ° and scattering intensity profile was measured for glucose in $[C_2mIm][CH_3HPO_3]$. After subtraction of background scattering, corrections for absorption,[9] polarization, and Compton scatterings[10,11] were performed on the scattering intensity of X-ray to obtain coherent scattering intensities, $I_{coh}(q)$ per stoichiometric volume. The experimental X-ray structure factor, $S^{exp}(q)$ and the radial distribution function, $G^{exp}(r)$ per stoichio-

metric volume were calculated as follows:

$$S^{\mathrm{exp}}(q) = \frac{I_{\mathrm{coh}}(q)/N^{\mathrm{s}} - \sum x_\alpha f_\alpha(q)^2}{\left\{\sum x_\alpha f_\alpha(q)\right\}^2} + 1$$
$$G^{\mathrm{exp}}(r) - 1 = \frac{1}{2\pi^2 r\rho_0}\int_0^{q_{\mathrm{max}}} q\left[S^{\mathrm{exp}}(q) - 1\right]\sin(qr)\frac{\sin(q\pi/q_{\mathrm{max}})}{q\pi/q_{\mathrm{max}}}\mathrm{d}q \qquad (2.1)$$

where $f_\alpha(q)$ and $x_\alpha$ mean the atomic scattering factor and the number fraction of atom $\alpha$ in the stoichiometric volume,[12] respectively. $N^{\mathrm{s}}$ is the total number of atoms in the stoichiometric volume. $\rho_0$ is the number density of atoms. $q$ is the magnitude of scattering vector defined as follows:

$$q = \frac{4\pi}{\lambda}\sin\theta \qquad (2.2)$$

In this study, the maximum of $q$ ($q_{\mathrm{max}}$) was 22 Å$^{-1}$. As shown in eq. (2.1), the Lorch window function was used in the inverse Fourier transformation procedure of $S^{\mathrm{exp}}(q)$ to $G^{\mathrm{exp}}(r)$.[13]

### 2.2.3 MD Simulations

An MD simulation was carried out using Materials Explorer 5.0 program (Fujitsu) in a cubic cell under $NTP$ ensemble of $T = 298$ K and $P = 1$ atm. The composition (number of the ion-pair and D-glucose) and the size of MD unit cell are listed in Table 2.1.

Table 2.1: Densities, compositions, and the size of the MD unit cells of the glucose/[$C_2$mIm][$CH_3HPO_3$] systems in the MD simulations.

| Conc.[a] [wt%] | $\rho^b_{\mathrm{MD}}$ [g cm$^{-3}$] | $\rho^c_{\mathrm{Exp.}}$ [g cm$^{-3}$] | Glucose | Cation | Anion | $L^d_{\mathrm{Cell}}$ [Å] |
|---|---|---|---|---|---|---|
| 0[e] | 1.178 | 1.172 | - | 256 | 256 | 42.1 |
| 10 | 1.201 | 1.203 | 40 | 300 | 300 | 45.7 |
| 20 | 1.228 | 1.235 | 80 | 280 | 280 | 46.0 |
| 30 | 1.251 | 1.243 | 120 | 240 | 240 | 45.5 |

[a]Weight fraction of glucose or cellobiose in [$C_2$mIm][$CH_3HPO_3$]
[b]Density values obtained from MD simulations.
[c]Experimental density values.
[d]Length of a side of the cubic MD unit cell.
[d]Neat [$C_2$mIm][$CH_3HPO_3$].

Here, temperature and pressure of the MD cell were controlled by a Nosé-Hoover thermostat[14,15] and a Parrinello-Rahman barostat,[16] respectively. The long-range interactions were treated using the Ewald method with real-space cutoff distance of 12 Å. It is well known that D-glucose has some structural isomers in aqueous solution.[17–20] However, the population in [$C_2$mIm][$CH_3HPO_3$] has never been reported

yet. Hence, in this work, I used $\beta$-D-glucopyranose shown in Figure 2.1 as an initial structure of glucose molecule in the MD simulations. At first, glucose and IL ions are randomly arranged in the MD cell. Then, the system was equilibrated at $NTP$ ensemble under $T = 2000$ K and $P = 10000$ atm for 0.5 ns with an interval of 0.2 fs to eliminate the effect of initial positions of atoms.[21] After that, the system was equilibrated for 1.0 ns with an interval of 0.2 fs at $T = 298$ K and $P = 1$ atm. The data collected at every 0.1 ps during 0.5 - 1.0 ns were used for analysis. Canongia Lopes and Padua (CLaP) and the optimized potentials for liquid simulation all-atom (OPLS-AA) force fields were used for IL ions and glucose, respectively.[22–26] The force fields include non-bonded Lennard-Jones and Coulombic interactions and intramolecular interactions with stretching, bending, and torsionional motion of covalent bonds. Mass density values obtained by the MD simulations showed excellent agreement with the experimental ones, which are listed in Table 2.1.

For comparison of the result of MD simulations with HEXTS experiment, I calculated the X-ray weighted structure factor, $S^{\mathrm{MD}}(q)$ based on the trajectories of atoms as follows:

$$S^{\mathrm{MD}}(q) = \frac{\sum_\alpha \sum_\beta w_{\alpha\beta}(q)}{\left\{\sum_\alpha \left(N_\alpha f_\alpha(q)/N\right)\right\}^2} \int_0^{r_{\max}} 4\pi r^2 \rho_0 \left(g^{\mathrm{MD}}_{\alpha-\beta}(r) - 1\right) \frac{\sin(qr)}{qr} \mathrm{d}r + 1 \quad (2.3)$$

$$w_{\alpha\beta}(q) \equiv \begin{cases} N_\alpha(N_\beta - 1) f_\alpha(q) f_\beta(q)/N(N-1) & (i = j) \\ 2N_\alpha N_\beta f_\alpha(q) f_\beta(q)/N^2 & (i \neq j) \end{cases} \quad (2.4)$$

where $N_\alpha$ and $N$ is the number of $\alpha$ atom and the total number of atoms in the simulation box. $g^{\mathrm{MD}}_{\alpha-\beta}(r)$ is the atom-atom pair correlation function between atom $\alpha$ and $\beta$ as calculated following.

$$g^{\mathrm{MD}}_{\alpha-\beta}(r) = \frac{1}{4\pi r^2 \Delta r} \frac{V}{N_\alpha N_\beta} \left\langle \sum_{m=1}^{N_\alpha} \Delta N_m^{\alpha\beta}(r) \right\rangle \quad \text{(Intermolecular correlations)} \quad (2.5)$$

$$g^{\mathrm{MD}}_{\alpha-\beta}(r) = \frac{1}{4\pi r^2 \Delta r} \frac{V}{N_\alpha} \left\langle \sum_{m=1}^{N_\alpha} \Delta N_m^{\alpha\beta}(r) \right\rangle \quad \text{(Intramolecular correlations)} \quad (2.6)$$

Here, $V$ denotes the volume of the MD cell. $\Delta N_m^{\alpha\beta}(r)$ is the number of $\beta$-atoms in the spherical shell of radius $r$ and thickness $\Delta r$ centered on a $m$ th $\alpha$-atom. The X-ray-weighted radial distribution function $G^{\mathrm{MD}}(r)$ was evaluated from the calculated $S^{\mathrm{MD}}(q)$ by the inverse Fourier transform, as shown in eq. (2.1).

## 2.3 HEXTS Experiments

Figure 2.3(a) shows the $S^{\mathrm{exp}}(q)$s for 0–30 wt% glucose in $[C_2\mathrm{mIm}][CH_3HPO_3]$ solutions. Intensity of the first peak at 1.55 $\mathrm{\AA}^{-1}$ decreased and the valley at 2.5

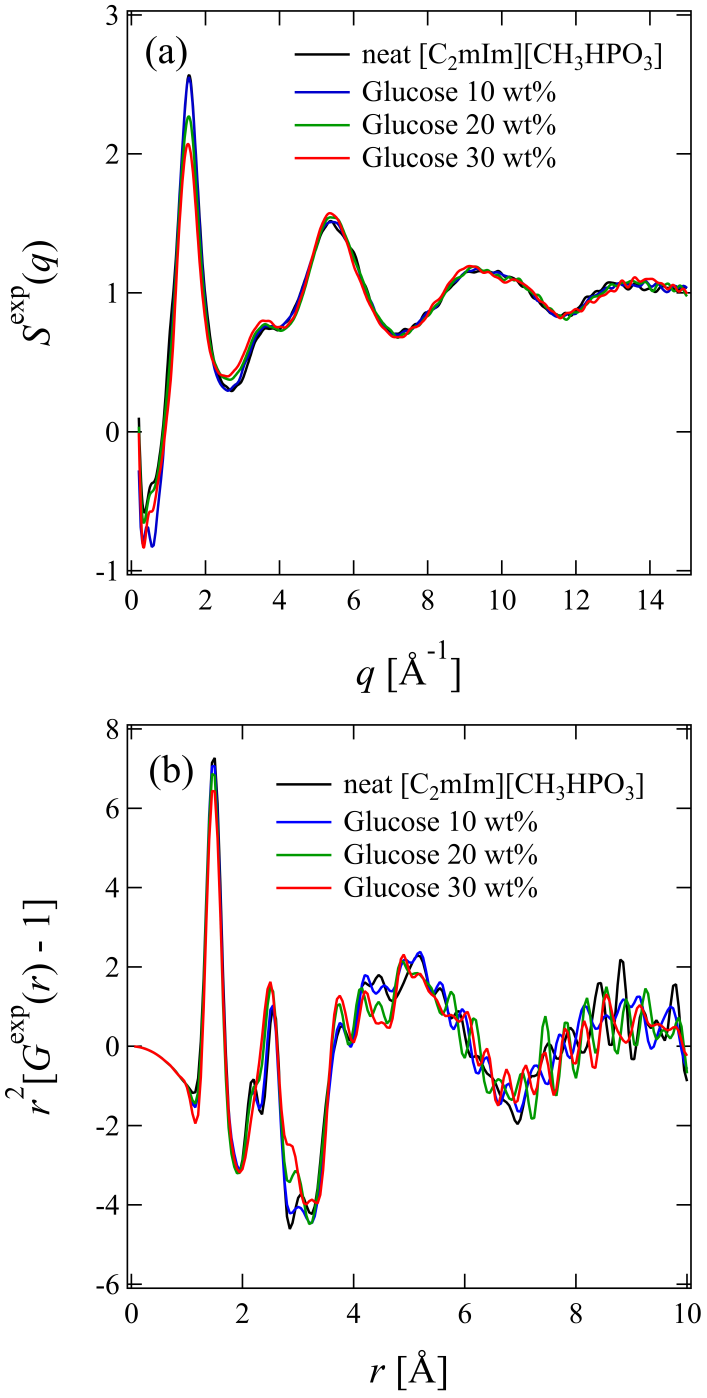


Figure 2.3: Experimental (a) structure factors, $S^{\mathrm{exp}}(q)$s and (b) radial distribution functions, $r^2[G^{\mathrm{exp}}(r) - 1]$s obtained for 0–30 wt% glucose in $[C_2mIm][CH_3HPO_3]$ solutions.

Å$^{-1}$ shallowed with increasing glucose concentration. Figure 2.3(b) shows the radial distribution function, $G^{\mathrm{exp}}(r)$s in a form of $r^2[G(r) - 1]$ for 0–30 wt% glucose in $[C_2mIm][CH_3HPO_3]$ solutions. In the $r^2[G^{\mathrm{exp}}(r) - 1]$, the peaks at 2.5 and 3.0 Å increased with increasing glucose concentration. It indicates that variation in solution structure caused by glucose dissolution is successfully reflected in $S^{\mathrm{exp}}(q)$ and $r^2[G^{\mathrm{exp}}(r) - 1]$. Our previous works on the liquid structure of ILs[27–31] show that the intermolecular correlation components in $G(r)$s overlap with the intramolecular ones in the $r$-range of 3 – 6 Å. For evaluation of the intermolecular interactions in the glucose/$[C_2mIm][CH_3HPO_3]$ solution system, I examined to extract the intermolecular correlation, $G_{\mathrm{inter}}(r)$ by means of all-atom MD simulation.

## 2.4 MD Simulations

Figure 2.4 shows the calculated radial distribution functions, $r^2[G^{\mathrm{MD}}(r) - 1]$s for neat $[C_2mIm][CH_3HPO_3]$ and glucose in $[C_2mIm][CH_3HPO_3]$ solutions, together with the corresponding $r^2[G^{\mathrm{exp}}(r) - 1]$s obtained by HEXTS experiments. As shown, $G^{\mathrm{exp}}(r)$ exhibited a high-frequency oscillation which was absent in $G^{\mathrm{MD}}(r)$. Such a "ripple" pattern is an inevitable artifact which originates from experimental fluctuation in the X-ray structure factor, $S^{\mathrm{exp}}(q)$. Such a fluctuation in $S^{\mathrm{exp}}(q)$ is transformed to the high-frequency oscillation in the experimental $G(r)$ via inverse Fourier transform procedure (eq. (2.1)). Except for the artifact, the MD result reproduced the experimental results well for all the glucose concentration examined here. It indicates that the trajectories of atoms obtained from MD simulations were valid. Furthermore, I extracted the intramolecular and intermolecular correlation components ($G^{\mathrm{MD}}_{\mathrm{intra}}(r)$s and $G^{\mathrm{MD}}_{\mathrm{inter}}(r)$s, respectively) to discuss the liquid structure of neat $[C_2mIm][CH_3HPO_3]$ and the solvation structure of glucose in $[C_2mIm][CH_3HPO_3]$. Figure 2.5 shows $r^2[G^{\mathrm{MD}}_{\mathrm{intra}}(r) - 1]$ and $r^2[G^{\mathrm{MD}}_{\mathrm{inter}}(r) - 1]$ calculated for glucose 30 wt% in $[C_2mIm][CH_3HPO_3]$ solution. As can be seen from Figure 2.5, the sharp peaks at 1.5, 2.5 and 3.0 Å in the $r^2[G(r) - 1]$ can be mainly assigned to the intramolecular correlations within glucose, $[C_2mIm]^+$, and $[CH_3HPO_3]^-$ components. The $G^{\mathrm{MD}}_{\mathrm{inter}}(r)$ is composed of intermolecular interactions between glucose and IL ions, which is discussed later.

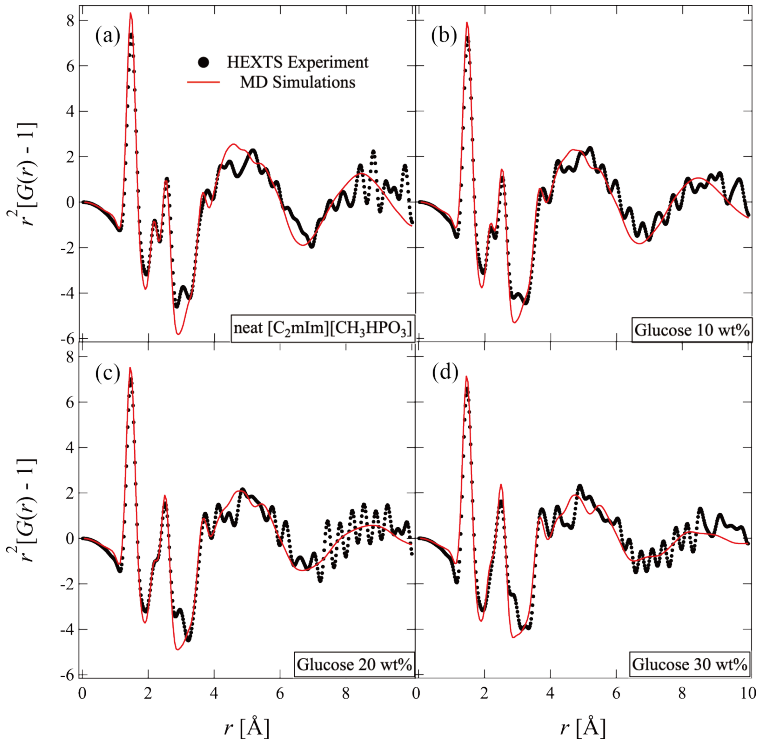


Figure 2.4: Radial distribution function $r^2[G(r)-1]$ for (a) 0 wt% (neat $[C_2mIm][CH_3HPO_3]$), (b) 10 wt%, (c) 20 wt% and (d) 30 wt% glucose in $[C_2mIm][CH_3HPO_3]$ solutions. The dots correspond to the experimental $r^2[G^{exp}(r)-1]$ and the solid line with red to the calculated $r^2[G^{MD}(r)-1]$ derived from MD simulations.

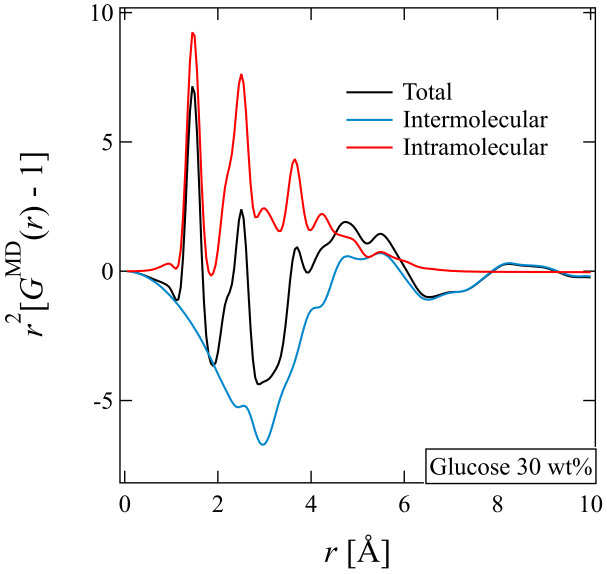


Figure 2.5: Intramolecular correlation component (red line) and intermolecular one (blue line) calculated for glucose 30 wt% in $[C_2mIm][CH_3HPO_3]$ solution system. The black line shows the total $r^2[G^{MD}(r)-1]$ that includes both of intramolecular and intermolecular correlations.

## 2.5 Liquid Structure of Neat $[C_2mIm][CH_3HPO_3]$

$[C_2mIm][CH_3HPO_3]$ has high hydrogen bond acceptor ability, which is one of important properties for ILs to dissolve cellulose.[6] As $[CH_3HPO_3]^-$ is a strong Lewis base, liquid structure of $[C_2mIm][CH_3HPO_3]$ is assumed to be different from that of well-known ILs with weak Lewis basic anion such as $[PF_6]^-$,[32] $[FSA]^-$,[31] and $[TFSA]^-$.[33] I discuss the liquid structure of neat $[C_2mIm][CH_3HPO_3]$ to characterize structural feature of the IL in liquid state. Figure 2.6 shows $G^{MD}_{inter}(r)$ in a form of $r^2[G(r)-1]$ and partial radial distribution functions for cation-anion, anion-anion and cation-cation correlations ($r^2[G^{MD}_{cat-an}(r)-1]$, $r^2[G^{MD}_{an-an}(r)-1]$, and $r^2[G^{MD}_{cat-cat}(r)-1]$, respectively). Here, the partial radial distribution functions, $r^2[G^{MD}_{i-j}(r)-1]$ are normalized by the combination number of the atom pairs and their X-ray scattering abilities, where $i$ and $j$ denote the components in the system: glucose, $[C_2mIm]^+$, and $[CH_3HPO_3]^-$. The total $r^2[G^{MD}_{inter}(r)-1]$ exhibited the peaks around 4.6, 8.5 and 12.0 Å. It is clear from Figure 2.6 that the peaks at $r = 4.6$ and 12.0 Å are mainly assigned to $r^2[G^{MD}_{cat-an}(r)-1]$ and one at $r = 8.5$ Å to both $r^2[G^{MD}_{an-an}(r)-1]$ and $r^2[G^{MD}_{cat-cat}(r)-1]$. Here, it should be noted that a shoulder is observed at around $r \approx 4$ Å in $r^2[G^{MD}_{cat-cat}(r)-1]$. It was reported that the similar shoulder is also found in the imidazolium-based ILs having strong Lewis basic anions such as $[C_1mIm][Cl]$[34] and $[C_2mIm][CH_3COO]$.[35] Such short-range interactions between imidazolium cations originate from a ring-stacking between imidazolium cations. In contrast, such shoulder have not been observed in the ILs with weak Lewis basic anions such as $[C_2mIm][TFSA]$[33] and $[C_2mIm][FSA]$.[31] Therefore, it was pointed out that packing structure of imidazolium cations in ILs having strong Lewis basic anions, including $[C_2mIm][CH_3HPO_3]$, is different from that in ILs with weak Lewis basic anions.

Figures 2.7 (a) and (b) show spatial distribution of $[CH_3HPO_3]^-$ around $[C_2mIm]^+$ calculated from the MD simulations. As can be seen from Figures 2.7 (a) and (b), the center of mass of $[CH_3HPO_3]^-$ locates around the $H_2$, $H_4$, $H_5$ (see Figure 2.1) of $[C_2mIm]^+$. Such space distributions of ions have been reported for several imidazolium-based ILs, [CnmIm][X] with X = $Cl^-$,[34] $[CH_3COO]^-$,[35] $[TFSA]^-$[33] and $[FSA]^-$,[31] where $n = 1$, 2 or 4. According to the reports, the anions with strong Lewis basicity ($Cl^-$ and $[CH_3COO]^-$) tend to locate along the $C_2$-$H_2$ bond to form hydrogen bonding interaction with the cation. In contrast, the anions with weak Lewis basicity ($[TFSA]^-$ and $[FSA]^-$) distribute above and below the imidazolium

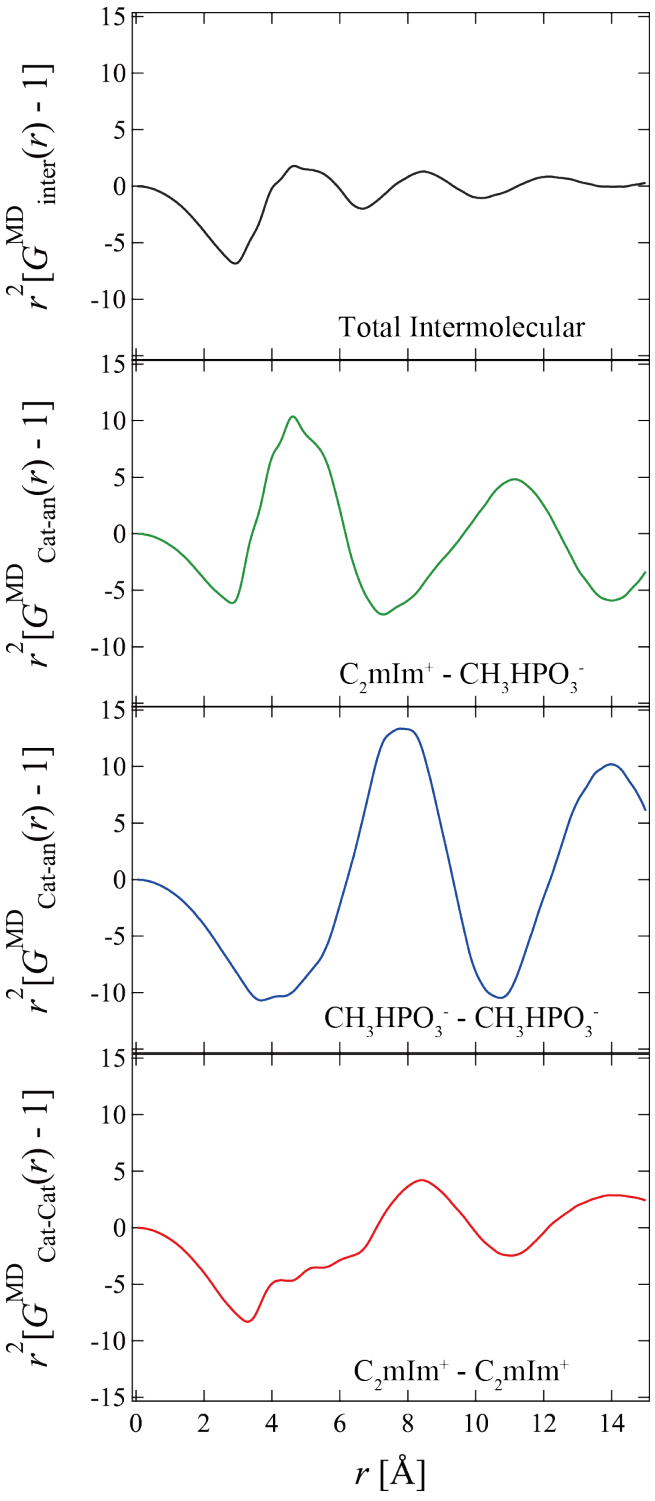


Figure 2.6: Total $G^{\mathrm{MD}}_{\mathrm{inter}}(r)$ as a form of $r^2[G(r)-1]$ obtained from MD simulations for neat $[\mathrm{C_2mIm}][\mathrm{CH_3HPO_3}]$, together with partial radial distribution functions for cation-anion ($r^2[G^{\mathrm{MD}}_{\mathrm{cat-an}}(r)-1]$), anion-anion ($r^2[G^{\mathrm{MD}}_{\mathrm{an-an}}(r)-1]$) and cation-cation ($r^2[G^{\mathrm{MD}}_{\mathrm{cat-cat}}(r)-1]$) interactions.

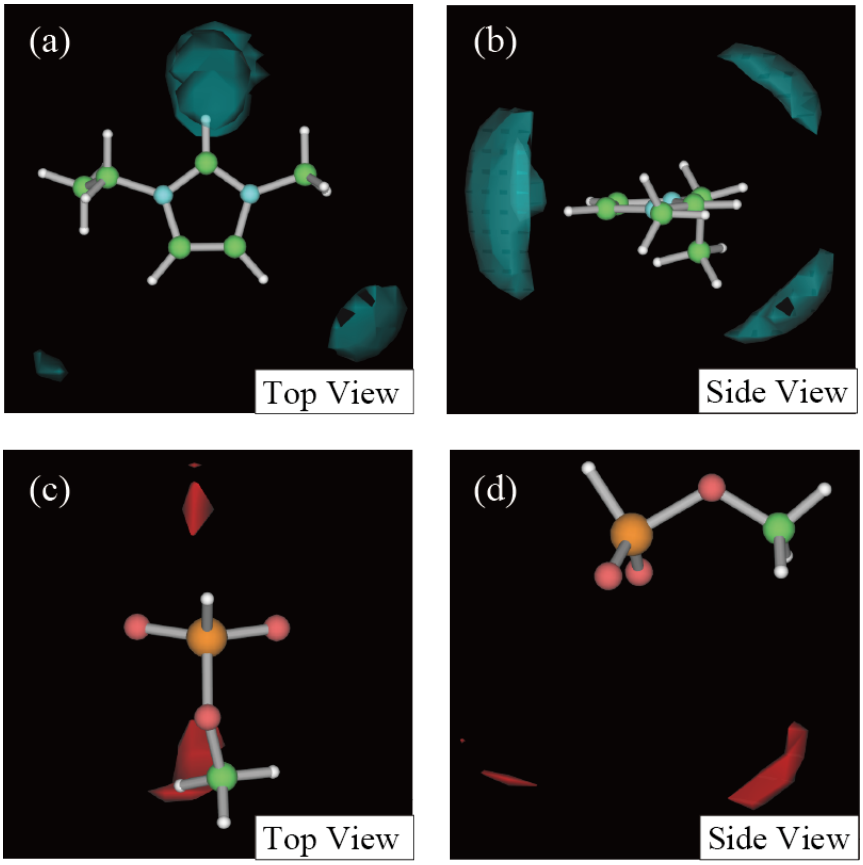


Figure 2.7: Spatial distribution of the center of mass of (a, b) $[CH_3HPO_3]^-$ around $[C_2mIm]^+$ and (c, d) $[C_2mIm]^+$ around $[CH_3HPO_3]^-$. The green and red clouds indicate the isoprobability surfaces of a given ion.

ring, where the cation-anion interactions are almost from an electrostatic contribution. In this work, $[CH_3HPO_3]^-$ distributes along the $C_2$-$H_2$, $C_4$-$H_4$ and $C_5$-$H_5$ bonds of $[C_2mIm]^+$, which is similar tendency with $Cl^-$ and $[CH_3COO]^-$. I conclude that $[CH_3HPO_3]^-$ form the hydrogen bond with $[C_2mIm]^+$ due to their strong Lewis basicity. Figures 2.7 (c) and (d) show spatial distribution of $[C_2mIm]^+$ around $[CH_3HPO_3]^-$. It was found that the $[C_2mIm]^+$ distributes around two $O_A$ atoms within $[CH_3HPO_3]^-$, indicating that the $O_A$ atoms act as hydrogen bond acceptors in the $[C_2mIm]^+$-$[CH_3HPO_3]^-$ interactions.

## 2.6 Solvation Structure of Glucose in $[C_2mIm][CH_3HPO_3]$

Figure 2.8(a) show $r^2[G^{MD}_{inter}(r) - 1]$s for 0 – 30 wt% glucose in $[C_2mIm][CH_3HPO_3]$ solutions. The partial radial distribution functions for glucose-anion and glucose-cation correlations ($r^2[G^{MD}_{glu-an}(r) - 1]$ and $r^2[G^{MD}_{glu-cat}(r) - 1]$) are shown in Figures 2.8 (b) and (c), respectively. The partial radial distrubution functions are normalized by the procedure mentioned above. The $r^2[G^{MD}_{inter}(r) - 1]$ exhibited a clear peak at $r$ = 2.6 Å which corresponds to the nearest neighbor interaction in the system. It is clearly seen from Figure 2.8 (b) that the nearest neighbor interaction can be assigned to the glucose-anion interactions. $r^2[G^{MD}_{glu-cat}(r) - 1]$ showed a shoulder at 3.5 Å indicating that $[C_2mIm]^+$ are secondly neighboring glucose. I conclude that the glucose molecules are preferentially solvated by $[CH_3HPO_3]^-$ in $[C_2mIm][CH_3HPO_3]$ and contributions of $[C_2mIm]^+$ to the solvation is relatively small. Figures 2.9 (a) and (b) show the space distribution of O atoms (averaged both $O_H$ and $O_E$ components) within hydroxyl groups of glucose molecules around $[CH_3HPO_3]^-$ calculated for 30 wt% glucose in $[C_2mIm][CH_3HPO_3]$ solution. O atoms (glucose) located along two P-$O_A$ bonds of $[CH_3HPO_3]^-$. Such an orientation indicates the existence of hydrogen bond between $O_A$ atoms ($[CH_3HPO_3]^-$) and hydroxyl groups within glucose. On the other hand, as shown in Figures 2.9(c), (d), the O atoms within glucose molecules distributed rather randomly around the $[C_2mIm]^+$. This is because the interactions between $[C_2mIm]^+$ and glucose originate from only Coulombic force.

To discuss local interactions in detail, I further calculated the atom-atom pair correlation functions, $g^{MD}_{i-j}(r)$s. Here, I focused on the closest atom-atom interactions in intermolecular glucose-anion, glucose-cation and glucose-glucose correlations. Figure 2.10 (a) shows the $g^{MD}_{OA-OX}(r)$ for $O_A$ within $[CH_3HPO_3]^-$ around the O atoms (X = H or E) within glucose. $g^{MD}_{OA-OH}(r)$ and $g^{MD}_{OA-OE}(r)$ exhibited the first peak

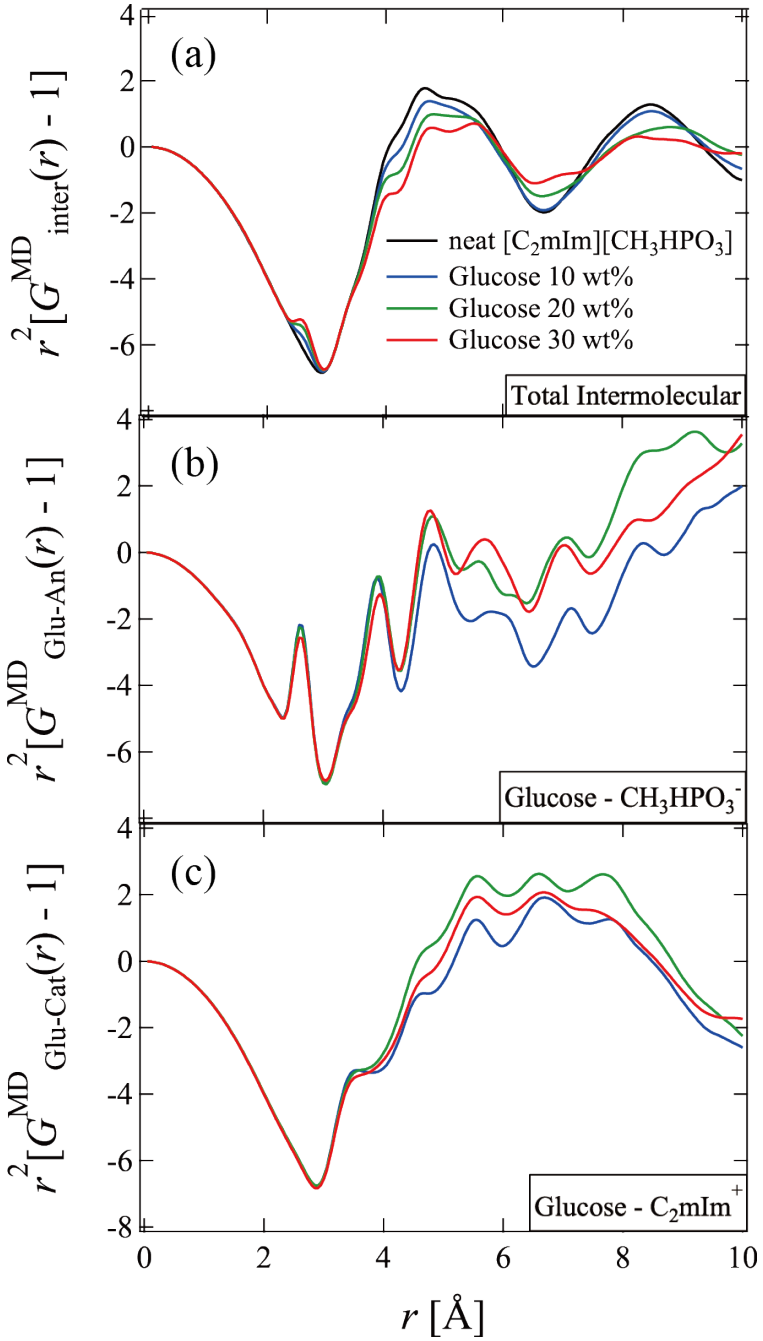


Figure 2.8: (a) total intermolecular correlation component ($r^2[G^{\mathrm{MD}}_{\mathrm{inter}}(r) - 1]$), (b) glucose-anion correlation component ($r^2[G^{\mathrm{MD}}_{\mathrm{glu-an}}(r) - 1]$), and (c) glucose-cation correlation component ($r^2[G^{\mathrm{MD}}_{\mathrm{glu-cat}}(r) - 1]$) obtained from MD simulations for 0 – 30 wt% glucose in [$C_2$mIm][$CH_3HPO_3$] systems.

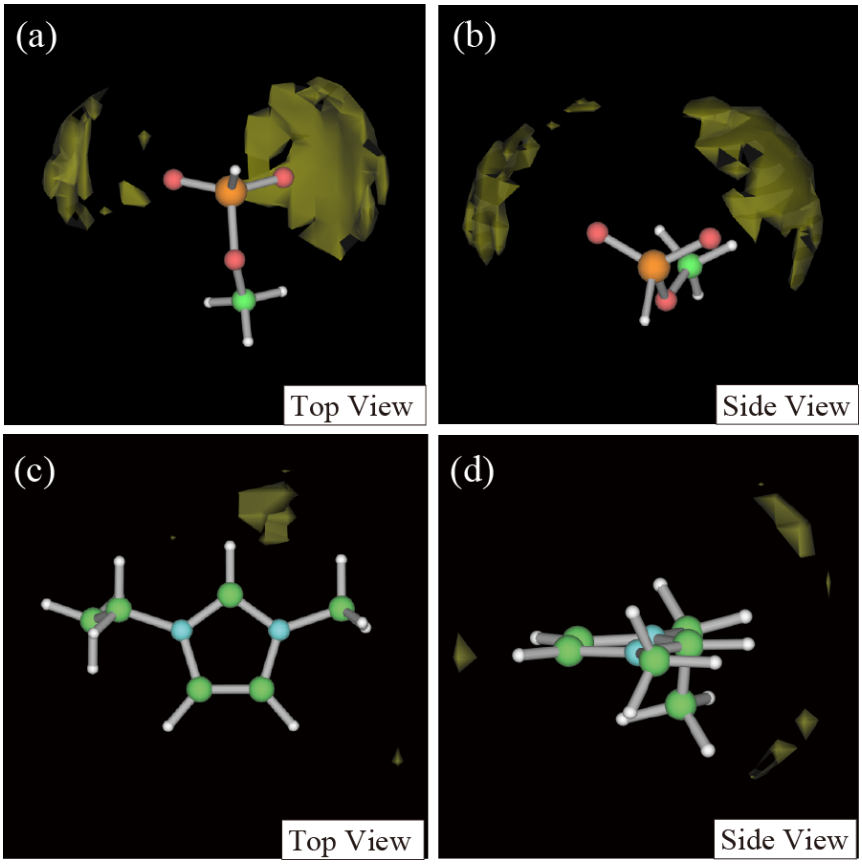


Figure 2.9: Spatial distribution of O atoms (averaged for both $O_E$ and $O_H$) within the hydroxyl groups of glucose around (a, b) $[CH_3HPO_3]^-$ and (c, d) $[C_2mIm]^+$ calculated for 30 wt% glucose in $[C_2mIm][CH_3HPO_3]$ system. The yellow clouds indicate the distribution of $O_E$ and $O_H$ atoms.

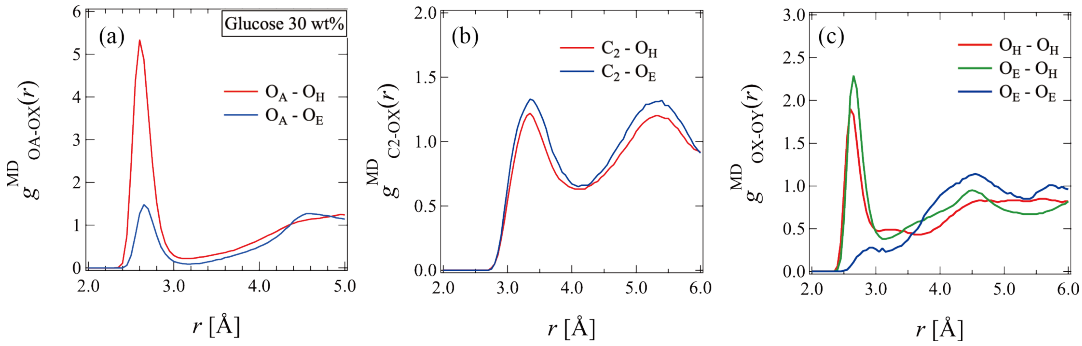


Figure 2.10: Atom-atom pair correlation functions, $g_{i-j}^{\mathrm{MD}}(r)$ for (a) $O_A$ (anion), (b) $C_2$ (cation), and (c) $O_H$ or $O_E$ (glucose) around O atoms within glucose calculated for 30 wt% glucose in $[C_2mIm][CH_3HPO_3]$ system.

at $r$ = 2.6 Å and $r$ = 2.7 Å respectively. The closest O (anion)—O (glucose) correlations observed in $g^{\mathrm{MD}}_{\mathrm{OA-OH}}(r)$ and $g^{\mathrm{MD}}_{\mathrm{OA-OE}}(r)$ mainly contribute to the first peak in the $r^2[G^{\mathrm{MD}}_{\mathrm{inter}}(r) - 1]$ shown in Figure 2.8 (a). Here, it should be noted that the first peak intensity of $O_A$—$O_H$ and $O_A$—$O_E$ is significantly different. The difference can be realized by considering the intramolecular hydrogen bonds within glucose molecules, as discussed later. Figure 2.10 (b) shows the $g^{\mathrm{MD}}_{\mathrm{C2-OX}}(r)$ for the $C_2$ carbon within $[C_2mIm]^+$ around the O atoms (X = H or E) within glucose. Both $g^{\mathrm{MD}}_{\mathrm{C2-OX}}(r)$s exhibited the first peak at $r$ = 3.4 Å. In comparison with the first peak position of $g^{\mathrm{MD}}_{\mathrm{OA-OX}}(r)$ (2.6 - 2.7 Å), it was indicated that the interactions between hydroxyl groups of glucose and $O_A$ in $[CH_3HPO_3]^-$ are stronger than between the hydroxyl groups and $C_2$-$H_2$ in $[C_2mIm]^+$. Figure 2.10 (c) shows the $g^{\mathrm{MD}}_{\mathrm{OX-OY}}(r)$s (X and Y = H or E) for the intermolecular O (glucose)—O (glucose) interactions between glucose molecules. The $g^{\mathrm{MD}}_{\mathrm{OH-OH}}(r)$ and $g^{\mathrm{MD}}_{\mathrm{OE-OH}}(r)$ exhibited the first peak at 2.6 and 2.7 Å, respectively. The peaks originate from the hydrogen bonds between glucose molecules. However, no significant peak was found in the $g^{\mathrm{MD}}_{\mathrm{OE-OE}}(r)$. The observed difference between $g^{\mathrm{MD}}_{\mathrm{OE-OE}}(r)$ and $g^{\mathrm{MD}}_{\mathrm{OH-OH}}(r)$ (or $g^{\mathrm{MD}}_{\mathrm{OE-OH}}(r)$) is caused by intramolecular hydrogen bonds within a glucose molecule.

For evaluation of the intramolecular hydrogen bonds within glucose molecules, I calculated the population of dihedral angle $O_C$-C-C-$O_E$, $\phi$ for the glucose molecules in the MD cell. Previous research by $^1$H NMR spectroscopy and MD simulations [18,36,37] on aqueous glucose solution established that glucose coexists as three conformers with $\phi = 60°$ (gauche-trans, $gt$), 180° (trans-gauche, $tg$), 300° (gauche-gauche, $gg$) in water, and their relative stability is in the order of $gg > gt > tg$. Figure 2.11 shows population of $\phi$ of the glucose molecules in $[C_2mIm][CH_3HPO_3]$ calculated by the MD simulations. The population was largest at $\phi = 325°$ ($gg$), followed by 35° ($gt$) and 170° ($tg$). In addition, the abundance ratio of the three conformers was calculated to be $gg : gt : tg = 51 : 38 : 11$, which is the same tendency as glucose in aqueous solution. In the two stable conformations, $gt$ and $gg$, $H_O$-$O_E$ of hydroxylmethylene group locates near $O_C$. It suggests that the conformations were stabilized by the intramolecular hydrogen bond, $O_C$ —$H_O$-$O_E$. Such an intramolecular hydrogen bond compete with the intermolecular hydrogen bonding interactions between glucose and $[CH_3HPO_3]^-$. Hence, the lower peak intensity in the $g^{\mathrm{MD}}_{\mathrm{OA-OE}}(r)$ among $g^{\mathrm{MD}}_{\mathrm{OA-OX}}(r)$s (shown in Figure 2.10(a)) is realized from the existence of the intramolecular hydrogen bond of $O_C$ —$H_O$-$O_E$. In contrast, with regard to the glucose-cation interaction, the $O_E$ (glucose) can interacts with the $C_2$-$H_2$ (cation) irrespective of the intramolecular

hydrogen bonds. That is the reason why there was no difference in the peak intensity among the $g^{\mathrm{MD}}_{\mathrm{C2-OX}}(r)$ (X = H, E) (Figure 2.10 (b)).

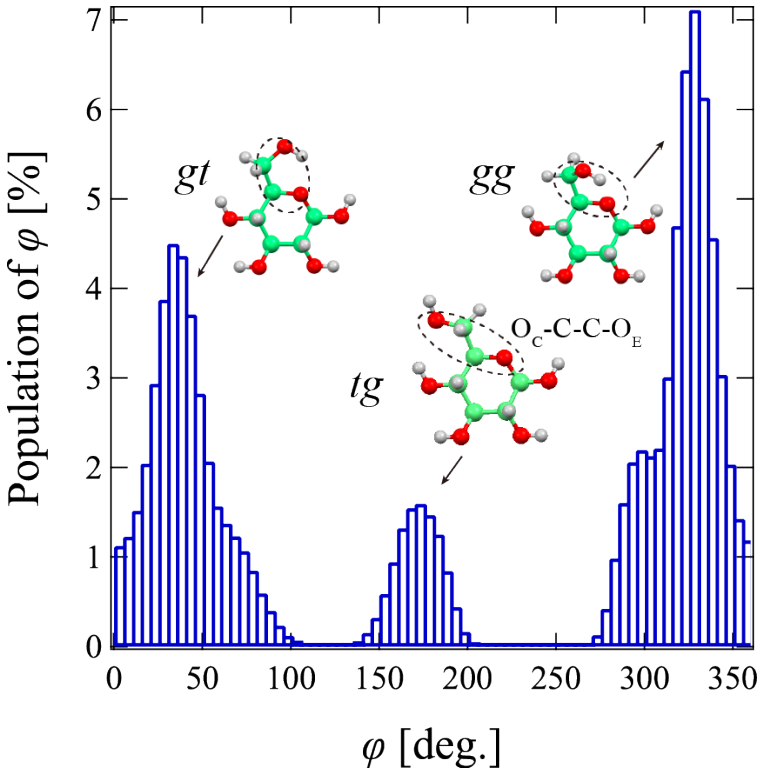


Figure 2.11: Histogram of dihedral angle $O_C$-C-C-$O_E$, $\phi$ of glucose molecules calculated for 30 wt% glucose in $[C_2mIm][CH_3HPO_3]$ system. The interval of $\phi$ is 5°.

The coordination numbers, $N_{\mathrm{X-OH}}$ of atoms (X = $O_A$ (anion), $O_H$ (glucose), and $O_E$ (glucose)) in the first coordination shell of $H_O$-$O_H$ (glucose) are calculated by the integration of $g^{\mathrm{MD}}_{\mathrm{X-OH}}(r)$ functions up to $R = 3.0$ Å:[31,38]

$$N_{\mathrm{X-OH}}(r) = \int_0^R \left( \frac{N_{\mathrm{X}}}{V} g^{\mathrm{MD}}_{\mathrm{X-OH}}(r) \right) 4\pi r^2 \mathrm{d}r \tag{2.7}$$

Here, $V$ and $N_{\mathrm{X}}$ is the volume of the MD cell and the number of X atoms in the MD cell. $N_{\mathrm{OA-OH}}$, $N_{\mathrm{OH-OH}}$, and $N_{\mathrm{OE-OH}}$ were listed in Table 2.2. Although the fraction of coordinating $O_H$ and $O_E$ (glucose) increased with increasing the concentration, the coordination of $O_A$ ($[CH_3HPO_3]^-$) is still dominant even in the highest concentration.

Table 2.2: Coordination number of atoms in the first solvation shell of $O_H$-$H_O$ within glucose.

| Conc.[a] / wt% | Coordination number[b] | | |
|---|---|---|---|
| | $O_A$ | $O_H$ | $O_E$ |
| 10 | 0.87 | 0.03 | 0.02 |
| 20 | 0.75 | 0.15 | 0.05 |
| 30 | 0.62 | 0.29 | 0.08 |

[a]Weight fraction of glucose in $[C_2mIm^+][CH_3(H)PO_3^-]$
[b]Calculated by integrating the first peak in the corresponding $g^{MD}_{X\text{-}OH}(r)$ from $r = 0$ to 3.0 Å.

## 2.7 Conclusions

Liquid structure of neat $[C_2mIm][CH_3HPO_3]$ and solvation structure of glucose in $[C_2mIm][CH_3HPO_3]$ were investigated by HEXTS experiments and all-atom MD simulations. The experimental radial distribution functions, $r^2[G^{\mathrm{exp}}(r) - 1]$s were well reproduced by MD simulations for all the glucose concentration examined here. With regard to liquid structure of neat $[C_2mIm][CH_3HPO_3]$, I pointed out that the hydrogen bond between $O_A$ (anion) and $C_2$-$H_2$ (cation) is predominant in the cation-anion interaction. As for solvation structure of glucose in $[C_2mIm][CH_3HPO_3]$, it is found that the glucose molecules are preferentially solvated with $[CH_3HPO_3]^-$ rather than $[C_2mIm]^+$. From analysis by the atom-atom pair correlation function, it is clarified that the glucose molecule is hydrogen bonded with $[CH_3HPO_3]^-$ to form $O_H$-$H_O$ (glucose)—$O_A$ (anion) interaction. However, the intramolecular hydrogen bond of $O_E$-$H_O$ — $O_C$ within glucose still remains even in $[C_2mIm][CH_3HPO_3]$. Such intramolecular hydrogen bonds compete with the intermolecular hydrogen bonds between glucose and $[CH_3HPO_3]^-$.

## Reference


[1] Ueki, T.; Watanabe, M. *Langmuir* **2007**, *23*, 988–990.

[2] Zu, A.; Wang, J.; Wang, H. *Green Chem.* **2010**, *12*, 268–275.

[3] Remsing, R. C.; Swatloski, R. P.; Rogers, R. D.; Moyna, G. *Chem. Commun.* **2006**, *12*, 1271–1273.

[4] Youngs, T. G. A.; Hardacre, C.; Holbrey, J. D. *J. Phys. Chem. B* **2007**, *111*, 13765–13774.

[5] Youngs, T. G. A.; Holbrey, J. D.; Mullan, C. L.; Norman, S. E.; Lagunas, M. C.; D'Agostino, C.; Mantle, M. D.; Gladden, L. F.; Bowron, D. T.; Hardacre, C. *Chem. Sci.* **2011**, *2*, 1594–1605.

[6] Fukaya, Y.; Hayashi, K.; Wada, M.; Ohno, H. *Green Chem.* **2008**, *10*, 44–46.

[7] Kohara, S.; Suzuya, K.; Kashihara, Y.; Matsumoto, N.; Umesaki, N.; Sakai, I. *Nucl. Instrum. Meth. A* **2001**, *467-468*, 1030–1033.

[8] Isshiki, M.; Ohishi, Y.; Goto, S.; Takeshita, K.; Oshikawa, T. *Nucl. Instrum. Meth. A* **2001**, *467-468*, 663–666.

[9] Sakai, S. *KEK Report*; National Laboratory for High Energy Physics: Tsukuba, Japan, 1990; Vol. 90-16.

[10] Cromer, D. T. *J. Chem. Phys.* **1969**, *50*, 4857–4859.

[11] Hubbell, J. H.; Veigele, W. J.; Briggs, E. A.; Brown, R. T.; Cromer, D.; Howerton, R. J. *J. Phys. Chem. Ref. Data* **1975**, *4*, 471–538.

[12] Maslen, E. N.; Fox, A. G.; O'Keefe, M. A. *International Tables for Crystallography*; Kluwer: Dorfrecht, The Netherlands, 1999; Vol. C.

[13] Lorch, E. *J. Phys. Chem.* **1969**, *2*, 229–237.

[14] Nosé, S. *Mol. Phys.* **1984**, *52*, 255.

[15] Hoover, W. G. *Phys. Rev. A* **1985**, *31*, 1695.

[16] Parrinello, M.; Rahman, A. *Phys. Rev. Lett* **1980**, *45*, 1196–1199.

[17] Lee, C. Y.; Acree, T. E.; Shallenberger, R. S. *Carbohydr. Res.* **1969**, *9*, 356–360.

[18] Nishida, Y.; Ohrui, H.; Meguro, H. *Tetrahedron Lett.* **1984**, *25*, 1575–1578.

[19] Maple, S. R.; Allerhand, A. *J. Am. Chem. Soc.* **1987**, *109*, 3168–3169.

[20] Le Barc' H, N.; Grossel, J. M.; Loosten, P.; Mathlouthi, M. *Food Chemistry* **2001**, *74*, 119–124.

[21] Kanzaki, R.; Umebayashi, Y.; Takeuchi, M.; Fujii, K. *Ensemble* **2007**, *9*, 18–21.

[22] Cornell, W. D.; Cieplak, P.; Bayly, C. I.; Gould, I. R.; Merz, K. M.; Ferguson, D. M.; Spellmeyer, D. C.; Fox, T.; Caldwell, J. W.; Kollman, P. A. *J. Am. Chem. Soc.* **1995**, *117*, 5179–5197.

[23] Damm, W.; Frontera, A.; Tirado-Rives, J.; Jorgensen, W. L. *J. Org. Chem.* **1997**, *18*, 1955–1970.

[24] Lopes, J. N. A. C.; Pádua, A. A. H. *J. Phys. Chem. B* **2004**, *108*, 2038–2047.

[25] Lopes, J. N. A. C.; Gomes, M. F. C.; Pádua, A. A. H. *J. Phys. Chem. B* **2006**, *110*, 16816–16818.

[26] Murzyn, K.; Bratek, M.; Pasenkiewicz-Gierula, M. *J. Phys. Chem. B* **2013**, *117*, 16388–16396.

[27] Umebayashi, Y.; Hamano, H.; Seki, S.; Minofar, B.; Fujii, K.; Hayamizu, K.; Tsuzuki, S.; Kameda, Y.; Kohara, S.; Watanabe, M. *J. Phys. Chem. B* **2011**, *115*, 12179–12191.

[28] Fukuda, S.; Takeuchi, M.; Fujii, K.; Kanzaki, R.; Takamuku, T.; Chiba, K.; Yamamoto, H.; Umebayashi, Y.; Ishiguro, S. *J. Mol. Liquids* **2008**, *143*, 2–7.

[29] Umebayashi, Y.; Chung, W.-L.; Mitsugi, T.; Fukuda, S.; Takeuchi, M.; Fujii, K.; Takamuku, T.; Kanzaki, R.; Ishiguro, S. *J. Comput. Chem. Jpn.* **2008**, *7*, 125–134.

[30] Kanzaki, R.; Mitsugi, T.; Fukuda, S.; Fujii, K.; Takeuchi, M.; Soejima, Y.; Takamuku, T.; Yamaguchi, T.; Umebayashi, Y.; Ishiguro, S. *J. Mol. Liquids,* **2009**, *147*, 77–82.

[31] Fujii, K.; Seki, S.; Ohara, K.; Kameda, Y.; Doi, H.; Saito, S.; Umebayashi, Y. *J. Solution Chem.* **2014**, *43*, 1655–1668.

[32] Hardacre, C.; McMath, S. E. J.; Nieuwenhuyzen, M.; Boeron, D. T.; Soper, A. K. *J. Phys.: Condens. Matter* **2003**, *15*, S159–S166.

[33] Fujii, K.; Soejima, Y.; Kyoshoin, Y.; Fukuda, S.; Kanzaki, R.; Umebayashi, Y.; Yamaguchi, T.; Ishiguro, S.; Takamuku, T. *J. Phys. Chem. B* **2008**, *112*, 4329–4336.

[34] Hardacre, C.; Holbrey, S. E. J.; McMath, S. E. J.; Boeron, D. T.; Soper, A. K. *J. Chem. Phys.* **2003**, *18*, 273–278.

[35] Bowron, D. T.; Agostino, C. D.; Gladden, L. F.; Hardacre, C.; Holbrey, J. D.; Lagunas, M. C.; McGregor, J.; Mantle, M. D.; Mullan, C. L.; Youngs, T. G. A. *J. Phys. Chem. B* **2010**, *1214*, 7760–7768.

[36] Corchado, J. C.; Sánchez, M. L.; Aguilar, M. A. *J. Am. Chem. Soc.* **2004**, *126*, 7311–7319.

[37] Bagno, A.; Rastrelli, F.; Saielli, G. *J. Org. Chem.* **2007**, *72*, 7373–7381.

[38] Fujii, K.; Hamano, H.; Doi, H.; Song, X.; Tsuzuki, S.; Hayamizu, H.; Seki, S.; Kameda, Y.; Dokko, K.; Watanabe, M.; Umebayashi, Y. *J. Phys. Chem. C* **2013**, *117*, 19314–19324.

# Chapter 3

# Solvated Structure of Cellulose in a Phosphonate-based Ionic Liquid



## 3.1 Introduction

In chapter 2, I evaluated microscopic intermolecular interactions between cellulose and [$C_2$mIm][$CH_3HPO_3$]. On the other hand, understanding of chain characteristics and aggregated structure of cellulose in [$C_2$mIm][$CH_3HPO_3$] is also important for improvement and optimization of the dissolution process. With regards to chain characteristics of cellulose in ILs, SAXS and SANS studies were performed on cellulose dissolved in pure IL ([$C_2$mIm][$CH_3COO$]) and IL containing a co-solvent (DMF/[$C_2$mIm][$CH_3COO$] mixture of the molar ratio of 9:1).[1,2] However, mesoscopic structure and dynamics of cellulose chains in pure ILs have not been adequately studied.

In this chapter, I investigated both (1) the microscopic inter- and intramolecular interactions and (2) the mesoscopic chain conformation and aggregated structure of cellulose in pure [$C_2$mIm][$CH_3HPO_3$] solution. Microscopic intramolecular interactions in cellulose molecules were studied by the HEXTS and MD simulation analysis on cellobiose (Figure 3.1(b)). The effect of the intramolecular hydrogen bonds can be studied more in detail by using cellobiose as a model molecule rather than glucose. The mesoscopic structure of cellulose chains was investigated by SAXS, SLS, and

DLS experiments. Eventually, the chain conformation of cellulose was realized based on the insight about microscopic intramolecular interactions in cellulose molecules.

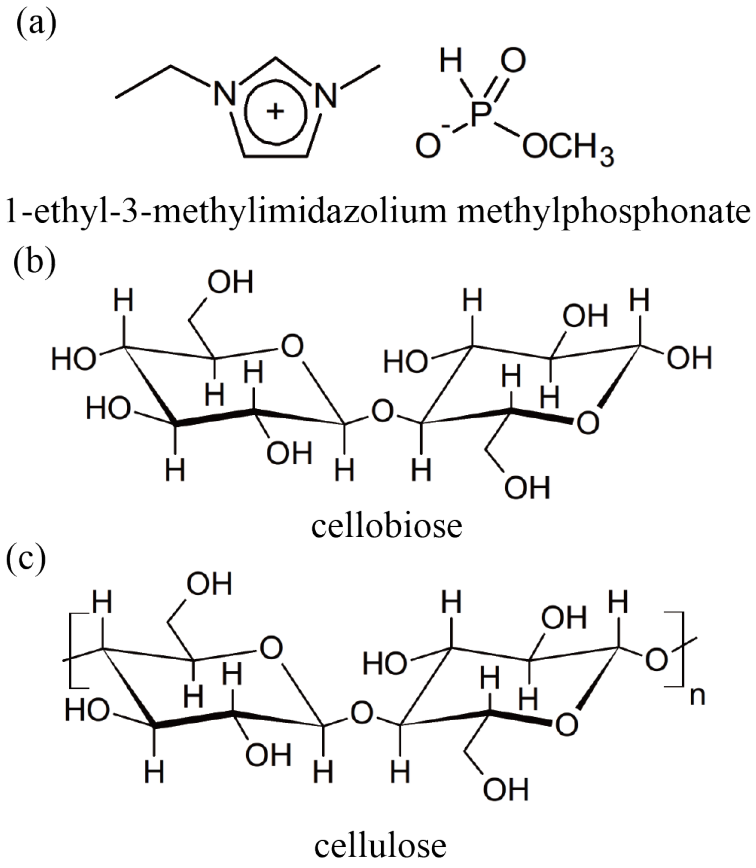


Figure 3.1: Chemical structures of (a) 1-ethyl-3-methylimidzolium methylphosphonate ($[C_2mIm][CH_3HPO_3]$), (b) cellobiose, and (c) cellulose.

## 3.2 Experimental

### 3.2.1 Materials

$[C_2mIm][CH_3HPO_3]$ was synthesized by the same procedure as described in Chapter 2. D-(+)-Cellobiose was purchased from Aldrich. Co. A kind of microcrystalline cellulose "Cellulose powder C" was purchased from Advantec. Co. Here, the molecular weight of the cellulose material was estimated to be approximately $10^5$ by liquid chromatography in a previous report.[3] Cellulose powder was dried at 90 °C for 24 h in vacuo prior to use. The preparation procedures of cellulose in $[C_2mIm][CH_3HPO_3]$ solutions are described below. At first, the dried cellulose powder was dispersed into $[C_2mIm][CH_3HPO_3]$ by vigorously stirring with a spatula at room temperature. Subsequently, the mixtures were heated at 50 °C for 5 h in vacuo to remove bubbles

and trace water in the solution. After the heating, clear and colorless solutions were obtained.

The absence of undissolved cellulose powder granules was confirmed via optical microscopy using BX51N-33P-O-SP, Olympus Co. Figure 3.2 shows optical microscope images of neat $[C_2mIm][CH_3HPO_3]$ and cellulose in $[C_2mIm][CH_3HPO_3]$ solutions of volume fraction, $\phi = 0.047$, which is the highest concentration examined in this study. Except for some bubbles, the cellulose solution looked almost the same as neat $[C_2mIm][CH_3HPO_3]$, indicating that undissolved cellulose powder granules did not exist in the prepared cellulose solutions.

### 3.2.2 HEXTS Experiments

HEXTS measurement was performed for Cellobiose 30 wt% in $[C_2mIm][CH_3HPO_3]$ solution at room temperature. Details of the experiment were described in Chapter 2. The structure factore $S^{\mathrm{exp}}(q)$ and radial distribution function $G^{\mathrm{exp}}(r)$ were calculated by eq. (2.1) in Chapter 2.

### 3.2.3 MD Simulations

An all-atom MD simulation was performed for an $NTP$ ensemble (298 K and 1 atm) in a cubic cell. The composition of cellobiose molecules and IL ions was set to be consistent with the sample solution measured in the HEXTS experiment (30 wt%): 70 cellobiose molecules were mixed into 250 ion pairs of $[C_2mIm][CH_3HPO_3]$. Similarly to the MD simulations on glucose in $[C_2mIm][CH_3HPO_3]$ system (Chapter 2), CLaP and OPLS-AA force fields were applied for IL ions and cellobiose, respectively.[4–8] The detailed procedures of the MD simulation were described in Chapter 2. In the cellobiose in $[C_2mIm][CH_3HPO_3]$ system, equilibration time was set to be 1.5 ns. Subsequently, trajectories of atoms were sampled every 0.1 ps during 1.5 - 2.0 ns. The mass density value obtained by the MD simulations (1.2593 g $cm^{-3}$) showed good agreement with the experimental value (1.2699 g $cm^{-3}$). X-ray weighted structure factor, $S^{\mathrm{MD}}(q)$ and the radial distribution function, $G^{\mathrm{MD}}(r)$ were calculated by eq. (2.1) and eq. (2.3) in Chapter 2.

### 3.2.4 SAXS Experiments

SAXS experiments were conducted at the BL03XU beamline of SPring-8 (JASRI, Japan). All measurements were carried out at room temperature. To suppress background scattering intensity from air and window materials, I employed a vacuum

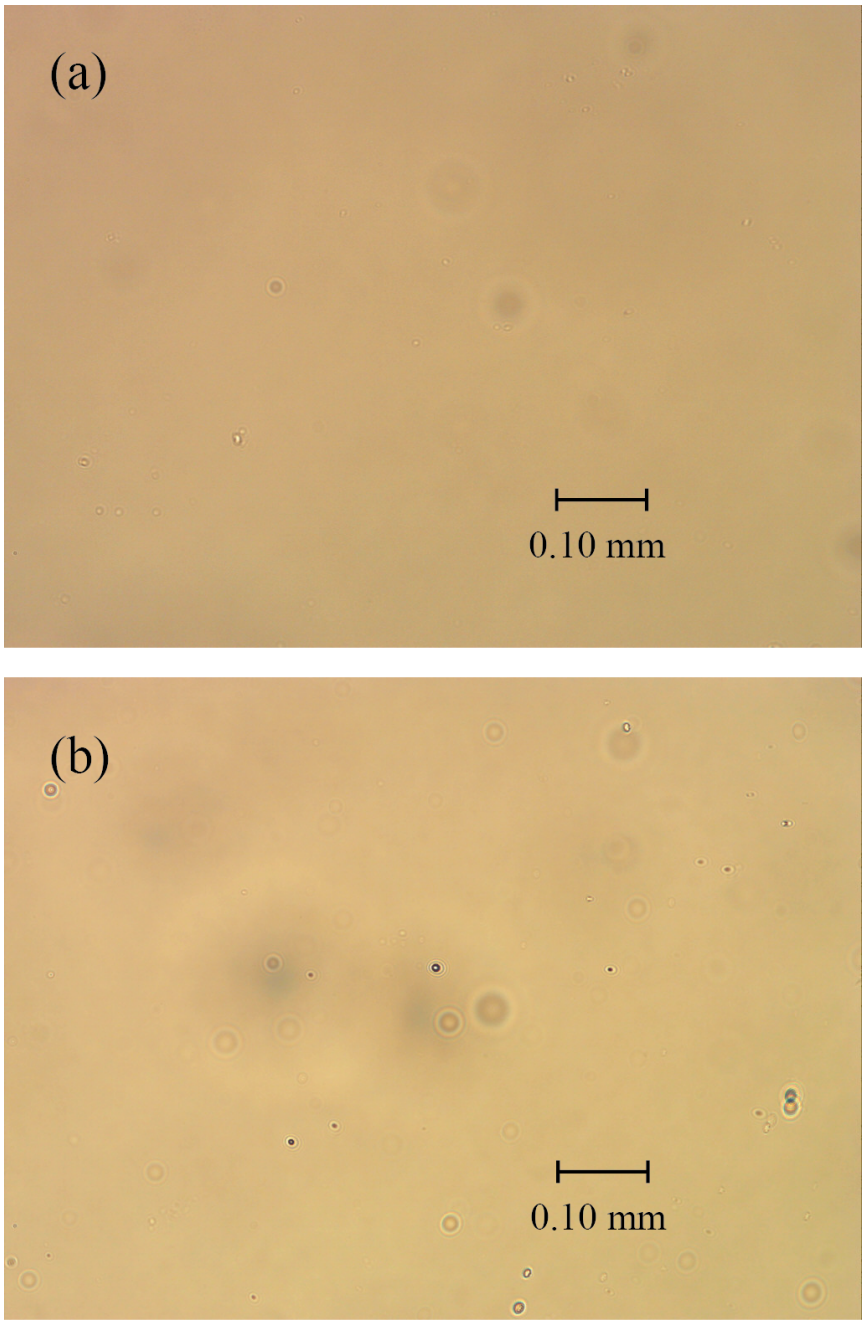


Figure 3.2: Optical microscope images of (a) neat $[C_2mIm][CH_3HPO_3]$ and (b) cellulose in $[C_2mIm][CH_3HPO_3]$ solution of volume fraction, $\phi = 0.047$. A scale bar of 0.10 mm is also shown in the images.

chamber setting in which the sample environment and the X-ray pathway were directly connected.[9] Sample solutions were injected into a homemade planar cell (sample thickness: 2 mm). After the injection, sample solution was annealed at 50 °C for 4 h to eliminate the effect of shear stress. A pair of borosilicate cover glasses (thickness: 30 $\mu$m) were used as optical windows for the sample cell. Wavelength of X-ray was 1.00 Å. All the sample solutions were irradiated for 30 s. X-ray scattering intensity was acquired by an area detector (PILATUS, Dectris®). After the correction for background scattering and absorption, the obtained X-ray scattering profiles were normalized to the absolute scale using glassy carbon as a secondary standard sample for intensity calibration. To obtain the scattering intensity profiles from cellulose molecules $I(q)$, the scattering intensity of pure $[C_2mIm][CH_3HPO_3]$, $I_{IL}(q)$, was subtracted from that of the sample solutions, $I_{sample}(q)$. To evaluate structure of cellulose molecules in $[C_2mIm][CH_3HPO_3]$ quantitatively, I carried out curve-fitting analysis with a model function of core-shell cylindrical scatterers as follows:[10]

$$I(q) = \rho P_L(q) P_{CS}(q) i(q) + Aq^{-2} \tag{3.1}$$

$$P_{CS}(q) = \left[ (b_{core} - b_{shell}) \left(\pi R_{core}^2\right) \frac{2J_1(qR_{core})}{qR_{core}} + (b_{shell} - b_{solv}) \left(\pi R_{out}^2\right) \frac{2J_1(qR_{out})}{qR_{out}} \right]^2 \tag{3.2}$$

$$P_L = L^2 \left[ \frac{2}{qL} \int_0^{qL} \frac{\sin t}{t} dt - \frac{4\sin^2(qL/2)}{(qL)^2} \right] \tag{3.3}$$

The parameters $L$, $R_{out}$, and $R_{core}$ are the length, the outer radius, and the core radius of the core-shell cylinder, respectively. Here, I adopted a decoupling approximation in which the form factor of the core-shell cylinder is given as a product of a longitudinal, $P_L(q)$ and a cross-section parts, $P_{CS}(q)$.[11] The approximation becomes valid when $L$ is sufficiently larger than $R_{out}$. $b_{core}$, $b_{shell}$, and $b_{solv}$ are the scattering length densities (SLD) of the core, shell, and bulk solvent, respectively. In the curve-fitting analysis, both $b_{core}$ and $b_{solv}$ were fixed to the SLD values calculated for glucose and $[C_2mIm][CH_3HPO_3]$, respectively. Here, the SLDs were calculated using the mass density and the atomic scattering factors. The number density of the core-shell cylinder ($\rho$) was calculated using $L$, $R$, and the actual volume fraction of the sample solutions. $J_1(x)$ is the first-order Bessel function. The power-law term $Aq^{-2}$ was introduced to reproduce the excess scattering in the low-$q$ region, where $A$ is a constant. The validity and physical meanings of the model function will be discussed later. The inter-particle interference between the core-shell cylinders is represented by the interference factor $i(q)$, which is empirically developed from the polymer reference

interaction site model as follows:[12–15]

$$
\begin{aligned}
i(q) &= \frac{1}{1+\beta c(q) P_{\mathrm{L}}(q)/L^2} \qquad (3.4)\\
c(q) &= \frac{3\left[\sin\left(2q(R_{\mathrm{out}}+l_{\mathrm{D}})\right) - 2q(R_{\mathrm{out}}+l_{\mathrm{D}}\cos\left(2q(R_{\mathrm{out}}+l_{\mathrm{D}})\right)\right]}{\left[2q(R_{\mathrm{out}}+l_{\mathrm{D}})\right]^3}\\
\beta &= \frac{\left(1+2(B+C)^2\right)+2D\left(1+B+\frac{5}{4}C\right)}{(1-B-C)^4} - 1\\
B &= \pi R_{\mathrm{out}}^2 L\rho, \quad C = \frac{4}{3}\pi R_{\mathrm{out}}^3\rho, \quad D = \frac{1}{2}\pi R_{\mathrm{out}} L^2\rho
\end{aligned}
$$

### 3.2.5 Light Scattering Experiments

Light scattering measurements were conducted using an SLS/DLS compact goniometer (ALV, Langen, 5022F-PCC-MS) coupled with a photon correlator. A He-Ne laser (wavelength, $\lambda = 632.8$ nm; 22 mW) was used as the incident beam. The scattering angle $2\theta$ was fixed to be 90° and temperature was controlled to be 25.0 °C. Each measurement required 30 s. The solvent IL, $[C_2mIm][CH_3HPO_3]$ was passed through a PTFE filter (pore size: 0.2 $\mu$m) prior to use. Sample solutions were injected into test tubes and annealed at 50 °C for 4 h in vacuo. The position ($p$) dependence of a time-averaged light scattering intensity ($\langle I\rangle_p$) and the time correlation function of light scattering intensity ($g_p^{(2)}(\tau)-1$) were measured by changing the relative position of the beam spot by manually rotating the test tube.

For analysis on scattering media containing frozen heterogeneity, such as polymer gels, a "partial-heterodyne" method has been established.[16] The analytical procedures are summerized below. The time correlation function of light scattering intensity at position $p$, $g_p^{(2)}(\tau) - 1$ is defined as follows:

$$
g_p^{(2)}(\tau) - 1 = \frac{\langle I(t+\tau)I(t)\rangle_p}{\langle I(t)^2\rangle_p} \qquad (3.5)
$$

where $I(t)$ is the light scattering intensity. When there are two diffusive modes in the media, $g_p^{(2)}(\tau) - 1$ can be approximated as follows:

$$
g_p^{(2)}(\tau) - 1 = \beta\sigma_{\mathrm{I}}^2\left[A\exp\left(-D_{\mathrm{A,fast},p}q^2\tau\right) + (1-A)\exp\left(-D_{\mathrm{A,slow},p}q^2\tau\right)\right]^2 \qquad (3.6)
$$

where $D_{\mathrm{A,fast,p}}$ and $D_{\mathrm{A,slow,p}}$ are the apparent diffusion coefficients for the fast mode and the slow mode, respectively. $\beta$ is the coherence factor and $A$ denotes the fraction of the fast mode. In light scattering experiment, $q$ is defined as follows:

$$
q = \frac{4\pi n}{\lambda}\sin\theta \qquad (3.7)
$$

where $n$ is the refractive index of the solvent. $\sigma_{\mathrm{I}}^2$ is related to the fraction of time-averaged scattering intensity originating from thermal fluctuation ($\langle I_{\mathrm{F}} \rangle$) in the total scattering intensity ($\langle I \rangle_p$) as follows:

$$\sigma_{\mathrm{I}}^2 = X_p(2 - X_p) \tag{3.8}$$

$$X_p = \frac{\langle I_{\mathrm{F}} \rangle}{\langle I \rangle_p} \tag{3.9}$$

These equations were derived for the situation in which scattering intensity from solute is sufficiently larger than background scattering intensity. When background scattering intensity ($I_{\mathrm{back}}$) is not negligible compared with scattering intensity from solute, one needs to subtract $I_{\mathrm{back}}$ from $\langle I \rangle_p$ in eq. (3.9). Then eq. (3.9) should be revised as follows:

$$X_p = \frac{\langle I_{\mathrm{F}} \rangle}{\langle I \rangle_p - I_{\mathrm{back}}} \tag{3.10}$$

The apparent diffusion coefficient $D_{\mathrm{A,fast,p}}$ is affected by the value of $X_p$ and thus $D_{\mathrm{A,fast,p}}$ depends on position. The true collective diffusion coefficient $D_{\mathrm{fast}}$ can be estimated from $D_{\mathrm{A,fast,p}}$ using the following relationship.

$$D_{\mathrm{fast}} = (2 - X_p)\, D_{\mathrm{A,fast,p}} \tag{3.11}$$

Based on eq. (3.10) and eq. (3.11), one can derive the following equation.

$$\frac{\langle I \rangle_p - I_{\mathrm{back}}}{D_{\mathrm{A,fast},p}} = \frac{2}{D_{\mathrm{fast}}} \left( \langle I \rangle_p - I_{\mathrm{back}} \right) - \frac{\langle I_{\mathrm{F}} \rangle}{D_{\mathrm{fast}}} \tag{3.12}$$

Eq. 3.12 indicates that $D_{\mathrm{fast}}$ can be obtained from the slope of the plot of $(\langle I \rangle_p - I_{\mathrm{back}})/D_{\mathrm{A,fast,p}}$ vs $(\langle I \rangle_p - I_{\mathrm{back}})$.

## 3.3 Microscopic Solvation Structure

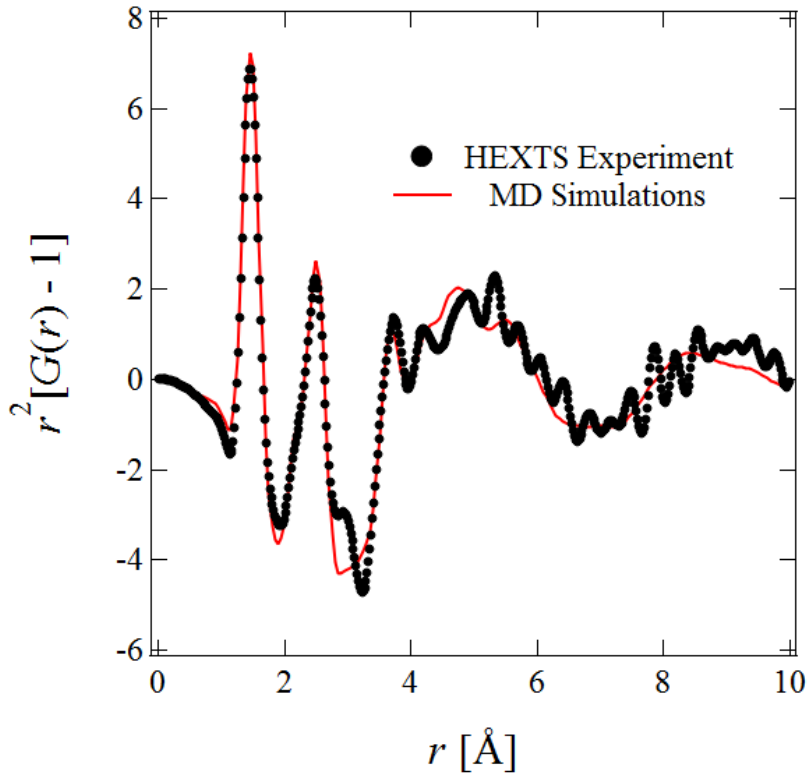


Figure 3.3: Radial distribution function, $G(r)$, of 30 wt% cellobiose in $[C_2mIm][CH_3HPO_3]$ solution, as a form of $r^2[G(r) - 1]$, obtained from the inverse Fourier transform of the structure factor, $S(q)$ (see eq. (2.1) and eq. (2.3) in Chapter 2). Black dots and solid red lines show the $G(r)$ obtained from the HEXTS experiment and MD simulations, respectively.

The black dots in Figure 3.3 show the experimental radial distribution function, $G^{exp}(r)$ as a form of $r^2[G^{exp}(r) - 1]$ obtained for 30 wt% cellobiose in $[C_2mIm][CH_3HPO_3]$ solution. As established in Chapter 2, the peaks at $r = 1.5$ and 2.5 Å can be mainly assigned to intramolecular correlations within IL ions and solutes. Similarly to Chapter 2, I performed all-atom MD simulations to evaluate the intermolecular correlation components. The radial distribution function obtained from MD simulations, $G^{MD}(r)$, is shown as the solid red line in Figure 3.3. Except for the "ripple"-like artifact in the experimental value, the MD result reproduced the experimental results well. This agreement between the HEXTS experiment and the MD simulations indicated that the trajectory of molecules obtained from the present MD simulations was valid.

Subsequently, I calculated the partial radial distribution functions, $G^{MD}_{partial}(r)$s related to the intermolecular interactions between cellobiose and $[C_2mIm][CH_3HPO_3]$.

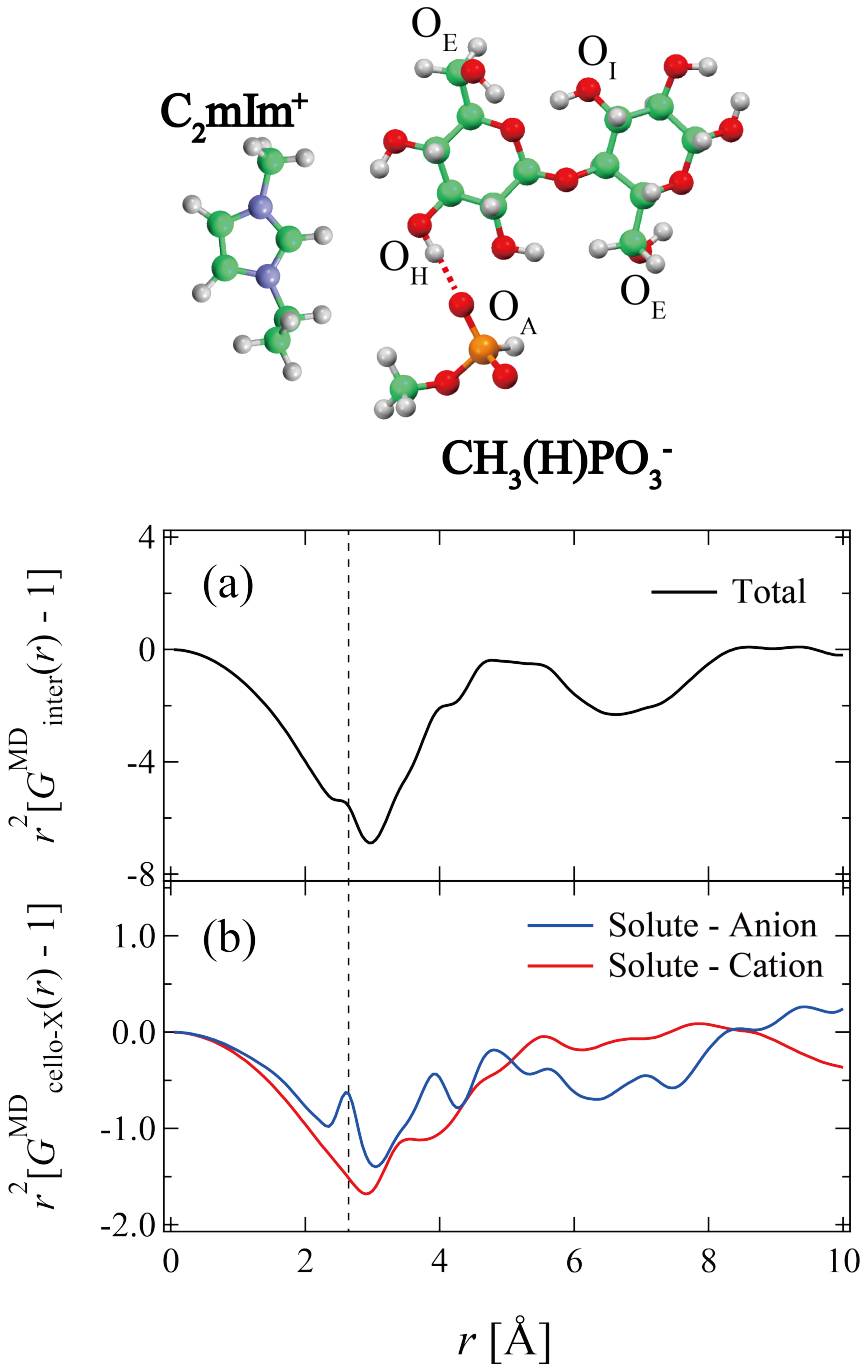


Figure 3.4: The partial radial distribution functions, $G^{\mathrm{MD}}(r)$ for (a) total intermolecular correlations, (b) cellobiose-$[CH_3HPO_3]^-$ correlations, and cellobiose-$[C_2mIm]^+$ correlations.

Figure 3.4(a) shows a partial radial distribution function, $r^2[G^{\mathrm{MD}}_{\mathrm{inter}}(r) - 1]$, that contains all of the intermolecular correlations in the 30 wt% cellobiose in $[C_2mIm][CH_3HPO_3]$ solution. The partial radial distribution functions for cellobiose-anion and cellobiose-cation interactions ($r^2[G^{\mathrm{MD}}_{\mathrm{cello-An}}(r)-1]$ and $r^2[G^{\mathrm{MD}}_{\mathrm{cello-Cat}}(r)-1]$), are also shown in Figure 3.4(b). As shown in Figure 3.4(a), the nearest intermolecular correlation is represented by a peak at $r = 2.6$ Å in the $r^2[G^{\mathrm{MD}}_{\mathrm{inter}}(r) - 1]$. Figure 3.4(b) clearly shows that a sharp peak at $r = 2.6$ Å in the $r^2[G^{\mathrm{MD}}_{\mathrm{inter}}(r) - 1]$ can be assigned to $r^2[G^{\mathrm{MD}}_{\mathrm{cello-An}}(r) - 1]$, not to $r^2[G^{\mathrm{MD}}_{\mathrm{cello-Cat}}(r) - 1]$. This indicates that the cellobiose-anion interactions is the predominant for dissolution of cellobiose into $[C_2mIm][CH_3HPO_3]$, which is completely the same tendency as in the case of glucose in the $[C_2mIm][CH_3HPO_3]$ system (Chapter 2).

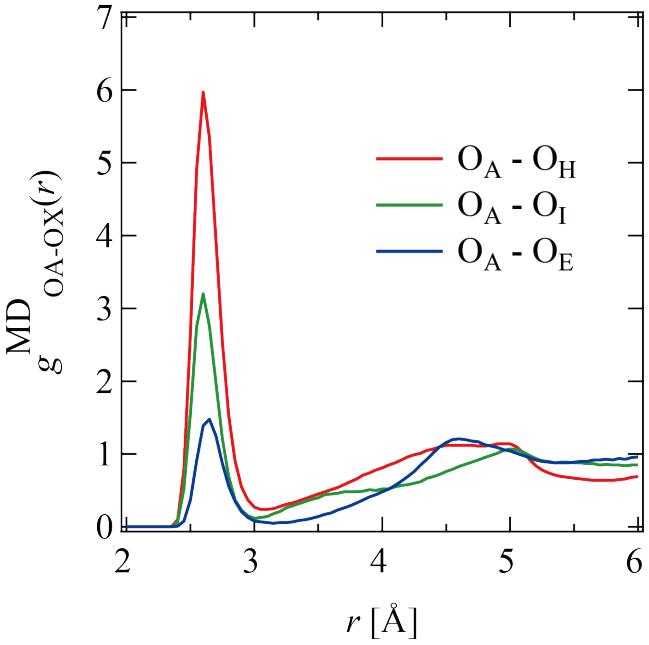


Figure 3.5: The atom-atom pair correlation functions, $g^{\mathrm{MD}}_{\mathrm{OA-OX}}(r)$s, for intermolecular hydrogen bonds between hydroxyl groups in cellobiose and the negatively charged oxygen atoms of $[CH_3HPO_3]^-$.

To discuss the local interactions more in detail, I calculated the atom-atom pair correlation functions, $g^{\mathrm{MD}}_{i-j}(r)$s. At first, I focused on the intermolecular cellobiose-anion interactions, especially the intermolecular hydrogen bonding. Figure 3.5 shows the $g^{\mathrm{MD}}_{\mathrm{OA-OX}}(r)$ which denotes the atom-atom correlation between $O_A$ within the $[CH_3HPO_3]^-$ and the O atoms (X = H, I, or E) of the hydroxyl groups within cellobiose (the indices are shown in Figure 3.4). Similarly to the corresponding one of glucose in $[C_2mIm][CH_3HPO_3]$ (Chapter 2), the $g^{\mathrm{MD}}_{\mathrm{OA-OX}}(r)$s for cellobiose in $[C_2mIm][CH_3HPO_3]$ systems exhibited an obvious peak at $r = 2.6$ Å reflecting

the hydrogen bond of $O_A$—$H_O$-$O_X$. It indicate that the intermolecular hydrogen bonds between cellulose are disrupted by the formation of hydrogen bonds between their hydroxyl groups and $[CH_3HPO_3]^-$.

There was a significant difference in the intensity of the first peaks of the $g^{MD}_{OA-OX}(r)$s. The differences can be ascribed to the intramolecular hydrogen bonds within cellobiose molecules, as discussed below.

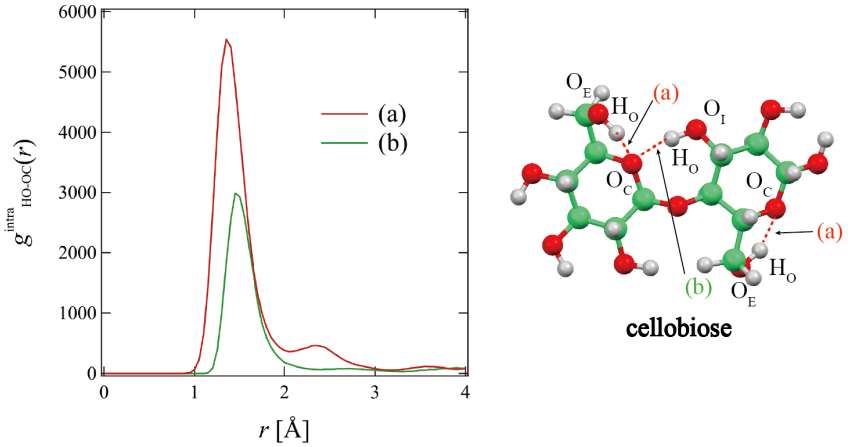


Figure 3.6: The atom-atom pair correlation functions, $g^{MD}_{HO-OC}(r)$s which denote the intramolecular hydrogen bonds of (a) $O_C$—$H_O$-$O_E$ and (b) $O_C$—$H_O$-$O_I$ within cellobiose molecules.

Figure 3.6 shows the $g^{MD}_{HO-OC}(r)$s which denote the intramolecular hydrogen bonds of (a) $O_C$—$H_O$-$O_E$ and (b) $O_C$—$H_O$-$O_I$ within cellobiose molecules. The $g^{MD}_{HO-OC}(r)$s corresponding to the intramolecular hydrogen bonds of (a) and (b) exhibited a peak at $r = 1.4$ Å and $r = 1.5$ Å, respectively. This indicated that the intramolecular hydrogen bonds within the cellulose molecules exist even in $[C_2mIm][CH_3HPO_3]$. The intramolecular hydrogen bonds prevented the hydroxyl groups of $O_E$-$H_O$ and $O_I$-$H_O$ from forming an intermolecular hydrogen bond with $[CH_3HPO_3]^-$. I deduced that the difference observed for the intensity of the first peaks of the $g^{MD}_{OA-OX}(r)$s (Figure 3.5) originated from the existence of intramolecular hydrogen bonds. As I have already established for the glucose system, here too, the $O_C$—$H_O$-$O_E$-type hydrogen bonds (Figure 3.6 (a) bonds) exist also in cellobiose in $[C_2mIm][CH_3HPO_3]$ solutions. On the contrary, the $O_C$—$H_O$-$O_I$ type hydrogen bond (Figure 3.6 (b) bonds) is a new observation. The intramolecular hydrogen bonds prevent the twisting motion of glucose units. In such a condition, the flexibility of the cellulose chain, which is composed of cellobiose units, is expected to be suppressed in $[C_2mIm][CH_3HPO_3]$ solutions. Therefore, considering the conformational entropy of cellulose, the existence

of the hydrogen bonds of $O_C$—$H_O$-$O_I$ is not favorable for dissolution of cellulose in ILs. I estimated the abundance ratio of the intramolecular hydrogen bonds of $O_C$—$H_O$-$O_I$ to the intermolecular hydrogen bonds, $O_A$ — $H_O$-$O_I$, between cellobiose and $[CH_3HPO_3]^-$ based on the coordination number. The coordination number of X-atoms around $H_O$ at the distance of $r$, $N_{X-HO}(r)$s were calculated as follows:

$$N_{X-HO}(r) = \int_0^r \left( \frac{N_X}{V} g^{MD}_{X-HO}(r') \right) 4\pi r'^2 dr' \tag{3.13}$$

The abundance ratio of the intramolecular hydrogen bonds to the intermolecular ones can be estimated from the ratio of $N_{OA-HO}(r)$ and $N_{OC-HO}(r)$ at the first coordination shell. As shown in Figure 3.7, both of $N_{OA-HO}(r)$ and $N_{OC-HO}(r)$

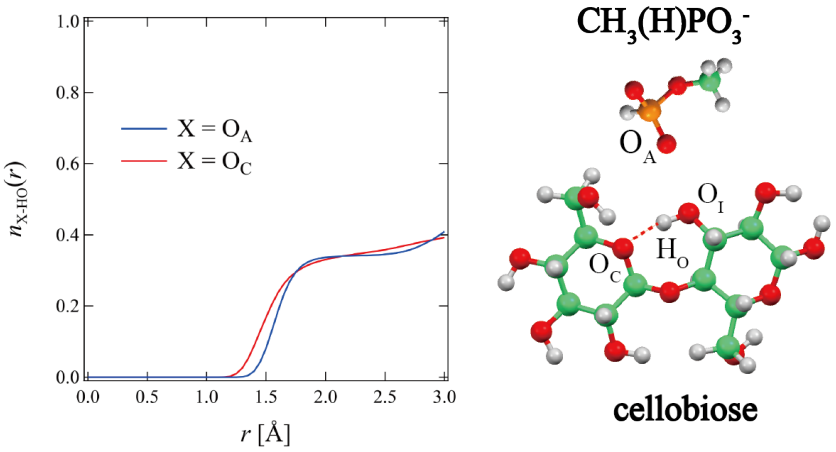


Figure 3.7: The coordination number of the atoms around $H_O$, $N_{X-HO}(r)$ (X= $O_A$, $O_C$)

reached a plateau at $r$ = 2.0 Å, corresponding to the distance of first coordination shell. The values of $N_{OA-HO}(r)$ and $N_{OC-HO}(r)$ at $r$ = 2.0 Å were 0.34 and 0.33, respectively. Hence, the abundance ratio was found to be close to 1:1, indicating that a significant proportion of $O_I$-$H_O$ bonds formed the intramolecular hydrogen bond of $O_C$—$H_O$-$O_I$.

## 3.4 Mesoscopic Solvation Structure

To investigate the solvated structure of cellulose at the mesoscopic scale, SAXS experiments was conducted for cellulose in $[C_2mIm][CH_3HPO_3]$. Figure 3.8 shows the SAXS profiles of cellulose molecules, $I(q)$ obtained for the cellulose in $[C_2mIm][CH_3HPO_3]$ solutions of various volume fractions ($\phi$). In the field of polymer physics, it is well established that the scattering profile of dispersed Gaussian

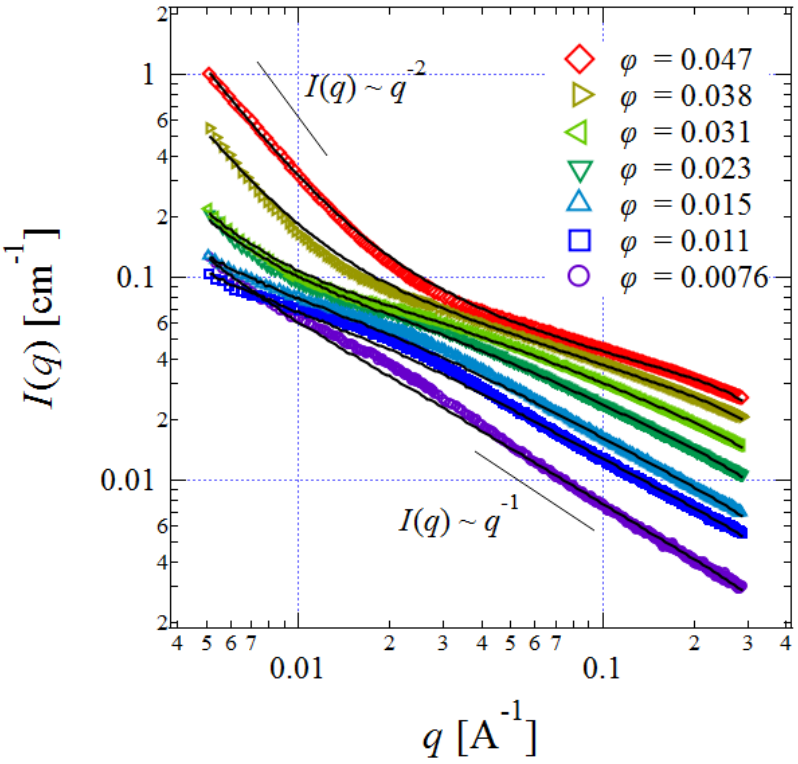


Figure 3.8: SAXS profiles obtained for cellulose in $[C_2mIm][CH_3HPO_3]$ solutions with various volume fractions, $\phi = 0.0076$-$0.047$ (symbols). The solid lines show the calculated scattering curve based on eq. (3.3).

chain in solution is represented by the Debye function, $P_{\mathrm{D}}(q)$ written as follows.

$$P_{\mathrm{D}}(q) = \frac{2}{x^2}\left[\exp(-x) - 1 + x\right] \quad \left(x \equiv R_{\mathrm{g}}^2 q^2\right) \tag{3.14}$$

The Debye function exhibits a power-law behavior, $I(q) \propto q^{-2}$.[17,18] The worm-like chain also shows the $I(q) \propto q^{-2}$ behavior when $q^{-1}$ is sufficiently larger than the Kuhn segment length.[19] However, in the present study, the SAXS profiles for low concentration solutions ($\phi < 0.038$) exhibited a power-law behavior of $I(q) \propto q^{-1}$, not $I(q) \propto q^{-2}$. The $I(q) \propto q^{-1}$ behavior corresponds to a characteristic scattering pattern of rod-like scatterers,[10] indicating that the cellulose chains exist as almost rod-like polymers in $[\mathrm{C_2mIm}][\mathrm{CH_3HPO_3}]$. The exponent of $I(q)$ decreased with increasing $\phi$. It indicated that contribution of the interchain-interference factor, $i(q)$ to $I(q)$ became significant with increasing concentration. In addition, in the low-$q$ region ($q < 0.02$ Å$^{-1}$), a large upturn emerged in the SAXS profiles for concentrated solutions ($\phi \geq 0038$), and the intensity of the upturn increased with increasing $\phi$. Here, the excess scattering exhibited a power-law behavior of $I(q) \propto q^{-2}$. I assumed that this excess scattering was an indication of aggregates formation. From such a viewpoint, the exponent of the excess scattering reflects mass fractal nature of the aggregates formed by rod-like cellulose chains. Actually, the fractal dimension of aggregates formed by rod-like particles is reported to be 1.81 - 2.26 in a previous study.[20] The observed fractal dimension of the cellulose aggregates in our study ($\approx$ 2) is consistent with the previously reported value for rod-like particle aggregates.

For a more quantitative discussion, I performed a curve fitting analysis on the SAXS profiles. At first, I examined a rather simple model function for solid cylindrical scatterers without a shell layer. However, the radius of the solid cylinder obtained from the curve fitting was unrealistically small, and the experimental scattering profiles were not reproduced sufficiently. It is because the experimental scattering profiles did not have any shoulders which represent the radius of solid cylinder. I conjectured that the cylinder model did not work well at high-$q$ region because complicated atomistic correlations were not negligible in the region. Thus I adopted the "core-shell" cylinder model to reproduce the scattering pattern from cellulose molecules surrounded by IL ions. Here, the introduction of "shell" layer is a rough approximation for the deviation of SLD in the solvation shell of cellulose molecules from that of bulk solvent; the "core" and "shell" layer roughly correspond to cellulose molecule itself and solvation shell, respectively. Such an approximation has been proposed in a characterization of blush-like semiflexible polymers in solution.[21] Eventually, the experimental SAXS profiles were fitted by eq. (3.3). Here, the Debye length, $l_{\mathrm{D}}$, was

fixed at 0 because the core-shell cylinders, which approximate cellulose molecules, are not charged. The solid lines in Figure 3.8 show resulting fitting curves. The experimental SAXS profiles were successfully reproduced by the model function, including their absolute scattering intensities.

The $R_{\mathrm{core}}$ and $R_{\mathrm{out}}$, obtained as fitting parameters, are shown in Figure 3.9(a). As shown, the $R_{\mathrm{core}}$ was independent of $\phi$, and its value was almost constant at $\approx 5$ Å, which is close to the thickness of a single cellulose molecule. The $R_{\mathrm{out}}$ was almost independent of $\phi$, and its value was $\approx 7$ Å. In the previous section, I showed the partial radial distribution function for cellobiose-anion and cellobiose-cation interactions, *i.e.*, $r^2[G^{\mathrm{MD}}_{\mathrm{Cello-An}}(r) - 1]$ and $r^2[G^{\mathrm{MD}}_{\mathrm{Cello-Cat}} - 1]$ (Figure 3.4(b)). Both functions converged to 0 when $r > 7$ Å. This means that the distance corresponding to the first coordination shell around cellulose is $r \approx 7$ Å. Considering this, the obtained value of $R_{\mathrm{out}} \approx 7$ Å is assumed to be valid. These results indicate that cellulose molecules exist as rigid rod-like polymer chains and are dispersed in $[C_2mIm][CH_3HPO_3]$ at the molecular level. The rigid conformation of cellulose chains can be ascribed to the existence of the intramolecular hydrogen bonds, as discussed in the previous section; the hydrogen bonds of $O_C$—$H_O$-$O_I$ restrict the thermal fluctuations of the cellulose chain segments. The scattering length density in the shell layer, $b_{\mathrm{shell}}$ was also shown in Figure 3.9(b). $b_{\mathrm{shell}}$ was lower than $b_{\mathrm{solv}}$. As shown in Figure 3.4(b), $r^2[G^{\mathrm{MD}}_{\mathrm{cello-X}}(r)$ - 1]s (X = anion or cation) were lower than 0 in the range of $r < 7$ Å. It indicates that the number density of atoms in the solvation shell of cellulose is lower than that of bulk solvent. Thus I conclude that $b_{\mathrm{shell}}$ obtained from the curve fitting on SAXS profiles is consistent with the results of MD simulations.

Very recently, two papers about solvated structure of cellulose in ILs, $[C_4mIm][Cl]$[22] and $[C_2mIm][CH_3COO]$,[23] were published. Both of the authors utilized SAXS measurements to investigate the chain conformation of cellulose in the ILs. Napso *et al.* reported that cellulose molecules are dispersed at molecular level and exist as rod-like polymers in $[C_2mIm][CH_3COO]$, which is the same conclusion with ours.[23] On the other hand, Jiang *et al.* reported that cellulose molecules exhibit relatively flexible conformation in $[C_4mIm][Cl]$.[22] Such conflicting results can be explained from a viewpoint of the size of IL anion. The sizes of $[CH_3HPO_3]^-$ (our study) and $[CH_3COO]^-$ are larger than $Cl^-$. It indicates that $Cl^-$ can more easily disrupt intramolecular hydrogen bonds within cellulose chains. Actually, it was reported that the intramolecular hydrogen bonds are disrupted in $[C_4mIm][Cl]$,[24] but they remain in $[C_2mIm][CH_3COO]$[25] based on MD simulations. Thus, I conclude

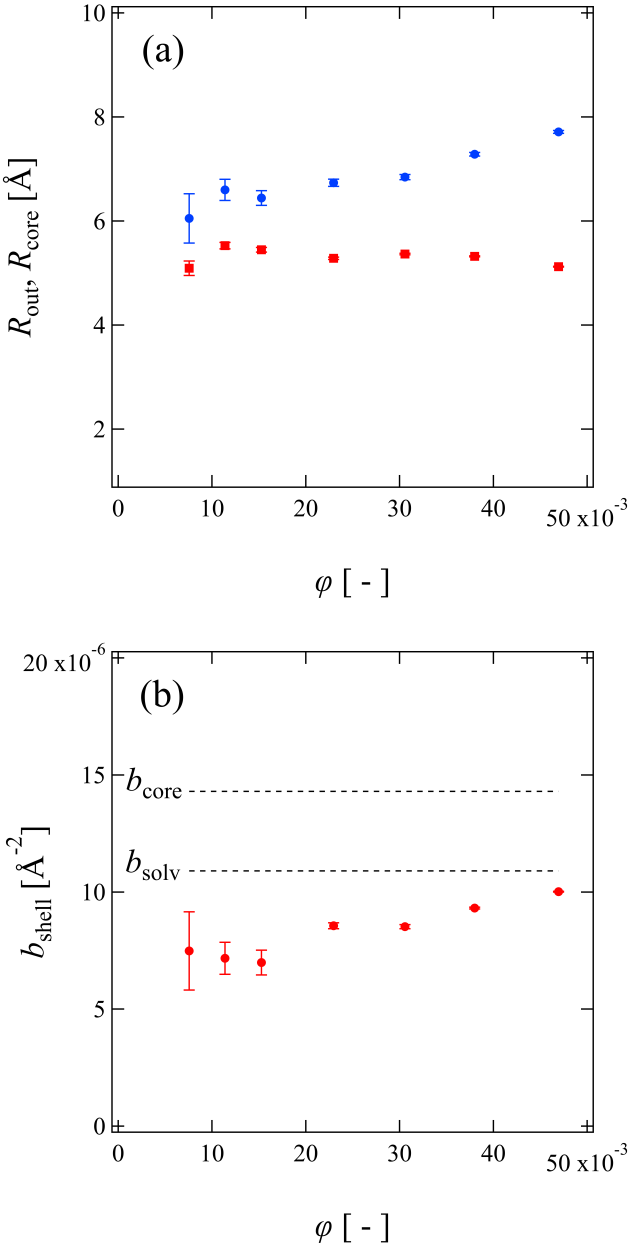


Figure 3.9: Obtained fitting parameters, (a) $R_{out}$ and $R_{core}$ and (b) $b_{shell}$ from the curve-fitting by the model function for core-shell cylinder (eq. (3.3)) on the SAXS profiles of cellulose in $[C_2mIm][CH_3HPO_3]$ solutions. The dotted lines in (b) are the calculated values of $b_{core}$ and $b_{solv}$.

that the flexibility of cellulose chains in the ILs is strongly related to the degree of disruption of the intramolecular hydrogen bonds.

## 3.5 Static Inhomogeneities

To investigate the spatial inhomogeneity of the cellulose solutions, I measured the position ($p$) dependence of the time-averaged light scattering intensity, $\langle I \rangle_p$. Figure 3.10 shows $p$-dependence of $\langle I \rangle_p$ measured for cellulose in $[C_2mIm][CH_3HPO_3]$ solutions with various $\phi$. Dilute solutions ($\phi < 0.038$) did not show any fluctuations for $\langle I \rangle_p$ with $p$. This indicated that the dilute cellulose solutions were homogeneous, like typical polymer solutions. On the contrary, the $\langle I \rangle_p$ measured for concentrated cellulose solutions ($\phi \geq 0038$) demonstrated an obvious $p$-dependence, *i.e.*, a speckle pattern. In general, a speckle pattern reflects the existence of frozen density fluctuations in the scattering media.[26] Hence, it is supposed that the translational diffusion of cellulose chains is restricted by pseudo cross-links originating from strong entanglement between rigid cellulose chains in the concentrated solutions. In addition, the threshold $\phi$ for the speckle pattern emergence ($\phi = 0.038$) corresponded to that of the upturn emergence in the SAXS low-$q$ region profiles (Figure 3.8). This means that the emergence of frozen inhomogeneity in the concentrated cellulose solutions was correlated to aggregates formation.

Figure 3.11(a) shows the time correlation function at a given measurement point, $g_p^{(2)}(\tau)-1$, of light scattering intensity obtained from cellulose in $[C_2mIm][CH_3HPO_3]$ solutions of various $\phi$. For all of the solution examined here, the time correlation function of light scattering intensity at point $p$, $g_p^{(2)}(\tau)-1$ showed two types of decay modes. The apparent diffusion coefficients, $D_{\mathrm{A,fast},p}$ and $D_{\mathrm{A,slow},p}$ for the observed fast mode and the slow mode were estimated by a curve-fitting procedure using eq. (3.6). The fitting curves are shown in Figure 3.11 as solid lines. As shown, the experimental $g_p^{(2)}(\tau)-1$ was successfully reproduced by the model function given in eq. (3.6). It is supposed that the slow mode originates from the diffusion of small amounts of aggregates, which is often observed in polymer solutions. Hence, I do not dwell on the properties of the slow mode at this time.

The true diffusion coefficient for the collective diffusion, $D_{\mathrm{fast}}$, was estimated using the partial-heterodyne method which is introduced in the experimental section. Figure 3.12 shows the plots of $(\langle I \rangle_p - I_{\mathrm{back}})/D_{\mathrm{A,fast,p}}$ vs $(\langle I \rangle_p - I_{\mathrm{back}})$ for cellulose in $[C_2mIm][CH_3HPO_3]$ solutions of various volume fractions. $D_{\mathrm{fast}}$ was obtained from the slope. I deduced that the fast mode reflects the collective diffusion of cellulose

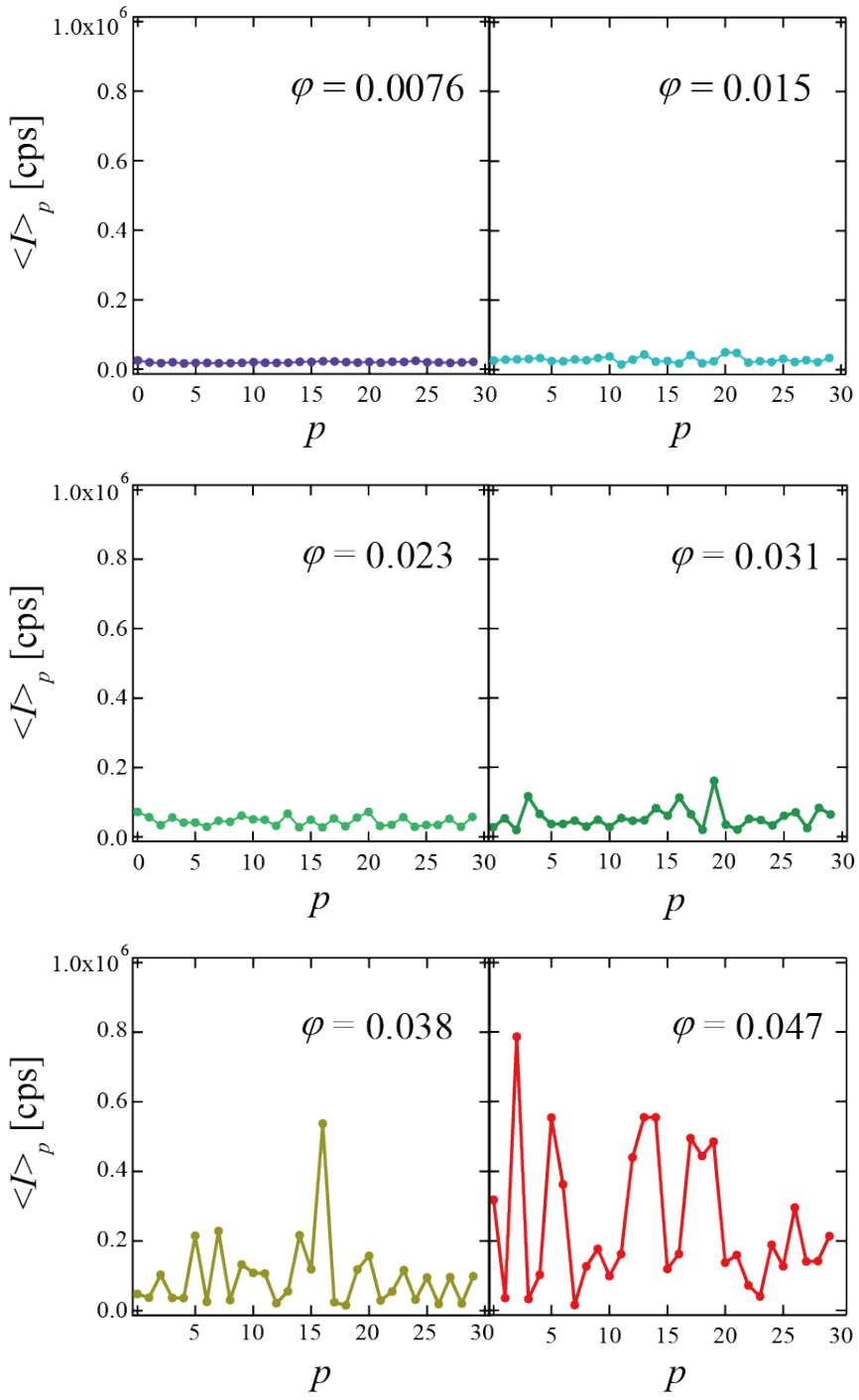


Figure 3.10: Position ($p$)-dependence of time-averaged scattering intensity of light $\langle I \rangle_p$ from cellulose in $[C_2mIm][CH_3HPO_3]$ solutions, $\phi$ = 0.0076-0.047.

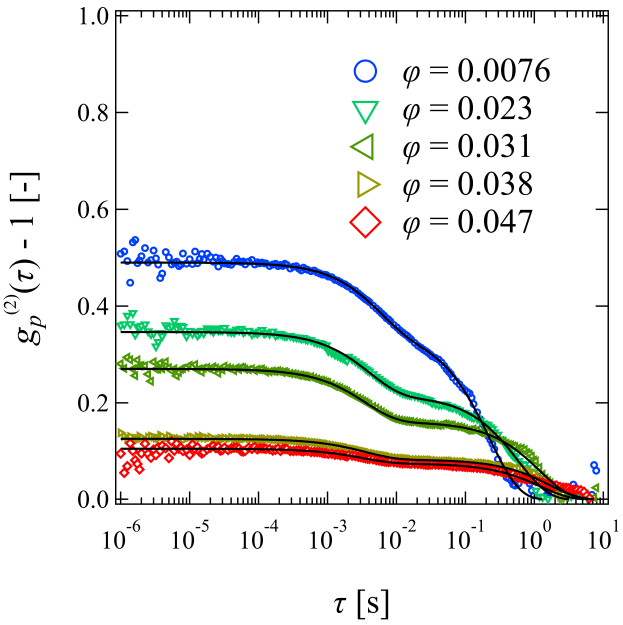


Figure 3.11: Representative time correlation functions of light scattering intensity at a given measurement point, $g_p^{(2)}(\tau) - 1$, obtained for cellulose in $[C_2mIm][CH_3HPO_3]$ solutions of various $\phi$.

chain segments and estimated the correlation length as follows:

$$\xi = \frac{k_B T}{6\pi\eta D_{\text{fast}}} \tag{3.15}$$

where $k_B$, $T$, and $\eta$ are the Boltzmann constant, absolute temperature, and the viscosity of $[C_2mIm][CH_3HPO_3]$, respectively. The Stokes-Einstein type equation is an established one that denotes the relationship between the cooperative diffusion coefficient and the correlation length of semi-dilute polymer solutions and polymer gels.[27] One can derive the equation from general scaling concepts, and thus it is applicable to stiff-polymer solutions. The $\phi$-dependence of the estimated $\xi$ is shown in Figure 3.13. The power-law behavior of $\xi \propto \phi^{-0.49\pm0.05}$ was observed. Based on the scaling concepts for semi-dilute polymer solutions, $\xi$ is scaled as $\xi \propto \phi^{\mu}$, where the exponent $\mu$ is related to the fractal dimension of the polymer chains, $d_p$: $\mu \propto -1/(3-d_p)$.[28] Hence, $\mu$ was easily predicted to be 1.0, 0.75, and 0.5 for the ideal chain ($d_p = 2$), real chain ($d_p = 5/3$), and rod-like polymer ($d_p = 1$), respectively. In the present study, the obtained value: $\mu = 0.49 \pm 0.05$, is close to the predicted value for a rod-like polymer. This result indicated that the cellulose chains existed as rigid rod-like polymers in $[C_2mIm][CH_3HPO_3]$, which was consistent with the SAXS results.

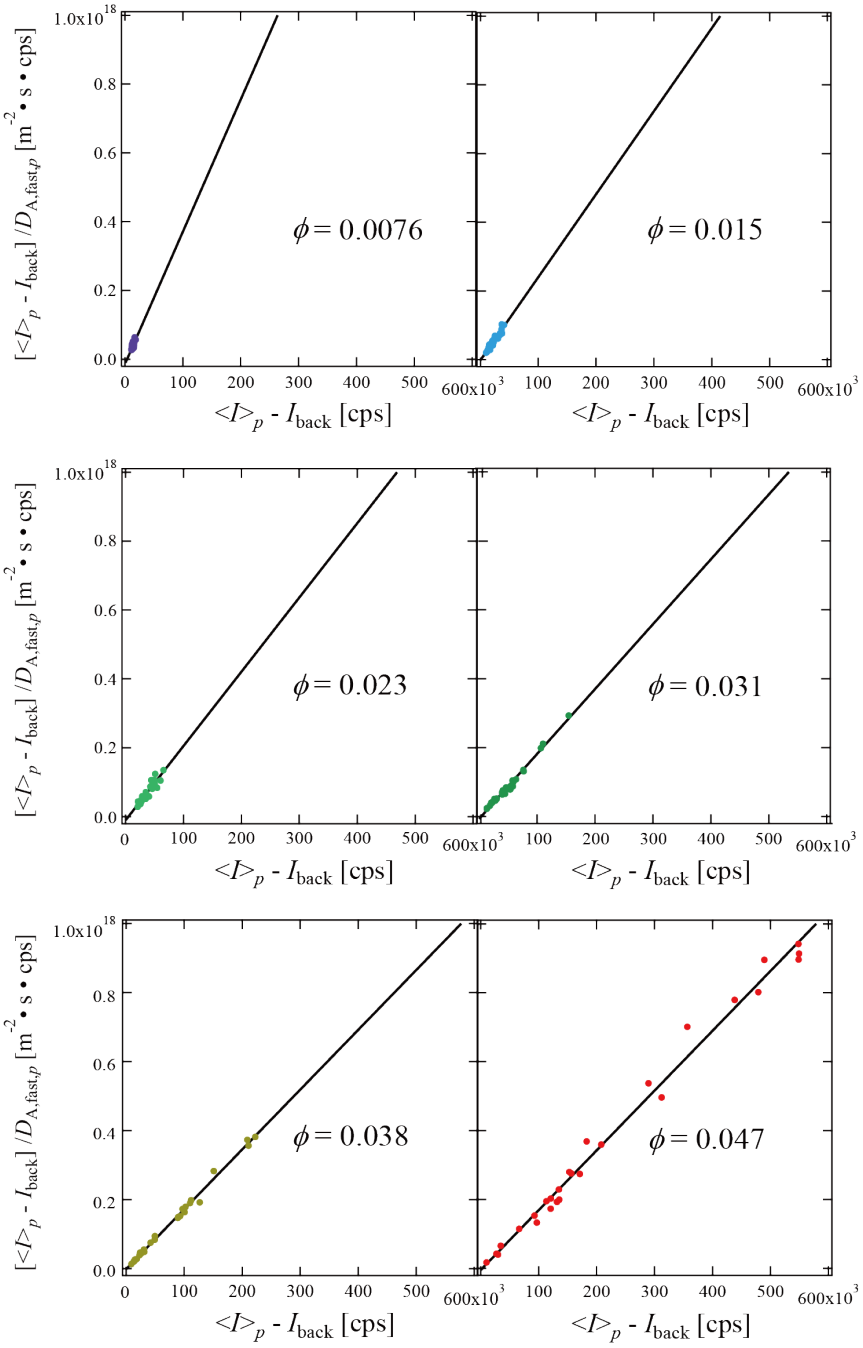


Figure 3.12: $(\langle I\rangle_p - I_{back})/D_{A,fast,p}$ vs $(\langle I\rangle_p - I_{back})$ plots for cellulose in $[C_2mIm][CH_3HPO_3]$ solutions of various volume fractions.

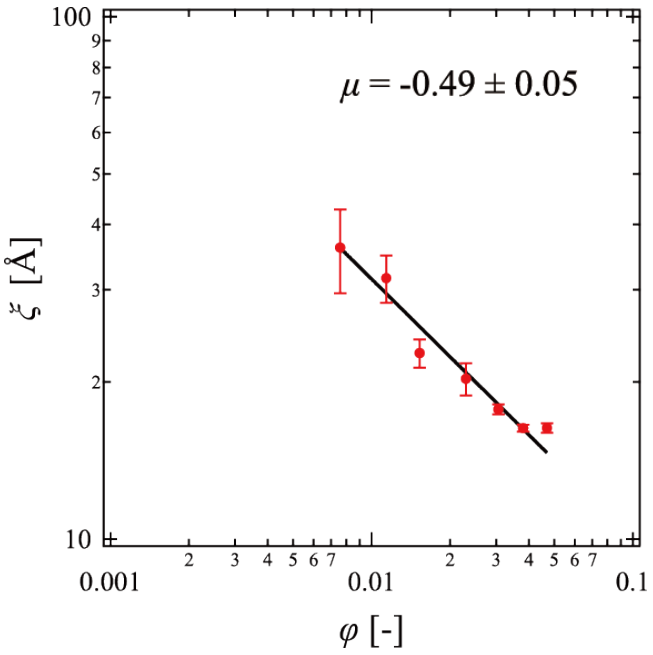


Figure 3.13: $\phi$-Dependence of the correlation length, $\xi$, estimated from the fast mode decay time based on the Einstein-Stokes equation (eq. (3.15))

## 3.6 Conclusions

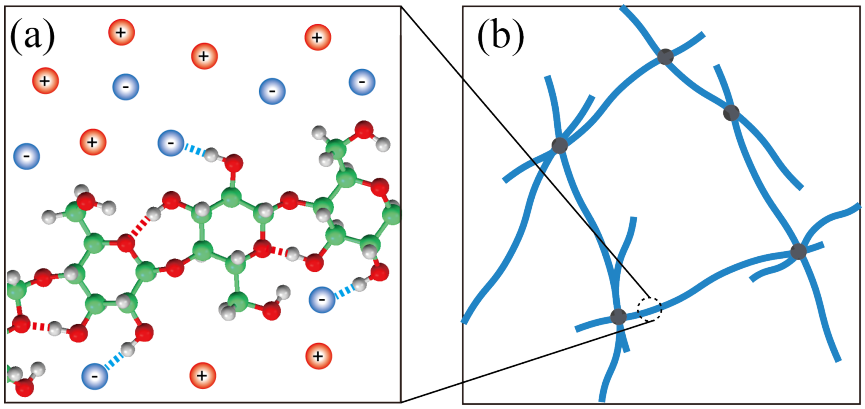


Figure 3.14: Picture of the solvated structure of cellulose solutions in $[C_2mIm][CH_3HPO_3]$ at the (a) microscopic scale and (b) mesoscopic scale.

A picture for the concentrated cellulose solutions in $[C_2mIm][CH_3HPO_3]$ obtained from HEXTS, MD simulations, SAXS, and light scattering experiments is shown in Figure 3.14. The microscopic solvation structure was investigated using HEXTS experiments and MD simulations. As shown in Figure 3.14(a), it was clarified that (1) negatively charged oxygen atoms in $[CH_3HPO_3]^-$ form hydrogen bonds to the hydroxyl groups of cellulose; (2) intramolecular hydrogen bonds between the adjacent glucose segments within cellulose molecules exist even when dissolved in $[C_2mIm][CH_3HPO_3]$. The mesoscopic structure of cellulose chains in $[C_2mIm][CH_3HPO_3]$ was investigated by SAXS and light scattering experiments. It was found that intermolecular hydrogen bonds between cellulose molecules are disrupted in $[C_2mIm][CH_3HPO_3]$ solutions; thus, cellulose molecules are dispersed at the molecular level. In addition, cellulose molecules exist as rod-like polymers because of the intramolecular hydrogen bonds within cellulose chains in $[C_2mIm][CH_3HPO_3]$. Furthermore, in concentrated regions, rod-like cellulose molecules are strongly entangled and cellulose in $[C_2mIm][CH_3HPO_3]$ solutions have frozen inhomogeneities that arise from pseudo cross-links between cellulose molecules.

# Reference


[1] Rein, D. M.; Khalfin, R.; Szekely, N.; Cohen, Y. *Carbohydr. Polym.* **2014**, *112*, 125–133.

[2] Endo, T.; Hosomi, S.; Fujii, S.; Ninomiya, K.; Takahashi, K. *Molecules* **2017**, *22*, 178.

[3] Kuroda, K.; Fukaya, Y.; Ohno, H. *Anal. Methods* **2013**, *5*, 3172–3176.

[4] Cornell, W. D.; Cieplak, P.; Bayly, C. I.; Gould, I. R.; Merz, K. M.; Ferguson, D. M.; Spellmeyer, D. C.; Fox, T.; Caldwell, J. W.; Kollman, P. A. *J. Am. Chem. Soc.* **1995**, *117*, 5179–5197.

[5] Damm, W.; Frontera, A.; Tirado-Rives, J.; Jorgensen, W. L. *J. Org. Chem.* **1997**, *18*, 1955–1970.

[6] Lopes, J. N. A. C.; Pádua, A. A. H. *J. Phys. Chem. B* **2004**, *108*, 2038–2047.

[7] Lopes, J. N. A. C.; Gomes, M. F. C.; Pádua, A. A. H. *J. Phys. Chem. B* **2006**, *110*, 16816–16818.

[8] Murzyn, K.; Bratek, M.; Pasenkiewicz-Gierula, M. *J. Phys. Chem. B* **2013**, *117*, 16388–16396.

[9] Masunaga, H.; Sakurai, K.; Akiba, I.; Ito, K.; Takata, M. *J. Appl. Cryst.* **2013**, *46*, 577–579.

[10] Livsey, I. *J. Chem. Soc., Faraday Trans.* **1987**, *83*, 1445–1452.

[11] Pedersen, J. S.; Schurtenberger, P. *J. Appl. Cryst.* **1996**, *29*, 646–661.

[12] Pedersen, J. S.; Schurtenberger, P. *Macromolecules* **1996**, *29*, 7602–7612.

[13] Pedersen, J. S.; Schurtenberger, P. *J. Polym. Sci. Part B: Polym. Phys.* **2004**, *42*, 3081–3094.

[14] Pedersen, J. S. In *Soft Matter Characterization*; Pecora, P., Borsali, R., Eds.; Springer-Verlag: New York, 2008; Vol. 1; Chapter 4, pp 192–227.

[15] Schweizer, K. S.; Yethiraj, A. *J. Chem. Phys.* **1993**, *98*, 9053–9079.

[16] Shibayama, M. *Bull. Chem. Soc. Jpn.* **2006**, *79*, 1799–1819.

[17] Debye, P.; Bueche, A. M. *J. Chem. Phys.* **1950**, *18*, 1423–1425.

[18] Debye, P. *J. Phys. Chem.* **1947**, *51*, 18–32.

[19] des Cloizeaux, J. *Macromolecules* **1973**, *6*, 403–407.

[20] Mohraz, A.; Moler, D. B.; Ziff, R. M.; Solomon, M. J. *Phys. Rev. Lett.* **2004**, *92*, 155503.

[21] Arakawa, S.; Terao, K.; Kitamura, S.; Sato, T. *Polym. Chem.* **2012**, *3*, 472–478.

[22] Jiang, X.; Kitamura, S.; Sato, T.; Terao, K. *Macromolecules* **2017**, *50*, 3979–3984.

[23] Napso, S.; Rein, D. M.; Khalfin, R.; Cohen, Y. *J. Polym. Sci. Part B: Polym. Phys.* **2017**, *55*, 888–894.

[24] Mostofian, B.; Cheng, X.; Smith, J. C. *J. Phys. Chem. B* **2014**, *118*, 11037–11049.

[25] Payal, R. S.; Balasubramanian, S. *Phys. Chem. Chem. Phys.* **2014**, *16*, 17458–17465.

[26] Shibayama, M. *Macromol. Chem. Phys.* **1998**, *199*, 1–30.

[27] de Gennes, P. G. *Scaling Concepts in Polymer Physics*; Cornell University: Ithaca, 1979.

[28] Daoud, M.; Cotton, J. P.; Farnoux, B.; Jannink, G.; Sarma, G.; Benoit, H.; Duplessix, R.; Picot, C.; de Gennes, P. G. *Macromolecules* **1975**, *8*, 804–818.

# Chapter 4

# SANS Study on the Solvated Structure and Molecular Interactions of a Thermo-respnsive Polymers in a Room Temperature Ionic Liquid

Reproduced from "Hirosawa, K.; Fujii, K.; Ueki, T.; Kitazawa, Y.; Littrell, K. C.; Watanabe, M.; Shibayama, M. SANS Study on the Solvated Structure and Molecular Interactions of a Thermo-responsive Polymer in a Room Temperature Ionic Liquid., *Phys. Chem. Chem. Phys.* **2016**, *18*, 17881" with permission from the Physical Chemistry Chemical Physics Owner Societies. The publication is available at Royal Society of Chemistry via https://doi.org/10.1039/C6CP02254E

## 4.1 Introduction

In Chapters 2 and 3, I focused on the cellulose dissolution phenomena in ILs and investigated the microscopic and mesoscopic solvated structure of cellulose in a phosphonate-type IL, $[C_2mIm][CH_3HPO_3]$. In Chapter 4 and the following Chapter 5, I extended the structural study to the stimuli-responsive phase transition of polymers in ILs.

It is well-known that poly(*N*-isopropylacrylamide) (PNIPAm) in aqueous solution shows a lower critical solution temperature (LCST)-type phase separation. Such LCST-type phase behavior is a common feature of aqueous polymer solution or hydrogel systems.[1–5] In the case of aqueous solution, the demixing by heating is driven by collapse of the hydration shell around hydrophobic side chains of polymers.[6–9] As mentioned in Chapter 1, LCST-type phase behavior is commonly observed also in IL

systems.[10–13] For example, poly(benzyl methacylate) (PBnMA) and its derivatives show LCST-type phase separation in a hydrophobic IL, 1-ethyl-3-methylimidazolium bis(trifluoromethanesulfonyl)amide ([$C_2$mIm][TFSA]).[14,15] It indicates that the ILs construct specific solvation structure around the polymer, as in the case of aqueous polymer solution. Actually, Fujii *et al.* investigated microscopic solvation structure of monomeric BnMA in [$C_2$mIm][$CH_3HPO_3$] and pointed out that [$C_2$mIm]$^+$ orderly locates above and below the benzyl group of BnMA.[16] Such ordered solvation structure is assumed to be the origin of LCST-type phase behavior in the IL system.

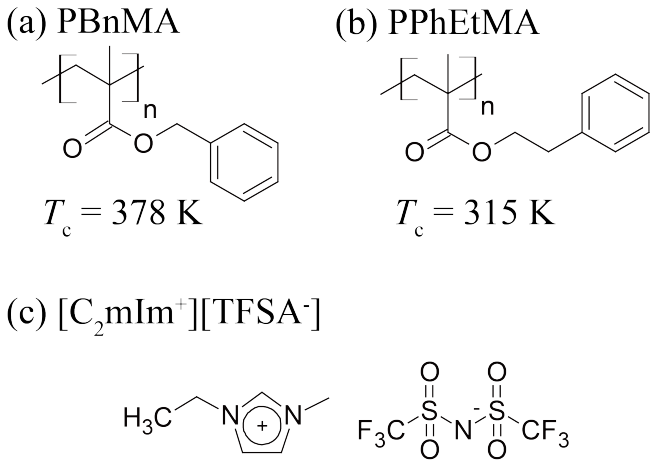


Figure 4.1: Chemical structures of (a) PPhEtMA, (b) PBnMA, and (c) [$C_2$mIm][TFSA] together with the previously reported cloud points, $T_c$.

One of the characteristics of the phase behavior of polymers in ILs is that their phase transition temperatures ($T_c$s) are strongly affected by slight chemical modification on polymer side chain or IL ions.[10,15] For example, LCST of poly(2-phenylethyl methacrylate) (PPhEtMA), having slightly different chemical structure from PBnMA, is 63 K lower than that of PBnMA.[10] This drastic effect of chemical modifications on $T_c$ indicates that one can control the phase behavior and physical properties of polymer/IL composite systems by designing the chemical structure of polymers or ILs.[17,18] Ueki *et al.* thermodynamically characterized the phase separation of polymer in IL, utilizing high-resolution differencial scanning calorimetry (DSC) measurement.[19] The values of the mixing enthalpy $\Delta H_m$ and the mixing entropy $\Delta S_m$ are evaluated for PBnMA in [$C_2$mIm][TFSA] by the DSC measurement, and it was found that both $\Delta H_m$ and $\Delta S_m$ are significantly smaller than those of PNIPAm in water. However, the mechanism of thermo-responsive phase separation of polymer in IL has not yet been adequetely clarified. Especially, understanding of the above-

mentioned strong dependence of $T_c$ on the chemical structure in IL system is still insufficient.

In this Chapter, I focused on the drastic effect of structural modification on the phase equilibrium of thermo-responsive polymers in ILs. I selected PPhEtMA in [$C_2$mIm][TFSA] solution as a model system. The solvated structure and thermodynamic parameters of PPhEtMA in [$C_2$mIm][TFSA] are evaluated by SANS and DLS experiments. In comparion with the previously reported SANS study on PBnMA in [$C_2$mIm][TFSA],[20] I discussed the origin of the large difference in LCST of PBnMA and PPhEtMA from the viewpoint of polymer-IL interactions.

## 4.2 Experimental

### 4.2.1 Materials

The thermo-responsive polymer, PPhEtMA was prepared by Dr. Yuzo Kitazawa in Prof. Masayoshi Watanabe group (Yokohama National University, Japan). It was synthesized by atom transfer radical polymerization (ATRP) following a previously-reported procedure.[17] The synthesized polymer was characterized using $^1$H-NMR spectroscopy and size exclusion chromatography (SEC). SEC was conducted using *N*,*N*-dimethylformamide (DMF) containing 0.01 mol $L^{-1}$ LiBr as the eluent. The number average molecular weight, $M_n$ was determined to be $M_n$ = 31.5 k by $^1$H-NMR and the polydispersity index ($M_w/M_n$) was measured to be $M_w/M_n$ = 1.30 using Tosoh columns calibrated with poly(methylmethacrylate) (PMMA) standards, where $M_w$ is the weight average molecular weight. The ionic liquid [$C_2$mIm][TFSA] and the partially deuterated ionic liquid $d_8$-[$C_2$mIm][TFSA] whose H atoms are substituted by D for the ethyl group and the imidazolium-ring were synthesized according to procedures reported before.[21,22] The deuteration ratio of $d_8$-[$C_2$mIm][TFSA] was estimated to be higher than 93 % based on $^1$H-NMR spectroscopy measurements. All of sample solutions were prepared using the cosolvent evaporation method with THF as the good solvent.[23,24]

### 4.2.2 Viscosity Measurement

Viscosity measurements were conducted for estimation of chain overlapping concentration. Viscosity of PPhEtMA in [$C_2$mIm][TFSA] solutions were measured using a rheometer (MCR501, Anton Paar, Austria) at 298 K with a cone-plate geometry and a shear rate of 10–1000 $s^{-1}$.

### 4.2.3 Dynamic Light Scattering (DLS) Measurement

DLS measurement was carried out in the same manner as described in Chapter 3. The solvent IL [$C_2$mIm][TFSA] was passed through a PTFE filter (pore size: 0.5 $\mu$m) prior to use. The temperature was changed at the average rate of approximately 0.5 K min$^{-1}$, and the solutions were stabilized for at least 5 min before DLS measurement. In a previous report, Kodama *et al.* reported a sharp transmittance change of PPhEtMA in [$C_2$mIm][TFSA] solution at its LCST through increasing temperature by 1 K min$^{-1}$. It indicates that the rate of temperature change is slow enough for equilibration of the system.[10] The rate of temperature change in this study is slower than the previous study, and assumed to be valid for measurement of equilibrated solution state.

The time correlation function of scattering intensity, $g^{(2)}(\tau) - 1$ is related to the distribution function of decay late, $G(\Gamma)$ as follows:

$$g^{(2)}(\tau) - 1 = \beta \left[ \int_0^\infty G(\Gamma) \exp(-\Gamma\tau) \right]^2 \tag{4.1}$$

Here, $\beta$ is the coherence factor. The decay late, $\Gamma$ is the inverse of decay time and related to the diffusion coefficient, $D$ and scattering vector, $q$ as $\Gamma = Dq^2$. $G(\Gamma)$ can be obtained by inverse Laplace transformation to $g^{(2)}(\tau) - 1$, using the well-established CONTIN program.[25] $G(\Gamma)$ was transformed into the distribution function of the hydrodynamic radius $G(R_\mathrm{h})$ by using the following Stokes-Einstein equation.

$$R_\mathrm{h} = \frac{k_\mathrm{B}T}{6\pi\eta D} = \frac{k_\mathrm{B}Tq^2}{6\pi\eta\Gamma} \tag{4.2}$$

Here, the temperature dependence of the viscosity of [$C_2$mIm][TFSA] was determined using the Vogel-Tammann-Fulcher (VTF) equation as previously reported.[26] The refractive index of [$C_2$mIm][TFSA] at each temperature was obtained from a previous report.[27]

### 4.2.4 Cloud Point Observation

PPhEtMA in [$C_2$mIm][TFSA] and $d_8$-[$C_2$mIm][TFSA] solutions were poured into test tubes immersed in a water bath. Temperature of the water bath was increased at the rate slower than 0.2 K min$^{-1}$, and the cloud point was determined by a rather primitive visual observation. I observed the highest temperature at which sample solution was transparent ($T_1$) and one at which it became opaque ($T_2$). I determined the cloud point ($T_\mathrm{c}$) as the middle between $T_1$ and $T_2$, *i.e.*, $T_\mathrm{c} = (T_1 + T_2)/2$. The uncertainty of $T_\mathrm{c}$ ($\Delta T_\mathrm{c}$) was also estimated as $\Delta T_\mathrm{c} = (T_2 - T_1)/2$. Kodama *et al.*

determined cloud points of various polymers in ILs as the temperature at which transmittance of polymer solution becomes smaller than 0.5.[10] In their report, the variation of transmittance at the cloud points was extremely sharp. I thus decided that this rather primitive visual observation is feasible for determination of the cloud points in the present system.

### 4.2.5 SANS Measurement

PPhEtMA in $d_8$-[$C_2$mIm][TFSA] solutions of polymer concentration, $c$ = 8 - 29 mg $mL^{-1}$ were injected into 2 mm thick spectroscopic grade quartz "banjo" cells, each containing 700 $\mu$l of sample. The temperature was changed from 288 K to 310 K at the rate of 0.5 K $min^{-1}$; the SANS measurements were performed at each temperature after stabilization for 20 min. The SANS measurements were conducted at the CG-2 General Purpose SANS instrument in the High Flux Isotope Reactor (HFIR) facility in Oak Ridge National Laboratory (ORNL, USA). Two instrument configurations were used to yield a $q$-range from 0.0028 $Å^{-1}$ – 0.46 $Å^{-1}$ where $q$ is the magnitude of the scattering vector defined as $q = (4\pi/\lambda)\sin\theta$ and $2\theta$ is the scattering angle. The configurations were (i) source-to-sample distance (SSD) = 17.3 m, sample-to-detector distance (SDD) = 19.3 m and (ii) SSD = 5.1 m and SDD = 2.8 m. Both configurations used an average wavelength of $\lambda$ = 4.72 Å. The obtained scattering intensity profiles were corrected for background scattering, transmission and detector efficiency according to standard protocol using the Igor Pro based software provided by ORNL. The corrected scattering profiles were scaled to absolute units using a calibrated attenuated direct-beam measurement. Incoherent scattering intensity was calculated from chemical composition and sample thickness.[28] The coherent scattering intensities of the sample solutions were obtained by subtraction of the incoherent scattering from experimental scattering intensity. Finally, I subtracted the coherent scattering intensity of the neat $d_8$-[$C_2$mIm][TFSA] from those of PPhEtMA/$d_8$-[$C_2$mIm][TFSA] solution to obtain the coherent scattering intensity of the PPhEtMA chains in $d_8$-[$C_2$mIm][TFSA], referred to hereafter as $I(q)$. The mass densities of [$C_2$mIm][TFSA], $d_8$-[$C_2$mIm][TFSA] and PhEtMA (monomer) were measured at 298.00 K using a digital density meter (DMA 4500, Anton Paar, Austria) to provide the values used for analysis; the results of density measurement are summarized in Table 4.1.

Table 4.1: Density values of [$C_2$mIm][TFSA], $d_8$-[$C_2$mIm][TFSA], and PhEtMA (monomer) at 298.00 K.

| Component | Density [g cm$^{-3}$] |
|---|---|
| [$C_2$mIm][TFSA] | 1.5180 |
| $d_8$-[$C_2$mIm][TFSA] | 1.5512 |
| PhEtMA | 1.0174 |

## 4.3 Cloud Points Observation

First of all, the cloud points $T_c$ of the PPhEtMA in [$C_2$mIm][TFSA] and in $d_8$-[$C_2$mIm][TFSA] solutions were determined by visual observation.

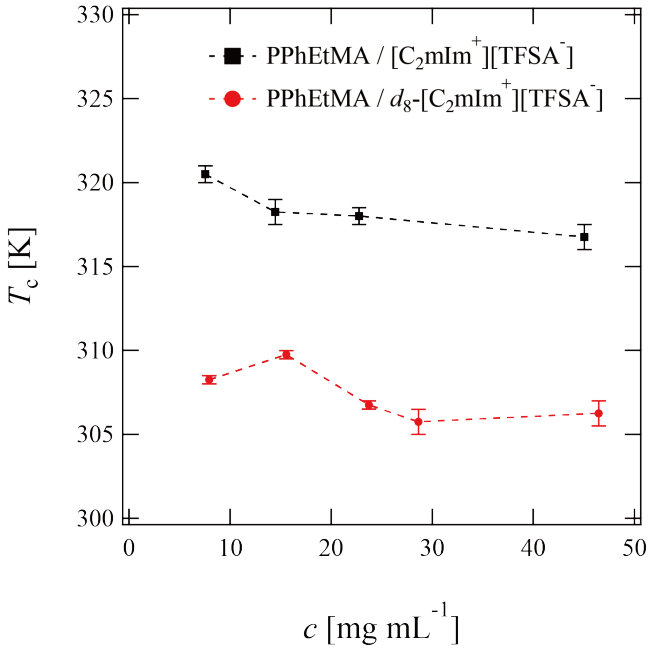


Figure 4.2: The cloud points of PPhEtMA in [$C_2$mIm][TFSA] (black squares) and $d_8$-[$C_2$mIm][TFSA] (red circles) solution at various polymer concentration. The broken lines are guides to eye. The error bars represent the uncertainty of the cloud points, $\Delta T_c$

Figure 4.2 shows the concentration dependence of $T_c$. As Figure 4.2 indicates, the $T_c$ of PPhEtMA was in the range of 306 K - 310 K in $d_8$-[$C_2$mIm][TFSA] which is significantly lower than in hydrogenated [$C_2$mIm][TFSA] (315 K - 320 K). Such an isotope effect on cloud point has been reported for aqueous polymer solutions,[29–31] a polymer in an organic solvent solution,[32] and also for a polymer in an IL solution.[33] For example, the $T_c$ of PNIPAm in $D_2O$ is 0.6 - 0.8 K higher than in $H_2O$. The origin of the isotope effect in aqueous PNIPAm solutions has been ascribed to the more

stable formation of hydration shell in $D_2O$ than in $H_2O$.[30,31] In general, the effect of deuteration on $T_c$ originates mainly from differences in molecular interactions in deuterated and hydrogenated solvents.[30,31,33]

Thus, It is expected that the observed isotope effect on $T_c$ of PPhEtMA in [$C_2$mIm][TFSA] solutions similarly originates from the isotope effect on molecular interactions. I conjecture that the lowering $T_c$ of PPhEtMA in $d_8$-[$C_2$mIm][TFSA] compared with in hydrogenated [$C_2$mIm][TFSA] can be ascribed to the slightly stronger cohesive interactions between deuterated IL ions.

## 4.4 Viscosity Measurement

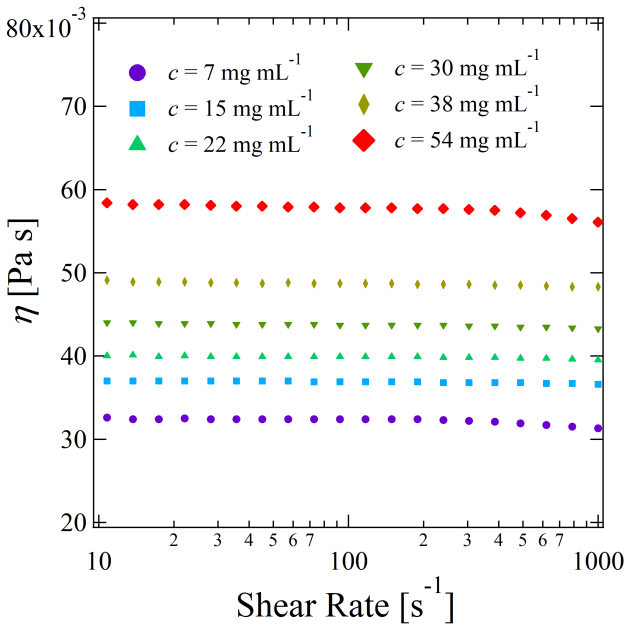


Figure 4.3: Shear-rate dependence of viscosity of PPhEtMA/[$C_2$mIm][TFSA] solutions, $\eta$.

Figure 4.3 shows shear-rate dependence of viscosity of PPhEtMA/[$C_2$mIm][TFSA] solutions, $\eta$. The viscosity of the solutions was independent of shear rate, indicating that the entanglement effect of the polymers is not significant in this concentrations.

It is well established that viscosity of polymer dilute solution can be written as a function of polymer mass concentration, $c$:[34]

$$\eta = \eta_s \left(1 + [\eta]\, c + k_H\, [\eta]^2\, c^2 + \dots\right) \tag{4.3}$$

where $[\eta]$ and $k_H$ are the intrinsic viscosity and the Huggins coefficient. $\eta_s$ is viscosity

of the solvent. From eq. (4.3), the following equations can be derived straightforwardly.

$$\frac{\eta - \eta_s}{\eta_s c} \equiv \frac{\eta_{sp}}{c} = [\eta] + k_H[\eta]^2 c + \dots \tag{4.4}$$

$$\begin{aligned} \frac{\ln(\eta/\eta_s)}{c} &= \frac{1}{c}\ln\left(1 + [\eta]c + k_H[\eta]^2 c^2 \dots\right) \\ &= [\eta] + \left(k_H - \frac{1}{2}\right)[\eta]^2 c + \dots \end{aligned} \tag{4.5}$$

Here, $\eta_{sp}$ was defined as $\eta_{sp} = (\eta - \eta_s)/\eta_s$. One can determine the intrinsic viscosity from the intercept at $c = 0$ of a plot of $\eta_{sp}c^{-1}$ or $\ln(\eta/\eta_s)c^{-1}$ vs $c$. When both plots of $\eta_{sp}c^{-1}$ and $\ln(\eta/\eta_s)c^{-1}$ give the same intercept, the higher-order terms can be safely ignored. Figure 4.4 shows $c$-dependence of $\eta_{sp}c^{-1}$ and $\ln(\eta/\eta_s)c^{-1}$ of PPhEtMA

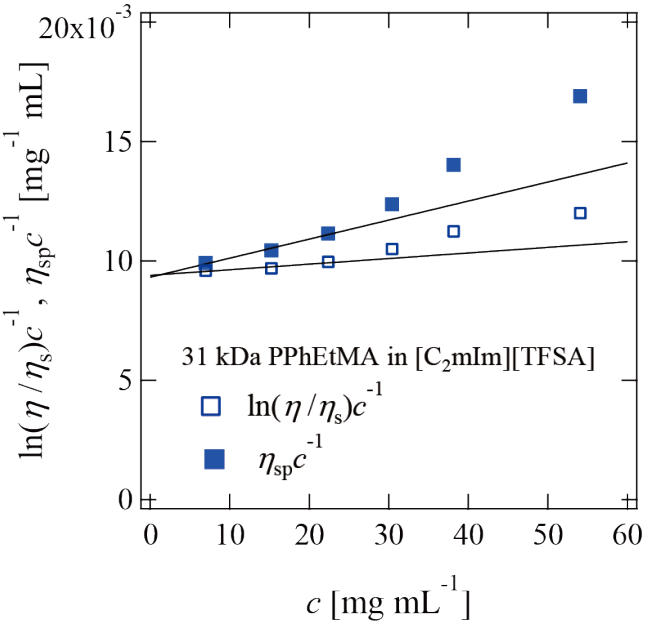


Figure 4.4: $c$ - dependence of $\eta_{sp}c^{-1}$ and $\ln(\eta/\eta_s)c^{-1}$ of PPhEtMA in [$C_2$mIm][TFSA] solutions. The intrinsic viscosity ($[\eta]$) was obtained by extrapolating the two plots to $c = 0$ (solid lines).

in [$C_2$mIm][TFSA] solutions. Here, viscosity values of PPhEtMA/[$C_2$mIm][TFSA] solutions at the shear rate of 100 $s^{-1}$ are used in the calculation. As can be seen from the Figure 4.4, the extrapolation lines for two plots gave the almost same intercept, $[\eta] = 0.0094$ $mg^{-1}$ mL. Furthermore, the chain-overlapping concentration ($c^\star$) can be estimated by the following equation;[35]

$$c^\star = \frac{1}{[\eta]} \tag{4.6}$$

According to the eq. (4.6), the $c^\star$ value was estimated to be approximately 1.1 $\times$ $10^2$ mg mL$^{-1}$ for PPhEtMA in [$C_2$mIm][TFSA]. In this study, DLS and SANS measurements for the PPhEtMA in [$C_2$mIm][TFSA] solution systems were performed at the condition of $c \ll c^\star$.

## 4.5 DLS Measurement

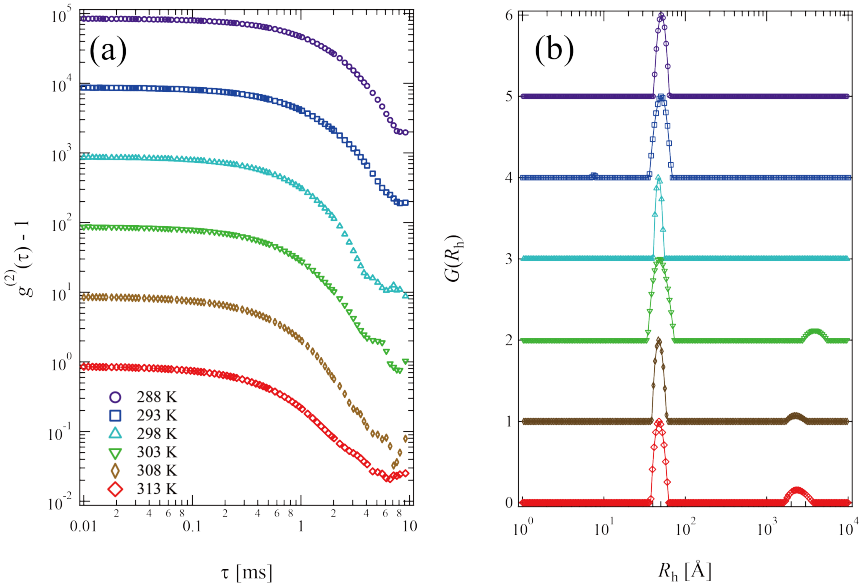


Figure 4.5: (a) $g^{(2)}(\tau) - 1$ and (b) $G(R_\mathrm{h})$ obtained for PPhEtMA in [$C_2$mIm][TFSA] solution of $c$ = 15 mg mL$^{-1}$ at various temperatures. The plots in (a) and (b) are vertically shifted for visiblity.

Figures 4.5(a) and (b) show the time-correlation function $g^{(2)}(\tau) - 1$ and the corresponding $R_\mathrm{h}$ distribution functions $G(R_\mathrm{h})$ observed for 15 mg mL$^{-1}$ PPhEtMA in [$C_2$mIm][TFSA] solution at various temperatures, respectively. All the measurement were carried out at temperatures below the cloud point temperature. The $G(R_\mathrm{h})$ data at $T < 303$ K showed a single sharp peak at around $R_\mathrm{h} \approx 45 - 50$ Å. In contrast, at higher temperature than 303 K, a small peak (corresponding to slow-mode in $g^{(2)}(\tau) - 1$) appeared at $R_\mathrm{h} > 1000$ Å whereas the peak at $R_\mathrm{h} \approx 45 - 50$ Å was still dominant. This slow-mode peak was also observed in the previous study of PBnMA in [$C_2$mIm][TFSA] system.[20] This result suggests that the dispersed PPhEtMA chains coexist with a small amount of aggregates in the vicinity of the cloud point.

Figure 4.6 shows the temperature dependence of $R_\mathrm{h}$ of PPhEtMA chains estimated from the peak position of the fast mode in $G(R_\mathrm{h})$. $R_\mathrm{h}$ did not show variation on temperature change. It means that molecular conformation of solvated PPhEtMA

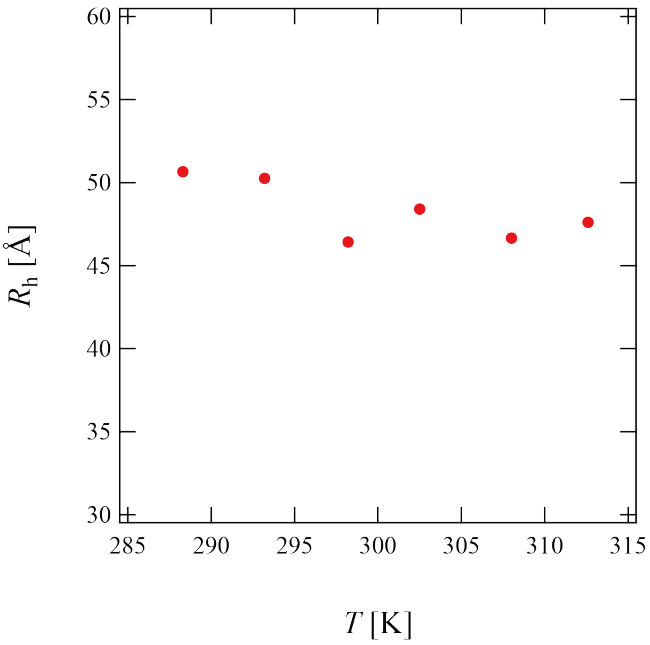


Figure 4.6: The temperature dependence of the $R_h$ values obtained for the PPhEtMA in [$C_2$mIm][TFSA] solution of $c$ = 15 mg mL$^{-1}$.

chains remained essentially unchanged in the examined temperature range.

## 4.6 SANS Measurement

I conducted SANS measurement for PPhEtMA in $d_8$-[$C_2$mIm][TFSA] solution to evaluate solvated structure of PPhEtMA, including chain conformation and thermodynamic parameters. The SANS curves observed for PPhEtMA in $d_8$-[$C_2$mIm][TFSA] solution ($c$ = 16 mg mL$^{-1}$) at various temperatures are shown in Figure 4.7. As shown in Figure 4.7, the scattering intensity slightly increased with increasing temperature, but then showed a steep upturn in the data at temperatures higher than $T_c$ ($\approx$ 309 K, see Figure 4.2). Here, the upturn in low-$q$ region ($q$ < 0.006 Å$^{-1}$) and the slope in middle-$q$ region (0.03 Å$^{-1}$ < $q$ < 0.13 Å$^{-1}$) exhibited a power-law behavior of $I(q) \approx q^{-4}$ and $I(q) \approx q^{-2}$, respectively. For quantitative evaluation of structural parameters, curve fitting analysis by the following scattering function was performed;[36,37]

$$I(q) = \frac{(\Delta\rho)^2}{N_A} \frac{V_2 \phi P_D(q)}{1 + (1 - 2\chi_{eff}) \left(\frac{V_2}{V_1}\right) \phi P_D(q)} \tag{4.7}$$

$$P_D(q) = \frac{2}{x^2} [\exp(-x) - 1 + x] \quad (x \equiv R_g^2 q^2)$$

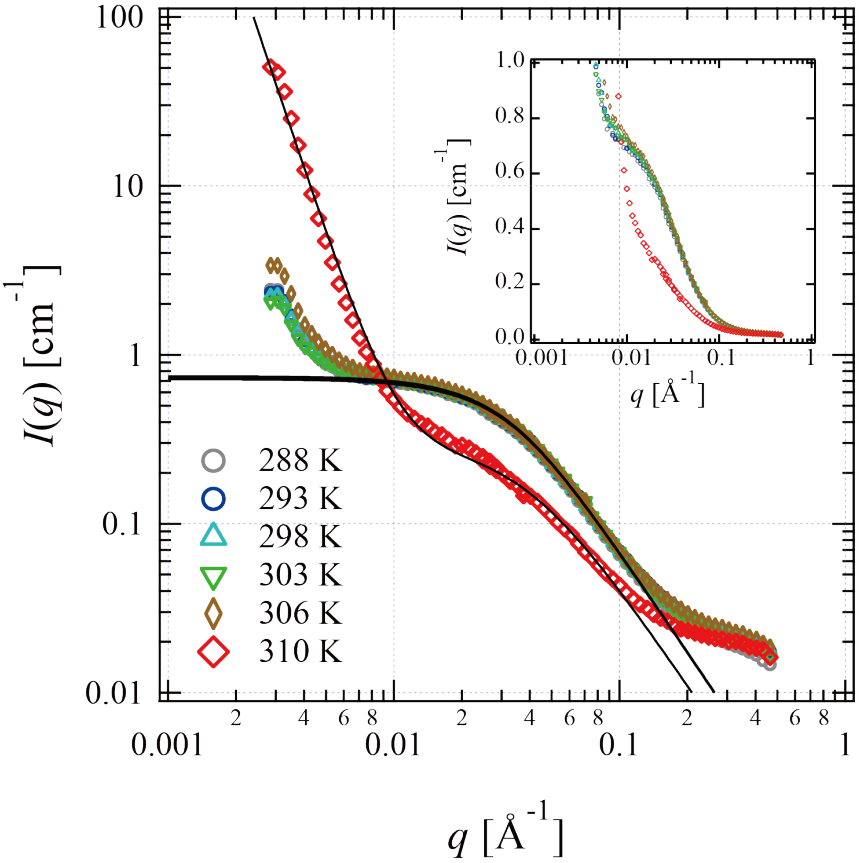


Figure 4.7: SANS profiles, $I(q)$ of PPhEtMA chains dissolved in $d_8$ - [$C_2$mIm][TFSA] solution ($c$ = 16 mg mL$^{-1}$) at various temperatures shown in the form of double logarithmic plot. The black solid lines show the fitting lines with eq. (4.7) for $I(q)$s at $T < 306$ K or eq. (4.9) function for $I(q)$ at $T = 310$ K. The SANS profiles are also shown in the form of the semi-logarithmic plot in the inset.

where, $\phi$, $\chi_{\text{eff}}$, $V_1$ and $V_2$ are the volume fraction of PPhEtMA, the effective interaction parameter, and the molar volumes of the solvent and solute components, respectively. Here, $N_{\text{A}}$ is the Avogadro number, $R_{\text{g}}$ is the radius of gyration, and $\Delta\rho$ is the difference in the scattering length density between the solute and solvent. The scattering function describes Gaussian chains dispersed in a dilute solution with a "single-contact" interchain interference. The solid lines in Figure 4.7 are the results of curve fitting by eq. (4.7). The scattering profiles at temperatures below the cloud point are successfully reproduced by eq. (4.7) except for a deviation in the low-$q$ region of $q < 0.006$ Å$^{-1}$ and in the high-$q$ region of $q > 0.2$ Å$^{-1}$. The slight upturn in the low-$q$ region can be attributed to the emergence of small amounts of cluster, as also observed in DLS (see Figure 4.5). Similar upturn was often observed in polymer solutions.[38,39] As indicated in DLS experiments (Figure 4.5), fraction of the cluster to the dispersed chains is negligible. I thus neglected this upturn in the curve fitting. In the high-$q$ region, there were deviations of experimental $I(q)$s from the theoretical lines which show power-law behavior of $I(q) \propto q^{-2}$ in the $q$-range. It indicates PPhEtMA chains do not behave as Gaussian chains in the microscopic scale; PPhEtMA has relatively rigid conformation. I do not dwell further on such a microscopic chain characteristics because the main purpose in this study is to evaluate the mesoscopic structure and the phase separation process of the system. In the curve fitting analysis, $R_{\text{g}}$ and $\chi_{\text{eff}}$ were obtained as fitting paramters. The obtained $R_{\text{g}}$ was almost constant at temperatures below $T_{\text{c}}$ (Figure 4.8), being consistent with DLS results (see Figure 4.6). $\chi_{\text{eff}}$ is discussed later. For the scattering profiles at $T > 309$ K, I performed curve fitting by using a sum of eq. (4.7) and Debye-Bueche functions,

$$I(q) = \frac{I(0)}{\left(1 + \Xi^2 q^2\right)^2} \approx \frac{I(0)}{q^4} \quad (q \gg \Xi) \tag{4.8}$$

where $\Xi$ is the characteristic size of inhomogeneities in the phase separated structure.[40] It is impossible to estimate $\Xi$ from the present SANS profiles because of the limited $q$-range. I thus employed an approximated form of the Debye-Bueche function as follows;

$$I(q) = \frac{(\Delta\rho)^2}{N_{\text{A}}} \frac{V_2 \phi P_{\text{D}}(q)}{1 + (1 - 2\chi_{\text{eff}}) \left(\frac{V_2}{V_1}\right) \phi P_{\text{D}}(q)} + A q^{-4} \tag{4.9}$$

where $A$ is a constant. The scattering profile at $T = 310$ K was successfully reproduced by the eq. (4.9). The result shows that PPhEtMA chains are homogeneously

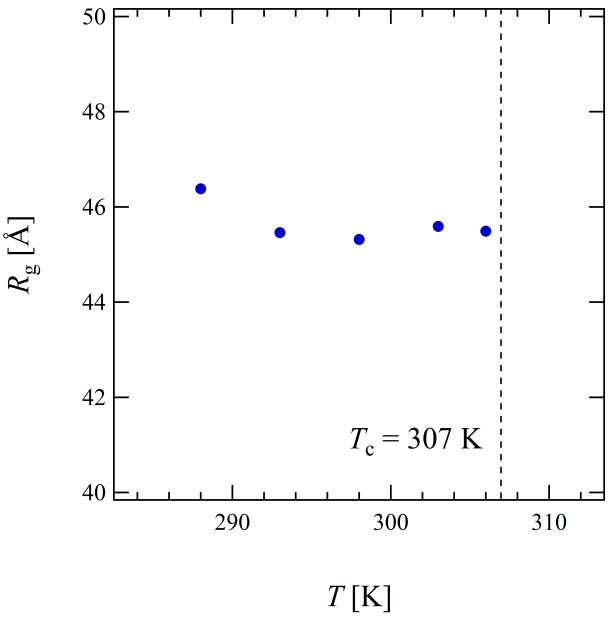


Figure 4.8: Temperature dependence of the radius of gyration ($R_g$) of dispersed PPhEtMA chains in $d_8$-[$C_2$mIm][TFSA] solution ($c$ = 16 mg mL$^{-1}$) obtained from a curve fitting for SANS profiles at various temperature. I used eq. (4.7) at $T < 307$ K and eq. (4.9) at $T = 310$ K as a fitting function.

dispersed as the Gaussian chains before the phase separation, and that they suddenly form large aggregates at the cloud point.

Large parts of scattering studies on the phase separation of polymer solutions have been performed on semi-dilute solution.[12,20,29,33,38,41–43] Regardless of the solvent species, small-angle scattering profiles of semi-dilute polymer solution showed characteristic behavior of the spinodal decomposition: divergence of both scattering intensity and the correlation length as the critical point is approached. In contrast, a recent study showed that the SANS profiles of PNIPAm dilute solution exhibited a discontinuous change at the cloud point.[44] In addition, the steepness of the change of SANS profiles decreased with increasing fraction of meso-diad in the PNIPAm chain, corresponding to decreasing of the cooperativity of hydration.[12,44,45] It means that the steepness of phase separation is strongly related to the cooperativity of solvation. In the present study, SANS profiles of PPhEtMA in $d_8$-[$C_2$mIm][TFSA] solutions suddenly changed at the cloud points, as in the case of the PNIPAm dilute aqueous solution. I conjecture that the discontinuous change in SANS profiles observed for PPhEtMA in $d_8$-[$C_2$mIm][TFSA] originates from cooperative dissociation of IL ions at $T_c$.

Furthermore, I carried out an analysis by Zimm plot. It is well established that

scattering intensity from a polymer solution $I(q)$ can be approximated as the following eq. (4.10) at the limit of low-$c$ and low-$q$:

$$\frac{Kc}{I(q)} = M_{\mathrm{w}}^{-1}\left(1 + \frac{R_{\mathrm{g},0}^2}{3}q^2\right) + 2A_2c \tag{4.10}$$

where $K = \Delta\rho^2/N_{\mathrm{A}}d_{\mathrm{polymer}}^2$ is the contrast factor. Here, $d_{\mathrm{polymer}}$, $R_{\mathrm{g},0}$ and $A_2$ are the mass density of PPhEtMA, the radius of gyration as $c \to 0$, and the second virial coefficient, respectively. I used the mass density of PhEtMA monomer (see Table 4.1) instead of the corresponding value of PPhEtMA in the analysis, because the mass density of PPhEtMA in solution is unknown.

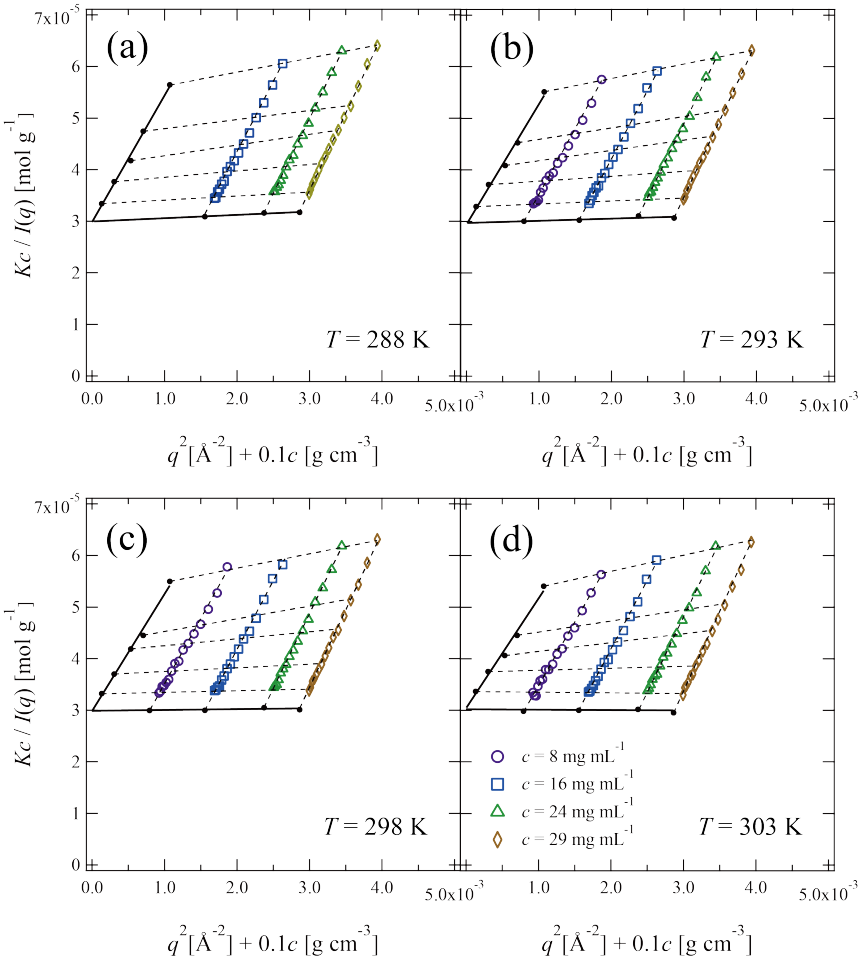


Figure 4.9: Zimm plots for the PPhEtMA in $d_8$-[$C_2$mIm][TFSA] solutions at (a) $T$ = 288 K, (b) $T$ = 293 K, (c) $T$ = 298 K, and (d) $T$ = 303 K.

Figure 4.9 shows Zimm plots at various temperatures (288, 293, 298, and 303 K) below $T_{\mathrm{c}}$. Here, the SANS profiles of $c$ = 8–29 mg mL$^{-1}$ in the range of $0.011 < q < 0.033$ were used for Zimm plot. Reasonable values of $M_{\mathrm{w}}$ were successfully obtained ($M_{\mathrm{w}}$: 32 - 34 kDa) from the intercept to $c \to 0$ and $q \to 0$ in the plot of $Kc/I(q)$ vs $q^2$+

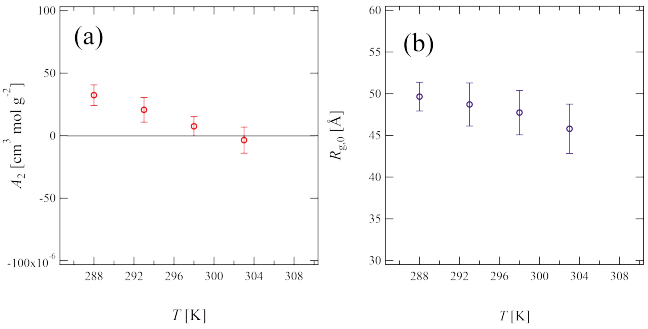


Figure 4.10: Temperature dependence of (a) $A_2$ and (b) $R_{g,0}$ obtained from Zimm plots at various tempreature (Figure 4.9).

0.1$c$, confirming the validity of the experiment and the analysis. Figure 4.10 shows the temperature dependence of (a) $A_2$ and (b) $R_{g,0}$ obtained from the Zimm plot analysis. As Figure 4.10(a) illustrates, $A_2$ decreased with increasing temperature and then changed its sign at $T = 301$ K, corresponding to the $\Theta$ temperature. It quantitatively shows that the compatibility of PPhEtMA in $d_8$-[$C_2$mIm][TFSA] decreases gradually with increasing temperature. As Figure 4.10(b) demonstrates, $R_{g,0}$ was independent of temperature within its error, similar to the results of the DLS experiments (see Figure 4.6).

## 4.7 Comparison between PPhEtMA and PBnMA

In the former sections, I performed precise characterization of PPhEtMA chains in $d_8$-[$C_2$mIm][TFSA] solution. Here, to explore the origin of the drastic effect of structural modification on $T_c$, I compare the obtained structural parameters of PPhEtMA with those of PBnMA in [$C_2$mIm][TFSA] solutions. There is a previous SANS study on PBnMA in deuterated [$C_2$mIm][TFSA] system in which the effective interaction parameter $\chi_{eff}$ in the dilute region was estimated in completely the same manner as the present study: the curve fitting by eq. (4.7).[20]

Figure 4.11 shows the comparison of the temperature dependence of $\chi_{eff}$ obtained for PPhEtMA and PBnMA in [$C_2$mIm][TFSA] solution systems. It is established that temperature dependence of $\chi_{eff}$ can be approximated as the following equation in the vicinity of the cloud point;

$$\chi_{eff} = \chi_S + \frac{\chi_H}{T} \tag{4.11}$$

where $\chi_S$ and $\chi_H$ are the entropic and enthalpic contributions to $\chi_{eff}$, respectively.[12,46] The value of $|\chi_H|$ obtained for PPhEtMA ($= 65 \pm 7$ K$^{-1}$) was slightly

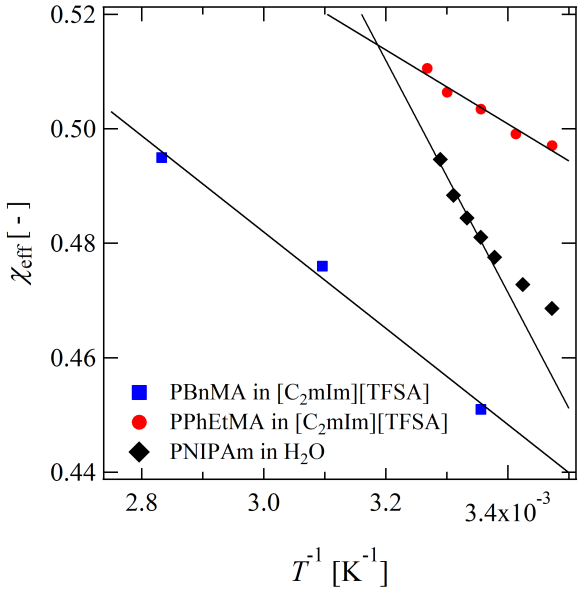


Figure 4.11: The temperature dependence of the effective interaction parameter $\chi_{\mathrm{eff}}$ of the PPhEtMA in [$C_2$mIm][TFSA] solution (red circles). Previously reported values for PBnMA in [$C_2$mIm][TFSA] solution[20](blue squares) and PNIPAm aqueous soluiton[44](black diamonds) are also shown. The solid lines are linear fits to $\chi_{\mathrm{eff}} = \chi_{\mathrm{S}} + \chi_{\mathrm{H}}/T$.

smaller than that for PBnMA ($= 84 \pm 7\ \mathrm{K}^{-1}$) whereas almost the same values of $|\chi_{\mathrm{S}}|$ were obtained for PPhEtMA ($\chi_{\mathrm{S}}= 0.72 \pm 0.02$) and PBnMA ($\chi_{\mathrm{S}} = 0.73 \pm 0.02$). The observed difference among $|\chi_{\mathrm{H}}|$ of PPhEtMA and PBnMA implies that the insertion of a methylene group into PBnMA side chains lowers the mixing enthalpy, resulting in the decrease of $T_{\mathrm{c}}$. As pointed out in a previous study,[16] the dominant interaction between PBnMA and [$C_2$mIm][TFSA] is cation-$\pi$ interactions between [$C_2$mIm]$^+$ and phenyl groups in PBnMA side chains. Thus, alkyl groups in the side chains of PBnMA or PPhEtMA do not contribute to the polymer-IL interactions. Hence, I conclude that the lower $|\chi_{\mathrm{H}}|$ value of PPhEtMA than that of PBnMA originates from an increase of unfavorable interactions by the insertion of the methylene group.

Furthermore, the values of $\chi_{\mathrm{S}}$ and $\chi_{\mathrm{H}}$ between in the IL systems are compared with that of PNIPAm in aqueous solution system. $\chi_{\mathrm{S}}$ and $\chi_{\mathrm{H}}$ values for PNIPAm dilute aqueous solution system were estimated by using a previously reported value of $\chi_{\mathrm{eff}}$.[44] As a result, the obtained values of both $|\chi_{\mathrm{S}}|$ and $|\chi_{\mathrm{H}}|$ for PNIPAm in aqueous solution ($|\chi_{\mathrm{S}}| = 1.15 \pm 0.07$, $|\chi_{\mathrm{H}}| = 203 \pm 22\ \mathrm{K}^{-1}$) were significantly larger than that of PPhEtMA and PBnMA in [$C_2$mIm][TFSA] solution. The smaller $|\chi_{\mathrm{S}}|$ and

$|\chi_H|$ in IL systems indicates that the phase equilibrium of the IL system is controlled by the smaller change in the free energy on mixing than in aqueous system. It is the consistent result with the DSC study on the system by Ueki *et al.*[19] That is the reason why the $T_c$s of the PBnMA derivatives in IL solution are sensitively affected by chemical modification to the polymer or IL which corresponds to a slight change in $|\chi_S|$ or $|\chi_H|$.

## 4.8 Conclusions

Solvated structure and phase behavior of PPhEtMA in [$C_2$mIm][TFSA] was investigated by utilizing DLS and SANS experiment. To explore physical origin of the drastic effect of chemical modification on $T_c$ of the IL systems, structural parameters obtained for PPhEtMA in [$C_2$mIm][TFSA] solution were compared with a previously reported values for PBnMA in [$C_2$mIm][TFSA] solution and further with PNIPAm aqueous solution. At first, precise structural characterization on PPhEtMA in [$C_2$mIm][TFSA] solution was conducted. SANS profiles of PPhEtMA in [$C_2$mIm][TFSA] solution showed a discontinuous change at cloud point temperature, indicative of structural change from dispersed Gaussian chains to large aggregates. The second virial coefficient $A_2$ was successfully evaluated by Zimm plot. The results showed that the compatibility of PPhEtMA in [$C_2$mIm][TFSA] gradually decreases with increasing temperature. Subsequently, $\chi_H$ and $\chi_S$ values were obtained from temperature dependence of $\chi_{eff}$ estimated from SANS profiles of PPhEtMA in [$C_2$mIm][TFSA] solution. The absolute value of $\chi_H$ obtained for PPhEtMA was smaller than that for PBnMA. This difference in $\chi_H$ reflects an increase of unfavorable interaction between the polymer and the IL by the insertion of the solvo-phobic methylene group. Furthermore, the obtained $|\chi_S|$ and $|\chi_H|$ values of both PPhEtMA and PBnMA in [$C_2$mIm][TFSA] systems were significantly smaller than those of PNIPAm aqueous solution system. It was pointed out the phase equilibrium of the IL system is controlled by smaller change in the free energy on mixing. That is the origin of the drastic effect of structural modification on the phase equilibrium of thermo-responsive polymers in ILs.

## Appendix: Accurate Determination of the Parameters Used in the Analysis of SANS Profiles

In the analysis of SANS profiles of PPhEtMA in $d_8$-[$C_2$mIm][TFSA] solution, I used the density of PhEtMA monomer and $d_8$-[$C_2$mIm][TFSA] at 298.00 K. It means that I neglected temperature dependence of density and the difference between the density of PPhEtMA and PhEtMA monomer. Furthermore, I compared the structural parameters of PPhEtMA in $d_8$-[$C_2$mIm][TFSA] solution with that of PBnMA in $d_{11}$-[$C_2$mIm][TFSA] solution which was reported by other authors.[20] To improve the reliability of the result, I performed additional experiments and re-analysis of SANS profiles.

### Density Measurement

2.5 wt% solutions of PPhEtMA in [$C_2$mIm][TFSA] and PBnMA in [$C_2$mIm][TFSA] were prepared by the cosolvent evaporation method with THF as a good solvent. The number averaged molecular weight of the polymers are listed in Table 4.2. Temperature dependence of the density of the solutions, neat [$C_2$mIm][TFSA], and neat $d_8$-[$C_2$mIm][TFSA] was measured by using a density meter (DMA-5000, Anton Paar, Austria) with an accuracy of $1 \times 10^{-5}$ g cm$^{-3}$. Temperature of the samples was increased at the rate of 0.4 K min$^{-1}$ and density was simultaneously measured at lower temperature than the cloud points.

Figure 4.12 shows temperature dependence of the density of neat [$C_2$mIm][TFSA], neat $d_8$-[$C_2$mIm][TFSA], PPhEtMA in [$C_2$mIm][TFSA] solution, and PBnMA in [$C_2$mIm][TFSA] solution. The density of the neat ILs ($\rho_s^*(T)$s) and the polymer solutions ($\rho_{Soln}(T)$s) showed a monotonic decrease with increasing temperature. In general, the density of polymer solution are given as

$$\rho_{Soln}(T) = \frac{M_p + M_s}{V_p(T) + V_s(T)} \tag{4.12}$$

Table 4.2: The number averaged molecular weight, $M_n$ of PPhEtMA and PBnMA used in the density measurements and the SANS experiments in this section. The ratio of the weight averaged molecular weight, $M_w$ and $M_n$ is also shown.

| Polymer | $M_n$ | $M_w/M_n$ |
|---|---|---|
| PPhEtMA | 29 kDa | 1.49 |
| PBnMA | 31 kDa | 1.17 |

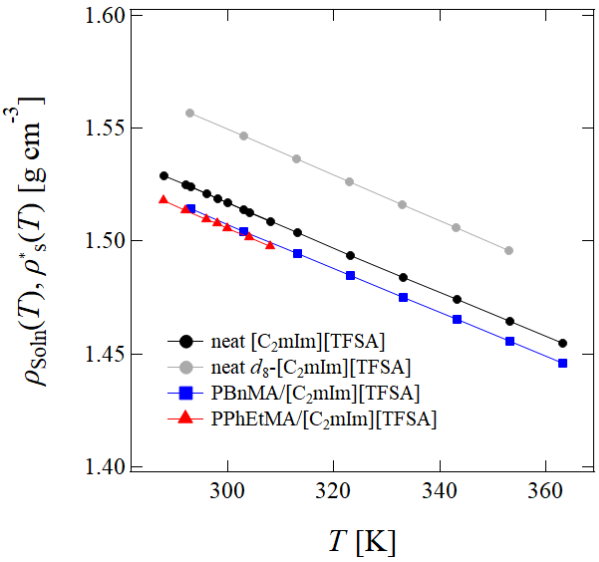


Figure 4.12: Temperature dependence of the density of neat [$C_2$mIm][TFSA] (black circles), neat $d_8$-[$C_2$mIm][TFSA] (grey circles), 2.5 wt% PBnMA in [$C_2$mIm][TFSA] (blue squares), and 2.5 wt% PPhEtMA in [$C_2$mIm][TFSA] solution (red triangles), repectively. The solid lines are guides to eyes.

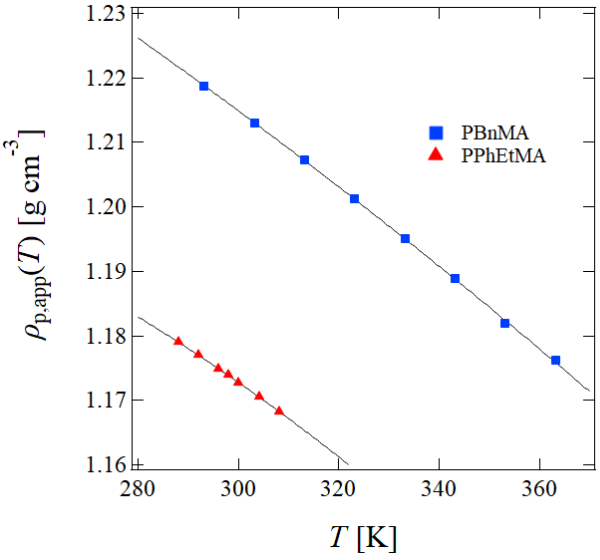


Figure 4.13: The apparent density, $\rho_{p,app}(T)$ of PBnMA (blue squares) and PPhEtMA (red triangles) in [$C_2$mIm][TFSA] solution. Solid lines are the fitting lines by the second-order polynomials.

where $V_p(T)$ and $V_s(T)$ are the volume which is occupied by the polymer and the solvent, respectively. $M_p$ and $M_s$ are the mass of the polymer and the solvent in the total volume, $V(T) = V_p(T) + V_s(T)$. Let $\rho_p(T) \equiv M_p/V_p(T)$ and $\rho_s(T) \equiv M_s/V_s(T)$ represent the density of the polymer and the solvent in solution, respectively, eq. (4.12) becomes

$$\rho_{Soln}(T) = \frac{M_p + M_s}{M_p\rho_p(T)^{-1} + M_s\rho_s(T)^{-1}} \tag{4.13}$$

Assuming $\rho_s(T) = \rho_s^*(T)$ in eq. (4.13), the following relationship is obtained for the apparent density of the polymers in solution, $\rho_{p,app}(T)$:

$$\frac{c_p}{\rho_{p,app}(T)} = \frac{1}{\rho_{Soln}(T)} - \frac{1 - c_p}{\rho_s^*(T)} \tag{4.14}$$

Figure 4.13 shows $\rho_{p,app}(T)$ of PPhEtMA and PBnMA in [$C_2$mIm][TFSA] solution. The temperature dependence of $\rho_{p,app}(T)$ of PBnMA and PPhEtMA in [$C_2$mIm][TFSA] could be described by an empirical second-order polynomials: $\rho_{p,app}(T) = a + bT + cT^2$.[47] The obtained coeffients for PBnMA and PPhEtMA in [$C_2$mIm][TFSA] were tabulated in Table 4.3. The coefficients for neat [$C_2$mIm][TFSA] and neat $d_8$-[$C_2$mIm][TFSA] were also shown. These coefficients were used for the estimation of the density at various temperature, as mentioned later.

Table 4.3: The coefficients $a, b, c$ of the second-order polynomials describing temperature dependence of $\rho(T) = a + bT + cT^2$.

| Component | $a$ [g cm$^{-3}$] | $b$ [$10^{-4}$ g cm$^{-3}$ K$^{-1}$] | $c$ [$10^{-7}$g cm$^{-3}$ K$^{-2}$] |
|---|---|---|---|
| $d_8$-[$C_2$mIm][TFSA] | 1.89±0.00 | -12.6±0.0 | 3.80±0.06 |
| [$C_2$mIm][TFSA] | 1.85±0.00 | -12.3±0.0 | 3.63±0.03 |
| PBnMA | 1.33±0.02 | -1.91±1.35 | 6.43±2.05 |
| PPhEtMA | 1.19±0.05 | -4.61±3.62 | 16.7±6.1 |

## SANS Experiment

I prepared 2.5 wt% solutions of PPhEtMA in $d_8$-[$C_2$mIm][TFSA] and PBnMA in $d_8$-[$C_2$mIm][TFSA] as sample. The cloud points of the solutions were determined by transmittance measurements to be 307 K for PPhEtMA in $d_8$-[$C_2$mIm][TFSA] solution and 377 K for PBnMA in $d_8$-[$C_2$mIm][TFSA] solution. SANS experiments were performed using QUOKKA installed at OPAL reactor, Australian Nuclear Science and Technology Organisation (ANSTO), Australia. We employed instrument

configurations with different SDDs of 1.3 and 8 m for PBnMA in $d_8$-[$C_2$mIm][TFSA] solution and 1.3, 8, and 20 m for PPhEtMA in $d_8$-[$C_2$mIm][TFSA] solution, respectively. Wavelength of the incident beam was 5.0 Å with the resolution of 10 %. The sample solutions were injected in 2 mm thickness quartz cells. Temperature was raised stepwise during the experiment at the temperatures lower than cloud points.

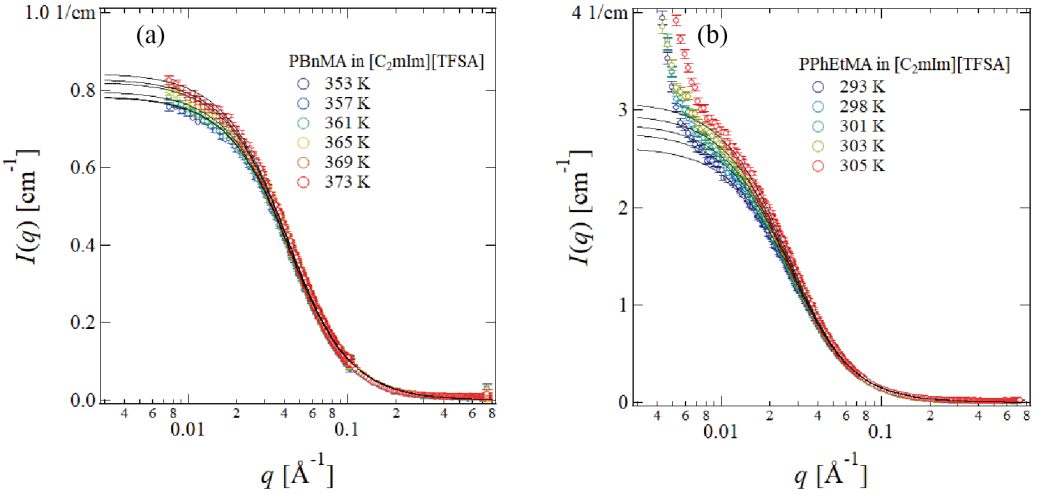


Figure 4.14: SANS profiles of (a) 2.5 wt% PBnMA in $d_8$-[$C_2$mIm][TFSA] and (b) PPhEtMA in $d_8$-[$C_2$mIm][TFSA] solutions. The solid lines are the fitting lines by eq. (4.7).

Figure 4.14 shows SANS profiles of 2.5 wt% PBnMA in $d_8$-[$C_2$mIm][TFSA] and PPhEtMA in $d_8$-[$C_2$mIm][TFSA] solutions at various temperatures. The scattering profiles showed the increase of scattering intensity with increasing temperature, which is the same tendency as Figure 4.7. Subsequently, I performed the curve fitting analysis using eq. (4.7) for the SANS profiles. Here, the parameters, $\Delta\rho$, $V_1$, $V_2$, and $\phi$ were calculated by using the density of $d_8$-[$C_2$mIm][TFSA], PBnMA, and PPhEtMA at each temperature. The density at each temperature was estimated by the coefficients listed in Table 4.1.

The obtained effective interaction parameter, $\chi_{\mathrm{eff}}$ for PPhEtMA and PBnMA in $d_8$-[$C_2$mIm][TFSA] solutions were shown in Figure 4.15. The entropic contribution, $\chi_{\mathrm{S}}$ and the enthalpic contribution, $\chi_{\mathrm{H}}$ was estimated through linear fits to $\chi_{\mathrm{eff}} = \chi_{\mathrm{S}} + \chi_{\mathrm{H}}/T$. The obtained values of $\chi_{\mathrm{S}}$ and $\chi_{\mathrm{H}}$ were larger than the values obtained in the previous analysis in section 4.7. It is mainly because I took into account the temperature dependence of the density values in this section. However, the qualitative tendency of the results in section 4.7 was not altered by the difference in the values of $\chi_{\mathrm{S}}$ and $\chi_{\mathrm{H}}$: $\chi_{\mathrm{H}}$ of PPhEtMA is smaller than that of PBnMA, and

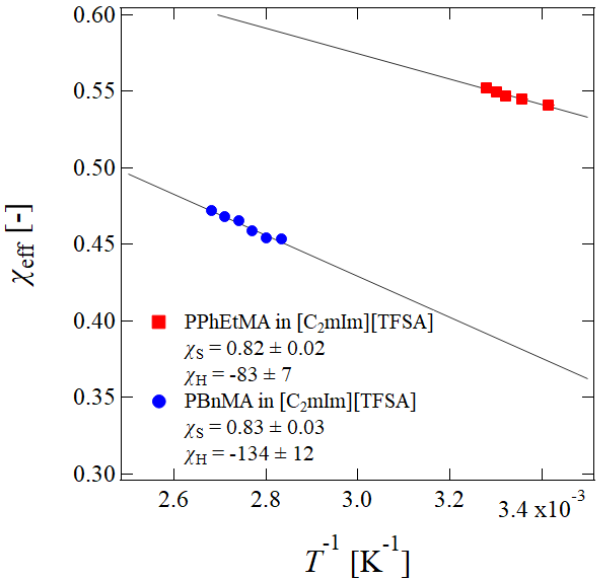


Figure 4.15: The temperature dependence of the effective interaction parameter $\chi_{\text{eff}}$ of the PPhEtMA (red squares) and PBnMA (blue circles) in $d_8$-[$C_2$mIm][TFSA] solution. The solid lines are linear fits to $\chi_{\text{eff}} = \chi_S + \chi_H/T$. The obtained values of $\chi_S$ and $\chi_H$ are also shown in the figure.

the values of both $\chi_H$ and $\chi_S$ is much smaller than in the case of aqueous PNIPAm solution.

## Reference


[1] Ito, S. *Koubunshi Ronbunshu* **1989**, *7*, 437–443.

[2] Aoki, S.; Koide, A.; Imabayshi, S.; Watanabe, M. *Chem. Lett.* **2002**, *11*, 1128–1129.

[3] Heymann, E. *Trans. Faraday Soc.* **1935**, *31*, 846–864.

[4] Chatterjee, T.; Nakatani, A. I.; Adden, R.; Brackhagen, M.; Redwine, D.; Shen, H.; Li, Y.; Wilson, T.; Sammler, R. L. *Biomacromolecules* **2012**, *13*, 3355–3369.

[5] Saeki, S.; Kuwahara, N.; Nakata, M.; Kaneko, M. *Polymer* **1977**, *18*, 1027–1031.

[6] Shibayama, M.; Mizutani, S.; Nomura, S. *Macromolecules* **1996**, *29*, 2019–2024.

[7] Ono, Y.; Shikata, T. *J. Am. Chem. Soc.* **2006**, *128*, 10030–10031.

[8] Frank, H. S.; Evans, M. W. *J. Chem. Phys.* **1945**, *13*, 507–532.

[9] Kauzmann, W. *Nature* **1987**, *325*, 763–764.

[10] Kodama, K.; Nanashima, H.; Ueki, T.; Kokubo, H.; Watanabe, M. *Langmuir* **2009**, *25*, 3820.

[11] Lee, H.-N.; Lodge, T. P. *J. Phys. Chem. Lett.* **2010**, *1*, 1962–1966.

[12] Hoarfrost, M. L.; He, Y.; Lodge, T. P. *Macromolecules* **2013**, *46*, 9464–9472.

[13] Kodama, K.; Tsuda, R.; Niitsuma, K.; Tamura, T.; Ueki, T.; Kokubo, H.; Watanabe, M. *Polymer Journal* **2011**, *43*, 242–248.

[14] Ueki, T.; Watanabe, M. *Langmuir* **2007**, *23*, 988–990.

[15] Ueki, T. *Polymer Journal* **2014**, *46*, 646–655.

[16] Matsugami, M.; Fujii, K.; Ueki, T.; Kitazawa, Y.; Umebayashi, Y.; Watanabe, M.; Shibayama, M. *Anal. Sci.* **2013**, *29*, 311–314.

[17] Kitazawa, Y.; Ueki, T.; Imaizumi, S.; Lodge, T. P.; Watanabe, M. *Chem. Lett.* **2014**, *43*, 204–206.

[18] Kitazawa, Y.; Ueki, T.; McIntosh, L. D.; Tamura, S.; Niitsuma, K.; Imaizumi, S.; Lodge, T. P.; Watanabe, M. *Macromolecules* **2016**, *49*, 1414–1423.

[19] Ueki, T.; Arai, A. A.; Kodama, K.; Kaino, S.; Takada, N.; Morita, T.; Nishikawa, K.; Watanabe, M. *Pure & Appl. Chem.* **2009**, *81*, 1829–1841.

[20] Fujii, K.; Ueki, T.; Niitsuma, K.; Matsunaga, T.; Watanabe, M.; Shibayama, M. *Polymer* **2011**, *52*, 1589–1595.

[21] Fujii, K.; Kanzaki, R.; Takamuku, T.; Kameda, Y.; Kohara, S.; Kanakubo, M.; Shibayama, M.; Ishiguro, S.; Umebayashi, Y. *J. Chem. Phys.* **2011**, *135*, 244502.

[22] Fujii, K.; Asai, H.; Ueki, T.; Sakai, T.; Imaizumi, S.; Chung, U.; Watanabe, M.; Shibayama, M. *Soft Matter* **2012**, *8*, 1756–1759.

[23] Snedden, P.; Cooper, A. I.; Scott, K.; Winterton, N. *Macromolecules* **2003**, *36*, 4549–4556.

[24] He, Y.; Li, Z.; Simone, P.; Lodge, T. P. *J. Am. Chem. Soc.* **2006**, *128*, 2745–2750.

[25] Provencher, S. W. *Comp. Phys. Comm.* **1982**, *27*, 213–227.

[26] Tokuda, H.; Hayamizu, K.; Ishii, K.; Susan, M. A. B. H.; Watanabe, M. *J. Phys. Chem. B* **2005**, *109*, 6103.

[27] Ueki, T.; Karino, T.; Kobayashi, Y.; Shibayama, M.; Watanabe, M. *J. Phys. Chem. B* **2007**, *111*, 4750–4754.

[28] Shibayama, M.; Nagao, M.; Okabe, S.; Karino, T. *J. Phys. Soc. Jpn.* **2005**, *74*, 2728–2736.

[29] Shibayama, M.; Tanaka, T.; Han, C. C. *J. Chem. Phys.* **1992**, *97*, 6829–6841.

[30] Shirota, H.; Horie, K. *Chem. Phys.* **1999**, *242*, 115.

[31] Shirota, H.; Kuwabara, N.; Ohkawa, K.; Horie, K. *J. Phys. Chem. B.* **1999**, *103*, 10400.

[32] Strazielle, C.; Benoit, H. *Macromolecules* **1975**, *8*, 203–205.

[33] Lee, H. N.; Newell, N.; Bai, Z.; Lodge, T. P. *Macromolecules* **2012**, *45*, 3627–3633.

[34] Rubinstein, M.; Colby, R. H. *Polymer Physics*; Oxford University, 2003.

[35] Teraoka, I. *Polymer Solutions: An Introduction to Physical Properties*; John Wiley & Sons, Inc.: New York, 2002.

[36] Benoit, H.; Benmouna, M. *Polymer* **1984**, *25*, 1059–1067.

[37] Benoit, H.; Picot, C.; Benmouna, M. *J. Polym. Sci. B Polym. Phys.* **1984**, *22*, 1545–1548.

[38] Xie, Y.; Ludwig Jr, K. F.; Bansil, R.; Gallagher, P. D.; Cao, X.; Morales, G. *Physica A* **1996**, *232*, 94–108.

[39] Hammouda, B.; Ho, D.; Kline, S. *Macrmolecules* **2002**, *35*, 8578–8585.

[40] Shibayama, M. *Bull. Chem. Soc. Jpn.* **2006**, *79*, 1799–1819.

[41] Nasimova, I.; Karino, T.; Okabe, S.; Nagao, M.; Shibayama, M. *Macromolecules* **2004**, *37*, 8721–8729.

[42] Melnichenko, Y. B.; Wignall, G. D.; Van Hook, A. W.; Szydlowski, J.; Wilczura, H.; Rebelo, L. P. *Macromolecules* **1998**, *31*, 8436–8438.

[43] Asai, H.; Fujii, K.; Ueki, T.; Sawamura, S.; Nakamura, Y.; Kitazawa, Y.; Watanabe, M.; Han, Y.-S.; Kim, T.-H.; Shibayama, M. *Macromolecules* **2013**, *46*, 1101–1106.

[44] Nishi, K.; Hiroi, T.; Hashimoto, K.; Fujii, K.; Hang, Y.-S.; Kim, T.-H.; Katsumoto, Y.; Shibayama, M. *Macromolecules* **2013**, *46*, 6225–6232.

[45] Zimm, B. H.; Bragg, J. K. *J. Chem. Phys.* **1959**, *31*, 526–535.

[46] Shultz, A. R.; Flory, P. J. *J. Am. Chem. Soc.* **1952**, *74*, 4760–4767.

[47] Rodriguez, H.; Brennecke, J. F. *J. Chem. Eng. Data.* **2006**, *51*, 2145–2155.

# Chapter 5

# Pressure Responce of a Thermoresponsive Polymer in an Ionic Liquid



## 5.1 Introduction

Several kinds of polymers exhibit LCST-type phase separation in aqueous solution; they are soluble in water at low temperature but insoluble at high temperature. From a thermodynamic viewpoint, the LCST-type phase behavior is characterized by negative change in both enthalpy and entropy upon mixing; $\Delta H_{\mathrm{m}} < 0$ and $\Delta S_{\mathrm{m}} < 0$, respectively. In the case of aqueous polymer solutions, the origin of negative $\Delta S_{\mathrm{m}}$ is formation of the hydration shell around hydrophobic side chains of polymers.[1–4] As already mentioned in Chapter 4, LCST-type phase behavior is commonly observed also for IL systems, for example, poly(benzyl methacrylate) (PBnMA) derivatives in $[C_2mIm][TFSA]$ solutions. For the PBnMA in $[C_2mIm][TFSA]$ system, it is reported that $[C_2mIm]^+$ orderly locates above and below the phenyl groups of PBnMA to form cation-$\pi$ interaction.[5] Formation of the liquid-clathlate-like structure around the polymer side chains is assumed to be the origin of negative $\Delta S_{\mathrm{m}}$ in the IL system.

Both in IL and aqueous system, demixing by heating is driven by collapse of a partially ordered solvation structure of solvent components around solutes. However, there is a fundamental difference in mechanism of the structural ordering among

them. In aqueous polymer solutions, formation of the hydration shell is caused by hydrogen bonding interactions between water molecules: "solvent-solvent" interactions. In contrast, in the case of PBnMA derivatives in IL solutions, the ordered solvation structure is formed by cation-$\pi$ interactions between polymer and IL ions: "solvent-solute" interactions. To characterize the difference in the structural ordering mechanism, we utilized pressure as an experimental variable. Until now, pressure effects on the miscibility of linear polymers[6–8] and proteins[4,9,10] in aqueous solutions have been investigated. Miscibility of solutes in solutions are often drastically varied by pressurization because pressure directly affects molecular volumes and intermolecular distance.[11] Therefore, pressure response of miscibility of solutes in solutions contains rich structural information such as packing of molecules and volumetric properties. There are several reports about pressure effects on phase transition of neat ILs,[12,13] miscibility of monomeric solutes in ILs,[14,15] and also polymer-IL interactions.[16,17] However, to the best of my knowledge, pressure effects on phase behavior of polymers in IL solution have not yet been observed directly. In this study, I investigated pressure dependence of the miscibility and solvated structure of a polymer in IL solution. Here, PPhEtMA in [$C_2$mIm][TFSA] solution was chosen as a typical thermo-responsive polymer in IL system. In comparison with aqueous polymer solutions, characteristics of polymer solvation by ILs are discussed based on the pressure responce.

## 5.2 Experimental

### 5.2.1 Materials.

[$C_2$mIm][TFSA] was synthesized according to previously reported procedures.[18] PPhEtMA was prepared by Dr. Yuzo Kitazawa in Prof. Masayoshi Watanabe group (Yokohama National University, Japan); it was synthesized by reversible addition-fragmentation chain transfer (RAFT) polymerization following the scheme in a previous work.[19] The synthesized PPhEtMA was characterized using $^1$H NMR spectroscopy and size exclusion chromatography (SEC). The number-average molecular weight ($M_n$) was calculated from the monomer conversion in reaction solution determined by $^1$H NMR to be $M_n$ = 29 kDa. The polydispersity $D$ ($M_w/M_n$, where $M_w$ is the weight-average molecular weight) was determined to be $D$ = 1.49 by SEC calibrated with PMMA standards using tetrahydrofuran (THF) as the eluent. The synthesized PPhEtMA was dissolved in [$C_2$mIm][TFSA] at concentration of 3 wt% using the co-solvent evaporation method with THF as the good solvent.[20] The pre-

pared solution was used as sample solution. The cloud point temperature of the sample solution at atmospheric pressure ($T_{c0}$) was measured to be $T_{c0}$ = 43 °C by visual observation.

### 5.2.2 Cloud Point Measurement and Dynamic Light Scattering Experiment.

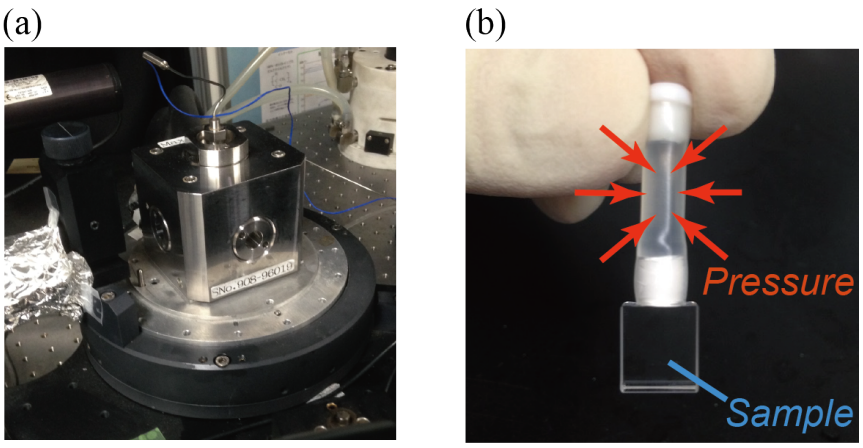


Figure 5.1: (a) A pressure cell for DLS measurement and cloud point measurement and (b) a quartz inner-cell with rubber tube.

DLS measurement and cloud point measurement were carried out under elevated pressure using a pressure cell having a set of sapphire optical windows (PCI-400, Syn. Co. Ltd., Kyoto, Japan, Figure 5.1(a)). The basic concept of the pressure cell is described elsewhere.[21] Sample solution was injected into an quartz inner-cell with rubber tube (Figure 5.1(b)). Hydrostatic pressure was applied to the pressure cell by a hand pump (HP-500, Syn. Co. Ltd., Kyoto, Japan) and the pressure was transfered to the sample solution via the rubber tube attached to the quartz inner-cell. A He-Ne laser with a power of 22 mW (wavelength, $\lambda$ = 632.8 nm) was used as the incident beam in the measurements. The time correlation function of light scattering intensity, $g^{(2)}(\tau) - 1$ was acquired by using a static/dynamic compact goniometer (SLS/DLS-5000, ALV, Langen, Germany). The scattering angle $2\theta$ was fixed to 90°. Each measurement required 30 s. Sample solution was passed through a PTFE filter (pore size: 0.2 $\mu$m) prior to use. The intensity of transmitted beam was monitored by power and energy analyzer (FieldMaster GS, Coherent Inc., USA) for the estimation of transmittance of sample solution.

Measurement of pressure dependence of transmittance was conducted as follows. Firstly, sample solution was pressurized at ambient temperature. Secondly, temperature was increased up to the desired value at isocoric condition; pressure of the

system increased simultaneously with temperature in this process. After temperature and pressure stabilization, the hydrostatic pressure was decreased stepwise under isothermal condition, and transmittance was measured at various pressures, $P$. Here, transmittance is defined as $I_{tr}/I_0$ where $I_{tr}$ and $I_0$ denote the transmitted light intensities from the sample solution and from an empty cell, respectively. Sample solution was stabilized for 3 min after changing pressure at each $P$ before the measurements. DLS measurements at elevated pressure was also conducted under the same pressure hysterisis as above.

## 5.3 Cloud Point Measurements and a $P$-$T$ Phase Diagram

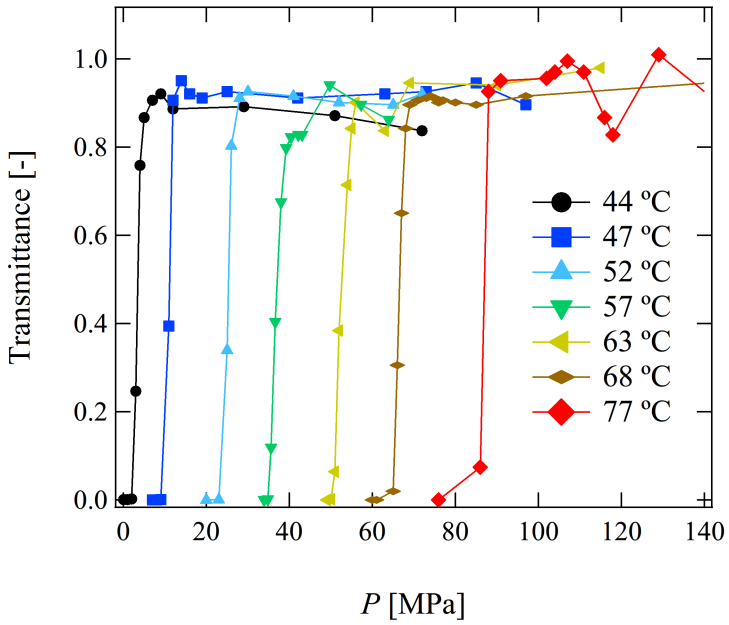


Figure 5.2: Pressure dependence of the transmittance of 3 wt% PPhEtMA/[$C_2$mIm][TFSA] solution at various temperatures.

Figure 5.2 shows the $P$-dependence of the transmittance of 3 wt% PPhEtMA/[$C_2$mIm][TFSA] solution at various temperatures of $T > T_{c0}$. As mentioned in the previous section, transmittance was measured under de-compression process. As a result, the transmittance of the solution suddenly decreased at certain cloud point pressures ($P_c$) for all the temperature examined here. It means that PPhEtMA is soluble at $P > P_c$ but undergoes phase separation at $P_c$. Here, reversibility of the $P$-induced phase transition was confirmed as following. At first, $P$ was decreased stepwise under isothermal condition and the transmittance was measured

at each $P$. After observing the decrease in the transmittance (corresponding to the $P$-induced phase separation), $P$ was subsequently increased and the transmittance was measured again. The transmittance of 3 wt% PPhEtMA in [$C_2$mIm][TFSA]) solution in both of the de-compression and the re-compression process was shown in Figure 5.3. Although there was large hysteresis, transmittance increased with $P$ in the re-pressurizing process at certain pressure. It indicates that the $P$-induced phase separation is reversible. According to a previous report, PPhEtMA in [$C_2$mIm][TFSA] solution exhibits the hysteresis also in $T$-induced phase separation.[22] The observed hysteresis can be ascribed to the metastable aggregation structure of PPhEtMA after the $P$-induced phase separation.

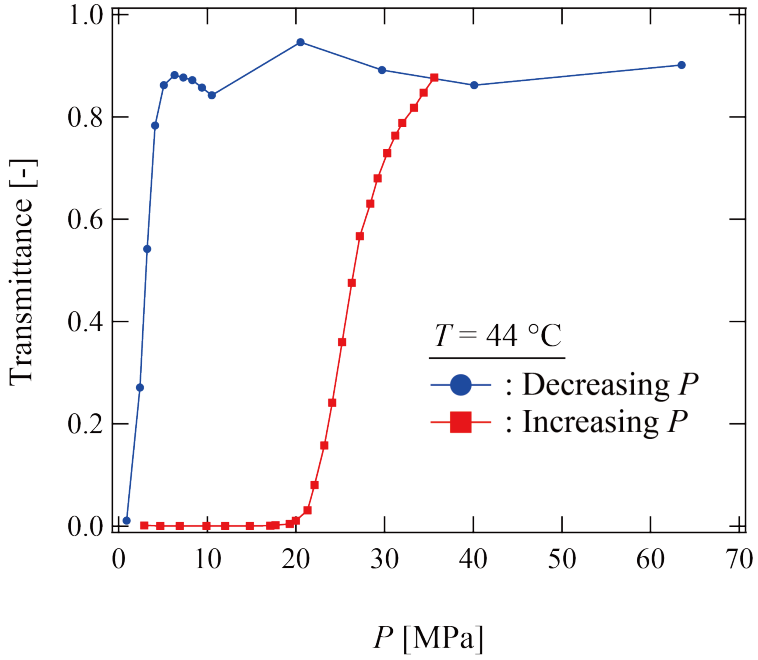


Figure 5.3: The transmittance of 3 wt% PPhEtMA in [$C_2$mIm][TFSA] solution in the depressurizing process (blue circles) and in the re-pressurizing process (red squares) after phase separation at $T$ = 44 °C.

Figure 5.2 also indicates that $P_c$ monotonically increased with increasing $T$. Although I also measured trasmittances at higher $P$ (140 MPa < $P$ < 364 MPa), any significant variation in transmittances was not observed. It suggests that the PPhEtMA/[$C_2$mIm][TFSA] system has only one $P_c$ in the examined range of $T$ and $P$ ($T$: 44 – 77 °C, $P$: 0.1 MPa – 364 MPa). Defining $P_c$ as the pressure at which the transmittance value becomes lower than 0.5, I constructed a $P$ - $T$ phase diagram which represents the pressure dependence of the cloud point temperature ($T_c$).

Figure 5.4 shows the $P$ - $T$ phase diagram obtained for the 3 wt%

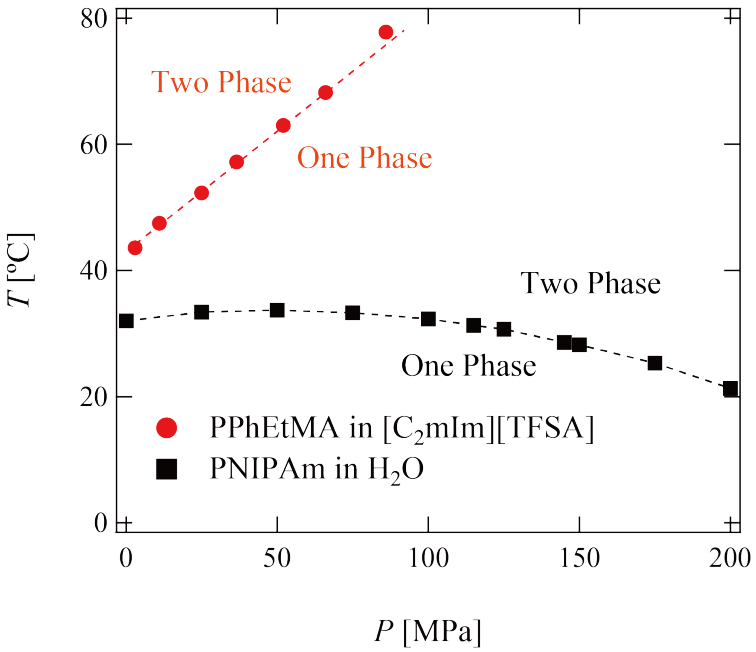


Figure 5.4: $P$ - $T$ phase diagram of 3 wt% PPhEtMA/[$C_2$mIm][TFSA] solution (red circles) constructed from the transmittance measurements (Figure 5.2. A previously reported phase diagram for aqueous 8 wt% PNIPAm solution (black squares) is also shown.[7]

PPhEtMA/[$C_2$mIm][TFSA] solution, together with that of the aqueous PNIPAm solution reported previously.[7] PNIPAm in aqueous solution exhibits a convex-upward $P$-dependence; it is commonly observed for aqueous solutions containing hydrophobic solutes, such as alkylbenzenes,[23,24] hydrophobic polymers,[8,25] and proteins.[4,9,10] In contrast, the $T_c$ of the PPhEtMA/[$C_2$mIm][TFSA] system increased monotonically with increasing $P$. In addition, the pressure dependence of $T_c$ of the PPhEtMA/[$C_2$mIm][TFSA] solution was much larger than that of the aqueous PNIPAm solution. The observed difference in pressure responce can be ascribed to the difference in solvation environments of the IL and the aqueous system.

In general, phase boundary line in the $P$ - $T$ phase diagram is given by the following Clapeyron-type equation:[11]

$$\frac{\mathrm{d}T}{\mathrm{d}P} = \frac{T\Delta V_\mathrm{m}(P)}{\Delta H_\mathrm{m}(P)} \tag{5.1}$$

where $\Delta H_\mathrm{m}(P)$ and $\Delta V_\mathrm{m}(P)$ denote the changes in the enthalpy and volume by mixing, respectively. It is established in Chpater 4 that $|\Delta H_\mathrm{m}|$ of the PPhEtMA in [$C_2$mIm][TFSA] solution at ambient pressure is smaller than that of the aqueous PNIPAm solution. Although there is no report about $\Delta V_\mathrm{m}(P)$ in the IL system, it is conjectured that the larger $|\mathrm{d}T/\mathrm{d}P|$ observed for the IL solution originates from the

smaller $|\Delta H_{\mathrm{m}}(P)|$ in the IL solution than the aqueous solution (Figure 5.4), based on eq. (5.1).

As can be seen from eq. (5.1), the sign of $\mathrm{d}T/\mathrm{d}P$ is determined by that of $\Delta V_{\mathrm{m}}(P)$. As $\Delta H_{\mathrm{m}}(P)$ must be negative for the system to exhibit LCST phase behavior, a negative $\Delta V_{\mathrm{m}}(P)$ results in a positive $\mathrm{d}T/\mathrm{d}P$ and vice versa.[11] Here, $\Delta V_{\mathrm{m}}(P)$ contains two contributions: the release of free volume upon ideal mixing ($\Delta V_{\mathrm{m,f}}(P)$) and the formation of solvation shell around polymer side chains ($\Delta V_{\mathrm{m,s}}(P)$), as illustrated in Figure 5.5(a). In the case of polymer solutions, the sign of $\Delta V_{\mathrm{m,f}}(P)$ is generally negative because a large free volume of polymer chains is released upon mixing into solvent.[23,24] The characteristics of polymer solvation is rather reflected in the magnitude and $P$-dependence of $\Delta V_{\mathrm{m,s}}(P)$ term.

The pressure response of the PPhEtMA/[$C_2$mIm][TFSA] solution and that of the aqueous PNIPAm solution can be characterized based on $|\Delta V_{\mathrm{m,s}}(P)|$ in each system. Figure 5.5(b) shows schematic models illustrating the solvation structure before and after pressurization for the aqueous PNIPAm solution and the PPhEtMA in [$C_2$mIm][TFSA] solution. In aqueous polymer solutions, the polymer is solubilized by a hydration shell formation around hydrophobic side chains; the structural ordering of water molecules are driven by hydrogen bonding interations between water molecules themselves. The formation of hydration shell causes expansion of the system upon mixing, leading to a positive $\Delta V_{\mathrm{m,s}}(P)$ in the aqueous system. As $|\Delta V_{\mathrm{m,f}}(P)|$ is a decreasing function of $P$,[23,24] a positive contribution from the $\Delta V_{\mathrm{m,s}}(P)$ overwhelms a negative contribution from the $\Delta V_{\mathrm{m,f}}(P)$ in the high-$P$ region. Therefore, the sign of $\Delta V_{\mathrm{m}}(P)$ ($= \Delta V_{\mathrm{m,s}}(P) + \Delta V_{\mathrm{m,f}}(P)$) changes from negative to positive at a certain pressure. Then, $\mathrm{d}T/\mathrm{d}P$ also changes its sign from positive to negative. This is the origin of the convex-upward $P$ - $T$ phase diagram in the aqueous polymer system.[23,26]

On the other hand, in the PPhEtMA in [$C_2$mIm][TFSA] solution, the polymer is mainly solubilized by direct cation-$\pi$ interactions between $[C_2\mathrm{mIm}]^+$ and phenyl groups in PPhEtMA side chains. In this case, there does not exist cavities between the polymer and the solvent. It indicates that the $|\Delta V_{\mathrm{m,s}}(P)|$ is negligible compared with $|\Delta V_{\mathrm{m,f}}(P)|$. Thus, $\Delta V_{\mathrm{m,s}}(P)$ does not cause a significant positive contribution to $\Delta V_{\mathrm{m}}(P)$, and the sign of $\Delta V_{\mathrm{m}}(P)$ remains negative even in the high-$P$ region. Such a picture is consitent with the observed results that the sign of $\mathrm{d}T/\mathrm{d}P$ remained positive even under the highest examined value of $P$.

Through the above discussion, the observed difference in $P$-$T$ phase diagram among the PPhEtMA in [$C_2$mIm][TFSA] solution and aqueous polymer solutions was

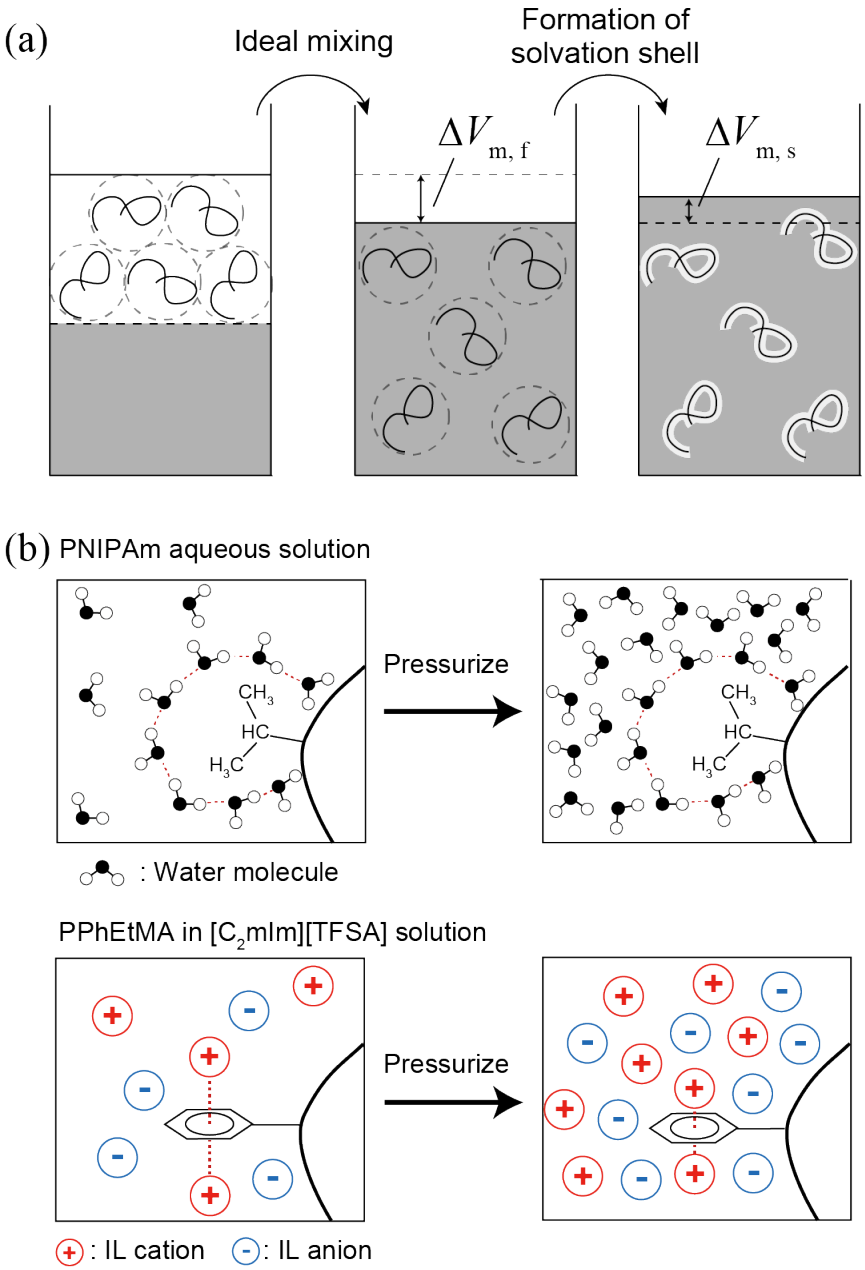


Figure 5.5: (a) Illustration of the volume change in the mixing process of polymer and solvent. (b) Schematic models showing the solvation structure of aqueous PNIPAm solution (above) and PPhEtMA/[$C_2$mIm][TFSA] solution (below) before and after pressurization.

successfully explained from a viewpoint of solvation environment in each systems.

## 5.4 Light Scattering Experiments under High Pressure

To obtain microscopic insight into the pressure effects, I performed DLS experiments on PPhEtMA in [$C_2$mIm][TFSA] solution at elevated pressure. Figure 5.6 shows (a) pressure dependence of $g^{(2)}(\tau) - 1$ and (b) the distribution function, $G(\Gamma^{-1})$ of decay time ($\Gamma^{-1}$) of 3 wt% PPhEtMA/[$C_2$mIm][TFSA] solution at $T = 44$ °C. Here, $G(\Gamma^{-1})$ was obtained by inverse Laplace transformation of $g^{(2)}(\tau) - 1$ using the well-established CONTIN program.[27] Pressure of the system was varied in the range of $P = 4$–12 MPa where $P_c$ at $T = 44$ °C was determined to be 3 MPa (Figure 5.2). As observed from Figure 5.6, a single decay mode was observed at $P > 7$ MPa. Here, the hydrodynamic radius ($R_h$) was estimated to be 7 nm from the decay time (refractive index[28] and viscosity[29] of the IL at $T = 317$ K and $P = 0.1$ MPa were used). The estimated value of $R_h = 7$ nm is reasonable as the size of a single polymer chains. It indicates that the decay mode observed in $g^{(2)}(\tau) - 1$ at $P > 7$ MPa corresponds to translational diffusion mode of dispersed PPhEtMA chains. In the vicinity of $P_c$ ($P \leq 5$ MPa), an additional slow mode was observed and its intensity increased with decreasing pressure. In addition, as shown in Figure 5.6(c), the time-averaged scattering intensity $\langle I \rangle_T$ diverged in the vicinity of $P_c$. These results indicate that aggregates of PPhEtMA are formed at $P \approx P_c$, resulting in the pressure-induced phase separation. This behavior was also observed in the temperature-induced phase separation of this system at ambient pressure (Chapter 4).

## 5.5 Conclusions

In conclusion, I observed a specific pressure effect on the LCST-type phase behavior of PPhEtMA in [$C_2$mIm][TFSA] solution. Compression of the solution resulted in a monotonic increase of the cloud point temperature in the IL system. It was a quite different pressure response from that of aqueous polymer solutions. The observed differences in the pressure response among aqueous polymer solutions and the polymer in IL solution reflected the characteristics of polymer solvation in each system; polymers are solubilized by hydration shell formation by hydrogen bonding interactions between water molecules in aqueous solution, but the polymer is solubilized by direct "solvent-polymer" interaction in the IL solution. Furthermore, dynamics of PPhEtMA in [$C_2$mIm][TFSA] solution was investigated by DLS experiments at

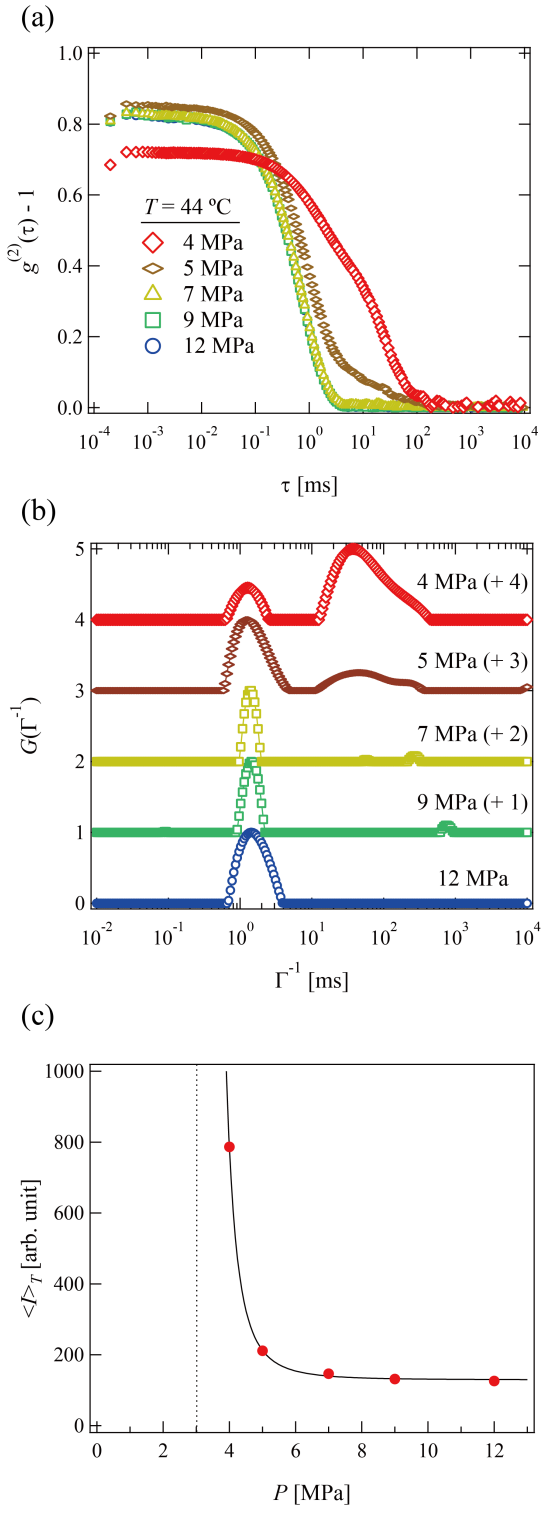


Figure 5.6: (a) Time correlation functions of scattering intensity, $g^{(2)}(\tau)-1$, measured at various pressures. The temperature is fixed at $T = 44$ °C. (b) The distribution function, $G(\Gamma^{-1})$ of decay time $(\Gamma^{-1})$ obtained from the inversed Laplace transformation procedure for $g^{(2)}(\tau) - 1$. (c) The time-averaged scattering intensity of light, $\langle I \rangle_T$ at various pressures.

elevated pressure. The appearance of a slow-mode in $g^{(2)}(\tau) - 1$, as well as the divergence of time-averaged scattering intensity, were observed in the vicinity of the cloud point pressure, indicating the formation of aggregates.

## Reference


[1] Shibayama, M.; Mizutani, S.; Nomura, S. *Macromolecules* **1996**, *29*, 2019–2024.

[2] Ono, Y.; Shikata, T. *J. Am. Chem. Soc.* **2006**, *128*, 10030–10031.

[3] Frank, H. S.; Evans, M. W. *J. Chem. Phys.* **1945**, *13*, 507–532.

[4] Kauzmann, W. *Nature* **1987**, *325*, 763–764.

[5] Matsugami, M.; Fujii, K.; Ueki, T.; Kitazawa, Y.; Umebayashi, Y.; Watanabe, M.; Shibayama, M. *Anal. Sci.* **2013**, *29*, 311–314.

[6] Otake, K.; Karaki, R.; Ebina, T.; Yokoyama, C.; Takahashi, S. *Macromolecules* **1993**, *26*, 2194–2197.

[7] Shibayama, M.; Isono, K.; Okabe, S.; Karino, T.; Nagao, M. *Macromolecules* **2004**, *37*, 2909–2918.

[8] Osaka, N.; Shibayama, M. *Phys. Rev. Lett.* **2006**, *96*, 048303(1)–048303(4).

[9] Smeller, L. *Biochimica et Biophysica Acta* **2002**, *1595*, 11–29.

[10] Osaka, N.; Takata, S.; Suzuki, T.; Endo, H.; Shibayama, M. *Polymer* **2008**, *49*, 2957–2963.

[11] Rebelo, L. P. N. *Phys. Chem. Chem. Phys.* **1999**, *1*, 4277–4286.

[12] Yoshimura, Y.; Abe, H.; Imai, Y.; Takekiyo, T.; Hamaya, N. *J. Phys. Chem. B* **2013**, *117*, 3264–3269.

[13] Yoshimura, Y.; Takekiyo, T.; Koyama, Y.; Takaku, M.; Yamamura, M.; Kikuchi, N.; Wakabayashi, D.; Funamori, N.; Matsuishi, K.; Abe, H.; Hamaya, N. *Phys. Chem. Chem. Phys.* **2017**, *in press*.

[14] Lachwa, J.; Szydlowski, J.; Najdanovic-Visak, V.; Rebelo, L. P. N.; Seddon, K. R.; da Ponte, M. N.; Esperança, H. J. R., J. M. S. S. Guades *J. Am. Chem. Soc.* **2005**, *127*, 6542–6543.

[15] Ferreira, R.; Blesic, M.; Trindade, J.; Marrucho, I.; Lopes, J. N. C.; Rebelo, L. P. N. *Green Chem.* **2008**, *10*, 918–928.

[16] Chang, H. C.; Tsai, T. T.; Kuo, M. H. *Macromolecules* **2014**, *47*, 3052–3058.

[17] Chang, H. C.; Zhang, R. L.; Hsu, D. T. *Phys. Chem. Chem. Phys.* **2015**, *17*, 27573.

[18] Fujii, K.; Kanzaki, R.; Takamuku, T.; Kameda, Y.; Kohara, S.; Kanakubo, M.; Shibayama, M.; Ishiguro, S.; Umebayashi, Y. *J. Chem. Phys.* **2011**, *135*, 244502.

[19] Kitazawa, Y.; Ueki, T.; McIntosh, L. D.; Tamura, S.; Niitsuma, K.; Imaizumi, S.; Lodge, T. P.; Watanabe, M. *Macromolecules* **2016**, *49*, 1414–1423.

[20] He, Y.; Li, Z.; Simone, P.; Lodge, T. P. *J. Am. Chem. Soc.* **2006**, *128*, 2745–2750.

[21] Matsumoto, M.; Murakoshi, K.; Wada, Y.; Yanagida, S. *Chem.Lett.* **2000**, *29*, 938–939.

[22] Kodama, K.; Nanashima, H.; Ueki, T.; Kokubo, H.; Watanabe, M. *Langmuir* **2009**, *25*, 3820–3824.

[23] Sawamura, S.; Kitamura, K.; Taniguchi, Y. *J. Phys. Chem.* **1989**, *93*, 4931–4935.

[24] Sawamura, S.; Nagaoka, K.; Machikawa, T. *J. Phys. Chem. B* **2001**, *105*, 2429–2436.

[25] Rebelo, L. P. N.; Visak, Z. P.; de Sousa, H. C.; Szydlowski, J.; Gomes de Azevedo, R.; Ramos, A. M.; Najdanovic-Visak, V.; Nunes da Ponte, M.; Klein, J. *Macromolecules* **2002**, *35*, 1887–1895.

[26] Nasimova, I.; Karino, T.; Okabe, S.; Nagao, M.; Shibayama, M. *Macromolecules* **2004**, *37*, 8721–8729.

[27] Provencher, S. W. *Comp. Phys. Comm.* **1982**, *27*, 213–227.

[28] Ueki, T.; Karino, T.; Kobayashi, Y.; Shibayama, M.; Watanabe, M. *J. Phys. Chem. B* **2007**, *111*, 4750–4754.

[29] Tokuda, H.; Hayamizu, K.; Ishii, K.; Susan, M. A. B. H.; Watanabe, M. *J. Phys. Chem. B* **2005**, *109*, 6103–6110.

# Summary

I performed structural investigation on cellulose and a thermo-reponsive polymer in IL solutions by complemetary utilizing X-ray, neutron, and light scattering techniques. I characterized their macroscopic solution property from viewpoints of microscopic molecular interactions and mesoscopic solvated structure of polymer chains. Furthermore, I investigated pressure response of a thermo-responsive polymer in an IL solution. The pressure response of the IL was discussed in comparison with conventional aqueous polymer solutions. The physicochemical characterizations of polymer in IL solutions is essential for futher development of novel composite systems of polymer and IL. The details of the respective chapters are summarized below.

In Chapters 2 and 3, I focused on the structure of cellulose in a phosphonate-type IL, $[C_2mIm][CH_3HPO_3]$. Glucose and cellobiose are used as model molecules to approximate microscopic structure of cellulose in Chapter 2 and 3, respectively.

Chapter 2

Liquid structure of neat $[C_2mIm][CH_3HPO_3]$ and solvation structure of glucose in $[C_2mIm][CH_3HPO_3]$ were investigated by high-energy X-ray toral scattering (HEXTS) experiments and all-atom molecular dynamics (MD) simulations. The experimental radial distribution functions were well reproduced by the MD simulations for all the glucose concentration examined. With regard to liquid structure of neat $[C_2mIm][CH_3HPO_3]$, I pointed out that hydrogen bond between negatively charged oxygens ($O_A$) within $[CH_3HPO_3]^-$ and acidic proton ($H_2$) on $C_2$ position of $[C_2mIm]^+$ is predominant in the cation-anion interaction. As for solvation structure of glucose in $[C_2mIm][CH_3HPO_3]$, it is found that the glucose molecules are preferentially solvated by $[CH_3HPO_3]^-$ rather than $[C_2mIm]^+$. From the atom-atom pair correlation function, it is clarified that the glucose molecule is hydrogen bonded with $[CH_3HPO_3]^-$ to form O-H (glucose)—$O_A$ (anion) interaction. It was also found that the intramolecular hydrogen bond within glucose still remains even in $[C_2mIm][CH_3HPO_3]$. Such

intramolecular hydrogen bonds compete with the intermolecular hydrogen bonds between glucose and $[CH_3HPO_3]^-$.

Chapter 3

The microscopic intramolecular structure of cellulose was investigated using HEXTS experiments and MD simulations. Here, cellobiose was used as a model molecule. It was clarified that intramolecular hydrogen bonds between the adjacent glucose segments within cellulose molecules exist even when dissolved in $[C_2mIm][CH_3HPO_3]$. Furthermore, the mesoscopic structure of cellulose chains in $[C_2mIm][CH_3HPO_3]$ was investigated by SAXS and light scattering experiments. It was found that intermolecular hydrogen bonds between cellulose molecules are disrupted in $[C_2mIm][CH_3HPO_3]$ solutions; thus, cellulose molecules are dispersed at the molecular level. In addition, cellulose molecules exist as rod-like polymers because of the intramolecular hydrogen bonds within cellulose chains in $[C_2mIm][CH_3HPO_3]$. Furthermore, in concentrated regions, rod-like cellulose molecules are strongly entangled and cellulose in $[C_2mIm][CH_3HPO_3]$ solutions have frozen inhomogeneities that arise from pseudo cross-links between cellulose molecules.

In Chapters 4 and 5, I extended the structural study to the stimuli-responsive phase transition of polymers in ILs. I particularly studied thermo- and pressure-responsive phase separation of poly(2-phenylethylmethacrylate), (PPhEtMA) in $[C_2mIm][TFSA]$.

Chapter 4

One of the characteristics of the phase behavior of polymers in ILs is that their phase transition temperatures ($T_c$s) are strongly affected by slight chemical modification on polymer side chain or IL ions. In Chapter 4, I focused on the drastic effect of structural modification on the phase equilibrium of thermo-responsive polymers in ILs. I selected PPhEtMA, having slightly different side chain structure from PBnMA, in $[C_2mIm][TFSA]$ solution as a model system. Solvated structure and phase behavior of PPhEtMA in $[C_2mIm][TFSA]$ was investigated by utilizing DLS and SANS experiment. To explore physical origin of the drastic effect of chemical modification on $T_c$ of the IL systems, structural parameters obtained for PPhEtMA in $[C_2mIm][TFSA]$ solution were compared with a previously reported values for PB-

nMA in [$C_2$mIm][TFSA] solution and further with PNIPAm aqueous solution. At first, precise structural characterization on PPhEtMA in [$C_2$mIm][TFSA] solution was conducted. SANS profiles of PPhEtMA in [$C_2$mIm][TFSA] solution showed a discontinuous change at cloud point temperature, indicative of structural change from dispersed Gaussian chains to large aggregates. The second virial coefficient $A_2$ was successfully evaluated by Zimm plot. The results showed that the compatibility of PPhEtMA in [$C_2$mIm][TFSA] gradually decreases with increasing temperature. Subsequently, the enthalpic and entropic contribution ($\chi_H$ and $\chi_S$, respectively) to $\chi_{eff}$ were estimated from SANS profiles of PPhEtMA in [$C_2$mIm][TFSA] solution. The absolute value of $\chi_H$ obtained for PPhEtMA was smaller than that for PBnMA. This difference in $\chi_H$ reflects an increase of unfavorable interaction between the polymer and the IL by the insertion of the solvo-phobic methylene group. Furthermore, the obtained $|\chi_S|$ and $|\chi_H|$ values of both PPhEtMA and PBnMA in [$C_2$mIm][TFSA] systems were significantly smaller than those of PNIPAm aqueous solution system. It was pointed out the phase equilibrium of the IL system is controlled by smaller change in the free energy on mixing. That is the origin of the drastic effect of structural modification on the phase equilibrium of thermo-responsive polymers in ILs.

Chapter 5

Pressure response of solutions contains rich structural information such as packing of molecules and volumetric properties. In Chapter 5, I utilized hydrostatic pressure as an experimental variable to investigate characteristics of solvation for polymers by ILs. I observed a specific pressure effect on the LCST-type phase behavior of PPhEtMA in [$C_2$mIm][TFSA] solution. Compression of the solution resulted in a monotonic increase of the cloud point temperature in the IL system. It was a quite different pressure response from that of aqueous polymer solutions. The observed differences in the pressure response among aqueous polymer solutions and the polymer in IL solution reflected the characteristics of polymer solvation in each system; polymers are solubilized by hydration shell formation by hydrogen bonding interactions between water molecules in aqueous solution, but the polymer is solubilized by direct "solvent-polymer" interaction in the IL solution. Furthermore, dynamics of PPhEtMA in [$C_2$mIm][TFSA] solution was investigated by DLS experiments at elevated pressure. The appearance of a slow-mode in the time-correlation function, as well as the divergence of time-averaged scattering intensity, were observed in the vicinity of the cloud point pressure. It indicates that aggregates were suddenly formed

at the cloud point pressure.

I succeeded in the physicochemical characterization of solvated structure and phase behavior of polymers in ILs. It was found that microscopic solvation of polymers by ILs significantly affects the macroscopic physical properties of the solutions. Such knowledge allows us to systematically develop superior polymer-IL composite systems based on the design of molecular structures of ILs and polymers. For example, in the case of cellulose in IL systems, I found that the rigidity of cellulose chains is strongly correlated to the existence of intramolecular hydrogen bonds within cellulose molecules. Thus, the chain conformation of cellulose in ILs can be controlled by appropriately designing the molecular structures of IL ions. It means that we can optimize the properties of cellulose in IL solution for our purpose, such as biomass processing of cellulose and the production of cellulose fiber. In addition, through the precise investigation of the phase behavior of polymers in ILs in response to temperature and pressure, I elucidated the relationship between phase-behavior and microscopic interactions. Especially, pressure response of polymers in IL solutions is an unexplored research field. This work would become an important opportunity for the application of ILs under extreme pressure, for example development of a pressure-responsive iongel which is applicable to an electrolyte of lithium ion batteries and a $CO_2$ separation membrane.

Eventually, I conclude that this work contributes to not only the fundamental understanding but also the systematic design of the physical properties of polymer-IL composite systems.

# Appendix: Theoretical Background

## Basic Theory of Scattering

Structure of materials are reflected in scattering profiles via interference of scattered waves from atomic nuclei or electrons. In the case of amorphous materials, the amount of structural information included in scattering profiles is limited because of lacks of the sharp diffraction peaks. Nevertheless, scattering experiments are still principal method to resolve structure of amorphous such as liquids, solutions, and glasses. In this Chapter, I introduce principles of scattering analysis for amorphous and polymeric materials.[1]

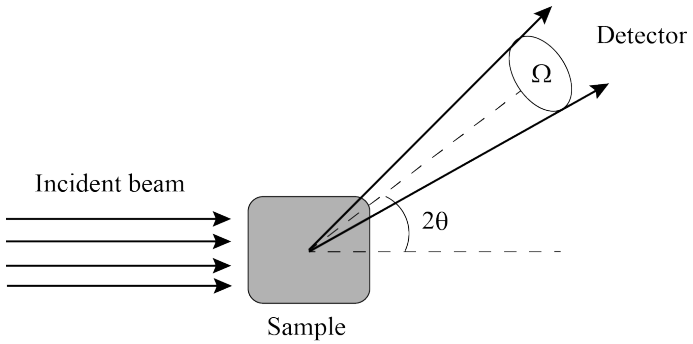


Figure 5.7: Illustration for a typical geometry of scattering experiment including the incident plane wave, the sample, the scattered spherical wave, and the detector. $2\theta$, $\Omega$ is the scattering angle and the solid angle.

Figure 5.7 shows a typical geometry of scattering experiment. The incident beam can be regarded as a plane wave when it is appropriately collimated. Intensity of plane waves is represented by the amount of energy (or particles) transmitted per unit area per unit of time. On the other hand, scattering wave from a sample is generally regarded as a spherical wave whose intensity is expressed by the amount of energy (or particles) transmitted through a unit solid angle per unit of time. One needs to evaluate the flux, $J$ of the scattered wave as a function of scattering direction.

The ratio of $J$ to the flux of incident beam, $J_0$ is generally used as a measure of the intensity of the scattering wave from the sample. The ratio, $J/J_0$ as a function of scattering direction is often called "the differencial scattering cross section" or "the absolute intensity", which have a unit of area. $J/J_0$ means the probability that a photon or neutron is scattered into a unit solid angle in a given direction. $J/J_0$ can be directly related to the structure of sample as described below.

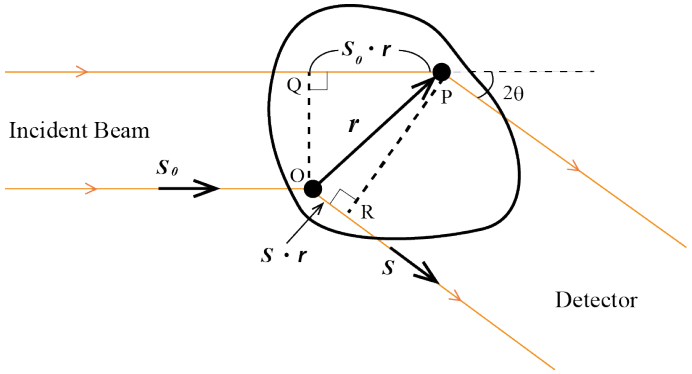


Figure 5.8: The path length difference between scatteirng waves from scattering points, O and P. $\boldsymbol{S}_0$ and $\boldsymbol{S}$ are the unit vectors of the incident beam and the scattered waves, respectively.

Both of neutron beam and X-ray are frequently used as a probe in scattering experiments. A primary scattering event of neutrons and X-ray by atomic nuclei and electrons should be discussed separately. Nevertheless, the interference effects of the scattered waves can be discussed in the same manner. At first, for a simplicity, I discuss the interference between scattering waves from only two scattering points, O and P as illustrated in Figure 5.8. Here, $\boldsymbol{S_0}$ and $\boldsymbol{S}$ denote the unit vectors of the incident beam and the scattered waves. Now, I assume the elastic scattering in which wavelength of the scattered wave is the same as that of the incident beam. If there is no phase change on scattering, the phase difference $\Delta\phi$ between the two scattering waves is given as

$$\begin{aligned} \Delta\phi &= \frac{2\pi}{\lambda}\left(\boldsymbol{S_0}\cdot\boldsymbol{r} - \boldsymbol{S}\cdot\boldsymbol{r}\right) \\ &= -\boldsymbol{q}\cdot\boldsymbol{r} \end{aligned} \tag{5.2}$$

where $\lambda$ is the wavelength of the incident beam and $\boldsymbol{q} \equiv 2\pi(\boldsymbol{S}-\boldsymbol{S_0})/\lambda$ is the scattering vector. The magnitude of the scattering vector is

$$|\boldsymbol{q}| = q = \frac{4\pi\sin\theta}{\lambda} \tag{5.3}$$

Considering the phase difference, the scattering waves from O and P ($A_1(x,t)$ and

$A_2(x,t)$, respectively) are written as follows:

$$A_1(x,t) = A_0 b \exp\left[2\pi i\left(\nu t - \frac{x}{\lambda}\right)\right] \tag{5.4}$$

$$A_2(x,t) = A_0 b \exp\left[2\pi i\left(\nu t - \frac{x}{\lambda}\right)\right] \exp[-i\boldsymbol{q}\cdot\boldsymbol{r}] \tag{5.5}$$

where $A_0$ and $\nu$ are the amplitude of the incident beam and frequency of the waves. $b$ is the scattering length which represents the scattering ability of the scattering points: it is independent of the energy of neutron or X-ray. Detector in the direction of $\boldsymbol{q}$ detects a superposition of the scattering waves, $A(\boldsymbol{q}) = A_1(x,t) + A_2(x,t)$. Then, the differencial scattering cross section is given as follows:

$$\begin{aligned}\frac{J(\boldsymbol{q})}{J_0} &= A_0^{-2}|A(\boldsymbol{q})|^2 = A_0^{-2}|A_1(x,t) + A_2(x,t)|^2 \\ &= b^2\left(1 + \exp[i\boldsymbol{q}\cdot\boldsymbol{r}]\right)\left(1 + \exp[-i\boldsymbol{q}\cdot\boldsymbol{r}]\right)\end{aligned} \tag{5.6}$$

When there are a lot of scattering points, the scattering wave detected by the detector is

$$A(\boldsymbol{q}) = b\sum_{j=1}^{N} \exp[-i\boldsymbol{q}\cdot\boldsymbol{r}_j] \tag{5.7}$$

As in eq. (5.7), $A_0$ and the $x$- and $t$-dependent terms are omitted hereafter. $N$ and $\boldsymbol{r}_j$ are the number of the scattering points in the irradiated volume and the position of scattering points. Furthermore, the summation in eq. (5.7) is substituted by an integral when the number of scattering points is sufficiently large. Introducing $n(\boldsymbol{r})$ as the number density of the scattering points in a volume element at $\boldsymbol{r}$, eq. (5.7) is rewritten as follows;

$$A(\boldsymbol{q}) = b\int_V n(\boldsymbol{r}) \exp[-i\boldsymbol{q}\cdot\boldsymbol{r}]\, d\boldsymbol{r} \tag{5.8}$$

$$= \int_V \rho(\boldsymbol{r}) \exp[-i\boldsymbol{q}\cdot\boldsymbol{r}]\, d\boldsymbol{r} \tag{5.9}$$

where the scattering length distribution, $\rho(\boldsymbol{r})$ is defined as $\rho(\boldsymbol{r}) \equiv bn(\boldsymbol{r})$. It means that $A(\boldsymbol{q})$ is related to $\rho(\boldsymbol{r})$ via three-diensional Fourier transform. Then, the differencial scattering cross section, $I(\boldsymbol{q})$ is the following:

$$\begin{aligned}I(\boldsymbol{q}) &= \left[\int_V \rho(\boldsymbol{u}) \exp[i\boldsymbol{q}\cdot\boldsymbol{u}]\, d\boldsymbol{u}\right]\left[\int_V \rho(\boldsymbol{u'}) \exp[-i\boldsymbol{q}\cdot\boldsymbol{u'}]\, d\boldsymbol{u'}\right] \\ &= \int_V \left[\int \rho(\boldsymbol{u})\rho(\boldsymbol{u}+\boldsymbol{r})\mathrm{d}\boldsymbol{u}\right] \exp[-i\boldsymbol{q}\cdot\boldsymbol{r}]\mathrm{d}\boldsymbol{r} \quad (\boldsymbol{r} = \boldsymbol{u'} - \boldsymbol{u}) \\ &= \int_V \Gamma_\rho(\boldsymbol{r}) \exp[-i\boldsymbol{q}\cdot\boldsymbol{r}]\mathrm{d}\boldsymbol{r}\end{aligned} \tag{5.10}$$

$\Gamma_\rho(\boldsymbol{r})$ is the autocorrelation function for $\rho(\boldsymbol{r})$ defined

$$\Gamma_\rho(\boldsymbol{r}) = \int_V \rho(\boldsymbol{u})\rho(\boldsymbol{u}+\boldsymbol{r})\mathrm{d}\boldsymbol{u} \tag{5.11}$$

Here, $\Gamma_\rho(\boldsymbol{r})$ is related to the ensemble average of $\rho(\boldsymbol{u})\rho(\boldsymbol{u}+\boldsymbol{r})$ as follows:

$$\langle\rho(\boldsymbol{u})\rho(\boldsymbol{u}+\boldsymbol{r})\rangle = \frac{\int_V \rho(\boldsymbol{u})\rho(\boldsymbol{u}+\boldsymbol{r})\mathrm{d}\boldsymbol{u}}{\int_V \mathrm{d}\boldsymbol{u}} = \frac{\Gamma_\rho(\boldsymbol{r})}{V} \tag{5.12}$$

Introducing $\eta(\boldsymbol{r}) \equiv \rho(\boldsymbol{r}) - \langle\rho\rangle$ as a deviation of $\rho(\boldsymbol{r})$ from averaged scattering length density, $\langle\rho\rangle$, the following relationship can be derived:

$$\begin{aligned}\Gamma_\rho(\boldsymbol{r}) &= \int_V \left[\eta(\boldsymbol{u}) + \langle\rho\rangle\right]\left[\eta(\boldsymbol{u}+\boldsymbol{r}) + \langle\rho\rangle\right]\mathrm{d}\boldsymbol{u} \\ &= \int_V \eta(\boldsymbol{u})\eta(\boldsymbol{u}+\boldsymbol{r})\mathrm{d}\boldsymbol{u} + \langle\rho\rangle^2\int_V \mathrm{d}\boldsymbol{u} + \langle\rho\rangle\int_V \eta(\boldsymbol{u})\mathrm{d}\boldsymbol{u} + \langle\rho\rangle\int_V \eta(\boldsymbol{u}+\boldsymbol{r})\mathrm{d}\boldsymbol{u} \\ &= \Gamma_\eta(\boldsymbol{r}) + \langle\rho\rangle^2 V\end{aligned} \tag{5.13}$$

Using eq. (5.13), (5.10) becomes

$$I(\boldsymbol{q}) = \int_V \Gamma_\eta(\boldsymbol{r})\exp\left[-i\boldsymbol{q}\cdot\boldsymbol{r}\right]\mathrm{d}\boldsymbol{r} + \langle\rho\rangle^2 V\delta(\boldsymbol{q}) \tag{5.14}$$

The second term in eq. (5.14) is not observable because it overlaps with the transmitted incident beam. Hence, $I(\boldsymbol{q})$ is directly related to $\Gamma_\eta(\boldsymbol{r})$ which represents the real-space structure.

### Zero Angle Scattering[2]

Scattering intensity at the limit of $q \to 0$ is detemined by thermodynamic properties of the materials. In this section, I summarize the classical theory of simple liquid and derive the relationship between scattering intensity and a thermodynamic parameter, the isothermal compressibility. Consider an isolated, macroscopic system consisting of $N$ idential, spherical particles of mass $m$ in volume $V$. The dynamical state of the system is completely specified by $3N$ coordinates $\boldsymbol{r}^N = \boldsymbol{r}_1, \ldots, \boldsymbol{r}_N$ and $3N$ momenta $\boldsymbol{p}^N = \boldsymbol{p}_1, \ldots, \boldsymbol{p}_N$ of the particles. The hamiltonian of the system, $\mathcal{H}$ is

$$\mathcal{H} = K_N(\boldsymbol{p}^N) + V_N(\boldsymbol{r}^N) + \Phi_N(\boldsymbol{r}^N) \tag{5.15}$$

where $K_N$, $V_N$, and $\Phi_N$ are the kinetic energy, the interatomic potential energy, and the potential energy arising from an external field. In this section, I discuss the properties of liquid or solutions under no external field: $\Phi_N(\boldsymbol{r}^N) = 0$. $K_N$ is given as

$$K_N = \sum_{i=1}^{N}\frac{|\boldsymbol{p}_i|^2}{2m} \tag{5.16}$$

The distribution of phase points of systems of the ensembles is represented by a phase space probability density $f^{|N|}(\boldsymbol{r}^N, \boldsymbol{p}^N; t)$. Here, $f^{|N|}(\boldsymbol{r}^N, \boldsymbol{p}^N; t)\mathrm{d}\boldsymbol{r}^N\mathrm{d}\boldsymbol{p}^N$ is the probability that the system is in a macroscopic state represented by a phase point lying in the infinitesimal $6N$-dimensional phase space element $\mathrm{d}\boldsymbol{r}^N\mathrm{d}\boldsymbol{p}^N$. Then, the integral of $f^{|N|}$ over phase space is

$$\iint f^{|N|}(\boldsymbol{r}^N, \boldsymbol{p}^N; t)\mathrm{d}\boldsymbol{r}^N\mathrm{d}\boldsymbol{p}^N = 1 \tag{5.17}$$

for all $t$. Normally we are interested only in the behavior of a subset of particles of size $N'$. Then, unnecessary information can be eliminated by performing integration of $f^{|N|}$ over the coordinates and the momenta of $(N - N')$ particles. Then, a reduced phase space distribution function $f^{(N')}(\boldsymbol{r}^{N'}, \boldsymbol{p}^{N'}; t)$ is defined as

$$f^{(N')}(\boldsymbol{r}^{N'}, \boldsymbol{p}^{N'}; t) \equiv \frac{N!}{(N - N')!} \iint f^{|N|}(\boldsymbol{r}^N, \boldsymbol{p}^N; t)\mathrm{d}\boldsymbol{r}^{N-N'}\mathrm{d}\boldsymbol{p}^{N-N'} \tag{5.18}$$

where $\boldsymbol{r}^{N'} \equiv \boldsymbol{r}_1, \ldots, \boldsymbol{r}_{N'}$ and $\boldsymbol{r}^{(N-N')} \equiv \boldsymbol{r}_{N'+1}, \ldots, \boldsymbol{r}_N$, etc. $f^{(N')}\mathrm{d}\boldsymbol{r}^{N'}\mathrm{d}\boldsymbol{p}$ is the probability of finding subset of $N'$ particles in the reduced phase element $\mathrm{d}\boldsymbol{r}^{N'}\mathrm{d}\boldsymbol{p}^{N'}$, irrespective of $\boldsymbol{r}^{(N-N')}$ and $\boldsymbol{p}^{(N-N')}$. $N!/(N - N')!$ is the conbinatorial factor that corresonds to the number of ways of choosing a subset of size $N'$.

**Canonical Ensemble**

A canonical ensemble is a collection of systems characterised by the same values of $N$, $V$, and temperature $T$. It corresponds to a system immesed in a heat bath. According to classical statistical mechanics, the equilibrium probability density for a system is

$$f_0^{|N|}(\boldsymbol{r}^N, \boldsymbol{p}^N) = \frac{1}{h^{3N}N!}\frac{\exp(-\beta\mathcal{H})}{Q_N} \tag{5.19}$$

where $h$ is Planck's constant and $\beta = T^{-1}$. $Q_N$ is the canonical partition function, given by

$$Q_N = \frac{1}{h^{3N}N!} \iint \exp(-\beta\mathcal{H})\mathrm{d}\boldsymbol{r}^N\mathrm{d}\boldsymbol{p}^N \tag{5.20}$$

The thermodynamic potential which is appropriate to describe properties of the canonical ensemble is the Helmholtz energy, $F$: it is obtained by Legendre transformation for the internal energy $U$ with respect to entropy $S$. $F$ becomes

$$F = U - TS \tag{5.21}$$

in thermodynamics. The equilibrium state at constant $N$, $V$, and $T$ is reached when $F$ is a minimum with respect to variations in any internal constraint. The

link between thermodynamic property and statistical mechanics is established by the following relationship.

$$F = -k_{\mathrm{B}}T \ln Q_N \tag{5.22}$$

When there is no external force, the change in the Helmholtz arising from infinitesimal changes in $N$, $V$, and $T$ is

$$\mathrm{d}F = -S\mathrm{d}T - P\mathrm{d}V + \mu \mathrm{d}N \tag{5.23}$$

and thus

$$S = -\left(\frac{\partial F}{\partial T}\right)_{V,N} \quad P = -\left(\frac{\partial F}{\partial V}\right)_{T,N} \quad \mu = \left(\frac{\partial F}{\partial N}\right)_{T,V} \tag{5.24}$$

Themodynamic parameters can be calculated from the partition function. For example, internal energy $U$ is given as

$$U = \frac{1}{h^{3N}N!Q_N}\iint \mathcal{H}\exp(-\beta\mathcal{H})\mathrm{d}\boldsymbol{r}^N\mathrm{d}\boldsymbol{p}^N = -\left(\frac{\partial \ln Q_N}{\partial \beta}\right)_V \tag{5.25}$$

where eq. (5.20) was used. Then, using eq. (5.22) and eq. (5.24),

$$P = k_{\mathrm{B}}T\left(\frac{\partial \ln Q_N}{\partial V}\right)_{T,N} \tag{5.26}$$

The partition function $Q_N$ can be rewritten as follows:

$$\begin{aligned} Q_N &= \frac{1}{h^{3N}N!}\iint \exp(-\beta\mathcal{H})\mathrm{d}\boldsymbol{r}^N\mathrm{d}\boldsymbol{p}^N \\ &= \frac{1}{h^{3N}N!}\int \exp(-\beta K_N(\boldsymbol{p}^N))\mathrm{d}\boldsymbol{p}^N \int \exp(-\beta V_N(\boldsymbol{r}^N))\mathrm{d}\boldsymbol{r}^N \\ &= \frac{1}{h^{3N}N!}(2m\pi k_{\mathrm{B}}T)^{\frac{3}{2}N}\int \exp(-\beta V_N(\boldsymbol{r}^N))\mathrm{d}\boldsymbol{r}^N \\ &= \frac{1}{N!}\frac{Z_N}{\Lambda^{3N}} \end{aligned} \tag{5.27}$$

Here, $\Lambda = (2\pi\beta\hbar^2/m)^{1/2}$ is the de Broglie wavelength. $Z_N$ is defined as follows:

$$Z_N = \int \exp(-\beta V_N(\boldsymbol{r}^N))\mathrm{d}\boldsymbol{r}^N \tag{5.28}$$

When $V_N = 0$ (ideal gas), $Z_N^{\mathrm{id}} = V^N$ and the corresponding partition function $Q_N^{\mathrm{id}}$ becomes

$$Q_N^{\mathrm{id}} = \frac{1}{N!}\frac{V^N}{\Lambda^{3N}} \tag{5.29}$$

Then, using Stirling's approximation for $lnN!$,

$$\begin{aligned} \frac{F^{\mathrm{id}}}{N} &= -\frac{1}{N}k_{\mathrm{B}}T\ln Q_N^{\mathrm{id}} \\ &= k_{\mathrm{B}}T(\ln \Lambda^3 n - 1) \end{aligned} \tag{5.30}$$

where $n$ is the number density of particles. The chemical potential $\mu^{\mathrm{id}}$ is given as

$$\mu^{\mathrm{id}} = \left(\frac{\partial F^{\mathrm{id}}}{\partial N}\right)_{T,V} = k_{\mathrm{B}}T \ln \Lambda^3 n \tag{5.31}$$

A similar factrization can be made of $f_0^{(N')}(\boldsymbol{r}^{N'}, \boldsymbol{p}^{N'})$:

$$\begin{aligned} f^{(N')}(\boldsymbol{r}^{N'}, \boldsymbol{p}^{N'}; t) &= \frac{N!}{(N-N')!} \iint \frac{1}{h^{3N} N!} \frac{\exp(-\beta \mathcal{H})}{Q_N} \mathrm{d}\boldsymbol{r}^{N-N'} \mathrm{d}\boldsymbol{p}^{N-N'} \\ &= \frac{N!}{(N-N')!} \frac{\exp\left[-\beta \sum_{i=1}^{N'} (|\boldsymbol{p}_i|^2/2m)\right]}{(2\pi m k_{\mathrm{B}} T)^{\frac{3}{2}N'}} \iint \frac{1}{h^{3N} N!} \frac{\exp(-\beta \mathcal{H})}{Q_N} \mathrm{d}\boldsymbol{r}^{N-N'} \mathrm{d}\boldsymbol{p}^{N} \\ &= \frac{N!}{(N-N')!} \frac{\exp\left[-\beta \sum_{i=1}^{N'} (|\boldsymbol{p}_i|^2/2m)\right]}{(2\pi m k_{\mathrm{B}} T)^{\frac{3}{2}N'}} \frac{1}{Z_N} \iint \exp(-\beta V_N) \mathrm{d}\boldsymbol{r}^{N-N'} \\ &= n_N^{(N')}(\boldsymbol{r}^{N'}) f_M^{(N')}(\boldsymbol{p}^{N'}) \end{aligned} \tag{5.32}$$

where $f_M^{(N')}$ is defined as

$$f_M^{(N')}(\boldsymbol{p}^{N'}) = \frac{1}{(2\pi m k_{\mathrm{B}} T)^{\frac{3}{2}N}} \exp\left[-\beta \sum_{i=1}^{N'} \left(\frac{|\boldsymbol{p}_i|^2}{2m}\right)\right] \tag{5.33}$$

The equilibrium $N'$-particle number density $n_N^{(N')}(\boldsymbol{r}^{N'})$ is

$$n_N^{(N')}(\boldsymbol{r}^{N'}) = \frac{N!}{(N-N')!} \frac{1}{Z_N} \iint \exp(-\beta V_N) \mathrm{d}\boldsymbol{r}^{N-N'} \tag{5.34}$$

The quantity $n_N^{(N')}(\boldsymbol{r}^{N'}) \mathrm{d}\boldsymbol{r}^{N'}$ determines the probability of finding $N'$ particles of the system with coordinates in the volume element $\mathrm{d}\boldsymbol{r}^{N'}$ irrespective of the positions and momenta of other $N - N'$ particles. The low-order particle density function, especially the pair distribution function $n_N^{(N')}(\boldsymbol{r}_1, \boldsymbol{r}_2)$, is important for calculation of the scattering intensity. From its definition in eq. (5.34),

$$\int n_N^{(N')}(\boldsymbol{r}_1, \boldsymbol{r}_2) \mathrm{d}\boldsymbol{r}^{N'} = \frac{N!}{(N-N')!} \tag{5.35}$$

In particular for $N' = 1$,

$$\int n_N^{(1)}(\boldsymbol{r}) \mathrm{d}\boldsymbol{r} = N \tag{5.36}$$

Therefore, the single particle density $n_N^{(1)}(\boldsymbol{r})$ is therefore equal to the overall number density:

$$n_N^{(1)}(\boldsymbol{r}) = \frac{N}{V} = n \tag{5.37}$$

The $N'$-particle distribution function $g_N^{N'}(\boldsymbol{r}^{N'})$ is defined as follows:

$$\begin{aligned} g_N^{(N')}(\boldsymbol{r}^{N'}) &= \frac{n_N^{(N')}(\boldsymbol{r}_1, \ldots, \boldsymbol{r}_{N'})}{\Pi_{i=1}^{N'} n_N^{(1)}(\boldsymbol{r}_i)} \\ &= n^{-N'} n_N^{(N')}(\boldsymbol{r}^{N'}) \quad \text{(for homogeneous systems)} \end{aligned} \tag{5.38}$$

When the system is isotropic, the pair distribution function $g_N^{(2)}(\boldsymbol{r}_1, \boldsymbol{r}_2)$ is a only function of $r = |\boldsymbol{r}_2 - \boldsymbol{r}_1|$ and written as $g(r)$: it is so-called radial distribution function. It is convenient to use an expression by $\delta$-function for $n$-particle density functions. From its definition,

$$\begin{aligned} \langle \delta(\boldsymbol{r} - \boldsymbol{r}_1) \rangle &= \iint \delta(\boldsymbol{r} - \boldsymbol{r}_1) f_0^{|N|}(\boldsymbol{r}^N, \boldsymbol{p}^N) \mathrm{d}\boldsymbol{r}^N \mathrm{p}^N \\ &= \frac{1}{Z_N} \int \delta(\boldsymbol{r} - \boldsymbol{r}_1) \exp\left[-\beta V_N(\boldsymbol{r}_1, \boldsymbol{r}_2, \ldots, \boldsymbol{r}^N)\right] \mathrm{d}\boldsymbol{r}^N \\ &= \frac{1}{Z_N} \int \exp[-\beta V_N(\boldsymbol{r}, \boldsymbol{r}_2, \ldots, \boldsymbol{r}_N)] \mathrm{d}\boldsymbol{r}^{N-1} \end{aligned} \tag{5.39}$$

Since the value of is independent on the particle label (taken to be 1 here), the summation for all of the particles is simply $N$ times the RHS. In comparison with eq. (5.34), we obtain

$$\begin{aligned} n_N^{(1)}(\boldsymbol{r}) &= N \frac{1}{Z_N} \int \exp\left[-\beta V_N\right] \mathrm{d}\boldsymbol{r}^{N-1} \\ &= \left\langle \sum_{i=1}^{N} \delta(\boldsymbol{r} - \boldsymbol{r}_i) \right\rangle \end{aligned} \tag{5.40}$$

Similarly, for a product of two $\delta$-functions,

$$\left\langle \delta(\boldsymbol{r} - \boldsymbol{r}_1) \delta(\boldsymbol{r}' - \boldsymbol{r}_2) \right\rangle = \frac{1}{Z_N} \int \exp\left[-\beta V_N(\boldsymbol{r}, \boldsymbol{r}', \boldsymbol{r}_3 \ldots, \boldsymbol{r}_N)\right] \mathrm{d}\boldsymbol{r}^{N-2} \tag{5.41}$$

and then

$$\begin{aligned} n_N^{(2)}(\boldsymbol{r}, \boldsymbol{r}') &= N(N-1) \frac{1}{Z_N} \int \exp\left[-\beta V_N\right] \mathrm{d}\boldsymbol{r}^{(N-2)} \\ &= \left\langle \sum_{i=1}^{N} \sum_{j \neq i}^{N} \delta(\boldsymbol{r} - \boldsymbol{r}_i) \delta(\boldsymbol{r}' - \boldsymbol{r}_j) \right\rangle \end{aligned} \tag{5.42}$$

Furthermore, the following $\delta$-function is correlated to the radial distribution function:

$$\begin{aligned} \left\langle \frac{1}{N} \sum_{i=1}^{N} \sum_{j \neq i}^{N} \delta(\boldsymbol{r} - \boldsymbol{r}_j + \boldsymbol{r}_i) \right\rangle &= \left\langle \frac{1}{N} \int \sum_{i=1}^{N} \sum_{j \neq i}^{N} \delta(\boldsymbol{r}' + \boldsymbol{r} - \boldsymbol{r}_j) \delta(\boldsymbol{r}' - \boldsymbol{r}_i) \mathrm{d}\boldsymbol{r}' \right\rangle \\ &= \frac{1}{N} \int n_N^{(2)}(\boldsymbol{r}' + \boldsymbol{r}, \boldsymbol{r}') \mathrm{d}\boldsymbol{r}' \\ &= \frac{1}{N} \int n^2 g_N^{(2)}(\boldsymbol{r}' + \boldsymbol{r}, \boldsymbol{r}') \mathrm{d}\boldsymbol{r}' \\ &= n g(r) \end{aligned} \tag{5.43}$$

### Grand Canonical Ensemble

The discussion of canonical ensemble is restricted to uniform systems containing a fixed number of particles. We now extend the argument to situations in which the number of particles varies by interchange with surroundings. The macroscopic state of such system is represented by the chemical potential, $\mu$, $V$ and $T$ and the corresponding thermodynamic potential is the grand potential, $\Omega$. $\Omega$ is obtained by Legendre transformation for the Helmholtz free energy $F$ with respect to the number of particle $N$ as follows:

$$\Omega = F - N\mu \tag{5.44}$$

The differential form of $\Omega$ and the relationship with thermodynamic parameters is

$$\mathrm{d}\Omega = -S\mathrm{d}T - P\mathrm{d}V - N\mathrm{d}\mu \tag{5.45}$$

$$S = -\left(\frac{\partial\Omega}{\partial T}\right)_{V,\mu} \quad P = -\left(\frac{\partial\Omega}{\partial V}\right)_{T,\mu} \quad N = -\left(\frac{\partial\Omega}{\partial\mu}\right)_{T,V} \tag{5.46}$$

An ensemble of systems having the same values of $\mu$, $V$ and $T$ is called a grand canonical ensemble. The phase space of the grand canonical ensemble is the union of phase spaces including all value of the variable $N$ for given $V$ and $T$. Thus, the equilibrium ensemble probability density is a function of $N$ given as

$$f_0(\boldsymbol{r}^N, \boldsymbol{p}^N; N) = \frac{\exp[-\beta(\mathcal{H} - N\mu)]}{\Xi} \tag{5.47}$$

where the grand partition function $\Xi$ is

$$\Xi = \sum_{N=0}^{\infty} \frac{\exp(N\beta\mu)}{h^{3N}N!} \iint \exp(-\beta\mathcal{H})\mathrm{d}\boldsymbol{r}^N\mathrm{d}\boldsymbol{p}^N = \sum_{N=0}^{\infty} \frac{z^N}{N!} Z_N \tag{5.48}$$

where $z = \exp(\beta\mu)/\Lambda^3$ is the activity. The definition of $f_0$ in the grand canonical ensemble means that $f_0$ is normalized as following:

$$\sum_{N=0}^{\infty} \frac{1}{h^{3N}N!} \iint f_0(\boldsymbol{r}^N, \boldsymbol{p}^N; N)\mathrm{d}\boldsymbol{r}^N\mathrm{d}\boldsymbol{p}^N = 1 \tag{5.49}$$

Here, the link between $\Omega$ and $\Xi$ is established by

$$\Omega = -k_\mathrm{B}T \ln \Xi \tag{5.50}$$

Let $p(N)$ represents the probability that a system of the ensemble contains $N$ particles, irrespective of their coordinates and momenta,

$$p(N) = \frac{1}{h^{3N}N!} \iint f_0(\boldsymbol{r}^N, \boldsymbol{p}^N; N)\mathrm{d}\boldsymbol{r}^N\mathrm{d}\boldsymbol{q}^N = \frac{1}{\Xi}\frac{z^N}{N!} Z_N \tag{5.51}$$

Then, the average number of particles in the system is

$$\langle N\rangle = \sum_{N=0}^{\infty} Np(N) = \frac{1}{\Xi}\sum_{N=0}^{\infty} N\frac{z^N}{N!}Z_N = \frac{z}{\Xi}\frac{\partial\Xi}{\partial z} = \frac{\partial \ln \Xi}{\partial \ln z} \tag{5.52}$$

A measure of the fluctuation in the number of particles about its average value is the mean-square deviation $\langle \Delta N^2\rangle$. $\langle \Delta N^2\rangle$ can be calculated by differenciating eq. (5.52) with respect to $\ln z$ as follows:

$$\begin{aligned}\frac{\partial \langle N\rangle}{\partial \ln z} &= z\frac{\partial}{\partial z}\left(\frac{1}{\Xi}\sum_{N=0}^{\infty} N\frac{z^N}{N!}Z_N\right)\\ &= \frac{1}{\Xi}\left(\sum_{N=0}^{\infty} N^2\frac{z^N}{N!}Z_N\right) - \left(\frac{1}{\Xi}\sum_{N=0}^{\infty} N\frac{z^N}{N!}Z_N\right)^2\\ &= \langle N^2\rangle - \langle N\rangle^2 = \langle \Delta N^2\rangle\end{aligned} \tag{5.53}$$

Using $\ln z = \beta\mu - 3\ln\Lambda$, eq. (5.53) becomes

$$\frac{\langle \Delta N^2\rangle}{\langle N\rangle} = \frac{k_{\mathrm{B}}T}{\langle N\rangle}\frac{\partial \langle N\rangle}{\partial \mu} \tag{5.54}$$

The ratio shown in eq. (5.54) is related to the isothermal compresibility $\chi_T$ defined as follows:

$$\chi_T = -\frac{1}{V}\left(\frac{\partial V}{\partial P}\right) \tag{5.55}$$

To show this, I express the Helmholtz free energy using the free energy par particle, $\phi(n,T)$ in the form

$$F = N\phi(n,T) \tag{5.56}$$

where the number density $n = N/V$. Using eq. (5.24),

$$\mu = \phi(n,T) + n\left(\frac{\partial\phi}{\partial n}\right)_T \tag{5.57}$$

$$\left(\frac{\partial\mu}{\partial n}\right)_T = 2\left(\frac{\partial\phi}{\partial n}\right)_T + n\left(\frac{\partial^2\phi}{\partial n^2}\right)_T \tag{5.58}$$

On the other hand,

$$P = n^2\left(\frac{\partial\phi}{\partial n}\right)_T \tag{5.59}$$

$$\begin{aligned}\left(\frac{\partial P}{\partial n}\right)_T &= \frac{1}{n\chi_T}\\ &= 2n\left(\frac{\partial\phi}{\partial n}\right) + n^2\left(\frac{\partial^2\phi}{\partial n^2}\right)_T\\ &= n\left(\frac{\partial\mu}{\partial n}\right)_T = N\left(\frac{\partial\mu}{\partial N}\right)_{V,T}\end{aligned} \tag{5.60}$$

From eq. (5.54), $\left\langle \Delta N^2 \right\rangle$ is related to $\chi_T$ as follows:

$$\frac{\left\langle \Delta N^2 \right\rangle}{\langle N \rangle} = n k_{\mathrm{B}} T \chi_T \tag{5.61}$$

In the grand canonical ensemble, the equilibrium $N'$-particle number density $n^{N'}(\boldsymbol{r}^{N'})$ is defined in terms of its canonical ensemble counterparts $n_N^{N'}(\boldsymbol{r}^{N'})$ (defined in eq. (5.34) as

$$\begin{aligned} n^{N'}(\boldsymbol{r}^{N'}) &\equiv \sum_{N \geq N'}^{\infty} p(N) \rho_N^{N'}(\boldsymbol{r}^{N'}) \\ &= \frac{1}{\Xi} \sum_{N \geq n}^{\infty} \frac{z^N}{(N-n)!} \int \exp(-\beta V_N) \mathrm{d}\boldsymbol{r}^{N-N'} \end{aligned} \tag{5.62}$$

Integrating eq. (5.62) over $\boldsymbol{r}_1, \boldsymbol{r}_2, \ldots, \boldsymbol{r}_{N'}$

$$\begin{aligned} \int n^{(N')}(\boldsymbol{r}^{N'}) \mathrm{d}\boldsymbol{r}^{N'} &= \sum_{N \geq n}^{\infty} p(N) \int n_N^{N'}(\boldsymbol{r}^{N'}) \mathrm{d}\boldsymbol{r}^{N'} \\ &= \left\langle \frac{N!}{(N-N')!} \right\rangle \end{aligned} \tag{5.63}$$

and in particular for $N' = 1$ and $N' = 2$,

$$\begin{aligned} \int n^{(1)}(\boldsymbol{r}) \mathrm{d}\boldsymbol{r} &= \langle N \rangle \\ \int n^{(2)}(\boldsymbol{r}_1, \boldsymbol{r}_2) \mathrm{d}\boldsymbol{r}_1 \mathrm{d}\boldsymbol{r}_2 &= \left\langle N^2 \right\rangle - \langle N \rangle \end{aligned} \tag{5.64}$$

The relation between the grand canonical $N'$-particle distribution function $g^{(N')}(\boldsymbol{r}^{N'})$ and the corresponding $N'$-particle density is the same as that introduced in the canonical ensemble:

$$\begin{aligned} g^{(N')}(\boldsymbol{r}^{N'}) &\equiv \frac{n^{(N')}(\boldsymbol{r}_1, \boldsymbol{r}_2, \ldots, \boldsymbol{r}_{N'})}{\Pi_{i=1}^{N'} n^{(1)}(\boldsymbol{r}_i)} \\ &= \frac{n^{(N')}(\boldsymbol{r}^{N'})}{n^{N'}} \quad \text{(for homogeneous system)} \end{aligned} \tag{5.65}$$

In the case of $N' = 2$, from eq. (5.62) and eq. (5.65),

$$g^{(2)}(\boldsymbol{r}_1, \boldsymbol{r}_2) = \frac{1}{n^2} \frac{1}{\Xi} \left[ z^2 \exp[-\beta V_N(\boldsymbol{r}_1, \boldsymbol{r}_2)] + z^3 \int \exp[-\beta V_N(\boldsymbol{r}_1, \boldsymbol{r}_2, \boldsymbol{r}_3) \mathrm{d}\boldsymbol{r}_3 + \cdots] \right] \tag{5.66}$$

As $n \to 0$, the chemical potential $\mu$ can be approximated by $\mu^{\mathrm{id}}$ (eq. (5.31)) and then $z \approx n \to 0$ and $\Xi \to 0$. Then we find that the low-density limit of the radial distribution function is equal to the Boltzmann factor of the pair potential $v(r)$:

$$\lim_{n \to 0} g(r) = \exp\left[-\beta v(r)\right] \tag{5.67}$$

In the grand canonical ensemble, the compressibility equation which expresses $\chi_T$ as an integral over $g(r)$ can be derived. The normalizations of eq. (5.64) show that

$$\iint [n^{(2)}(\boldsymbol{r}_1, \boldsymbol{r}_2) - n^{(1)}(\boldsymbol{r}_1) n^{(2)}(\boldsymbol{r}_2)] \mathrm{d}\boldsymbol{r}_1 \mathrm{d}\boldsymbol{r}_2 = \left\langle N^2 \right\rangle - \langle N \rangle - \langle N \rangle^2 \tag{5.68}$$

For the homogeneous system it follows that

$$1 + n \int [g(r) - 1] \, \mathrm{d}\boldsymbol{r} = \frac{\langle N \rangle^2 - \langle N \rangle^2}{\langle N \rangle} = n k_{\mathrm{B}} T \chi_T \tag{5.69}$$

Now, let $n(\boldsymbol{r})$ represents the microscopic particle density which is defined as a sum of $\delta$-function.

$$n(\boldsymbol{r}) = \sum_{i=1}^{N} \delta(\boldsymbol{r} - \boldsymbol{r}_i) \tag{5.70}$$

The average microscopic density at a point $\boldsymbol{r}$ corresponds to the single-particle density $n(\boldsymbol{r})$:

$$\langle n(\boldsymbol{r}) \rangle = n^{(1)}(\boldsymbol{r}) \tag{5.71}$$

Then, similarly to eq. (5.11), the autocorrelation function of $n(\boldsymbol{r}) - n^{(1)}(\boldsymbol{r})$, $\Gamma_n(\boldsymbol{r})$ is calculated as follows:

$$\begin{aligned}
\Gamma_n(\boldsymbol{r}) &= \int_V [n(\boldsymbol{r}') - n^{(1)}(\boldsymbol{r}')][n(\boldsymbol{r} + \boldsymbol{r}') - n^{(1)}(\boldsymbol{r} + \boldsymbol{r}')] \mathrm{d}\boldsymbol{r}' \\
&= V \left\langle \left[ n(\boldsymbol{r}') - n^{(1)}(\boldsymbol{r}') \right] \left[ n(\boldsymbol{r} + \boldsymbol{r}') - n^{(1)}(\boldsymbol{r} + \boldsymbol{r}') \right] \right\rangle \\
&= V \left[ \left\langle \sum_{i=1}^{N} \sum_{j=1}^{N} \delta(\boldsymbol{r}' - \boldsymbol{r}_i) \delta(\boldsymbol{r} + \boldsymbol{r}' - \boldsymbol{r}_j) \right\rangle - n^{(1)}(\boldsymbol{r}') n^{(1)}(\boldsymbol{r} + \boldsymbol{r}') \right] \\
&= V \left[ \left\langle \sum_{i=1}^{N} \sum_{j \neq i}^{N} \delta(\boldsymbol{r}' - \boldsymbol{r}_i) \delta(\boldsymbol{r} + \boldsymbol{r}' - \boldsymbol{r}_j) \right\rangle + \delta(\boldsymbol{r}) \left\langle \sum_{i=1}^{N} \delta(\boldsymbol{r}' - \boldsymbol{r}_i) \right\rangle - n^{(1)}(\boldsymbol{r}') n^{(1)}(\boldsymbol{r} + \boldsymbol{r}') \right] \\
&= V \left[ n^{(2)}(\boldsymbol{r}', \boldsymbol{r} + \boldsymbol{r}') + n^{(1)}(\boldsymbol{r}') \delta(\boldsymbol{r}) - n^{(1)}(\boldsymbol{r}') n^{(1)}(\boldsymbol{r} + \boldsymbol{r}') \right] \\
&= V \left[ n^2 (g(r) - 1) + n \delta(r) \right] \quad \text{(for isotropic and homogeneous systems.)}
\end{aligned} \tag{5.72}$$

where $r = |\boldsymbol{r}|$. I already showed that scattering intensity of a system is given by Fourier transform of the autocorrelation function of $\rho(\boldsymbol{r}) - \langle \rho \rangle$ where $\rho(\boldsymbol{r})$ and $\langle \rho \rangle$ are the scattering length density profile and the averaged scattering length density. From eq. (5.14), and eq. (5.72), we can derive the scattering intensity par unit volume,

$I_u(q)$ as follows:

$$\begin{aligned} I_u(q) &= \frac{1}{V}\int_V \Gamma_\eta(r)\exp(-i\boldsymbol{q}\cdot\boldsymbol{r})\mathrm{d}\boldsymbol{r} \\ &= \frac{1}{V}b^2\int_V \Gamma_n(r)\exp(-i\boldsymbol{q}\cdot\boldsymbol{r})\mathrm{d}\boldsymbol{r} \\ &= b^2n^2\int_V (g(r)-1)4\pi r^2\frac{\sin qr}{qr}\mathrm{d}r + nb^2 \end{aligned} \tag{5.73}$$

Where $b$ is the scattering length of a particle. At the limit of $q \to 0$, the scattering intensity is related to the isothermal compressibility by using eq. (5.69).

$$\begin{aligned} \lim_{q\to 0} I_u(q) &= b^2n^2\int_0^\infty (g(r)-1)4\pi r^2\mathrm{d}r + nb^2 \\ &= b^2n^2k_\mathrm{B}T\chi_T \end{aligned} \tag{5.74}$$

## X-ray Structural Analysis for Short Range Order in Amorphous Materials

Amorphous materials, such as liquids and solutions, do not have long-range order. Therefore, scattering spectra from amorphous look almost featureless compared with that from crystalline materials. Nevertheless, the scattering profiles from amorphous contain rich information about short-range order, for example concentration fluctuation, packing of molecules, and solvation structure. In this section, I summarize the method of X-ray scattering analysis on amorphous.

### In the Case of Single Atomic Species

Based on eq. (5.7), scattering intensity of X-ray from amorphous is given as

$$I(\boldsymbol{q}) = \left[b\sum_{j=1}^{N_\mathrm{e}}\exp[-i\boldsymbol{q}\cdot\boldsymbol{r}_j]\right]\left[b\sum_{k=1}^{N_\mathrm{e}}\exp[i\boldsymbol{q}\cdot\boldsymbol{r}_k]\right] \tag{5.75}$$

where $\boldsymbol{r}_j$ and $\boldsymbol{r}_k$ denote the positions of electrons. $N_\mathrm{e}$ and $b$ are the number of electrons in the irradiated volume and the scattering length of an electron, respectively. When $\boldsymbol{r}_j$ and $\boldsymbol{r}_k$ are regarded as the positions of atomic center, the equation is rewritten as follows:

$$I(\boldsymbol{q}) = \left[f(q)\sum_{j=1}^{N}\exp[-i\boldsymbol{q}\cdot\boldsymbol{r}_j]\right]\left[f(q)\sum_{k=1}^{N}\exp[i\boldsymbol{q}\cdot\boldsymbol{r}_k]\right] \tag{5.76}$$

Here, $N$ is the number of atoms in the irradiated volume. $f(q)$ is the atomic scattering factor which represents the scattering ability of atoms. $f(q)$ reflects the distribution

of electrons around the atomic center and thus it is $q$-dependent. Splitting the terms with $j = k$, we can write eq. (5.76) as

$$I(\boldsymbol{q}) = Nf(q)^2 + f(q)^2 \sum_{j=1}^{N} \sum_{k \neq j} \exp[-i\boldsymbol{q} \cdot \boldsymbol{r}_{jk}] \tag{5.77}$$

where $\boldsymbol{r}_{jk} = \boldsymbol{r}_j - \boldsymbol{r}_k$. The first term is the independent scattering intensity from $N$ atoms. Introducing the two-particle number density $n^{(2)}(\boldsymbol{r})$ that represents the average number of atoms included in a volume element $\mathrm{d}\boldsymbol{r}$ which is displaced by $\boldsymbol{r}$ from an atom. Then eq. (5.77) is written as

$$I(\boldsymbol{q}) = Nf(q)^2 + Nf(q)^2 \int_V n_2(\boldsymbol{r}) \exp[-i\boldsymbol{q} \cdot \boldsymbol{r}] \mathrm{d}\boldsymbol{r} \tag{5.78}$$

where the summation is replaced by the integral. $n^{(2)}(\boldsymbol{r})$ is related to the pair distribution function $g^{(2)}(\boldsymbol{r})$ as follows:

$$g^{(2)}(\boldsymbol{r}) = \frac{n^{(2)}(\boldsymbol{r})}{\langle n \rangle} \tag{5.79}$$

Then, eq. (5.78) can be further transformed as

$$\begin{aligned} I(\boldsymbol{q}) &= Nf(q)^2 + Nf(q)^2 \int_V \left( n^{(2)}(\boldsymbol{r}) - \langle n \rangle \right) \exp[-i\boldsymbol{q} \cdot \boldsymbol{r}] \mathrm{d}\boldsymbol{r} + Nf(q)^2 \langle n \rangle \delta(\boldsymbol{q}) \\ &= Nf(q)^2 + Nf(q)^2 \langle n \rangle \int_V \left( g^{(2)}(\boldsymbol{r}) - 1 \right) \exp[-i\boldsymbol{q} \cdot \boldsymbol{r}] \mathrm{d}\boldsymbol{r} \quad (\boldsymbol{q} \neq \boldsymbol{0}) \end{aligned} \tag{5.80}$$

The interference function between atoms is defined as follows:

$$i(\boldsymbol{q}) \equiv \frac{I(\boldsymbol{q}) - Nf(q)^2}{Nf(q)^2} = \langle n \rangle \int_V \left( g^{(2)}(\boldsymbol{r}) - 1 \right) \exp[-i\boldsymbol{q} \cdot \boldsymbol{r}] \mathrm{d}\boldsymbol{r} \tag{5.81}$$

Eq. (5.81) means that the radial distribution function of atoms, $g(\boldsymbol{r})$ can be evaluated by three-dimensional inverse Fourier transform of $i(\boldsymbol{q})$:

$$g^{(2)}(\boldsymbol{r}) - 1 = \frac{1}{(2\pi)^3 \langle n \rangle} \int_V i(\boldsymbol{q}) \exp[i\boldsymbol{q} \cdot \boldsymbol{r}] \mathrm{d}\boldsymbol{q} \tag{5.82}$$

For isotropic systems, $g^{(2)}(\boldsymbol{r})$ is simply equal to the radial distribution function $g(r)$ which is evaluated as follows:

$$g(r) - 1 = \frac{1}{2\pi^2 \langle n \rangle r} \int_0^\infty q i(q) \sin qr \mathrm{d}q \tag{5.83}$$

### In the Case of Polyatomic Species

When the system is composed of more than one atomic species, the relation between X-ray scattering profiles and radial distribution functions is more complicated than in the case of single atomic systems. For description of the structure of the polyatomic

system, one needs to introduce the partial pair distribution functions, $g^{(2)}_{\alpha\beta}(\boldsymbol{r})$ between $\alpha$ atoms and $\beta$ atoms, for example, $\alpha$ is carbons and $\beta$ is hydrogens. $g^{(2)}_{\alpha\beta}(\boldsymbol{r})$ is defined as follows:

$$g^{(2)}_{\alpha\beta}(\boldsymbol{r}) \equiv \frac{n^{(2)}_{\alpha\beta}(\boldsymbol{r})}{\langle n_\beta \rangle} \tag{5.84}$$

$n^{(2)}_{\alpha\beta}(\boldsymbol{r})\mathrm{d}\boldsymbol{r}$ denotes the number of $\beta$ atoms in the volume element $\mathrm{d}\boldsymbol{r}$ displaced from an arbitrary $\alpha$ atom by $\boldsymbol{r}$. Here, $n^{(2)}_{\alpha\beta}(\boldsymbol{r})$ is averaged for each $\alpha$ atoms in the system. $\langle n_\beta \rangle$ is the average number density of $\beta$ atoms. Obviously, $g^{(2)}_{\alpha\beta}(\boldsymbol{r}) = g^{(2)}_{\beta\alpha}(\boldsymbol{r})$. By using $n^{(2)}_{\alpha\beta}(\boldsymbol{r})$ and $g^{(2)}_{\alpha\beta}(\boldsymbol{r})$, eq. (5.76) is generalized as

$$\begin{aligned}
I(\boldsymbol{q}) &= \left[\sum_{j=1}^{N} f_j(q)\exp[-i\boldsymbol{q}\cdot\boldsymbol{r}_j]\right]\left[\sum_{k=1}^{N} f_k(q)\exp[-i\boldsymbol{q}\cdot\boldsymbol{r}_k]\right] \\
&= \sum_{j=1}^{N} N_j f_j(q)^2 + \sum_{j=1}^{N}\sum_{j\neq k} f_j(q) f_k(q)\exp[-i\boldsymbol{q}\cdot\boldsymbol{r}_{jk}] \\
&= \sum_{\alpha=1}^{m} N_\alpha f_\alpha(q)^2 + \sum_{\alpha=1}^{N} f_\alpha(q)\sum_{j=1}^{N_\alpha}\sum_{j\neq k} f_k(q)\exp[-i\boldsymbol{q}\cdot\boldsymbol{r}_{jk}] \\
&= \sum_{\alpha=1}^{m} N_\alpha f_\alpha(q)^2 + \sum_{\alpha=1}^{m} N_\alpha f_\alpha(q)\sum_{\beta=1}^{m} f_\beta(q)\int_V n^{(2)}_{\alpha\beta}(\boldsymbol{r})\exp[-i\boldsymbol{q}\cdot\boldsymbol{r}]\mathrm{d}\boldsymbol{r} \\
&= \sum_{\alpha=1}^{m} N_\alpha f_\alpha(q)^2 + \sum_{\alpha=1}^{m} N_\alpha f_\alpha(q)\sum_{\beta=1}^{m} f_\beta(q)\langle n_\beta\rangle\int_V \left(g^{(2)}_{\alpha\beta}(\boldsymbol{r})-1\right)\exp[-i\boldsymbol{q}\cdot\boldsymbol{r}]\mathrm{d}\boldsymbol{r} \\
&= N\sum_{\alpha=1}^{m} x_\alpha f_\alpha(q)^2 + N\langle n\rangle\sum_{\alpha=1}^{m}\sum_{\beta=1}^{m} x_\alpha x_\beta f_\alpha(q) f_\beta(q)\int_V \left(g^{(2)}_{\alpha\beta}(\boldsymbol{r})-1\right)\exp[-i\boldsymbol{q}\cdot\boldsymbol{r}]\mathrm{d}\boldsymbol{r}
\end{aligned} \tag{5.85}$$

where $f_\alpha(q)$ and $N_\alpha$ are the atomic scattering factor of $\alpha$ atoms and the number of $\alpha$ atoms in the irradiated volume. $m$ is the number of atomic species in the system. $x_\alpha$ is the atomic number fraction of $\alpha$ atoms. The null scattering terms were neglected in eq. (5.85). In the case of the polyatomic system, the interference factor $i(\boldsymbol{q})$ is often defined as follows:[3]

$$i(\boldsymbol{q}) \equiv \frac{I(\boldsymbol{q})/N - \sum_{\alpha=1}^{m} x_\alpha f_\alpha(q)^2}{\left[\sum_{\alpha=1}^{m} x_\alpha f_\alpha(q)\right]^2} \tag{5.86}$$

Assuming isotropic systems, the following equation can be derived.

$$\begin{aligned}
i(q) &= \langle n\rangle\sum_{\alpha=1}^{m}\sum_{\beta=1}^{m}\frac{x_\alpha x_\beta f_\alpha(q) f_\beta(q)}{\left[\sum_{\alpha=1}^{m} x_\alpha f_\alpha(q)\right]^2}\int_V \left(g^{(2)}_{\alpha\beta}(\boldsymbol{r})-1\right)\exp[-i\boldsymbol{q}\cdot\boldsymbol{r}]\mathrm{d}\boldsymbol{r} \\
&= \langle n\rangle\sum_{\alpha=1}^{m}\sum_{\beta=1}^{m}\frac{x_\alpha x_\beta f_\alpha(q) f_\beta(q)}{\left[\sum_{\alpha=1}^{m} x_\alpha f_\alpha(q)\right]^2}\int_0^\infty 4\pi r^2\left(g_{\alpha\beta}(r)-1\right)\frac{\sin qr}{qr}\mathrm{d}r
\end{aligned} \tag{5.87}$$

In the case of single atomic systems, inverse Fourier transformation of $i(q)$ is directly related to the radial distribution function of atoms (see eq. (5.83)). As can be seen from eq. (5.87), the situation is rather complicated in the polyatomic systems. Eq. (5.87) is rewritten as

$$i(q) = \sum_{\alpha=1}^{m} \sum_{\beta=1}^{m} x_\alpha x_\beta F_{\alpha\beta}(q) i_{\alpha\beta}(q) \tag{5.88}$$

by introducing the weighting factor $F_{\alpha\beta}(q)$ and the partial interference factor $i_{\alpha\beta}(q)$ defined as follows:

$$F_{\alpha\beta}(q) \equiv \frac{f_\alpha(q) f_\beta(q)}{\left[\sum_{\alpha=1}^{m} x_\alpha f_\alpha(q)\right]^2} \tag{5.89}$$

$$i_{\alpha\beta}(q) = \langle n \rangle \int_0^\infty 4\pi r^2 \left(g_{\alpha\beta}(r) - 1\right) \frac{\sin qr}{qr} \mathrm{d}r \tag{5.90}$$

Now, we define the apparent radial distribution function $G(r)$ as the three-dimensional inverse Fourier transform of $i(q)$.

$$G(r) - 1 \equiv \frac{1}{2\pi^2 \langle n \rangle r} \int_0^\infty q i(q) \sin qr \mathrm{d}q \tag{5.91}$$

Introducing $j_{\alpha\beta}(r)$ as the one-dimensional Fourier transform of $F_{\alpha\beta}(q)$ and using eq. (5.90), $G(r) - 1$ can be expressed as an weighed summation of convolution product of $r(g_{\alpha\beta}(r) - 1)$ and $j_{\alpha\beta}(r)$ as follows:

$$\begin{aligned} G(r) - 1 &= \frac{1}{2\pi^2 \langle n \rangle r} \sum_{\alpha=1}^{m} \sum_{\beta=1}^{m} x_\alpha x_\beta \int_0^\infty q F_{\alpha\beta}(q) i_{\alpha\beta}(q) \sin qr \mathrm{d}q \\ &= \frac{1}{r} \sum_{\alpha=1}^{m} \sum_{\beta=1}^{m} x_\alpha x_\beta j_{\alpha\beta}(r) * [r(g_{\alpha\beta}(r) - 1)] \end{aligned} \tag{5.92}$$

By assuming an approximation for the individual atomic scattering factors of each atom, one can simplify the interpretation of $G(r)$. For example, the following approximation is often utilized

$$f_\alpha(q) = K_\alpha f_\mathrm{e}(q) \tag{5.93}$$

where $K_\alpha$ is a constant coefficient whose value is close to the atomic number of $\alpha$ atom, $Z_\alpha$. $f_\mathrm{e}(q)$ is an average scattering factor per electron, typically estiamted as follows:

$$f_\mathrm{e}(q) = \frac{\sum f_\alpha(q)}{\sum Z_\alpha} \tag{5.94}$$

The summation are taken over a stoichiometric unit. Under the approximation as eq. (5.93), $F_{\alpha\beta}(q)$ becomes independent of $q$ and thus $j_{\alpha\beta}(r)$ becomes equal to a delta function. Then, eq. (5.92) can be simplified as follows:

$$G(r) - 1 = \sum_{\alpha=1}^{m} \sum_{\beta=1}^{m} x_\alpha x_\beta \frac{K_\alpha K_\beta}{[\sum x_\alpha K_\alpha]^2} \left(g_{\alpha\beta}(r) - 1\right) \tag{5.95}$$

Here, $G(r)$ is obtained as an appropriately weighed summation of the true partial radial distribution functions, $g_{\alpha\beta}(r)$s without convolution product terms. Hence, eq. (5.86) is a convenient definition of the interference factor for polyatomic systems.

### Experimental Determination of the Interference Factor

In actual experiments, the X-ray scattering intensity profiles is measured in arbitrary units. Thus, one needs to perform appropriate correction for the scattering profiles to obtain structural information. The observed X-ray scattering intensity $I_{\mathrm{obs}}(q)$ can be expressed by

$$I_{\mathrm{obs}}(q) = P(\theta)A(\theta)L(\theta)\left[I_{\mathrm{coh}}(q) + I_{\mathrm{Comp}}(q) + I_{\mathrm{cell}}(q)\right] \tag{5.96}$$

where $P(\theta)$ and $A(\theta)$ are the polarization factor and the absorption factor, respectively.[4] $L(\theta)$ is the geometric factor which depends on the experimental geometries of sample, detector, and the incident beam. When the detector moves on the concentric circles around sample, $L(\theta)$ becomes $\theta$-independent. $I_{\mathrm{coh}}(q)$ is the coherent scattering intensity per stoichiometric volume which corresponds to a normalized form of eq. (5.85). $I_{\mathrm{Comp}}(q)$ is the Compton scattering intensity from the sample and $I_{\mathrm{cell}}(q)$ is the scattering intensity of the sample cell.

#### Polarization Factor

Suppose a free electron is placed at position O and irradiated with polarized X-ray propagating in the direction of the $X$-axis, as in Figure 5.9. The detector is at the position $P$ at a distance of $R$ in the $XY$ plane. According to classical electromagnetic theory, $Y$ and $Z$ component of the scattered wave ($E_y$ and $E_z$, respectively) at $P$ is proportional to those of incident beam ($E_{0y}$ and $E_{0z}$) as follows:

$$E_z = E_{0z}\frac{e^2}{mc^2}\frac{1}{R} \tag{5.97}$$

$$E_y = E_{0y}\frac{e^2}{mc^2}\frac{\cos 2\theta}{R} \tag{5.98}$$

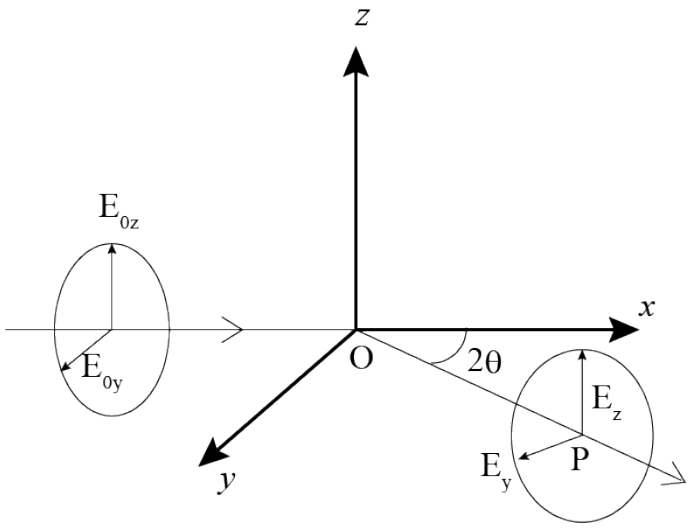


Figure 5.9: Scattering of X-ray by a single free electron at the origin, O.

where $e$ and $m$ are the electronic charge and mass. $c$ is the speed of light. Let $p$ represents the direction of the polarization on $YZ$ plane,

$$E_0^2 = E_{0y}^2 + E_{0z}^2 \tag{5.99}$$

$$E_{0y}^2 = (1-p)E_0^2,\ E_{0z}^2 = pE_0^2 \tag{5.100}$$

Then, the intensity of the scattered wave becomes

$$E^2 = E_y^2 + E_z^2 \tag{5.101}$$

$$= E_0^2 \left(\frac{e^2}{mc^2}\right)^2 \left[1 + (p-1)\sin^2 2\theta\right] \tag{5.102}$$

It is convenient to adopt eq. (5.102)-type $\theta$-dependence as $P(\theta)$ for the incident beam from a synchrotron radiation.

$$P(\theta) = 1 + (p-1)\sin^2 2\theta \tag{5.103}$$

**Absorption Factor**

Figure 5.10 shows a typical geometries of sample cell and the incident beam in the case of a symmetrical transmission technique, so-called $\theta - 2\theta$ scan. As shown, the effective irradiated volume by a beam of cross-sectional area $\Phi$ is equal to $\Phi \mathrm{d}x / \cos\theta$ in the layer of thickness $\mathrm{d}x$ at depth $x$. The length of X-ray path ($l$) is $l = (t_\mathrm{s} + 2t_\mathrm{c}) / \cos\theta$ where $t_\mathrm{s}$ and $t_\mathrm{c}$ are the thickness of the sample and the cell. Then, the following proportion relationship can be derived for the intensity of scattering ($\mathrm{d}I(2\theta, x)$) due

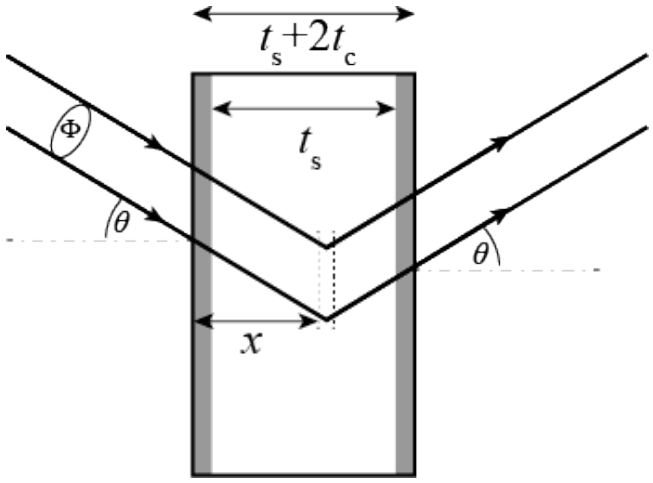


Figure 5.10: Illustration of the path of X-ray that passes through the sample filled in a planar-type sample cell. A symmetric scattering geometry is assumed here.

to the layer d$x$:

$$\mathrm{d}I(2\theta, x) \propto \begin{cases} P(\theta)\left(I_{\mathrm{coh}}(2\theta) + I_{\mathrm{Comp}}(2\theta)\right)\dfrac{\Phi \mathrm{d}x}{\cos\theta}\exp\left[-\dfrac{\mu_{\mathrm{s}}t_{\mathrm{s}} + 2\mu_{\mathrm{c}}t_{\mathrm{c}}}{\cos\theta}\right] & (t_{\mathrm{c}} \le x \le t_{\mathrm{s}} + t_{\mathrm{c}}) \\ P(\theta)I_{\mathrm{cell}}(2\theta)\dfrac{\Phi \mathrm{d}x}{\cos\theta}\exp\left[-\dfrac{\mu_{\mathrm{s}}t_{\mathrm{s}} + 2\mu_{\mathrm{c}}t_{\mathrm{c}}}{\cos\theta}\right] & (0 \le x < t_{\mathrm{c}},\ t_{\mathrm{s}} + t_{\mathrm{c}} < x \le t_{\mathrm{c}} + 2t_{\mathrm{c}}) \end{cases} \tag{5.104}$$

where $\mu_{\mathrm{s}}$ and $\mu_{\mathrm{c}}$ are the linear absorption coefficient of the sample and the cell. $\mu_{\mathrm{s}}$ can be calculated by using the number density of $\alpha$ atoms in the sample, $n_\alpha$ and the absorption cross section of an $\alpha$ atom, $\sigma_{\alpha,\mathrm{abs}}$.

$$\mu_{\mathrm{s}} = \sum_\alpha \sigma_{\alpha,\mathrm{abs}} n_\alpha \tag{5.105}$$

Here, $\sigma_{\alpha,\mathrm{abs}}$ is defined as the number of photons absorbed per unit of time by an atom, devided by the flux of the incident beam, and it is listed in literature.[5] Integrating eq. (5.104) from $x = 0$ to $x = t_{\mathrm{s}} + 2t_{\mathrm{c}}$,

$$I(2\theta) \propto P(\theta)\frac{\Phi}{\cos\theta}\exp\left[-\frac{\mu_{\mathrm{s}}t_{\mathrm{s}} + 2\mu_{\mathrm{c}}t_{\mathrm{c}}}{\cos\theta}\right]\left[t_{\mathrm{s}}I_{\mathrm{coh}}(q) + t_{\mathrm{s}}I_{\mathrm{Comp}}(q) + 2t_{\mathrm{c}}I_{\mathrm{cell}}(q)\right] \tag{5.106}$$

and thus the absorption factor $A(\theta)$ is given as

$$A(\theta) = \frac{1}{\cos\theta}\exp\left[-\frac{\mu_{\mathrm{s}}t_{\mathrm{s}} + 2\mu_{\mathrm{c}}t_{\mathrm{c}}}{\cos\theta}\right] \tag{5.107}$$

Similarly, a measurement of the empty cell gives an attenuated scattering intensity of the sample cell, $I_{\mathrm{cell}}^{\mathrm{obs}}(q)$ as

$$I_{\mathrm{cell}}^{\mathrm{obs}}(q) \propto P(\theta)\frac{2t_{\mathrm{c}}}{\cos\theta}\exp\left[-\frac{2\mu_{\mathrm{c}}t_{\mathrm{c}}}{\cos\theta}\right]I_{\mathrm{cell}}(q) \tag{5.108}$$

When the energy of the incident beam is high and $t_c$ is sufficiently small, the $\mu_c t_c$ term becomes negligible and thus

$$I(2\theta) \propto P(\theta)A(\theta)\left[t_s I_{coh}(q) + t_s I_{Comp}(q) + 2t_c I_{cell}(q)\right] \tag{5.109}$$

$$A(\theta) \approx \frac{1}{\cos\theta}\exp\left[-\frac{\mu_s t_s}{\cos\theta}\right] \tag{5.110}$$

$$2t_c I_{cell}(q) \approx \frac{\cos\theta}{P(\theta)} I_{cell}^{obs}(q) \tag{5.111}$$

**Calculation of the Interference Factor and the Radial Distribution Function**

After the correction for $P(\theta)$, $A(\theta)$, and $I_{cell}$, one obtain a corrected scattering intensity as follows;

$$I_{cor}(q) = k\left[I_{coh}(q) + I_{Comp}(q)\right] \tag{5.112}$$

where $k$ is a $q$-independent scaling factor. $I_{coh}(q)$ should converge to the independent scattering of atoms (the first term in eq. (5.85)) at high-$q$ where the interference between scattering waves from different atoms are smeared out.

$$I_{cor}(q) \approx k\left[N^s \sum_{\alpha=1}^{m} x_\alpha f_\alpha(q)^2 + N^s \sum_{\alpha=1}^{m} x_\alpha I_{\alpha,Comp}(q)\right] \tag{5.113}$$

Here, $N^s$ is the averaged number of atoms in the stoichiometric volume. The theoretical values of the atomic scattering factor for atoms can be approximated by an analytical form as

$$f_\alpha(q) = \sum_{i=1} A_{i,\alpha}\exp\left(-B_{i,\alpha}\left(\frac{q}{4\pi}\right)^2\right) + C_\alpha \tag{5.114}$$

where the parameters $A_{i,\alpha}$, $B_{i,\alpha}$, and $C_\alpha$ are listed in literature, for example "International Tables for X-ray Crystallography Vol. C".[6] The compton scattering intensity of atoms are also listed in literature[7,8] and the following approximated form is available.[1]

$$I_{\alpha,comp}(q) \approx r_e^2\left[Z_\alpha - \frac{f(q)^2}{Z_\alpha}\right]\left(\frac{\lambda}{\lambda'}\right)^3 \tag{5.115}$$

Here, $r_e = \sqrt{e^2/mc^2}$ is the classical radius of the electron. The factor $(\lambda/\lambda')^3$ is called the Breit-Dirac recoil factor which arise from the change in the wavelength on scattering. Thus, one can calculate the terms on the RHS of eq. (5.113) based on chemical composition of the sample, and the normalization factor $k$ can be estimated by comparing the experimental $I_{cor}(q)$ and the calculated value at high-$q$. Eventually,

$I_{\mathrm{coh}}(q)$ is scaled to the absolute scale and then the experimental interference factor $i^{\mathrm{exp}}(q)$ can be obtained as

$$i^{\mathrm{exp}}(q) = \frac{I_{\mathrm{coh}}(q)/N^{\mathrm{s}} - \sum_{\alpha=1}^{m} x_\alpha f_\alpha(q)^2}{\left[\sum_{\alpha=1}^{m} x_\alpha f_\alpha(q)\right]^2} \tag{5.116}$$

Theoretically, the radial distrubution function is calculated by inverse Fourier transform of $i(q)$ which calls for $i(q)$ values from $q = 0$ to $q = \infty$ (see eq. (5.91)). However, there is the upper limit of $q$ ($= q_{\max}$) in the experimental determination of $i^{\mathrm{exp}}(q)$. Inverse Fourier transformation of $i^{\mathrm{exp}}(q)$ at the limited $q$-range results in unrealistic high frequency oscillation in the radial distribution function, which is called truncation effect. Such truncation effect can be suppressed by an appropriate modification of $i^{\mathrm{exp}}(q)$ in high-$q$ region. Then, the experimental radial distribution function $G^{\mathrm{exp}}(r)$ is calculated as follows:

$$G^{\mathrm{exp}}(r) - 1 = \frac{1}{2\pi^2 \langle n \rangle r} \int_0^{q_{\max}} q i^{\mathrm{exp}}(q) \sin qr M(q) \mathrm{d}q \tag{5.117}$$

The modification functions, $M(q)$ need to be equal to unity at $q = 0$ but smoothly deceases to zero as $q$ approches $q_{\max}$. Several functional forms of $M(q)$ have been proposed, for example

$$M(q) = \frac{\sin(\pi q/q_{\max})}{\pi q/q_{\max}} \tag{5.118}$$

which is called Lorch modification function.[9]

### Comparison with Molecular Dynamics Simulations

For the discussion of the structure of polyatomic systems, the partial radial distribution function $g_{\alpha\beta}(r)$ is necessary. However, as described above, what we can obtain from X-ray scattering experiment is only the apparent radial distribution function, $G(r)$. $G(r)$ is a kind of weighed summation of $g_{\alpha\beta}(r)$s and thus it is impossible to evaluate an individual $g_{\alpha\beta}(r)$ from the experiments. Molecular dynamics (MD) simulation is one of the powerful tool to evaluate $g_{\alpha\beta}(r)$. $g_{\alpha\beta}(r)$ can be calculated from MD trajectories of atoms as follows:

$$g_{\alpha\beta}^{\mathrm{MD}}(r) = \begin{cases} \dfrac{1}{4\pi r^2 \Delta r} \dfrac{V}{N_\alpha (N_\beta - 1)} \left\langle \displaystyle\sum_{m=1}^{N_\alpha} \Delta N_m^{\alpha\beta}(r) \right\rangle & (\alpha = \beta) \\ \dfrac{1}{4\pi r^2 \Delta r} \dfrac{V}{N_\alpha N_\beta} \left\langle \displaystyle\sum_{m=1}^{N_\alpha} \Delta N_m^{\alpha\beta}(r) \right\rangle & (\alpha \neq \beta) \end{cases} \tag{5.119}$$

Here, $V$ denotes the volume of the MD cell. $N_\alpha$ is the number of $\alpha$ atoms in the MD cell. $\Delta N_m^{\alpha\beta}(r)$ is the number of $\beta$-atoms in the spherical shell of radius $r$ and thickness $\Delta r$ centered on a $m$ th $\alpha$-atom. For comparison with scattering experiments, the interference factor $i^{\mathrm{MD}}(q)$ can be calculated according to eq. (5.87).

$$i^{\mathrm{MD}}(q) = \langle n \rangle \frac{\sum_\alpha \sum_\beta w_{\alpha\beta}(q)}{\left[\sum_\alpha \left(N_\alpha f_\alpha(q)/N\right)\right]^2} \int_0^{r_{\max}} 4\pi r^2 \left(g_{\alpha\beta}^{\mathrm{MD}}(r) - 1\right) \frac{\sin qr}{qr} \mathrm{d}r \tag{5.120}$$

Here, the weighting factor $w_{\alpha\beta}(q)$ is defined as follows.

$$w_{\alpha\beta}(q) \equiv \begin{cases} N_\alpha (N_\beta - 1) f_\alpha(q) f_\beta(q)/N(N-1) & (\alpha = \beta) \\ N_\alpha N_\beta f_\alpha(q) f_\beta(q)/N^2 & (\alpha \neq \beta) \end{cases} \tag{5.121}$$

The apparent radial distribution function $G^{\mathrm{MD}}(r)$ is obtained by the same manner as the experimental $G(r)$ (eq. 5.117).

$$G^{\mathrm{MD}}(r) - 1 = \frac{1}{2\pi^2 r \langle n \rangle} \int_0^{q_{\max}} q i^{\mathrm{MD}}(q) \sin(qr) M(q) \mathrm{d}q \tag{5.122}$$

As a first step, one need to check the validity of trajectories of atoms obtained from MD simulation by comparing experimental scattering functions ($i^{\mathrm{exp}}(q)$ and $G(r)^{\mathrm{exp}}$) and calculated ones ($i^{\mathrm{MD}}(q)$ and $G(r)^{\mathrm{MD}}$). After confirming that MD simulations reproduce experimental scattering functions, detailed structure of the systems can be analyzed based on the MD trajectories: for example, coordination distance, three dimensional distribution of components, and orientation of the molecular interactions.

## Small-Angle Scattering[1,10]

Small-angle X-ray scattering (SAXS) and small-angle neutron scattering (SANS) experiments allow as to evaluate mesoscopic (typically 1 – 1000 nm scale) structures of materials. As the name indicates, scattering angle $2\theta$ is very small in small-angle scattering experiments; the typical value of $2\theta$ is less than $2^\circ$. Thus one can obtain scattering profiles of materials at very low-$q$ range which corresponds to large size scale in real space. Although the basic principles discussed in the previous sections are also applicable, there are theoretical results that have been developed specifically for small-angle scattering. Large parts of the theories are based on common assumptions that are only appricable to small-angle scattering: for example, any structures smaller than 1 nm are neglected. Thus, solvent molecules in polymer solutions or particle dispersion systems are regarded as continuous medium in small-angle scattering: solvent properties are taken into account via intermolecular interference or excluded volume of solutes. Furthermore, in the case of SAXS, we can neglect $q$-dependence of the atomic scattering factor $f(q)$, the absorption factor, the polarization factor, and Compton scattering because $q$-range of SAXS is usually very narrow; typically $q = 10^{-3}$ – $10^{-1}$ Å$^{-1}$. In this section, I will derive small-angle scattering functions of several systems.

### Independent Scattering

In sufficiently dilute solution, the positions of the solutes are uncorrelated so that the scattered waves by different particles are incoherent. Then the overall scattering intensity is simply the sum of the scattering from individual solutes. The independent scattering functions are derived for solutes having various shapes.

#### Hard Sphere

The simplest example of the derivation is for a solid sphere. The scattering length density $\rho(\boldsymbol{r})$ of a solid sphere of radius $R$ is given by

$$\rho(r) = \begin{cases} \rho_0 & (r \leq R) \\ 0 & (r > R) \end{cases} \tag{5.123}$$

Scattering wave from a solid sphere $A(q)$ is then calculated as

$$\begin{aligned} A(q) &= \int_V \rho(r) \exp\left[-i\boldsymbol{q}\cdot\boldsymbol{r}\right] \mathrm{d}\boldsymbol{r} \\ &= \int_0^\infty \rho(r) 4\pi r^2 \frac{\sin qr}{qr} \mathrm{d}r \\ &= \rho_0 v \frac{3\left(\sin qR - qR\cos qR\right)}{(qR)^3} \quad \left(v \equiv \frac{4}{3}\pi R^3\right) \end{aligned} \tag{5.124}$$

Therefore the scattering intensity $I(q)$ is

$$I(q) = \rho_0^2 v^2 \frac{9\left(\sin qR - qR\cos qR\right)^2}{(qR)^6} \tag{5.125}$$

**Core-shell Cylinder**

The similar calculation procedure is applicable for particles having more complicated shape. Now we consider the scattering function of a "core-shell" cylinder.[11] As shown

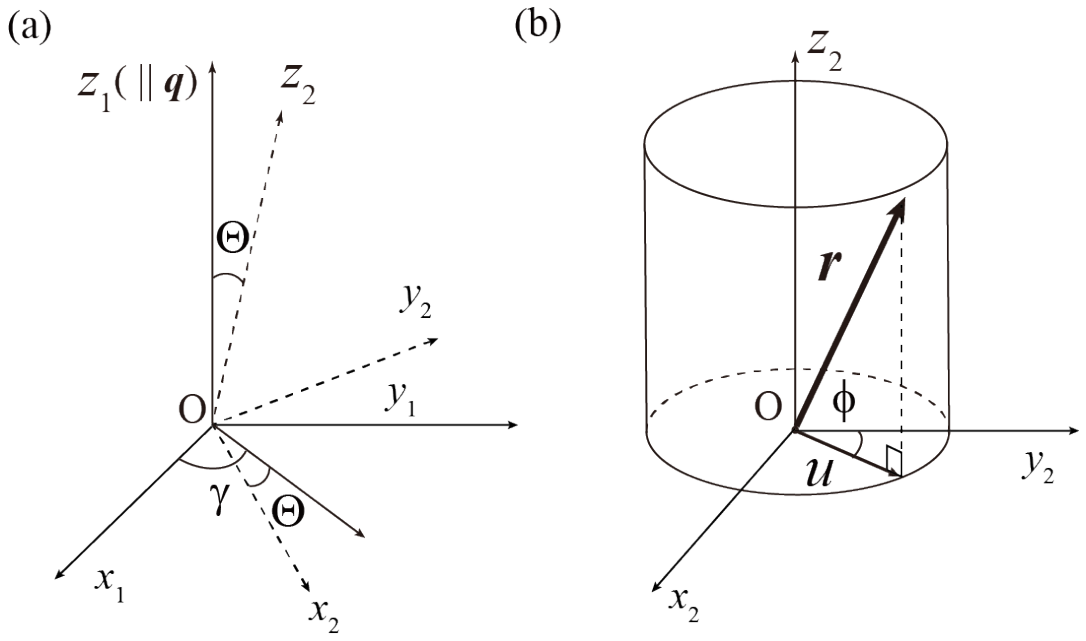


Figure 5.11: (a) Space fixed system of coordinates ($\boldsymbol{z}_1 \parallel \boldsymbol{q}$), $O_{x_1y_1z_1}$ and (b) cylindrical coordinates system, $O_{x_2y_2z_2}$.

in Figure 5.11, we assume that the core-shell cylinder of length $L$ is oriented to the direction which is defined by $\Theta$ and $\gamma$: $\Theta$ is the angle formed by $\boldsymbol{q}$ and the orientation vector of the cylinder, $\boldsymbol{z}_2$. The scattering wave $A_{\mathrm{cyl}}(\boldsymbol{q}, \Theta, \gamma)$ from the cylinder is

$$A_{\mathrm{cyl}}(\boldsymbol{q}, \Theta, \gamma) = \int_V \rho(\boldsymbol{r}) \exp\left[-i\boldsymbol{q}\cdot\boldsymbol{r}\right] \mathrm{d}\boldsymbol{r}$$

Now we consider a cartesian coordinates system $O_{x_1y_1z_1}$ and a cylindrial coordinates system $O_{x_2y_2z_2}$. Here, $O_{x_1y_1z_1}$ and $O_{x_2y_2z_2}$ have unit vectors $\boldsymbol{i}_1$, $\boldsymbol{j}_1$, $\boldsymbol{k}_1$, and $\boldsymbol{i}_2$, $\boldsymbol{j}_2$,

$\boldsymbol{k}_2$, respectively. $\boldsymbol{k}_1$ is set to be parallel to $\boldsymbol{q}$ and thus the following relationship is obtained

$$\boldsymbol{q} = q\boldsymbol{k}_1 = q\left\{-\boldsymbol{i}_2 \sin\Theta + \boldsymbol{k}_2 \cos\Theta\right\} \tag{5.126}$$

$$\boldsymbol{r} = x_2\boldsymbol{i}_2 + y_2\boldsymbol{j}_2 + z_2\boldsymbol{k}_2 \tag{5.127}$$

$$x_2 = u\sin\phi, \quad y_2 = u\cos\phi, \quad z_2 = z_2 \tag{5.128}$$

Therefore,

$$\boldsymbol{q}\cdot\boldsymbol{r} = -uq\sin\phi\sin\Theta + qz_2\cos\Theta \tag{5.129}$$

For the core-shell cylinder of the core radius $R_{\mathrm{core}}$ and the outer radius $R_{\mathrm{out}}$, $\rho(\boldsymbol{r})$ is given as

$$\rho(\boldsymbol{r}) = \begin{cases} \rho_1 - \rho_0 & (0 < u \le R_{\mathrm{core}}, |z_2| \le \frac{L}{2}) \\ \rho_2 - \rho_0 & (R_{\mathrm{core}} < u \le R_{\mathrm{out}}, |z_2| \le \frac{L}{2}) \\ 0 & (u > b \text{ or } |z_2| > \frac{L}{2}) \end{cases} \tag{5.130}$$

where $\rho_1$, $\rho_2$, and $\rho_0$ are the scattering length density of the core layer, the shell layer and solvent, respectively. Using the following equations, eq. (5.126) becomes

$$\begin{aligned}
A_{\mathrm{cyl}}(\boldsymbol{q},\Theta,\gamma) &= (\rho_1-\rho_0)\int_{-\frac{L}{2}}^{\frac{L}{2}}\int_0^{2\pi}\int_0^a u\exp\left[-i\boldsymbol{q}\cdot\boldsymbol{r}\right]\mathrm{d}u\mathrm{d}\phi\mathrm{d}z_2 \\
&\qquad + (\rho_2-\rho_0)\int_{-\frac{L}{2}}^{\frac{L}{2}}\int_0^{2\pi}\int_a^b u\exp\left[-i\boldsymbol{q}\cdot\boldsymbol{r}\right]\mathrm{d}u\mathrm{d}\phi\mathrm{d}z_2 \\
&= (\rho_1-\rho_2)\int_{-\frac{L}{2}}^{\frac{L}{2}}\int_0^{2\pi}\int_0^a u\exp\left[-i\boldsymbol{q}\cdot\boldsymbol{r}\right]\mathrm{d}u\mathrm{d}\phi\mathrm{d}z_2 \\
&\qquad + (\rho_2-\rho_0)\int_{-\frac{L}{2}}^{\frac{L}{2}}\int_0^{2\pi}\int_0^b u\exp\left[-i\boldsymbol{q}\cdot\boldsymbol{r}\right]\mathrm{d}u\mathrm{d}\phi\mathrm{d}z_2 \\
&= (\rho_1-\rho_2)\int_{-\frac{L}{2}}^{\frac{L}{2}}\exp\left[-iqz_2\cos\Theta\right]\mathrm{d}z_2\int_0^a\int_0^{2\pi} u\exp\left[iqu\sin\phi\sin\Theta\right]\mathrm{d}\phi\mathrm{d}u \\
&\quad + (\rho_2-\rho_0)\int_{-\frac{L}{2}}^{\frac{L}{2}}\exp\left[-iqz_2\cos\Theta\right]\mathrm{d}z_2\int_0^b\int_0^{2\pi} u\exp\left[iqu\sin\phi\sin\Theta\right]\mathrm{d}\phi\mathrm{d}u \\
&= (\rho_1-\rho_2)\,\pi R_{\mathrm{core}}^2 L F_{\mathrm{z}}(q,\Theta)F_{CS}(R_{\mathrm{core}},q,\Theta) \\
&\qquad + (\rho_2-\rho_0)\,\pi R_{\mathrm{out}}^2 L F_{\mathrm{z}}(q,\Theta)F_{CS}(R_{\mathrm{out}},q,\Theta) \\
&= LF_{\mathrm{z}}(q,\Theta)[(\rho_1-\rho_2)\,\pi R_{\mathrm{core}}^2 F_{CS}(R_{\mathrm{core}},q,\Theta) \\
&\qquad + (\rho_2-\rho_0)\,\pi R_{\mathrm{out}}^2 F_{CS}(R_{\mathrm{out}},q,\Theta)]
\end{aligned} \tag{5.131}$$

The contribution from longitudinal part and cross sectional one, $F_{\rm z}(q,\Theta)$ and $F_{CS}(R,q,\Theta)$ respectively, is given as

$$\begin{aligned} F_{\rm z}(q,\Theta) &\equiv \frac{1}{L}\int_{-\frac{L}{2}}^{\frac{L}{2}} \exp\left[-iqz\cos\Theta\right]{\rm d}z \\ &= \frac{\sin\left(qL\cos\Theta/2\right)}{qL\cos\Theta/2} \end{aligned} \tag{5.132}$$

$$\begin{aligned} F_{CS}(R,q,\Theta) &\equiv \frac{1}{\pi R^2}\int_0^R\int_0^{2\pi} u\exp\left[iqu\sin\phi\sin\Theta\right]{\rm d}\phi{\rm d}u \\ &= \frac{2}{R^2}\int_0^R uJ_0\left(qu\sin\Theta\right){\rm d}u \\ &= \frac{2}{R^2}\int_0^1 tJ_0\left(qRt\sin\Theta\right){\rm d}t \quad \left(t\equiv\frac{r}{R}\right) \\ &= \frac{2J_1\left(qR\sin\Theta\right)}{qR\sin\Theta} \end{aligned} \tag{5.133}$$

$J_0(x)$ and $J_1(x)$ are the zeroth-order and the first order Bessel function defined as follows:

$$J_0(x) \equiv \frac{1}{\pi}\int_0^\pi \exp\left[ix\cos\phi\right]{\rm d}\phi \tag{5.134}$$

$$\frac{1}{x}J_1(x) \equiv \int_0^1 tJ_0(xt){\rm d}t \tag{5.135}$$

When the orientation of the cylinder is isotropic, $I_{\rm cyl}(q)$ is calculated by taking orentational average with respect to $\Theta$ and $\gamma$.

$$\begin{aligned} I_{\rm cyl}(q) &= \frac{\displaystyle\int_0^{2\pi}\int_0^\pi \left|A_{\rm cyl}(\boldsymbol{q},\Theta,\gamma)\right|^2\sin\Theta{\rm d}\Theta{\rm d}\gamma}{\displaystyle\int_0^{2\pi}\int_0^\pi \sin\Theta{\rm d}\Theta{\rm d}\gamma} \\ &= \frac{1}{2}\int_0^\pi \left|A_{\rm cyl}(\boldsymbol{q},\Theta,\gamma)\right|^2\sin\Theta{\rm d}\Theta \end{aligned} \tag{5.136}$$

For a particle with $L \gg R$, $F_z(q,\Theta)$ term only contributes when $\cos\Theta$ is small (when $\Theta = \pi/2$) and we can approximate $\sin\alpha$ by $\sin(\pi/2) = 1$ in the cross sectional contribution term. Then, eq. (5.136) becomes

$$\begin{aligned} I_{\rm cyl}(q) &\approx \frac{1}{2}L^2\int_0^\pi F_{\rm z}^2(q,\Theta)\sin\Theta{\rm d}\Theta[(\rho_1-\rho_2)\,\pi R_{\rm core}^2 F_{CS}(R_{\rm core},q,\pi/2) \\ &\qquad + (\rho_2-\rho_0)\,\pi R_{\rm out}^2 F_{CS}(R_{\rm out},q,\pi/2)]^2 \\ &= L^2\frac{2}{qL}\left[\int_0^{qL}\frac{\sin x}{x}{\rm d}x - \frac{2\sin^2(qL/2)}{(qL)^2}\right] \\ &\qquad \left[(\rho_1-\rho_2)\,\pi R_{\rm core}^2\frac{2J_1(qR_{\rm core})}{qR_{\rm core}} + (\rho_2-\rho_0)\,\pi R_{\rm out}^2\frac{2J_1(qR_{\rm out})}{qR_{\rm out}}\right]^2 \end{aligned} \tag{5.137}$$

**Gaussian Chain**

First of all, I introduce the radius of gyration, $R_{\rm g}$ as a measure for the size of a polymer chain. For the polymer chain consisting of $z$ identical segments, $R_{\rm g}$ is given by

$$R_{\rm g}^2 = \frac{1}{z}\sum_{j=1}^{z}\left\langle (\boldsymbol{r}_j - \boldsymbol{r}_{\rm G})^2 \right\rangle \tag{5.138}$$

where $\boldsymbol{r}_{\rm G}$ is the position of the center of mass of the polymer. $\langle \dots \rangle$ means ensemble average. As is clear from the definition of $\boldsymbol{r}_{\rm G}$,

$$\begin{aligned}\sum_{j=1}^{N}\sum_{i=1}^{N}\left\langle (\boldsymbol{r}_i - \boldsymbol{r}_j)^2 \right\rangle &= \sum_{j=1}^{N}\sum_{i=1}^{N}\left\langle [(\boldsymbol{r}_i - \boldsymbol{r}_{\rm G}) - (\boldsymbol{r}_j - \boldsymbol{r}_{\rm G})]^2 \right\rangle \\ &= 2z\sum_{i=1}^{N}\left\langle (\boldsymbol{r}_i - \boldsymbol{r}_{\rm G})^2 \right\rangle - 2\sum_{j=1}^{N}\sum_{i=1}^{N}\langle (\boldsymbol{r}_i - \boldsymbol{r}_{\rm G})\cdot(\boldsymbol{r}_i - \boldsymbol{r}_{\rm G})\rangle \\ &= 2z\sum_{i=1}^{N}\left\langle (\boldsymbol{r}_i - \boldsymbol{r}_{\rm G})^2 \right\rangle \end{aligned} \tag{5.139}$$

and thus

$$R_{\rm g} = \frac{1}{2z^2}\sum_{j=1}^{N}\sum_{i=1}^{N}\left\langle (\boldsymbol{r}_i - \boldsymbol{r}_j)^2 \right\rangle \tag{5.140}$$

When $q \ll R_{\rm g}^{-1}$ and the system is dilute, the following Guinier law can be used to estimate $R_{\rm g}$ irrespective of the shape of the solutes.

$$I(q) \approx \rho_0^2 v^2 \exp\left[-\frac{1}{3}q^2 R_g^2\right] \tag{5.141}$$

Here, $\rho_0$ and $v$ is the scattering length density and the volume of the solute.

One can calculate $R_{\rm g}$ of a Gaussian chain consisting of $z$ segments as below. When one end of the chain is at the origin, the probability density $w(p, r)$ that the $p$ th segment is found at distance $r$ is given by the Gaussian approximation

$$w(p, r) = \left(\frac{3}{2\pi p l^2}\right)^{3/2}\exp\left[-\frac{3r^2}{2pl^2}\right] \tag{5.142}$$

where $l$ is the length between each segment. Then, the mean square distance between two monomers $(\boldsymbol{r}_1, \boldsymbol{r}_2)$ separated by $p_2$ segments is calculated as follows:

$$\begin{aligned}\left\langle (\boldsymbol{r}_1 - \boldsymbol{r}_2)^2 \right\rangle &= \int (\boldsymbol{r}_1 - \boldsymbol{r}_2)^2\, w(p_2, |\boldsymbol{r}_1 - \boldsymbol{r}_2|)\mathrm{d}(\boldsymbol{r}_1 - \boldsymbol{r}_2) \\ &= p_2 l^2 \end{aligned} \tag{5.143}$$

One can calculate $R_{\rm g}$ of the whole chain placing $\boldsymbol{r}_1$ at the $p_1$ th segment and $\boldsymbol{r}_2$ at the

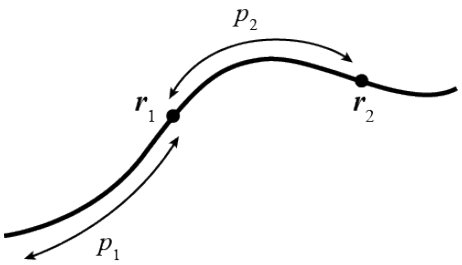


Figure 5.12: Two points, $\boldsymbol{r}_1$ at $p_1$ th segment and $\boldsymbol{r}_2$ at $p_1 + p_2$ th segment of a Gaussian chain.

$p_1 + p_2$ segment on the chain, respectively and then taking average of $\left\langle (\boldsymbol{r}_1 - \boldsymbol{r}_2)^2 \right\rangle$ with respect to $p_1$ and $p_2$ (Figure 5.12). Using eq. (5.140),

$$R_{\mathrm{g}}^2 = \frac{1}{2z^2} 2 \int_0^z \mathrm{d}p_1 \int_0^{z-p_1} \mathrm{d}p_2 \left\langle (\boldsymbol{r}_1 - \boldsymbol{r}_2)^2 \right\rangle = \frac{z^2 l}{6} \tag{5.144}$$

We now consider the scattering function of a Gaussian chain. Based on eq. (5.7), the scattering intensity from a Gaussian chain $I(q)$ is given by

$$I(q) = \rho_0^2 v_u^2 \sum_{j=1}^{z} \sum_{k=1}^{z} \exp\left[-i\boldsymbol{q} \cdot \boldsymbol{r}_{jk}\right] \tag{5.145}$$

where $\boldsymbol{r}_{jk} = \boldsymbol{r}_j - \boldsymbol{r}_k$ and $v_u$ is the volume of each segment. Replacing the summation by an integration,

$$I(q) = \rho_0^2 v_u^2 \int_V N(r) \exp\left[-i\boldsymbol{q} \cdot \boldsymbol{r}_{jk}\right] \mathrm{d}\boldsymbol{r} \tag{5.146}$$

$N(r)$ represents the number of bead pairs that have their members separated from each other by $\boldsymbol{r}$, and is related to $w(p, r)$ as follows:

$$N(r) = \sum_{K=1}^{z} 2(z - K) w(K, r) \tag{5.147}$$

Here, the factor $2(z - K)$ denotes the number of pairs separated by $K$ segments. Substituting eq. (5.147) into eq. (5.146) and approximating the summation by an integration,

$$\begin{aligned} I(q) &= 2\rho_0^2 v_u^2 \sum_{K=0}^{z} (z - K) \exp\left[-K \frac{q^2 l^2}{6}\right] \\ &= 2\rho_0^2 v_u^2 z \sum_{K=0}^{z} (1 - u) \exp\left[-u \frac{z q^2 l^2}{6}\right] \quad \left(u \equiv \frac{K}{z}\right) \\ &= 2\rho_0^2 v_u^2 z^2 \int_0^1 (1 - u) \exp\left[-u \frac{z q^2 l^2}{6}\right] \mathrm{d}u \\ &= \rho_0^2 v_u^2 z^2 D(x) \end{aligned} \tag{5.148}$$

where $D(x)$, so-called Debye function, is defined as

$$D(x) = \frac{2}{x^2}\left[\exp(-x) + x - 1\right] \quad \left(x \equiv \frac{zq^2l^2}{6} = q^2R_g^2\right) \tag{5.149}$$

### Scattering from Polymer Solutions

Scattering from polymer solutions can not be described by an simple summation of independent scattering from polymer chains: it is affected by an interchain interference effects. As derived later, the interference effects reflects solvent quality for polymer chains.

#### Thermodynamics of Polymer Solution

At first, I introduce a classical theory for the mixing of polymer and solvent, so-called Flory-Huggins theory.[12] Now we consider the mixing of flexible homopolymer chains

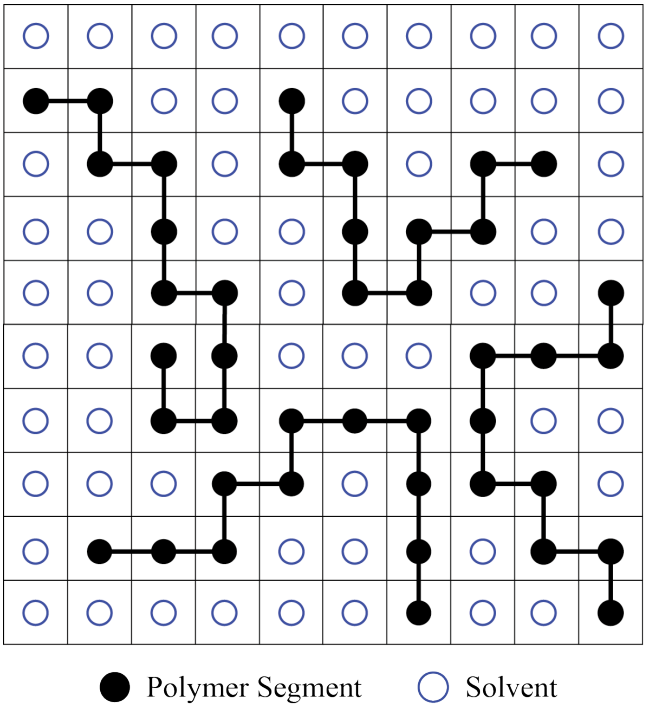


Figure 5.13: Illustration of flexible polymer chains and solvent molecules in a lattice.

in solvent. Figure 5.13 illustrates flexible polymer chains and solvent molecules in a virtual two dimensional lattice. The volume of each cell, $v_0$, is set to be equal to the volume of a solvent molecule. In the lattice model, polymer chains are divided into segments whose volume is equal to $v_0$. The total number of cells in the lattice is $\Omega = V/v_0$ where $V$ is the total volume of the lattices. The configurational entropy, $S(N_0, N_1)$ of $N_0$ solvent molecules and $N_1$ polymer chains are related to the number

of possible configuration $W(N_0, N_1)$ as follows:

$$S(N_0, N_1) = k_{\mathrm{B}} \ln W(N_0, N_1) \tag{5.150}$$

Taking reference state as pure solvent and amorphous bulk polymer, the mixing entropy change $\Delta S_{\mathrm{mix}}$ is defined by

$$\Delta S_{\mathrm{mix}} = S(N_0, N_1) - S(0, N_1) - S(N_0, 0) \tag{5.151}$$

Let $\nu_{j+1}$ represents the expected number of possible configuration of the $j+1$ th polymer chain under the coexistence of $j$ polymer chains. Then, $W(N_0, N_1)$ is calculated as

$$W(N_0, N_1) = \frac{1}{N_1! 2^{N_1}} \prod_{j=0}^{N_1 - 1} \nu_{j+1} \tag{5.152}$$

The number of available cells for the first monomer of $j+1$ th chain is equal to the number of vacant cells, $\Omega - jz$ where $z$ is the number of segments in a polymer chain. For the second segment, $s(1-p_j)$ cells are available where $s$ denotes the number of adjacent cell to the first segment. $p_j$ is the possibility that a cell is occupied by a segment of other polymers and $p_j \approx jz/\Omega$ under a mean field approximation. Similarly, $(s-1)(1-p_j)$ cells are available to the third segment because one of the adjacent cells of the second segment is occupied by the first segment. Eventually, $\nu_{j+1}$ can be estimated as follows:

$$\nu_{j+1} = s(s-1)^{z-2}(\Omega - jz)(1-p_j)^{z-1} \tag{5.153}$$

Substituting eq. (5.152) and eq. (5.153) into eq. (5.150), the following equation is obtained for $S(N_0, N_1)$.

$$S(N_0, N_1) = k_{\mathrm{B}} \left[ -N_1 \ln \phi_1 - N_0 \ln \phi_0 + N_1 \ln \left( \frac{zs(s-1)^{z-2}}{2e^{z-1}} \right) \right] \tag{5.154}$$

Here, Stirling's approximation is used.[1)] $\phi_0 = N_0/\Omega$ and $\phi_1 = zN_1/\Omega$ are volume fraction of solvent and polymer chains. The third term is equal to $S(0, N_1)$ representing disorientation entropy of polymer chains: it corresponds to the entropy change of bulk polymer chains during phase transition from virtual crystalline state to amorphous state. Considering $S(N_0, 0) = 0$, the mixing entropy change becomes

$$\Delta S_{\mathrm{mix}} = -k_{\mathrm{B}} \left[ N_0 \ln \phi_0 + N_1 \ln \phi_1 \right] \tag{5.155}$$

[1)] $\ln n! \approx n \ln n - n$ for positive integer, $n$

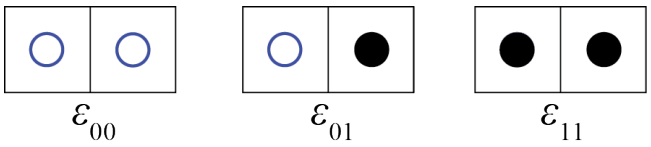


Figure 5.14: Illustration for contacts of a solvent molecule and a polymer segment in the lattice model.

Next, we consider the mixing energy. Figure 5.14 illustrate the three kinds of contacts of a solvent molecule and a polymer segment on the lattice model. Let $\epsilon_{00}$, $\epsilon_{01}(=\epsilon_{10})$, and $\epsilon_{11}$ represent the interaction energy corresponding to solvent-solvent, solvent-polymer, and polymer-polymer contacts, respectively. Under a mean-field approximation, the number of solvent-polymer contacts for a given polymer segment is estimated to be $(s-2)\phi_0$. Therefore, the total number of solvent-polymer contact $N_{01} = N_{10} = zN_1(s-2)\phi_0$. Similarly, $N_{00} = N_0 s\phi_0/2$ and $N_{11} = zN_1(s-2)\phi_1$. Approximating $s-2$ by $s$, the mixing energy becomes

$$\begin{aligned}\Delta U_{\mathrm{mix}} &= \left[szN_1\phi_0\epsilon_{01} + \frac{s}{2}N_0\phi_0\epsilon_{00} + \frac{s}{2}zN_1\phi_1\epsilon_{11}\right] - \left[\frac{s}{2}zN_1\epsilon_{11} + \frac{s}{2}N_0\epsilon_{00}\right] \\ &= k_{\mathrm{B}}T\Omega\phi_0\phi_1\chi(T) \end{aligned} \tag{5.156}$$

Here, the defition of the interaction parameter $\chi(T)$ is

$$\chi(T) \equiv \frac{s}{k_{\mathrm{B}}T}\left[\epsilon_{01} - \frac{1}{2}\left(\epsilon_{00}+\epsilon_{11}\right)\right] \tag{5.157}$$

Eventually, the mixing free energy of polymer solution is given as

$$\begin{aligned}\Delta F_{\mathrm{mix}} &= \left[\Delta U_{\mathrm{mix}} - T\Delta S_{\mathrm{mix}}\right] \\ &= k_{\mathrm{B}}T\left[N_0\ln\phi_0 + N_1\ln\phi_1 + \Omega\chi(T)\phi_0\phi_1\right] \end{aligned} \tag{5.158}$$

and then the mixing free energy per unit cell is

$$\Delta f_{\mathrm{mix}} = k_{\mathrm{B}}T\left[(1-\phi)\ln(1-\phi) + \frac{\phi}{z}\ln\phi + \chi(T)\phi(1-\phi)\right] \tag{5.159}$$

where $\phi_1$ is rewritten as $\phi$. Chemical potential of solvent molecule is calculated based on eq. (5.158).[2)]

$$\Delta\mu_0 \equiv \frac{\partial\Delta F_{\mathrm{mix}}}{\partial N_0} = k_{\mathrm{B}}T\left[\ln(1-\phi) + \left(1-\frac{1}{z}\right)\phi + \chi(T)\phi^2\right] \tag{5.160}$$

Here, The reference state of $\mu_0$ is pure solvent. Osmotic pressure $\pi$ is therefore

$$\begin{aligned}\pi \equiv -\frac{\Delta\mu_0}{v_0} &= \frac{k_{\mathrm{B}}T}{v_0}\left[\ln(1-\phi) + \left(1-\frac{1}{n}\right)\phi + \chi(T)\phi^2\right] \\ &= \frac{k_{\mathrm{B}}T}{v_0}\left[\frac{1}{z}\phi + \left(\frac{1}{2}-\chi(T)\right)\phi^2 + \frac{1}{3}\phi^3 + \cdots\right] \end{aligned} \tag{5.161}$$

[2)] Take care of the following partial differential: $\dfrac{\partial\phi_0}{\partial N_0} = \dfrac{1-\phi_0}{\Omega}$, $\dfrac{\partial\phi_1}{\partial N_0} = -\dfrac{\phi_1}{\Omega}$

On the other hand, $\pi$ can be generally represented in the form of virial expansion.

$$\pi = RT\left[\frac{c}{M} + A_2c^2 + A_3c^3 + \cdots\right] \tag{5.162}$$

Here, $M$, $A_2$, and $A_3$ are molecular weight of the polymer chain, the second virial coefficient, and the third virial coefficient, respectively. $c$ is the weight concentration defined as $c \equiv zmN_1/N_\mathrm{A}V = \phi m/N_\mathrm{A}v_0$ ($m$: molecular weight of the segment, $N_\mathrm{A}$: Avogadro constant). Comparing eq. (5.161) and eq. (5.162),

$$A_2 = \frac{N_\mathrm{A}v_0}{m^2}\left[\frac{1}{2} - \chi(T)\right] \tag{5.163}$$

It indicates that $\Theta$ condition ($A_2$ =0) is equivalent to $\chi(\Theta) = 1/2$ where $\Theta$ is so-called theta temperature. For the temperature dependence of $\chi(T)$, the following expansion of $1/2 - \chi(T)$ around $\Theta$ with respect to temperature difference $1 - \Theta/T$ was proposed by Flory.[12]

$$\frac{1}{2} - \chi(T) = \psi\left(1 - \frac{\Theta}{T}\right) \tag{5.164}$$

As is clear from the derivation of eq. (5.158), $\chi(T)$ contains only energetic term. However, many experimental results have indicated that $\chi(T)$ has significant entropic contribution[13] which is represented by $\psi$ in eq. (5.164). The following expression for $\chi(T)$ is often used for description of experimental results.

$$\chi(T) = \chi_S + \frac{\chi_H}{T} \tag{5.165}$$

Here, $\chi_S$ and $\chi_H$ respresents entropic and enthalpic contribution to $\chi(T)$: $\chi_S$ can be regarded as the effect of local ordering arising from contact of solvent and polymer.

Let us derive the relationship between $\chi(T)$ or $A_2$ and excluded volume $V_\mathrm{ex}$ of a polymer chain. Now we consider dilute solution in which $N_1$ identical polymer chains of excluded volume $V_\mathrm{ex}$ are randomly distributed over a volume $V$. The first polymer chain effectively excludes volume $V_\mathrm{ex}$ and consequently the available space for the second molecule becomes $V - V_\mathrm{ex}$. Then, the total number of configurations of $N_1$ chains is written as

$$W = \text{Const.} \times \prod_{j=0}^{N_1-1}(V - jV_\mathrm{ex}) \tag{5.166}$$

Considering that energetic term is automatically contained in $V_\mathrm{ex}$, the mixing free energy becomes

$$\begin{aligned}\Delta F_\mathrm{mix} &= -k_\mathrm{B}T\ln W \\ &= -k_\mathrm{B}T\left[N_1\ln V + \sum_{j=1}^{N_1-1}\ln\left(1 - \frac{jV_\mathrm{ex}}{V}\right)\right] + \text{Const.}\end{aligned} \tag{5.167}$$

Since $jV_{\mathrm{ex}} \ll V$ in the sufficiently dilute solution, expansion of the second term in the RHS gives

$$\begin{aligned}\Delta F_{\mathrm{mix}} &\approx -k_{\mathrm{B}}T\left[N_1 \ln V - \frac{V_{\mathrm{ex}}}{V}\sum_{j=1}^{N_1-1} j\right] + \text{Const.} \\ &\approx -N_1 k_{\mathrm{B}}T\left[\ln V - \frac{N_1}{2}\frac{V_{\mathrm{ex}}}{V}\right] + \text{Const.}\end{aligned} \tag{5.168}$$

Through the similar procedure to eq. (5.160) and eq. (5.161), we obtain osmotic pressure as

$$\begin{aligned}\pi &\approx k_{\mathrm{B}}T\left[\frac{N_1}{V} + \frac{N_1^2}{2}\frac{V_{\mathrm{ex}}}{V^2}\right] \\ &= RT\left[\frac{c}{M} + \frac{N_{\mathrm{A}}V_{\mathrm{ex}}}{2M^2}c^2\right] \quad \left(c = \frac{M}{N_{\mathrm{A}}}\frac{N_1}{V}\right)\end{aligned} \tag{5.169}$$

In comparison with eq. (5.162) and eq. (5.163), we can obtain the following relationship.

$$V_{\mathrm{ex}} = \frac{2M^2}{N_{\mathrm{A}}}A_2 \tag{5.170}$$

$$V_{\mathrm{ex}} = z^2 v_0\left[1 - 2\chi(T)\right] \tag{5.171}$$

**Single Contact Approximation[14]**

Now we consider scattering function of dilute polymer solution. First of all, scattering intensity of polymer solution per unit volume is given as

$$I_u(q) = \frac{(\Delta\rho v_0)^2}{V}\left|\sum_{\alpha=1}^{N}\sum_{j=1}^{z}\exp\left[-i\boldsymbol{q}\cdot\boldsymbol{r}_{\alpha j}\right]\right|^2 \tag{5.172}$$

where $N$ denotes total number of polymer chain in irradiated volume $V$ and $\Delta\rho$ is scattering length density of the polymer segment. $\boldsymbol{r}_{\alpha j}$ is the position of the $j$ th segment on $\alpha$ th polymer chain. Separating the intramolecular from the intermolecular term,

$$\begin{aligned}I_u(q) &= \frac{(\Delta\rho v_0)^2}{V}\left[N\left|\sum_{j=1}^{z}\exp\left[-i\boldsymbol{q}\cdot\boldsymbol{r}_j\right]\right|^2 + \sum_{\alpha=1}^{N}\sum_{\beta\neq\alpha}^{N}\sum_{j=1}^{z}\sum_{l=1}^{z}\exp\left[-i\boldsymbol{q}\cdot\boldsymbol{r}_{\alpha j\beta l}\right]\right] \\ &= \frac{(\Delta\rho v_0)^2}{V}\left[Nz^2 D(x) + N(N-1)\sum_{j=1}^{z}\sum_{l=1}^{z}\left\langle\exp\left[-i\boldsymbol{q}\cdot(\boldsymbol{r}_{1j2l})\right]\right\rangle\right]\end{aligned} \tag{5.173}$$

Here, $\boldsymbol{r}_{\alpha j\beta l} \equiv \boldsymbol{r}_{\alpha j} - \boldsymbol{r}_{\beta l}$ and $\langle\dots\rangle$ denotes the ensemble average. The first term corresponds to Debye function which is derived in eq. (5.148). Now we assume that a polymer chain in the solution contacts other polymer chains at only single

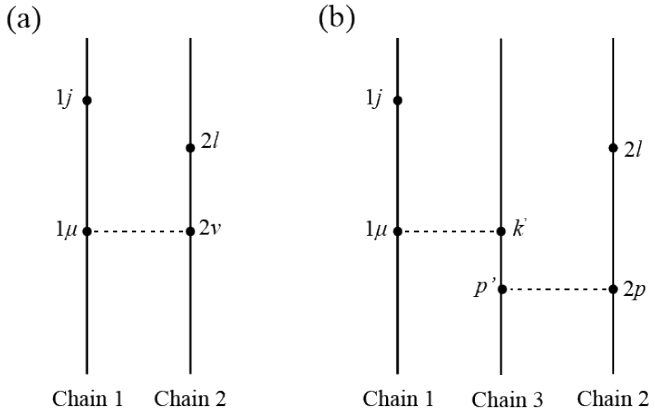


Figure 5.15: (a) Direct single contact interaction of chain 1 and chain 2. (b) Indirect interaction between chain 1 and chain 2 through single contacts of chain 1-3 and chain 3-2.

point, so-called single contact approximation. Assuming the condition that chain 1 directly contacts chain 2 as shown in Figure 5.15(a), $\boldsymbol{r}_{1j2l}$ can be expressed to be $\boldsymbol{r}_{1j2l} = \boldsymbol{r}_{1j1\mu} + \boldsymbol{r}_{1\mu2\nu} + \boldsymbol{r}_{2\nu2l}$. Then, the three vectors $\boldsymbol{r}_{1j1\mu}$, $\boldsymbol{r}_{1\mu2\nu}$, and $\boldsymbol{r}_{2\nu2l}$ are independent and the second term of eq. (5.173) can be decomposed as follows:

$$\langle \exp\left[-i\boldsymbol{q}\cdot\boldsymbol{r}_{1j2l}\right]\rangle = \sum_{\mu=1}^{z}\sum_{\nu=1}^{z} \langle \exp\left[-i\boldsymbol{q}\cdot\boldsymbol{r}_{1j1\mu}\right]\rangle \langle \exp\left[-i\boldsymbol{q}\cdot\boldsymbol{r}_{1\mu2\nu}\right]\rangle \langle \exp\left[-i\boldsymbol{q}\cdot\boldsymbol{r}_{2\nu2l}\right]\rangle \tag{5.174}$$

For the second term,

$$\langle \exp\left[-i\boldsymbol{q}\cdot\boldsymbol{r}_{1\mu2\nu}\right]\rangle = \int_V w(r_{1\mu2\nu}) \exp\left[-i\boldsymbol{q}\cdot\boldsymbol{r}_{1\mu2\nu}\right] \mathrm{d}\boldsymbol{r}_{1\mu2\nu} \tag{5.175}$$

where $w(r_{1\mu2\nu})$ represents the probability distribution of $\boldsymbol{r}_{1\mu2\nu}$. Introducing the excluded volume of a segment as $v_{\mathrm{ex}} \equiv V_{\mathrm{ex}}/z^2 \equiv 4\pi a^3/3$,[3)] interaction potential $U(r_{1\mu2\nu})$ can be written as

$$U(r_{1\mu2\nu}) = \begin{cases} \infty & (r_{1\mu2\nu} \le a) \\ 0 & (r_{1\mu2\nu} > a) \end{cases} \tag{5.176}$$

where $a$ is the radius of the excluded volume. Then $w(r_{1\mu2\nu})$ is given as follows:

$$w(r_{1\mu2\nu}) = \frac{1}{V}\exp\left[-\frac{U(r_{1\mu2\nu})}{k_{\mathrm{B}}T}\right] = \begin{cases} 0 & (r_{1\mu2\nu} \le a) \\ V^{-1} & (r_{1\mu2\nu} > a) \end{cases} \tag{5.177}$$

[3)] For a polymer, there are $z^2$ possibilities of contact with another polymer.

and eq. (5.175) becomes

$$\begin{aligned}\langle \exp\left[-i\boldsymbol{q}\cdot\boldsymbol{r}_{1\mu 2\nu}\right]\rangle &= \frac{(2\pi)^3}{V}\delta(\boldsymbol{q}) - \int_0^\infty \left(\frac{1}{V} - w(r_{1\mu 2\nu})\right) 4\pi r^2 \frac{\sin qr}{qr} \mathrm{d}r_{1\mu 2\nu} \\ &= -\frac{v_{\mathrm{ex}}}{V}\frac{3\left(\sin qa - qa\cos qa\right)}{(qa)^3} \quad (q \neq 0) \\ &\approx -\frac{v_{\mathrm{ex}}}{V} \quad (qa \to 0) \end{aligned} \tag{5.178}$$

Substituting eq. (5.174) and eq. (5.178) into eq. (5.173), we obtain

$$\begin{aligned} I_u(q) &= \frac{(\Delta\rho v_0)^2}{V}\left[Nz^2D(x) - N^2\frac{v_{\mathrm{ex}}}{V}\sum_{j=1}^{z}\sum_{\mu=1}^{z}\langle\exp\left[-i\boldsymbol{q}\cdot\boldsymbol{r}_{1j1\mu}\right]\rangle\sum_{l=1}^{z}\sum_{\nu=1}^{z}\langle\exp\left[-i\boldsymbol{q}\cdot\boldsymbol{r}_{2\mu 2l}\right]\rangle\right] \\ &= \frac{(\Delta\rho v_0)^2}{V}\left[Nz^2D(x) - N^2\frac{v_{\mathrm{ex}}}{V}(z^2D(x))^2\right] \end{aligned} \tag{5.179}$$

where $N(N-1)$ is approximated by $N^2$.

Next, let us consider another type of interaction which is illustrated in Figure 5.15(b): chain 1 and chain 2 interact through contacts with chain 3. Similarly to the preceding discussion, $\boldsymbol{r}_{1j2l}$ can be expressed as the sum of $\boldsymbol{r}_{1j1\mu}$, $\boldsymbol{r}_{1\mu k'}$, $\boldsymbol{r}_{k'p'}$, $\boldsymbol{r}_{p'2p}$, and $\boldsymbol{r}_{2p2l}$ (see Figure 5.15). Assuming that the five vectors are independent, the contribution term from the interaction of Figure 5.15(b) takes the form

$$\left(\frac{v_{\mathrm{ex}}}{V}\right)^2 N^3[z^2D(x)]^3 \tag{5.180}$$

More generally, the contribution term which corresponds to the interaction through $(p-1)$ chains becomes

$$\left(-\frac{v_{\mathrm{ex}}}{V}\right)^p N^{p+1}[z^2D(x)]^{p+1} \tag{5.181}$$

Considering the multi-chain interaction, we can obtain $I(q)$ as follows:

$$I_u(q) = \frac{(\Delta\rho v_0)^2}{V}\left[\sum_{p=0}^{\infty}\left(-\frac{v_{\mathrm{ex}}}{V}\right)^p N^{p+1}[z^2D(x)]^{p+1}\right] \tag{5.182}$$

When $(v_{\mathrm{ex}}/V)Nz^2D(x) < 1$, this series can be summed and we obtain eventually

$$\begin{aligned} I_u(q) &= \frac{(\Delta\rho v_0)^2}{V}\frac{Nz^2D(x)}{1 + (v_{\mathrm{ex}}/V)Nz^2D(x)} \\ &= \Delta\rho^2\frac{v_p\phi D(x)}{1 + (1-2\chi)(v_p/v_0)\phi D(x)} \end{aligned} \tag{5.183}$$

where $v_p = zv_0$ is the volume of a polymer chain. Furthermore, using the Guinier approximation for $D(x)$, this equation can be rewritten as

$$\begin{aligned} \frac{Kc}{I_u(q)} &= \frac{1}{M}D(x)^{-1} + 2A_2c \\ &\approx \frac{1}{M}\left(1 + \frac{R_g^2}{3}q^2\right) + 2A_2c \quad (x \to 0) \end{aligned} \tag{5.184}$$

Here, the contrast factor $K$ is defined as $K \equiv \Delta\rho^2/N_{\mathrm{A}}d_{\mathrm{polymer}}$ ($d_{\mathrm{polymer}}$: mass density of the polymer in solution). The plot of $Kc/I(q)$ against $q^2 + c$ is called Zimm plot. The extrapolation of $q \to 0$ and $c \to 0$ in Zimm plot allow as to evaluate the molecular weight of polymer chain.

## Experimental Data Reduction and Absolute Scaling[15]

Small-angle scattering apparatus typically utilize two dimensional detectors to obtain information about anisotropic structures in sample. Even for isotropic samples, two dimensional detectors are advantageous because one can improve the statistical accuracy of scattering intensity profile through a circular averaging. This section summarize the data reduction procedure in small-angle scattering experiments with a two-dimensional detector.

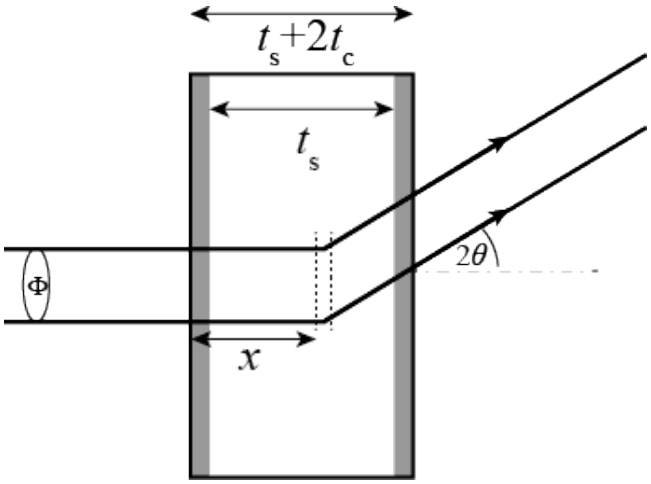


Figure 5.16: The path of X-ray that passes through the sample filled in a planar-type sample cell. The scattering geometry is illustrated to be assymetric as is the case in typical small-angle scattering experiments.

Now we consider the scattering intensity from a planar sample of thickness $t_s$ injected into a planar-type sample cell of thickness $t_c$ (see Figure 5.16). In small-angle scattering, $\theta$-dependence of the absorption factor, the polarization factor, and the irradiated volume can be neglected. Then, similarly to eq. (5.104), the scattering intensity per solid angle $\mathrm{d}I(2\theta, x)$ due to the layer $\mathrm{d}x$ can be calculated as follows:

$$\mathrm{d}I(2\theta,x) = \begin{cases} I_0\Phi\dfrac{\partial\sigma^{\mathrm{s}}}{\partial\Omega}(\theta)\mathrm{d}x\exp\left[-\left(\mu_{\mathrm{s}}t_{\mathrm{s}}+2\mu_{\mathrm{c}}t_{\mathrm{c}}\right)\right] & (t_{\mathrm{c}}\le x\le t_{\mathrm{s}}+t_{\mathrm{c}}) \\ I_0\Phi\dfrac{\partial\sigma^{\mathrm{c}}}{\partial\Omega}(\theta)\mathrm{d}x\exp\left[-\left(\mu_{\mathrm{s}}t_{\mathrm{s}}+2\mu_{\mathrm{c}}t_{\mathrm{c}}\right)\right] & (x<t_{\mathrm{c}}, x>t_{\mathrm{s}}+t_{\mathrm{c}}) \end{cases} \tag{5.185}$$

$I_0$, $\Phi$, $\mu$, and $\partial\sigma/\partial\Omega$ are the flux of incident beam, cross sectional area of the incident beam, the linear attenuation coefficient,[4)] and the differencial scattering cross section per unit volume, respectively. Hereafter, the indices "s" and "c" are used for the physical properties of the sample and the cell. Then, let $I_i^{s+c}$ represents the number

[4)] Both scattering and absorption contribute to the beam attenuation in the sample. In the case of X-ray, the effect of absorption is dominant and $\mu$ can be regarded as the linear "absorption" coefficient.

of photon or neutron which is detected on $i$ th pixel of the two-dimensional detector per unit of time,

$$\begin{aligned} I_i^{\mathrm{s+c}} &= \eta_i \Delta\Omega_i \int_0^{t_\mathrm{s}+2t_\mathrm{c}} \mathrm{d}I(2\theta, x)\mathrm{d}x + I_i^{\mathrm{noise}} \\ &= I_0 \Phi \eta_i \Delta\Omega_i T_{\mathrm{s+c}} \left[ t_s \frac{\mathrm{d}\sigma^s}{\mathrm{d}\Omega}(\theta) + 2t_c \frac{\mathrm{d}\sigma^c}{\mathrm{d}\Omega}(\theta) \right] + I_i^{\mathrm{noise}} \end{aligned} \tag{5.186}$$

$\eta_i$ and $\Delta\Omega_i$ is the detection efficiency of $i$ th pixel and the solid angle incident on $i$ th pixel. $I_i^{\mathrm{noise}}$ is the intensity arising from background noise. $T_{\mathrm{s+c}} = \exp[-(\mu_\mathrm{s} t_\mathrm{s} + 2\mu_\mathrm{c} t_\mathrm{s})]$ is the transmission of the sample with the cell. To obtain $\partial\sigma^{\mathrm{s}}(\theta)/\partial\Omega$, we need to do corrections for the unnecessary prefactors, the scattering intensity of the cell, and $I_i^{\mathrm{noise}}$.

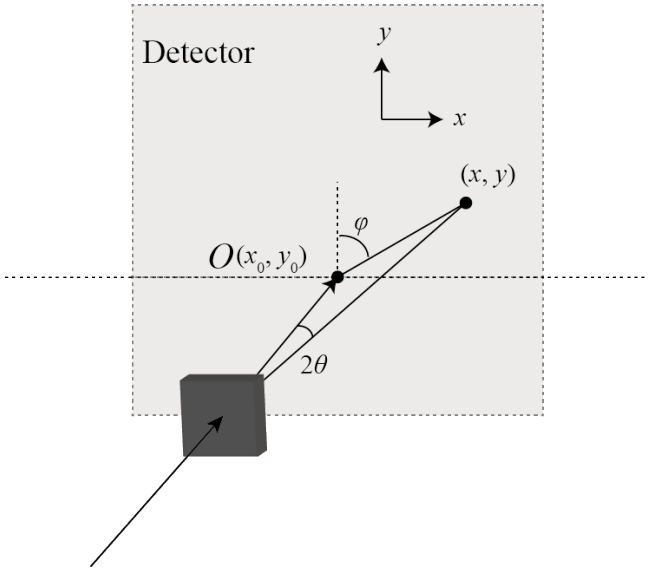


Figure 5.17: Typical scattering geometry of a sample, a two-dimensional detector, and the incident beam in small-angle scattering experiment.

Now we consider a pixel on the coordinates $(x, y)$ in the two-dimensional detector (Figure 5.17). The distance from beam center $(x_0, y_0)$ to the pixel is

$$r = \sqrt{(x - x_0)^2 + (y - y_0)^2} \tag{5.187}$$

and the corresponding scattering angle $\theta$ and the scattering vector $q$ is given as

$$\theta = \frac{1}{2} \arctan\left(\frac{r}{L}\right) \tag{5.188}$$

$$q = \frac{4\pi}{\lambda} \sin\left[\frac{1}{2} \arctan\left(\frac{r}{L}\right)\right] \tag{5.189}$$

Here, the solid angle incident on a pixel, $\Delta\Omega_i$ is given as

$$\begin{aligned}\Delta\Omega_i &= \frac{\Delta S_i \cos 2\theta}{L_i^2} \\ &= \frac{\Delta S_i \cos^3 2\theta}{L^2} \quad (L_i \cos 2\theta = L)\end{aligned} \tag{5.190}$$

where $\Delta S_i$ and $L_i$ is the area of the pixel and the distance from sample position to $i$ th pixel, respectively. $L$ is the sample to detector distance. In additin, the intensity of background noise, $I_i^{\mathrm{noise}}$ can be easily measured by inserting a strongly absorbing material into the sample position. Performing the correction for the solid angle and the background noise, we obtain the corrected scattering intensity of the sample $I_{i,\mathrm{cor}}^{\mathrm{s+c}}$ as follows:

$$I_{i,\mathrm{cor}}^{\mathrm{s+c}} = \frac{I_i^{\mathrm{s+c}} - I_i^{\mathrm{noise}}}{\cos^3 2\theta} \tag{5.191}$$

Assuming that $\Delta S_i$ and $\eta_i$ are constant for each individual pixel, one-dimensional scattering profile is obtained by the following circular averaging:

$$\begin{aligned}I_{\mathrm{cor}}^{s+c}(q) &= \frac{1}{\Delta N} \sum_{r' \le r < r' + \Delta r} I_{i\mathrm{cor}}^{\mathrm{s+c}} \\ &= I_0 \Phi \eta_i T_{s+c} \left[ t_s \frac{\mathrm{d}\sigma^s}{\mathrm{d}\Omega}(\theta) + 2t_c \frac{\mathrm{d}\Sigma^c}{\mathrm{d}\Omega}(\theta) \right] \frac{\Delta S}{L^2}\end{aligned} \tag{5.192}$$

Here, the summation is taken over $\Delta N$ pixels that exist in the area of $r' \le r < r' + \Delta r$. The $q$ value corresponding to the area element is calculated as

$$q = \frac{4\pi}{\lambda} \sin \left[ \frac{1}{2} \arctan \left( \frac{r + \Delta r/2}{L} \right) \right] \tag{5.193}$$

$I_{\mathrm{cor}}^{s+c}(q)$ is the averaged scattering intensity among an iso-$q$ circumference on the two-dimensional detector. Thus, the standard deviation of $I_{\mathrm{cor}}^{s+c}(q)$ is $\Delta N^{1/2}$ times smaller than that of individual $I_{i,\mathrm{cor}}^{\mathrm{s+c}}$.

When we measure an empty sample cell, the one-dimensional scattering intensity $I_{\mathrm{cor}}^{\mathrm{c}}(q)$ becomes

$$I_{\mathrm{cor}}^{\mathrm{c}} = I_0 \Phi \eta_i T_c \left[ 2t_c \frac{\mathrm{d}\sigma^c}{\mathrm{d}\Omega}(\theta) \right] \frac{\Delta S}{L^2} \tag{5.194}$$

where $T_{\mathrm{c}} = \exp[-2\mu_{\mathrm{c}} t_{\mathrm{c}}]$ is the transmission of an empty sample cell. According to eq. (5.192) and eq. (5.194), the corrected scattering intensity of sample is obtained as

$$\begin{aligned}I_{\mathrm{cor}}^{s}(q) &= \left[ \frac{I_{\mathrm{cor}}^{s+c}(q)}{T_{s+c}} - \frac{I_{\mathrm{cor}}^{c}(q)}{T_c} \right] \frac{1}{t_s} \\ &= I_0 \Phi \eta \frac{\Delta S}{L^2} \frac{\mathrm{d}\Sigma^s}{\mathrm{d}\Omega}(\theta)\end{aligned} \tag{5.195}$$

For the determination of the $q$-independent prefactors in eq. (5.195), we need a measurement of a standard sample. As a secondary standard material, glassy carbon is often used in small-angle scattering. The corrected scattering intensity of glassy carbon is given as

$$I_{\mathrm{cor}}^{\mathrm{GC}}(q) = I_0 \Phi \eta \frac{\Delta S}{L^2} \frac{\mathrm{d}\sigma^{\mathrm{GC}}}{\mathrm{d}\Omega}(\theta) \tag{5.196}$$

When the differencial scattering cross section per unit volume of glassy carbon is already known, the normalization factor for absolute scaling, $A_{\mathrm{GC}}$ can be estimated by

$$A_{\mathrm{GC}} = \left( I_0 \Phi \eta \frac{\Delta S}{L^2} \right)^{-1} = \frac{\mathrm{d}\sigma^{\mathrm{GC}}}{\mathrm{d}\Omega}(\theta) \Big/ I_{\mathrm{cor}}^{\mathrm{GC}}(q) \tag{5.197}$$

Eventually, the differencial scattering cross section per unit volume of sample is obtained as follows:

$$\frac{\mathrm{d}\sigma^{s}}{\mathrm{d}\Omega}(\theta) = A_{\mathrm{GC}} I_{\mathrm{cor}}^{s}(q) \tag{5.198}$$

## Reference


[1] Roe, R. J. *Methods of X-Ray and Neutron Scattering in Polymer Science*; Oxford University Press, 2000.

[2] Hansen, J. P.; MacDonald, I. R. *Theory of Simple Liquids with Applications to Soft Matter*, 4th ed.; Elsevior, 2013.

[3] Pings, C. J.; Waser, J. *J. Chem. Phys.* **1968**, *48*, 3016.

[4] Waseda, Y. *The Structure of Non-crystalline Materials*; McGraw-Hill, 1980.

[5] Sakai, S. *KEK Report*; National Laboratory for High Energy Physics: Tsukuba, Japan, 1990; Vol. 90-16.

[6] Wilson, A. J. C. *International Tables for Crystallograph, Vol. C*; Kluwer Academic Publications, 1992.

[7] Cromer, D. T. *J. Chem. Phys.* **1969**, *50*, 4857–4859.

[8] Hubbell, J. H.; Veigele, W. J.; Briggs, E. A.; Brown, R. T.; Cromer, D.; Howerton, R. J. *J. Phys. Chem. Ref. Data* **1975**, *4*, 471–538.

[9] Lorch, E. *J. Phys. Chem.* **1969**, *2*, 229–237.

[10] Higgins, J. S.; Benoit, H. C. *Polymers and Neutron Scattering*; Oxford University Press, 1994.

[11] Livsey, I. *J. Chem. Soc., Faraday Trans.* **1987**, *83*, 1445–1452.

[12] Flory, P. J. *Principles of Polymer Chemistry*; Cornell University, 1953.

[13] Shultz, A. R.; Flory, P. J. *J. Am. Chem. Soc.* **1952**, *74*, 4760–4767.

[14] Benoit, H.; Benmouna, M. *Polymer* **1984**, *25*, 1059–1067.

[15] Wignall, G. D.; Bates, F. S. *J. Appl. Cryst.* **1987**, *20*, 28–40.

# List of Publications

## Original Papers

1. Hirosawa, K.; Fujii, K.; Hashimoto, K.; Umebayashi, Y.; Shibayama, M. Microscopic Solvation Structure of Glucose in 1-Ethyl-3-methylimidazolium Methylphosphonate Ionic Liquid., *J. Phys. Chem. B.* **2015**, *119*, 6262
(**chapter 2**)

2. Hirosawa, K.; Fujii, K.; Hashimoto, K.; Shibayama, M. Solvated Structure of Cellulose in a Phosphonate-based Ionic Liquid., *Macromolecules* **2017**, *50*, 6509
(**chapter 3**)

3. Hirosawa, K.; Fujii, K.; Ueki, T.; Kitazawa, Y.; Littrell, K. C.; Watanabe, M.; Shibayama, M. SANS Study on the Solvated Structure and Molecular Interactions of a Thermo-responsive Polymer in a Room Temperature Ionic Liquid., *Phys. Chem. Chem. Phys.* **2016**, *18*, 17881
(**chapter 4**)

4. Hirosawa, K.; Fujii, K.; Ueki, T.; Kitazawa, Y.; Watanabe, M.; Shibayama, M. Pressure Response of a Thermoresponsive Polymer in an Ionic Liquid., *Macromolecules* **2016**, *49*, 8249
(**chapter 5**)

## Other publications

- Li, X.; Hirosawa, K.; Sakai, T.; Gilbert, E. P.; Shibayama, M. SANS Study on Critical Polymer Clusters of Tetra-functional Polymers., *Macromolecules* **2017**, *50*, 3655

- Fujii, K.; Ueki, T.; Hashimoto, K.; Kobayashi, Y.; Kitazawa, Y.; Hirosawa, K.; Matsugami, M.; Ohara, K.; Watanabe, M.; Shibayama, M. Microscopic Structure of Solvated Poly(benzyl methacrylate) in an Imidazolium-based Ionic Liq-

uid: High-Energy X-ray Total Scattering and All-atom MD Simulations Study., *Macromolecules* **2017**, *50*, 4780

# Acknowledgement

This dissertation is based on the study carried out in the research group of Professor Mitsuhiro Shibayama at Department of Advanced Materials Science, Graduate School of Frontier Sciences, The University of Tokyo from 2013 to 2018.

First of all, I would like to thank **Professor Mitsuhiro Shibayama**. This dissertation is supported by his patient instruction in all aspects of my research. He took so much time for discussion with me, and always provided me with fundamental advice from his deep and broad range of knowledge in polymer physics. Furthermore, as a Ph. D student, I learned a lot from his attitude as a scientist.

I am deeply grateful to **Associate Professor Kenta Fujii** for introducing me into the field of ionic liquids and solution chemistry. He gave me a crucial instruction about methodology to investigate microscopic structure of ionic liquid systems. His advices as a physical chemist provided unique viewpoints for me to perform structural study on polymer solution systems; and it accounts for a large part in significance of this dissertation.

I would also like to thank **Professor Masayoshi Watanbe**, **Dr. Takeshi Ueki**, **Dr. Yuzo Kitazawa**, and **Ms. Yumi Kobayashi** for their kind support related to the work on thermo-responsive polymers in ionic liquids, including preparation of the polymers. Without their deep knowledge about polymer in ionic liquid systems, I can not conduct this research.

In all-atom MD simulations, **Professor Yasuhiro Umebayashi** and **Assosiate Professor Masaru Matsugami** kindly provided me with rich environment for the calculation. They also gave me an instruction about analysis of data obtained by the MD simulations. I would also like to thank them.

In SAXS experiments at BL03XU in SPring-8, **Dr. Hiroyasu Masunaga**, **Dr. Taizo Kabe**, and **Dr. Atsushi Izumi** helped me with configuration of the apparatus and general discussion about data acquisition in the experiment. My beamtime at SPring-8 was often in midnight but they supported me for the experiment. I am

very grateful to their kind support.

I would also like to thank **Dr. Kenneth C. Littrell** for his kind support in my SANS experiment at GP-SANS in Oak Ridge National Laboratory. It was the first time that I obtained beautiful SANS profile, totally thanks to him.

I am also grateful to the members in Neutron Science Laboratory in the Institute of Solid State Physics. Especially, I would like to thank the members in Shibayama research group. I learned almost all of experimental techniques, such as synthesis of ionic liquids, small-angle scattering experiments, HEXTS experiment, and light scattering experiments from senior students in Shibayama group, **Dr. Kengo Nishi**, **Dr. Takumi Kusano**, **Dr Kei Hashimoto**, and **Assistant Professor Takashi Hiroi**. As staffs in Shibayama group, **Assistant Professor Xiang Li**, **Assistant Professor Ken Morishima**, and **Assistant Professor Shintaro Nakagawa** gave me meaningful suggestions in daily discussion about my research. **Ms. Mariko Abo** and **Ms. Marie Suzuki**, as secretaries of Shibayama group, supported me in procedures for performing research. I would also like to thank them.

I acknowledge the financial support, Materials Education program for the future leaders in Research, Industry, and Technology (MERIT) and research fellowships for young scientists (DC2), from Japan Society for the Promotion of Science (JSPS).

At last, I would like to express the will of the greatest thanks to my parents and brothers.

February, 2018

Kazu Hirosawa